

**Designer antibodies rope immune  
cells into attacking cancer** p. 930

**Ecosystem responses to  
invasive plants** pp. 934 & 967

**Automated synthesis of  
whole proteins** pp. 941 & 980

# Science

\$15  
29 MAY 2020

AAAS

## BACTERIA IN TUMORS

Microbes reside in many  
human cancers

pp. 938 & 973



# RESTORING HOPE



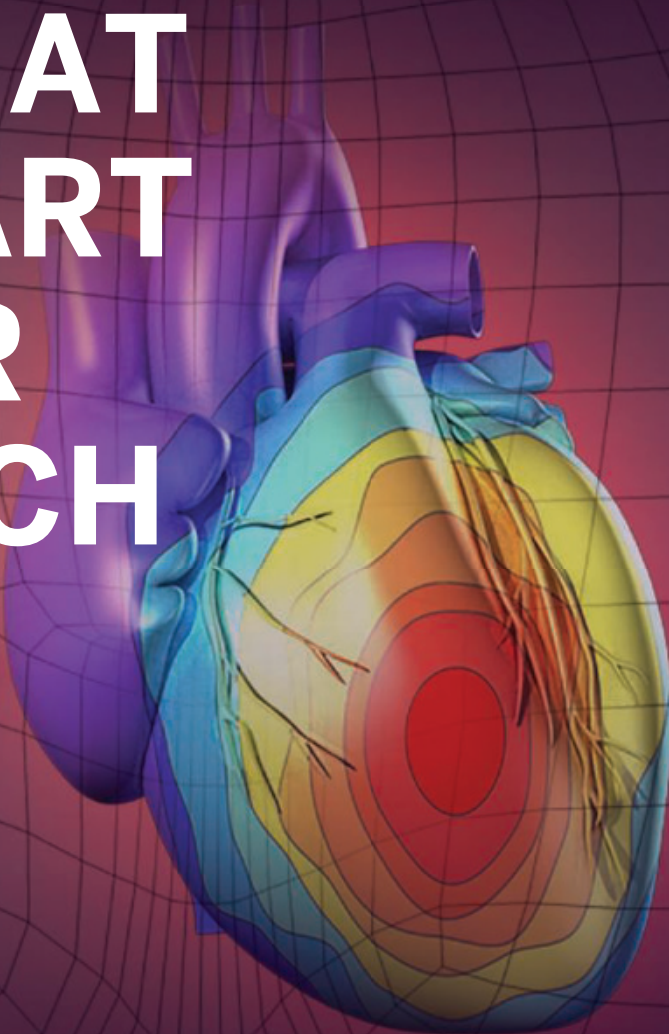
Beijing PINS Medical Equipment Co. Ltd. was established in 2008.

As an innovative high-tech enterprise with focus on neuromodulation, PINS Medical has developed a variety of clinical products, which include stimulators for deep brain, vagus nerve, spinal cord, and sacral nerve stimulation therapies. PINS Medical devotes itself to providing cutting-edge treatments for patients who suffer from neurological disorders, such as Parkinson's disease, epilepsy, chronic pain, and uroclepsia.



The name of PINS is derived from a Chinese word with the original meaning of "Magic Pin," the ability to cure disease. PINS is also an abbreviation of "Patient Is No. 1 always." This message clearly represents the goal of PINS Medical for "restoring hope," not simply as an innovation company but also across society to citizens.

# PUT HUMAN HEALTH AT THE HEART OF YOUR RESEARCH

Submit your research:  
**[cts.ScienceMag.org](https://cts.sciencemag.org)**



Science  
Translational  
Medicine  
 AAAS

 Twitter: @ScienceTM  
 Facebook: @ScienceTranslationalMedicine

# VERTEX PHARMACEUTICALS PROVES DRUG DISCOVERY IS THE ULTIMATE TEAM SPORT

Vertex Pharmaceuticals has always championed a culture of innovation, one that empowers its employees to tackle tough problems, pivot toward novel solutions, and tap creative resources in order to help patients. While the company, headquartered in Boston with research sites in San Diego and Oxford, United Kingdom, has numerous projects underway, its main mission for the last several years has been to treat cystic fibrosis (CF), a genetic disease that affects the lungs, liver, gastrointestinal tract, pancreas, sinuses, sweat glands, and reproductive tract. In the lungs, this leads to the buildup of abnormally thick, sticky mucus that can cause chronic lung infections and inflammation, often resulting in progressive lung damage and eventually leading to death. According to the Cystic Fibrosis Foundation Patient Registry, there are more than 30,000 people in the United States living with CF (and more than 70,000 worldwide), and approximately 1,000 new cases of CF are diagnosed each year.

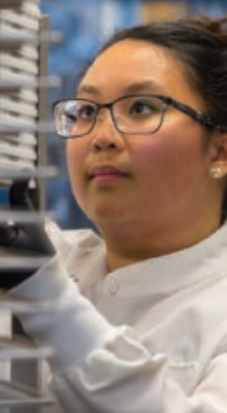
But CF is only one of several serious diseases that Vertex is working on. And by investing in science and going after the root cause of disease, the company empowers its diverse teams to “make the impossible possible,” says Reshma Kewalramani, Vertex’s chief executive officer and president. “We go after some of the most difficult scientific problems, knowing that our unique approach to drug discovery, coupled with the perseverance and commitment of our team, will get us to solutions that ultimately help patients.”

## It starts with picking the right problem

Across all of its R&D programs, Vertex has championed an innovative approach to drug discovery. “It starts with picking the right problems to go after,” says David Altshuler, Vertex’s chief scientific officer. “We only work on diseases where we have a deep understanding of the underlying human biology, validated targets, and biomarkers that translate well from the lab into people. We select diseases for which we believe we can have a transformative impact for patients, not just an incremental benefit. Then we research and develop therapeutic approaches that are most likely to succeed. Rather than looking for problems we can solve with only the tools we’ve used before, we figure out the problems that need to be solved for the diseases we’re going after and invent the tools to fix them.”



There is no “I” in “team.” Vertex is proud of its collaborative, corporate culture.



This strategy is central to Vertex and has fundamentally shaped the company's pipeline of R&D programs. It starts with a scientific problem waiting to be solved. "We first 'crack the biology' of a disease, meaning we ensure our biological target plays a causal role in the disease. Then we 'pour on the chemistry or technology' to find potential treatments," says Kewalramani. "We spend a lot of time and effort validating our laboratory assays and clinical biomarkers upfront, which gives us higher confidence that a potential therapy will succeed when we investigate it in the clinic."

Investing in scientific research is clearly where the company is focused. In 2019, 73% of the company's operating expenses were dedicated to R&D, a disproportionately large amount when compared to the average biotech and pharma companies in the industry. In addition, three out of five employees work in R&D, which Altshuler credits as the most important aspect of drug discovery.

"Discovering potential new medicines is the ultimate team sport," says Altshuler. "It takes hundreds of scientists and researchers working together to bring a new medicine to patients who are waiting."

## Team Impossible is on the case

Indeed, "I often refer to our teams as 'Team Impossible,' because no matter how big the challenge, they always find solutions that seem to defy what's possible," says Kewalramani. "This sense of urgency is incredibly important to the people living with serious diseases."

Vertex spearheads novel systems and processes to foster this velocity and tenacity. For example, in 2015, Vertex became one of the first companies to implement drug product continuous manufacturing (CM) technology in the development and production of its investigational and commercial medicines. With CM, raw materials are added into one continuously running system, and quality control takes place throughout the production process. "Continuous manufacturing results in faster, more streamlined manufacturing process development and scale-up," says Stuart Arbuckle, Vertex's chief commercial officer. "We've successfully integrated this technology into our process development, clinical and commercial supply production processes."

Another way Vertex reduces development timelines is by doing clinical studies and other development activities in parallel, where possible, instead of one at a time. "We're always looking for ways we can do multiple things at the same time, because having these faster timelines gives us the potential to get

medicines to patients quicker, and the sooner we can get medicines to patients the better," explains Carmen Bozic, Vertex's chief medical officer.

Vertex's innovations aren't just happening in the lab or in clinical studies. Nia Tatsis, Vertex's chief regulatory officer, views the company's partnerships with regulators as a critical piece of the puzzle. "Part of my goal is to ensure regulations are keeping pace with scientific innovation," she says. "Our science is evolving rapidly, and we need strong working relationships and trust with regulators to achieve our shared goal of bringing new medicines to patients who need them."

None of these advancements would be possible if not for the enterprise's prime directive: "We have developed a very special, inclusive culture at Vertex," Kewalramani shares. "More than half of our global employees are women and five out of 10 of our directors are diverse on a gender or ethnic basis—and it's that diversity of thought and experience that ensures we make the best decisions for patients and our business."

## To infinity and beyond: Tackling the next set of disease targets

"Our mission is to use scientific innovation to bring treatment options to people with serious diseases. So we're applying what we've learned in CF to a number of other serious diseases in which we understand the causal human biology and have validated targets and biomarkers with high fidelity from bench to bedside, such as sickle cell disease, alpha-1 antitrypsin deficiency, and Duchenne muscular dystrophy," says Kewalramani. "We're leveraging multiple therapeutic modalities such as cell therapies, gene editing, and mRNA [messenger RNA] therapies."

Vertex continuously asks the following questions: What else can we do to advance medicines? Where else can we apply our research in helping patients? How can we bring medicines to patients faster? By using the power of biology, chemistry, emerging technologies, creativity, and teamwork to address serious diseases, Vertex will continue to pioneer advances in science and medicine in the service of patients who are waiting for them.

Sponsored by





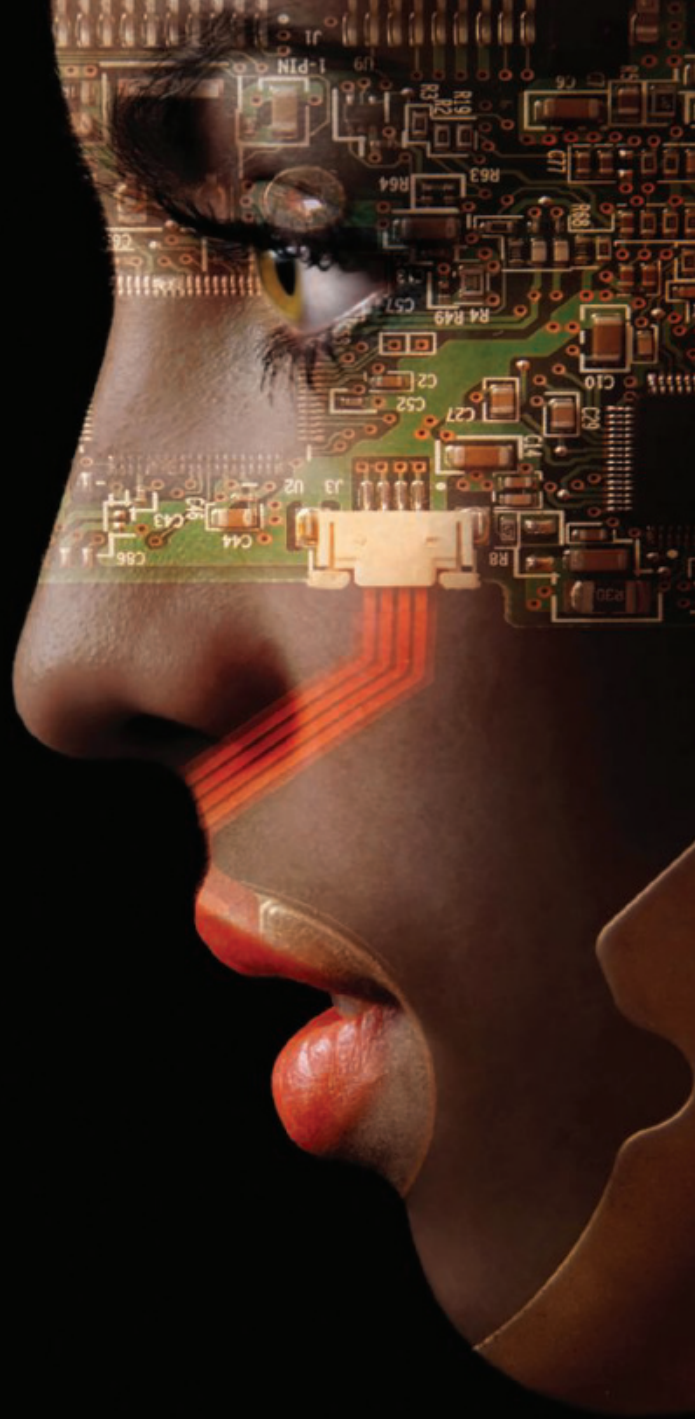
ScienceRobotics.org

# DOESN'T YOUR RESEARCH DESERVE THE BEST READERS?

Submit your research: [cts.ScienceMag.org](https://cts.sciencemag.org)

ScienceRobotics  
 AAAS

 Twitter: @SciRobotics  
 Facebook: @ScienceRobotics



# READY FOR A TRULY LIFE-CHANGING MOMENT? APPLY NOW.

The *Science* & SciLifeLab Prize for Young Scientists is an annual prize awarded to early-career scientists. The prize is presented in four categories: Cell and Molecular Biology; Genomics, Proteomics, and Systems Biology Approaches; Ecology and Environment; and Molecular Medicine.

As a winner, you will have your essay published by *Science*, win up to USD 30,000 and be invited to Sweden where you will receive your award, present your research and meet with leading scientists in your field.

**Get ready for a life-changing moment in your scientific career  
– apply now, deadline is July 15!**

**[SCIENCEPRIZE.SCILIFELAB.SE](https://scienceprize.scilifelab.se)**



2019 winners (from left): Longzhi Tan, Zibo Chen, Barbara Klump and Humsa Venkatesh.

# FORCED INTO BATTLE

Bispecific antibodies unleash T cells against cancer  
by physically tethering them to tumor cells

QQ群: 970508760

**A**my Boland has gone through many ups and downs since she noticed lumps under her arms 12 years ago and learned she had cancer of the lymph system. For about 6 years, conventional chemotherapy helped shrink her lymphoma tumors, but they started to grow again. A succession of other cancer therapies, including a bone marrow transplant and a class of drugs called checkpoint inhibitors, either failed or only brought temporary relief. In one elaborate effort, physicians harvested her T cells, engineered those immune cells to kill her lymphoma, and infused them back into her body. The cancer vanished, but 2 years later bounced back. “Nothing was really working,” says oncologist Stephen Schuster of the University of Pennsylvania (UPenn).

So in October 2018, Boland joined a clinical trial testing another way to harness her immune system to kill the tumor cells. The idea of the trial, which Schuster co-leads, was to use a molecular rope known as a bispecific antibody to tether her natural T cells to the tumor cells so the immune warriors would attack. Like the engineered T cells she had received earlier, the experimental infusions sometimes made her sick enough to spend a couple of nights in the hospital. But the antibody rapidly sent her into remission. Today, more than 1 year after going off the Roche drug, mosunetuzumab, Boland, now 60, appears to be free of cancer and leads a normal life. “I’m feeling really good. I’m so grateful,” she says.

The ongoing trial Boland participated in made headlines in December 2019.

By **Jocelyn Kaiser**

At a meeting of the American Society of Hematology, Schuster reported that the antibody shrank fast-growing non-Hodgkin lymphoma tumors in 46 of 124 patients in whom other treatments had failed. For some of those people, like Boland, the failures included having their immune cells altered to attack the cancer. Those engineered cells, known as chimeric antigen receptor (CAR) T cells, have achieved remarkable results in some cancers. Yet at the same meeting, data from a small clinical trial suggested a bispecific antibody might work equally well on myeloma, another blood cancer. Bispecific antibodies for cancer are “superhot,” says Janice Reichert, executive director of the Antibody Society, who has tracked their development.

That’s the culmination of a slow boil. Scientists have worked on bispecific cancer drugs for decades and the first clinical success came 12 years ago. That result jump-started the field for a while, but other therapies, including CAR T cells, raced forward, in part because the cancer-fighting antibodies proved challenging to design and produce. But companies have now made those protein drugs safer and more potent. Variants are being tested in dozens of clinical trials, in the hope they can rival or surpass the engineered cells.

“If bispecific antibodies can do what CAR T cells can do, this would represent a big advance” and a “potentially fundamental change,” said Johns Hopkins Medicine hematologist Robert Brodsky at a press preview for the meeting where Schuster

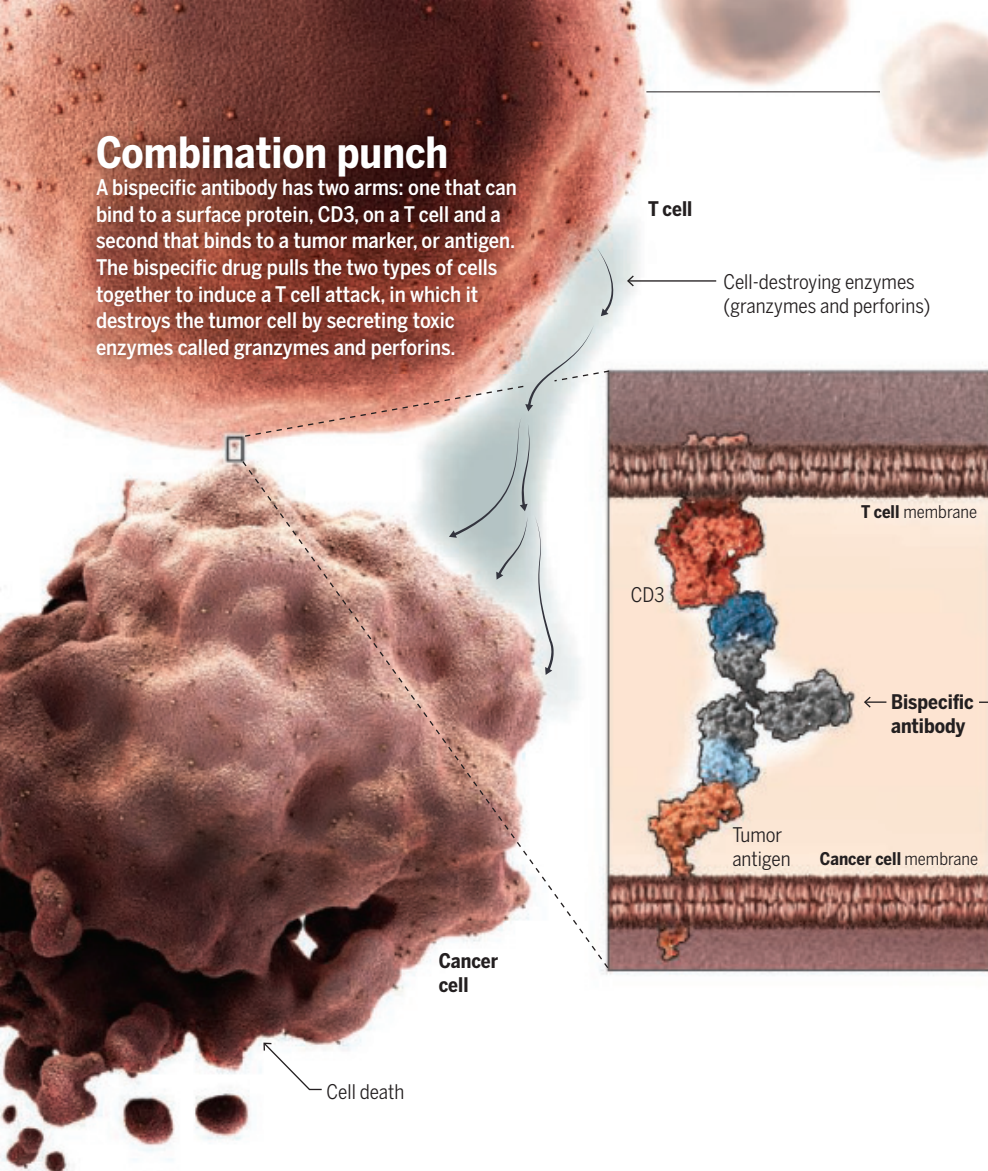
presented. A major advantage of bispecific antibodies is that they can be mass-produced in advance. CAR T cells, by contrast, must be prepared for each cancer patient. That process is costly and, for some very sick patients, takes too long.

Those new players in immunotherapy are no panacea yet. For some blood cancers, the bispecific antibodies aren’t giving patients the long-lasting remissions often seen with CAR T cells. As happened with CAR T cells, several patients have died in trials testing bispecific antibodies, possibly from overzealous immune responses sparked by the drugs. And bispecific antibodies may prove less effective against solid tumors, such as those of the colon and lungs, than against blood and lymph cancers—a drawback shared with CAR T cells. “There are a lot of open questions. But it’s also a field moving quickly, and a lot of really smart people are working on it,” says Paul Carter, an antibody researcher at Genentech, a Roche subsidiary.

**ANTIBODIES HAVE A LONG HISTORY** as a cancer treatment. The Y-shaped proteins are normally pathogen fighters, latching onto an antigen—a protein or a bit of one—on viruses, bacteria, or other microbes. The binding, which takes place at the tips of the Y, can directly disable and clear a pathogen or can signal the immune system to attack it. Cancer researchers first learned to exploit that natural system by making many copies of a specific antibody that latches onto an antigen unique to a particular cancer. This marks the cancer for destruction by com-

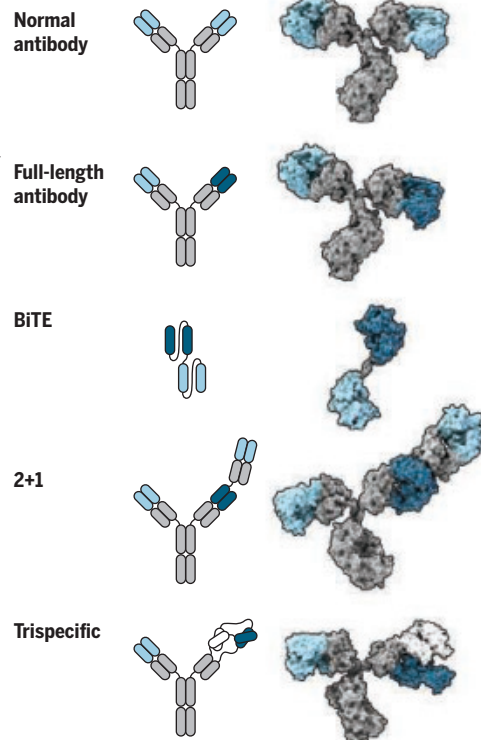
## Combination punch

A bispecific antibody has two arms: one that can bind to a surface protein, CD3, on a T cell and a second that binds to a tumor marker, or antigen. The bispecific drug pulls the two types of cells together to induce a T cell attack, in which it destroys the tumor cell by secreting toxic enzymes called granzymes and perforins.



## Design gallery

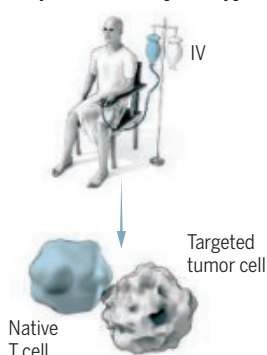
Arms of typical antibodies have identical tips (light blue) that can bind to a tumor. Bispecific antibodies that enlist T cells also have a binding site (dark blue) for the immune cells. Variants include a bispecific T cell engager (BiTE), which lacks a stem; a “2+1” antibody that has two sites that bind the same tumor antigen; and a trispecific, which binds two different surface proteins on a T cell.



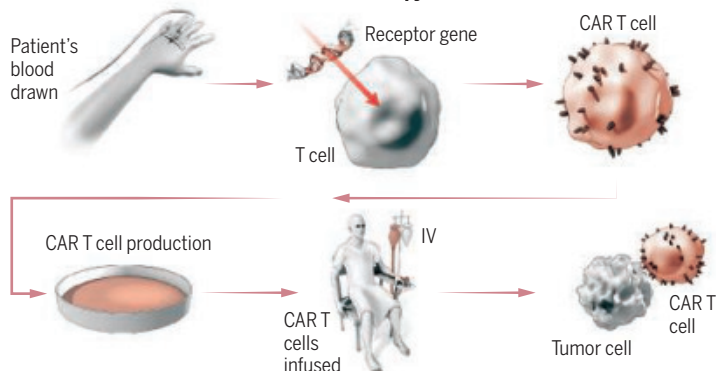
## Dueling treatments

Bispecific antibodies are off-the-shelf drugs given intravenously. That’s a simpler treatment than chimeric antigen receptor (CAR) T cells, made by harvesting T cells from a patient’s blood, engineering them to have receptors for a tumor antigen, growing the cells, and infusing them back into the patient.

### Bispecific antibody therapy



### CAR T cell therapy



ponents of the immune system other than T cells. Some of the most effective, and best-selling, cancer drugs are such monoclonal antibodies, including the breast cancer drug trastuzumab, better known as Herceptin.

Newer anticancer strategies enlist T cells. Tumor cells can appear foreign enough for the body to sometimes “train” these cells to attack them. But CAR T cells, altered to carry a receptor that targets a cancer cell

antigen, can deliver a more powerful response. Checkpoint inhibitors, drugs that release the molecular brakes that can restrain T cells, can also boost the T cell attack (*Science*, 20 December 2013, p. 1432).

Bispecific antibodies offer a third way to harness T cells. In the mid-1980s, cancer researchers began to engineer antibodies that had two tips—one matched to a cancer cell antigen and the other to a T cell surface

protein called CD3. The idea was to directly link T cells to tumor cells, thereby skipping the need for T cells to learn to attack a cancer. “It’s mimicking what naturally happens, but the advantage is that you can engage all T cells,” not just those trained to attack the tumor, says Dirk Nagorsen, a vice president and cancer researcher at Amgen. In 1985, the field was galvanized by two reports in *Nature* that such a “bispecific” antibody

Amy Boland has fought lymphoma for more than a decade, but her cancer vanished after treatment with bispecific antibodies.



could destroy cancer cells in a dish; studies soon showed those antibodies could shrink tumors in mice.

The drugs were hard to make. Antibodies are modular, with two identical “heavy” chains, making up the stem and half of each arm of the Y, and two identical “light” chains, each of which completes one arm. Trying to assemble bispecific antibodies from those complex components, protein chemists got 10 versions of each molecule. That outcome meant laborious efforts to sift out the one researchers wanted.

And the excitement faded when tests of bispecific antibodies moved from lab animals and cells to cancer patients. In an early clinical trial, one antibody appeared to shrink lymphoma. But researchers had to stop treating patients before the study yielded definitive results because the antibody’s maker ran out of the drug. The

antibodies also sometimes triggered serious side effects, including liver damage and an immune overreaction in which white blood cells pump out signals called cytokines that can be toxic in large quantities. Such cytokine “storms” cause fevers and, in severe cases, organ damage. (CAR T cells can cause the same overreaction.)

Two immunologists at the Ludwig Maximilian University of Munich, Peter Kufer and Gert Riethmüller, pressed ahead anyway with an idea some colleagues thought would fail: a stripped-down bispecific antibody with two tips linked by a flexible peptide instead of the traditional stem. The simplified design made the antibody easier to manufacture, but because the stem was missing, the kidneys cleared it from the blood within 2 hours. In its first clinical test, for non-Hodgkin lymphoma, patients had to wear a pump to continually infuse

the antibody. Still, tiny doses of the drug shrank tumors in all seven lymphoma patients in the trial, run by Micromet, a German biotech Riethmüller co-founded. “We thought, ‘Oh my God, there’s something amazing happening here,’” says molecular biologist Patrick Baeuerle, then-chief scientific officer of Micromet, who dubbed the concept a bispecific T cell engager (trade-marked as BiTE).

The small trial, published in *Science* in 2008, sparked interest from companies and academics. “The whole field realized, ‘This is a big deal. We want in on this,’” says John Desjarlais, chief scientific officer of the biotech Xencor. At about the same time, CAR T cells began to show impressive results in some leukemia patients—which boosted interest in other, potentially simpler immunotherapies such as bispecific antibodies. Like CAR T cells, T cells stimulated by BiTEs

PHOTO: MARY BOLAND

release toxic molecules called granzymes and perforins that punch holes in tumor cells and cause them to self-destruct. “I see bispecifics [such as BiTEs] as an off-the-shelf CAR T cell,” says Elad Sharon, senior investigator with the National Cancer Institute’s Cancer Therapy Evaluation Program.

The first bispecific antibody for cancer was approved in Europe in 2009. It was meant to mop up the malignant cells that cause abdominal fluid to build up in some cancer patients—but it didn’t work that well, so the drug only stayed on the market a few years. The field regained momentum, however, after Amgen snapped up Micromet in 2012 and later showed that its BiTE drug, blinatumomab (Blinicyto), doubled the survival time of patients with advanced acute lymphocytic leukemia. Beginning in 2014, the Food and Drug Administration approved the drug to treat several adult and pediatric forms of the disease. Amgen is now testing BiTEs for other cancers, including myeloma and lung, prostate, and brain cancers.

**OTHERS HAVE RUSHED** to improve on BiTEs by using protein engineering tricks to create desired bispecific antibodies. Some firms have restored the antibodies’ stem, known as the Fc receptor, so that the protein stays in the blood longer—but with modifications that make it less toxic to the liver. Cancer patients such as Boland no longer have to wear a fanny pack containing a pump, but can now receive the drug as an intravenous drip every 3 weeks.

Industry scientists have also added a second copy of the tumor antigen-binding site to one tip of the antibody (see graphic, p. 931). Known as a “2+1” bispecific antibody, this particular design is meant to make the antibody more selective for cancer cells and less likely to target healthy cells carrying small amounts of the cancer antigen.

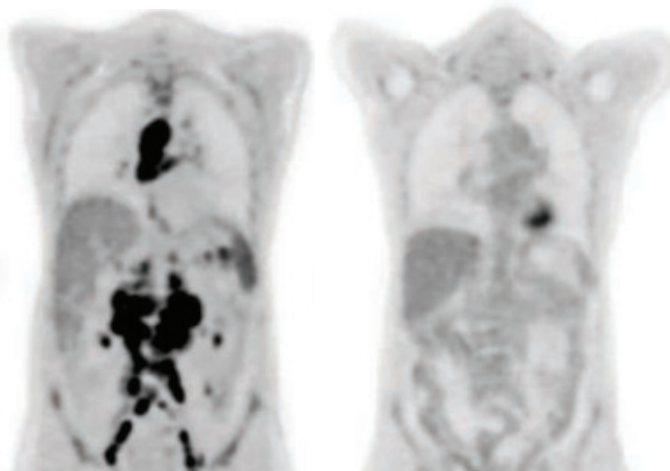
To reduce the risk of triggering a cytokine storm, researchers are also designing bispecifics that, instead of T cells, snag a different kind of immune cells called natural killers (NK). Several companies have started or are readying clinical trials of such antibodies, which bind to an NK cell surface protein called CD16. “NK cells are very potent tumor cell killers if activated, and the cytokine release is significantly reduced with this cell type,” says Dmitri Wiederschain, head of cancer immunology at one such company, Sanofi.

These variants and scores of other bispecifics are easier to synthesize now. “An-

tibody engineering has become so sophisticated, it’s possible to make these molecules quite efficiently,” says biochemist Christoph Rader of Scripps Research in Jupiter, Florida.

By Reichert’s count, more than 60 T cell-directing bispecific antibodies for cancer are in early- or later-stage clinical trials. One Amgen BiTE has shown hints of shrinking tumors in a few patients with advanced prostate cancer, the company reported last year.

Solid tumors are a challenging target for bispecifics in part because tumors often lack a unique antigen for the antibodies to grab. Many tumors are also surrounded by blood vessels, tissue, and immune cells that form a barrier T cells can’t easily penetrate. But findings from mouse studies suggest some bispecific antibodies can drive T cells into tumors, says Nai-Kong Cheung of Memorial Sloan Kettering Cancer Center. His lab has systematically tweaked design factors, such



Amy Boland’s cancer scans showed a dramatic disappearance of her lymphoma tumors from the start of her bispecific antibody treatment (left) to 12 weeks later.

as how binding sites are arranged, to learn what optimizes the molecules’ potency.

And some companies hope to boost the attack on solid tumors with antibodies that bind not only to CD3, but also to another receptor on T cells known as a “second signal,” which stimulates the cells to grow. For years, says Regeneron Senior Vice President Israel Lowy, industry has been “afraid to touch” that protein, called CD28, because of a devastating mishap: An antibody designed to bind to it made six healthy volunteers critically ill from cytokine release syndrome in a 2006 U.K. clinical trial.

Findings from new studies, however, suggest it’s possible to exploit that cell growth trigger safely. Last year in *Nature Cancer*, a Sanofi team reported that a “trispecific” antibody with arms matched to CD28, CD3, and a cancer antigen wiped out myeloma tumors in mice. Other firms have split up

the task by creating two bispecifics. One targets a tumor antigen and CD28 or another growth-signal receptor; the other binds to the tumor antigen plus CD3. “One of our hopes is that this costimulatory bispecific may help us unlock responses in solid tumors,” says Lowy, whose company reported in *Science Translational Medicine* in January that such a two-drug combination shrank ovarian tumors and slowed prostate tumor growth in mice.

Could those next-generation bispecifics eclipse CAR T cells for some cancers? UPenn’s Carl June, a CAR T cell pioneer, is skeptical. Many leukemia patients who get blinatumomab eventually relapse because cancer cells become resistant to the drug, he notes, so oncologists use it mainly as a “bridge” until a very sick patient can get a stem cell transplant or CAR T cells. June adds that bispecifics may not work in the many cancer patients whose T cells have become depleted or “exhausted,” leaving too few to attack the cancer. CAR T cell treatment, by contrast, replenishes the immune ranks by growing the cells outside the body—something “not possible with bispecifics,” June says.

Schuster, who has a foot in both camps—he runs Boland’s study and has led CAR T trials with June—says bispecifics are still proving themselves. He points to an Amgen report last year that some lymphoma patients who responded well to blinatumomab were still alive after 7 years, suggesting they could stay in remission long term. “I am confident that within the next 2 to 5 years you’re going to see quantum leaps in our ability to target resistant tumors, including solid tumors,” Schuster says.

He and other cancer researchers see CAR T cells, checkpoint inhibitors, and bispecific antibodies as interchangeable. “Why not do all of the above?” asks Schuster, who’s preparing a trial that will give patients CAR T cells and then a bispecific drug. “All these approaches to manipulate the cellular immune system to treat cancer are essentially different means to the same end.” Doubling up the treatments can be risky, however—last year, two patients died in such a trial after developing cytokine release syndrome.

Boland, who has seen all three of her children grow up and go off to college during her cancer fight, welcomes the progress. A bispecific drug is keeping her lymphoma in check for now, she notes. “I hope it’ll last, but if not, I feel confident that there’s always more treatments. You just don’t worry about it. Nobody knows what will happen.” ■

# INSIGHTS

## PERSPECTIVES

### ECOLOGY

## Exotic plants get a little help from their friends

Interactions with herbivores and microbes link exotic-plant success with carbon cycling

By **Carlos Urcelay**<sup>1</sup> and **Amy T. Austin**<sup>2</sup>

**T**errestrial ecologists have identified multifaceted controls—climate, biogeography, disturbances, and their interactions—that shape how plant communities in natural ecosystems organize in space and time. Multiple documented interactions directly link plant diversity with other biotic guilds (herbivores, root symbionts, bacteria, and pathogens) and ecosystem processes [carbon (C) and nutrient cycling] (1). However, all appears to go awry when exotic (non-native) plant species invade and establish themselves without human intervention; such changes affect the functioning and diversity of natural ecosystems (2). On page 967 in this issue, Waller *et al.* (3) provide insight into pathways that explain the underlying relationship between

plant invasions and acceleration of a crucial ecosystem process: C turnover.

Changes in plant diversity, species dominance, or nutrient cycling as a result of exotic plant invasion can alter ecosystems so substantially that they may be virtually unrecognizable from their original state. So what makes a non-native species a successful invader? Can scientists predict which species will have large impacts on ecosystems? It might seem straightforward to identify characteristics of success for exotic invader species, including faster growth rate, thinner leaves, or root anatomy (4–6), often with consequences for accelerated C turnover (2). However, definitive conclusions as to what traits predict invasive success remain elusive; this is due in part to the interactions between above- and belowground components of an invaded

ecosystem (including plants with contrasting life-history strategies) seldom having been examined simultaneously. Using a comprehensive, manipulable, outdoor experimental system (mesocosm), Waller *et al.* revealed that as the proportion of exotic plants increases, interactive effects from herbivore and soil-microorganism communities alter C cycling and other processes. Thus, changes in C cycling are indirectly mediated by the plant invaders through changes in these biotic interactions.

In an extensive experimental effort, the authors used plants and soils from subalpine grassland in New Zealand to establish 160 experimental outdoor ecosystems (mesocosms) that contained 20 singular combinations of eight plant species that varied in their proportions of exotic and native woody plants (see the photo). The plant

PHOTO: WARWICK ALLEN



Mini-ecosystems (aerial view, left; inside a single mesocosm, right) allow interactions among plants, herbivores, and soil biota to be manipulated.

communities were grown in soils previously conditioned by them (“home”) and in soils conditioned by plant species not present in the community (“away”), a technique that is commonly used to evaluate the importance of plant-soil feedbacks (6). Last, herbivore interactions were evaluated by adding invertebrate herbivores (such as leafhoppers, aphids, moths, beetles, and slugs) to half of the mesocosms. With plant traits as covariates, linear mixed-effects models were used to test how the proportion of exotics, herbivores, and soil treatments affected biotic

interactions and ecosystem processes. In addition, structural equation modeling was used to explore how exotic-plant functional types (those with different growth forms such as grasses, shrubs, and trees) and various other plant traits influence C cycling directly and indirectly (through modifying herbivore and soil-microorganism biomass).

A noteworthy aspect of the new study is the use of different functional types of plants, including woody species with various symbiotic strategies. This is relevant because the success of exotic plant species and their effects on new environments might be strongly determined by their symbiotic interactions (7). Chief among them are mycorrhizal fungi and nitrogen-fixing bacteria that associate with plant roots, providing access to soil nutrients and stress alleviation (8). The insights observed by Waller *et*

*al.* likely derive not from C-cycle changes that occur with exotic-plant dominance but from the mechanistic underpinnings that reveal why these changes occur.

Whereas plant richness (number of species) decreased with an increasing proportion of exotics, likely through competitive exclusion of natives, total plant biomass remained constant. Key to understanding the impacts of exotic plants on biotic interactions and C cycling is the widely explored plant trait that expresses the thickness of the leaves [called specific leaf area (SLA)], which is linked to herbivore palatability and nutrient-conservation strategies (9). Community-weighted SLA increased, at the community scale, with a growing presence of exotic plants and appears to have mediated some of the exotic-plant effects on biotic interactions and C cycling. For example, the increasing proportion of exotic species was accompanied by an increase in herbivore biomass, which could be explained by the presence of exotic nitrogen (N)-fixing herbs of high nutrient content and higher SLA, both of which imply enhanced leaf palatability (10). Soil microbial guilds also were affected. The biomass of arbuscular mycorrhizal fungi (AMF) decreased with an increase in the proportion of nonmycorrhizal exotic plant species with high SLA. An increase in bacterial biomass was associated with symbiotic N-fixing exotic woody species.

There is an emerging understanding of how the composition of soil fungi and bacteria can affect soil respiration (carbon dioxide production from soil microorganisms and roots) (11). In the Waller *et al.* study, the increased proportion of exotics triggered an increase in total soil respiration but only in the presence of herbivores and microbial guilds in the away soil. This process was positively influenced by the presence of exotic N-fixing woody plants and high community-weighted SLA. In turn, basal plant respiration (that which occurs without plant roots) increased in the presence of away soil biota, which was attributed to the activity of saprophytic fungi (non-AMF). The combination of exotic-plant traits and changes in the relative abundance of soil microbial guilds boosted nutrient and C cycling. Why total respiration increased only with aboveground herbivory remains unknown but reveals the complex pathways that drive plant-soil interactions.

The authors also showed that the increasing proportion of exotic plants accelerated decomposition of a standard substrate of black tea leaves indirectly through the exotic

plants' effects on soil fungi and herbivory. The increases in non-AMF biomass could be explained by the increasing presence of exotic N-fixing woody plants, together with reductions in nonsaprophytic AMF biomass by exotic non-N-fixing plants. This evidence provides support for the importance of life-history strategies in structuring below-ground fungal communities (12) and their interactions with herbivores. However, it is difficult to draw conclusions about direct links between ecosystem changes and exotic-plant traits because litter decomposition was evaluated with tea leaves from species not included in the experiments. The chemical and morphological characteristics of plant-litter identity (13) could contribute to the complexity of the patterns observed in the new study. Thus, the complex linkages among plant invasions, soil biota, and litter decomposition deserve further exploration.

The new work by Waller *et al.* highlights the fundamental role of biotic interactions in C-cycling processes in an experimental setting. It remains unclear how these results will scale up to field communities with more complex biological networks. Future research will unearth whether these interactive pathways are maintained or accentuated with adult woody species in invaded natural ecosystems or in other invasive scenarios, such as those lacking N-fixing invaders or those dominated by other mycorrhizal types. What seems evident from this study is that linkages between plant invasions and ecosystem processes are of pivotal importance for understanding the interplay of how plants interact with other organisms (14). Researchers must delve further into this complexity to better predict how these links will respond to global changes. ■

#### REFERENCES AND NOTES

1. W. W. Weisser *et al.*, *Basic Appl. Ecol.* **23**, 1 (2017).
2. J. G. Ehrenfeld, *Annu. Rev. Ecol. Syst.* **41**, 59 (2010).
3. L. P. Waller *et al.*, *Science* **368**, 967 (2020).
4. P. A. Tecco, S. Díaz, M. Cabido, C. Urcelay, *J. Ecol.* **98**, 17 (2010).
5. I. Jo, J. D. Fridley, D. Frank, *Biol. Invasions* **17**, 1545 (2015).
6. R. A. Wilschut *et al.*, *Nat. Commun.* **10**, 1564 (2019).
7. M. P. Thakur, W. H. van der Putten, M. M. P. Cobben, M. van Kleunen, S. Geisen, *Nat. Rev. Microbiol.* **17**, 621 (2019).
8. F. M. Martin, S. Uroz, D. G. Barker, *Science* **356**, eaad4501 (2017).
9. S. Díaz *et al.*, *J. Veg. Sci.* **15**, 295 (2004).
10. M. Schädler, G. Jung, H. Auge, R. Brandl, *Oikos* **103**, 121 (2003).
11. J. Whitaker *et al.*, *J. Ecol.* **102**, 1058 (2014).
12. D. Francioli *et al.*, *Plant Soil* (2020). 10.1007/s11104-020-04454-y
13. L. Vivanco, A. T. Austin, *J. Ecol.* **96**, 727 (2008).
14. A. T. Austin, C. L. Ballaré, *New Phytol.* **204**, 257 (2014).

#### ACKNOWLEDGMENTS

This work was supported by CONICET-UNC, the Secretariat of Science and Technology, and Ministerio de Ciencia de la Provincia de Córdoba (C.U.) and the New Phytologist Trust (A.T.A.)

10.1126/science.abc3587

#### SYNTHETIC BIOLOGY

# Remote activation of cellular signaling

Electric fields stimulate genetically modified pancreatic  $\beta$  cells to secrete insulin in mice

By **Matthew I. Brier**<sup>1</sup>  
and **Jonathan S. Dordick**<sup>1,2</sup>

**R**emote modulation of cell signaling has biological ramifications across the cellular, tissue, and organismal levels, with applications as diverse as medicine and biomanufacturing. External approaches to regulating biological processes invariably require genetic manipulation. Platforms with orthogonal means of remotely controlling cell function include optogenetics (1, 2), mechanogenetics (3, 4), and magnetogenetics (5–7). An array of techniques make use of various pathways to control cell signaling and enable in-depth studies of cell processes and the development of therapeutic tools. An external stimulus can control one or more cellular pathways leading to, for example, control of ion channels, temporal production of proteins, or neural circuit modulation. On page 993 of this issue, Krawczyk *et al.* (8) advance the use of electrogenetics, a method that uses electric fields to control cell function, through the development of a wearable device that releases insulin from bioengineered cells and controls blood glucose concentrations in vivo.

Electrogenetics uses cells that have been engineered to respond to electrical stimulation through the expression of voltage-dependent receptors, such as voltage-gated ion channels. Krawczyk *et al.* exploited a voltage-gated calcium channel ( $\text{Ca}_v1.2$ ) coupled to an inwardly rectifying potassium channel ( $\text{K}_{ir}2.1$ ) to complete a voltage-gated circuit and provide a high degree of control over gene expression in human embryonic kidney cells (see the figure, top left). Using voltage-controlled square pulses, the authors demonstrated electrostimulation-driven expression of a simple marker protein, secreted embryonic alkaline phosphatase, with the amount expressed controlled by the applied voltage, pulse length, and duration of stimulation.

Having demonstrated model protein production at the transcriptional level, Krawczyk *et al.* then engineered a similar set of genetic constructs into a monoclonal pancreatic  $\beta$  cell line ( $\text{Electro}\beta$  cells) with vesicular insulin secretion functionality decoupled from glucose sensitivity. This modification enabled insulin to accumulate in the  $\text{Electro}\beta$  cell vesicles and to be released upon electrostimulation, rather than in response to changes in glucose concentrations. Peak secretion occurred within 10 min after starting stimulation. The authors extended these in vitro results to a diabetic mouse model by encasing  $\text{Electro}\beta$  cells in an electrostimulation device that could be subcutaneously implanted. Implants facilitated reuse of the  $\text{Electro}\beta$  cells for several weeks. Wireless activation could induce electrostimulation and secretion of stored insulin to counteract perturbations in blood glucose concentrations within minutes.

This electrogenetics approach shows capabilities similar to those of optogenetics, perhaps the most well-studied means to control cell function remotely, in which precise wavelengths of light stimulate wavelength-specific light-sensitive receptors and ion channels (see the figure, top right) (1, 2). The discovery of bacterial channelrhodopsin (ChR) as a calcium ion-conducting photoreceptor (9) led to myriad applications, including control of neuronal action potentials with millisecond-time scale spatiotemporal control (2). Mutations made to ChR family members have introduced new functionalities, including on-off switching and  $\text{Cl}^-$  conductance (10). However, the poor tissue penetration depth of light requires fiber-optic implants, although recent studies with near-infrared light to activate lanthanide-doped nanoparticles to emit visible light may help to overcome accessibility restrictions (11).

Alternatively, mechanogenetics involves physical stimuli that have deep tissue penetration depths, such as focused ultrasound (FUS), to actuate mechanosensitive receptors. As an example, two-pore domain potassium ion channels genetically introduced into rat hippocampal neurons in vitro were activated by FUS to drive membrane depolarization and action potentials (3). In a related approach, microbubbles decorated

<sup>1</sup>Department of Chemical and Biological Engineering and Center for Biotechnology and Interdisciplinary Studies, Rensselaer Polytechnic Institute, Troy, NY 12180, USA.

<sup>2</sup>Departments of Biomedical Engineering and Biological Sciences, Rensselaer Polytechnic Institute, Troy, NY 12180, USA. Email: dordick@rpi.edu

with streptavidin and targeted to biotinylated Piezo1 mechanosensitive channels were used to transduce 150-MHz ultrasound and gate  $\text{Ca}^{2+}$  flux into chimeric antigen receptor T cells, thereby controlling  $\text{Ca}^{2+}$ -dependent gene expression as a potential cancer therapy (see the figure, bottom left) (4).

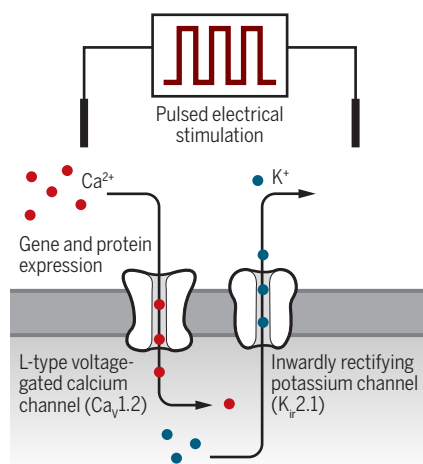
Another remote physical technique with similar spatiotemporal control and tissue penetration is magnetogenetics, which uses time-variant magnetic fields to activate magnetic nanoparticles targeted to cell receptors. Early studies in magnetogenetics used external magnetic iron oxide nanoparticles localized to target receptors, such as the transient receptor potential (TRP) vanilloid 1 (TRPV1) cation channel, that were exposed to magnetic stimulation to control  $\text{Ca}^{2+}$  entry into cells (5). More recently, several variations of this platform have been developed using genetically encoded ferritin, an endogenous cage protein responsible for maintaining iron homeostasis by sequestering iron as a magnetic nanoparticle, engineered to bind to TRP channels (see the figure, bottom right) (6, 7). Exposure of cells expressing the ferritin-conjugated TRPV1 platform to 465-kHz alternating magnetic field (AMF) stimulation allowed control of  $\text{Ca}^{2+}$ -dependent insulin production in vitro (6) and of blood glucose concentrations and feeding behavior in mice (12).

Despite promising results, magnetogenetics has been the subject of vigorous debate over the underlying mechanism and the veracity of the results to date. Although localized heating or mechanical torque in the vicinity of the exogenously added nanoparticles were viewed as logical means to gate TRP channels, arguments targeting deficiencies in ferritin's magnetic properties suggested that such mechanisms could not explain the observed phenomenon (13). Nonetheless, alternative mechanisms have been proposed, including magnetocaloric heating resulting from changes in the magnetic entropy of the iron biomineralized core within ferritin that could conceivably gate TRP channels (14). Chemical mechanisms have also been advanced that attribute gating of TRP channels to iron release from ferritin in the presence of AMFs; free iron results in localized formation of reactive oxygen species and lipid oxidation of the cell membrane in the channel's vicinity, both of which gate TRP channels (15).

We can now add electrogenetics to the mix of technologies for rapid and remote spatiotemporal control over complex biological functions. Electrogenetics represents the next tool in an expanding toolbox for engineering remote solutions for human therapeutics. Despite their inherent limitation, each of these platforms has shown applicability, and the potential for combinations of these orthogonal platforms to exert fine-tuned con-

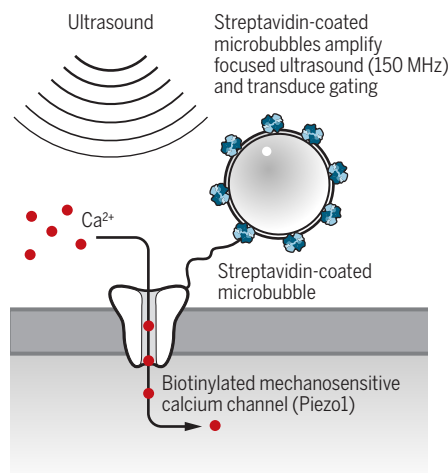
## Remote control of cells

Krawczyk *et al.* report an electrogenetic approach to stimulate cells. This method joins three others for actuating genetically modified cell membrane ion channels to initiate signal transduction and control cell function.



### Electrogenetics

Krawczyk *et al.* use pulsed electrical stimulation to control a voltage-gated circuit. The change in  $\text{Ca}^{2+}$  concentration leads to expression of a simple marker protein, secreted embryonic alkaline phosphatase, and vesicular insulin secretion (8).



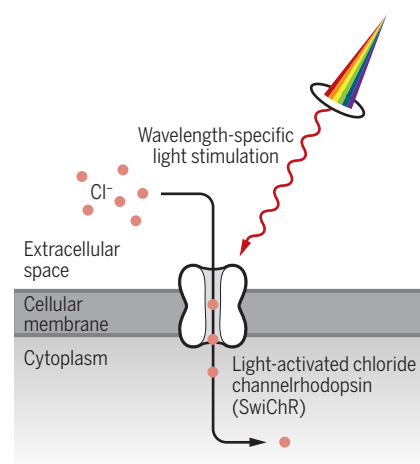
### Mechanogenetics

Streptavidin-coated microbubbles targeted to biotinylated Piezo1 mechanosensitive channels transduce focused ultrasound to gate  $\text{Ca}^{2+}$  flux into chimeric antigen receptor T cells (4).

trol in complex systems is within our grasp. Research into synergistic use of these approaches could be the next step. For example, self-contained implants could act as multimodal monitoring and treatment devices for targeted diseases that have proven elusive to the current toolbox of modern medicine. ■

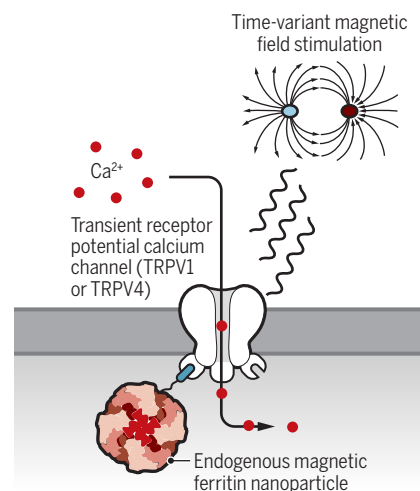
### REFERENCES AND NOTES

1. F. Zhang *et al.*, *Cell* **147**, 1446 (2011).
2. E. S. Boyden *et al.*, *Nat. Neurosci.* **8**, 1263 (2005).
3. J. Kubanek *et al.*, *Sci. Rep.* **6**, 24170 (2016).
4. Y. Pan *et al.*, *Proc. Natl. Acad. Sci. U.S.A.* **115**, 992 (2018).
5. H. Huang *et al.*, *Nat. Nanotechnol.* **5**, 602 (2010).



### Optogenetics

Precise wavelengths of light stimulate light-sensitive receptors and ion channels, in this case SwiChR ( $\text{Cl}^-$ -conducting step-waveform inhibitory channelrhodopsin) (10).



### Magnetogenetics

Exposing cells expressing ferritin-conjugated TRPV1 to an alternating magnetic field controls  $\text{Ca}^{2+}$ -dependent insulin production in vitro (6).

6. S. A. Stanley *et al.*, *Nat. Med.* **21**, 92 (2015).
7. A. A. Mosabir, K. Truong, *ACS Synth. Biol.* **7**, 718 (2018).
8. K. Krawczyk *et al.*, *Science* **368**, 993 (2020).
9. G. Nagel *et al.*, *Proc. Natl. Acad. Sci. U.S.A.* **100**, 13940 (2003).
10. A. Berndt *et al.*, *Science* **344**, 420 (2014).
11. S. Chen *et al.*, *Science* **359**, 679 (2018).
12. S. A. Stanley *et al.*, *Nature* **531**, 647 (2016).
13. M. Meister, *eLife* **5**, e17210 (2016).
14. G. Duret *et al.*, *Biophys. J.* **114**, 669a (2018).
15. M. Hernández-Morales *et al.*, *Cell Rep.* **30**, 3250 (2020).

### ACKNOWLEDGMENTS

Supported by NIH grant R01NS097184.

10.1126/science.abb9122

## CANCER

# Probing the tumor micro(b)environment

Bacteria are widespread in tumors, are found within cells, and differ by cancer type

By **Chloe E. Atreya<sup>1</sup>** and **Peter J. Turnbaugh<sup>2,3</sup>**

**B**acteria have been implicated in the initiation and progression of cancers originating on mucosal surfaces that either harbor a diverse microbial community (microbiota) or are routinely exposed to microbes from the environment (1–3). Far less is known about the potential for bacteria to influence tumors in body sites that are typically considered sterile. One hypothesis is that the abundant and diverse microbiotas found on mucosal surfaces may exert “remote control” by releasing small molecules into circulation (4, 5). An alternative, non-conflicting hypothesis is that the tumor microenvironment harbors microbes that exert local effects. This hypothesis is supported by the detection of bacteria in a growing number of tumor types (6, 7), although the reliability of distinguishing low-abundance bacteria from contamination has been questioned (8). On page 973 of this issue, Nejman *et al.* (9) present the most rigorous and comprehensive survey of bacteria in human tumor samples to date.

Nejman *et al.* use a new five-region 16S ribosomal RNA gene sequencing method, microscopy, and cell culture to characterize tumor-residing bacteria at known and previously uncharacterized sites. They report that most cancers harbor bacteria, albeit at low diversity except in breast cancer. Surprisingly, these bacteria appear to be intracellular within both cancer and immune cells. Moreover, they report associations between specific bacteria and tumor type and subtype, smoking status, and immunotherapy response.

These results raise multiple important questions for future study (see the figure). For example, is the level of diversity and

physiological status of these bacterial cells sufficient to constitute a “microbiota”? Although the defining characteristics of microbiotas remain in flux, two general themes are extensive microbe-microbe and host-microbe interactions, often over long time scales. Are the tumor-residing bacteria found within human cells able to communicate with each other? Prior work (6) suggests that bacteria found in tumors can metabolize drugs; however, the overall viability and metabolic activity of tumor-residing bacteria are unclear.

sue from the mammary glands of patients and even healthy controls (9). In precancerous conditions, the detection of enterotoxigenic bacteria may portend a generalized procarcinogenic inflammatory state (10). After tumorigenesis, disruptions to physical and molecular barriers, together with relative immunosuppression, may increase the potential for bacterial translocation to sites that are normally sterile. This “leakiness” of the tumor microenvironment has been extensively described in the context of vascular permeability; however, the degree to which leakiness enables bacterial invasiveness remains unclear. Additionally, the observation that tumor-associated bacteria are intracellular raises the possibility that the bacteria do not actually move freely into tumors or adjacent tissues—they may be transported there, intact or in fragments, through the migration of immune or cancerous cells.

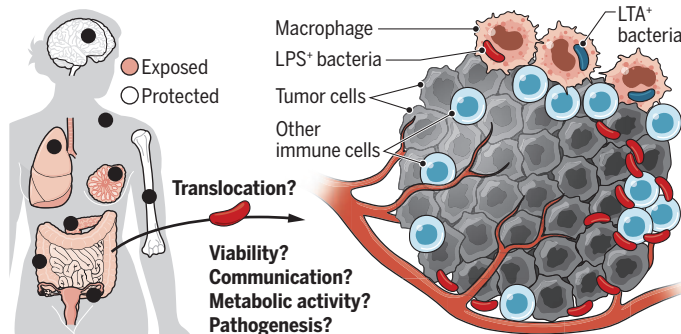
A key barrier to progress is the lack of representative models for studying tumor-residing bacteria or other low-biomass microbial communities (8). Studies of colorectal cancer demonstrate the persistence of viable *Fusobacterium* over successive passages of human tumors in immunodeficient mice (11). However, laboratory mice harbor microbial communities

(12) and immune profiles that are distinct from those found in humans. Development of “triple-humanized” models wherein cancer, immune, and microbial cells are transplanted from patients into germ-free mice may be necessary.

These models could help to untangle the relationships between tumor-residing bacteria and treatment response. By contrast, there is abundant evidence that gut bacteria modulate the immunotherapy responsiveness of cancers, even at distant sites (4). Immune cells in the tumor microenvironment also play major and actionable roles, but does this extend to tumor-associated microbes? For a given cancer type, it will be important to determine the contribution of microbial composition relative to other tumor cell intrinsic and

## The hidden microbiota inside cancer

Intratumoral bacteria have been detected in both mucosal (exposed) body sites and protected sites. Nejman *et al.* examined bacterial occurrence in multiple primary tumor sites (black dots) and found that tumor cells and immune cells may harbor lipopolysaccharide-expressing (LPS<sup>+</sup>) bacteria, whereas macrophages contain at least remnants of LPS<sup>+</sup> and lipoteichoic acid-expressing (LTA<sup>+</sup>) bacteria. These findings raise numerous questions that require further study.



The stability of bacterial diversity in tumors remains to be determined. Are tumor-residing bacteria seeded early on in tumorigenesis, or does the tumor alter the microenvironment such that bacteria can continually invade? In mouse models of pancreatic cancer (7), the gut microbiota appears to determine which bacteria are found in tumors, suggesting that there is a potential for bacteria to migrate into tumors at later stages. Longitudinal studies in patients with paired analyses of microbial diversity in tumors and mucosal surfaces are an important next step.

Why are bacteria found in tumors? One possibility raised by Nejman *et al.* is that there are always low amounts of bacteria in human tissue, which is supported by analyses of matched normal adjacent tis-

<sup>1</sup>Department of Medicine, Division of Hematology and Oncology, and Helen Diller Family Comprehensive Cancer Center, University of California, San Francisco, CA, USA.

<sup>2</sup>Department of Microbiology and Immunology, G.W. Hooper Research Foundation, University of California, San Francisco, CA, USA. <sup>3</sup>Chan Zuckerberg Biohub, San Francisco, CA, USA. Email: peter.turnbaugh@ucsf.edu

extrinsic factors that drive malignancy.

The conceptual shift toward studying bacteria within tumors provides challenges and opportunities for translational research. Unlike the microbiotas found on mucosal surfaces, tumor-residing bacteria are not readily manipulatable. Current options for microbiota modulation rely on dietary, pharmaceutical, and microbiological perturbations (13). It remains unknown if tumor-residing bacteria depend at all on dietary substrates or if they subsist entirely on host-derived nutrients. Targeting intracellular tumor-residing bacteria also poses drug-delivery challenges; it may be possible to co-opt antibody-drug conjugates or other methods to specifically target bacteria. Although there is a long history of delivering viable bacteria to tumors (14), the risks and benefits of this approach need to be carefully considered.

Nejman *et al.* emphasize that diverse bacteria are found on and in the human body. Continued investigation may benefit from the rich history of research on intracellular bacteria in insects and plants. Intracellular bacterial pathogens harbor elaborate machinery to manipulate host cellular pathways (15); it will be interesting to see if tumor-residing bacteria encode similar effectors that enable their survival and dissemination. Achieving a comprehensive understanding of the tumor microenvironment is a daunting yet critical step toward an organism-wide mechanistic model of cancer progression and, if successful, may unlock the next wave of precision cancer diagnostics and therapeutics. ■

#### REFERENCES AND NOTES

1. D. Börnigen *et al.*, *Sci. Rep.* **7**, 17686 (2017).
2. A. D. Kostic *et al.*, *Genome Res.* **22**, 292 (2012).
3. K. L. Greathouse *et al.*, *Genome Biol.* **19**, 123 (2018).
4. V. Gopalakrishnan *et al.*, *Science* **359**, 97 (2018).
5. E. N. Bess *et al.*, *Nat. Microbiol.* **5**, 56 (2020).
6. L. T. Geller *et al.*, *Science* **357**, 1156 (2017).
7. E. Riquelme *et al.*, *Cell* **178**, 795 (2019).
8. M. C. de Goffau *et al.*, *Nature* **572**, 329 (2019).
9. D. Nejman *et al.*, *Science* **368**, 973 (2020).
10. C. M. Dejea *et al.*, *Science* **359**, 592 (2018).
11. S. Bullman *et al.*, *Science* **358**, 1443 (2017).
12. J. Walter, A. M. Armet, B. B. Finlay, F. Shanahan, *Cell* **180**, 221 (2020).
13. K. N. Lam, M. Alexander, P. J. Turnbaugh, *Cell Host Microbe* **26**, 22 (2019).
14. M. Sedghi *et al.*, *Cancer Med.* **8**, 3167 (2019).
15. S. M. Moss *et al.*, *Cell Host Microbe* **25**, 454 (2019).

#### ACKNOWLEDGMENTS

Support is provided by NIH (R21CA227232) and the Damon Runyon Cancer Research Foundation (DRR-42-16). C.E.A. is on the scientific advisory board for Pionyr Immunotherapeutics and has research funding from Bristol Myers Squibb, Guardant Health, Merck, and Novartis. P.J.T. is on the scientific advisory boards for Kaleido, Pendulum, Seres, and SNIPR Biome.

#### GEOLOGY

## Tracking the rapid pace of a retreating ice sheet

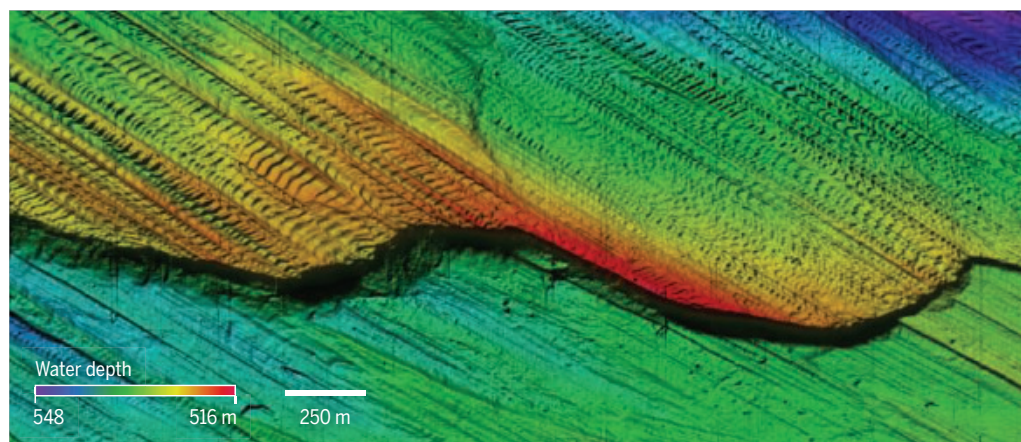
Seafloor mapping shows that Antarctic ice sheets retreated faster during the last deglaciation than today

By Martin Jakobsson<sup>1,2</sup>

Glaciers and ice sheets that extended from land into the ocean left traces behind on the seafloor called submarine glacial landforms. If mapped in sufficient detail and interpreted correctly, they can provide comprehensive information into past behaviors of glaciers and ice sheets. On page 1020 of this issue, Dowdeswell *et al.* (1) describe the mapping of glacial landforms in the seafloor created by a rapidly retreating ice sheet on the eastern Antarctic Peninsula. The high-resolution data suggest that the retreat rate was paced by ocean tides and at least an order of magnitude faster than modern rates observed in other sensitive areas, such as West Antarctica where the ice sheet drains into the ocean at several locations (2). The retreat on the eastern Antarctic Peninsula took place more than 10,000 years ago, pointing out the challenges in predicting the sea-level rise contribution from retreating glaciers and ice sheets in a warming climate.

Glacial landforms have long been used to reconstruct ice-sheet extent and, specifi-

cally, its retreat pace and dynamics. At a meeting in Stockholm 1889 (3), the Swedish geologist Gerard De Geer presented observations of moraines, a general term to describe glacial landforms that consist of a mixture of debris (mainly sediments and rock fragments) deposited and sometimes molded by glacier ice. The moraines were observed in Sweden northwest of Stockholm. They generally took the form of ridges, between 1 and 5 m high and a few to slightly more than 10 m wide, gently winding through the landscape for several kilometers. There were several parallel lines of the moraines mapped in the landscape 200 to 300 m apart. De Geer compared the distances between the parallel moraines with the notion prevailing at the time that Swiss glaciers could retreat up to 70 m during 1 year. He put forward a hypothesis that the moraines were deposited during winter along the margin of the Scandinavian Ice Sheet when it made a seasonal halt during its retreat over the landscape. The distance between the moraines of 200 to 300 m represented therefore a yearly retreat rate of the ice sheet. About 11,000 years ago, when the Scandinavian Ice Sheet's margin was located in the area northwest of Stockholm, land was depressed below the contemporary water level of the Baltic Sea (4). This meant that the moraines described by



Seafloor imagery of the shape and depth of a grounding-zone wedge complex (where ice transitions from a grounded ice sheet to a floating ice shelf) was derived from an autonomous underwater vehicle-deployed multibeam echo-sounder as it surveyed part of Larsen Inlet, Antarctica. Grid cell-size is 1 m.

De Geer were formed at the ice margin under water. It would, however, take nearly a century after De Geer's presentation before geophysical seafloor mapping reached the technical capacity to be able to survey features with reliefs of only a meter or so. These "De Geer moraines" are similar in some aspects to the submarine glacial landforms from Antarctica mapped, described, and interpreted by Dowdeswell *et al.*

Dowdeswell *et al.* describe the appearance of the glacial landforms as if "ladders with numerous rungs" had been left embedded in the seafloor (see the figure). Similar features have been mapped and described previously, although often at lower resolution, around Antarctica (5–7) and in the Arctic (8). However, subtle differences with respect to appearances and settings led to different interpretations of the formation mechanisms. What is common to all previous studies and that of Dowdeswell *et al.* is that the proposed formation mechanisms involve ocean tides as a "pacemaker." The glacier ice, either of an iceberg or the margin of an outlet glacier draining an ice sheet into the ocean, can be slightly lifted from the seafloor during high tide. When settling again during low tide, a small ridge is formed on the seafloor by squeezing of sediments along the bottom edge of the iceberg or the outlet glaciers' margin. The submarine glacial landforms mapped in previous studies, referred to as "corrugation ridges" or "wash-

board patterns," were interpreted to have been formed in the wake of large grounded icebergs (7), or at the trailing end of drifting armadas of mega-sized icebergs calved during an ice shelf break-up (5), or underneath a thick ice shelf that floated close above the seafloor but bearing a protruding ice keel that could ground periodically with the tidal movement (6). All of these proposed formations of small, extremely regular ridge-like features in seafloor sediments take place at the tail end of the ice or by a bulging ice keel, moving away from the newly formed ridge without running over and destroying them. The ladders and rungs, by contrast, are formed at the front of the grounded ice margin, implying that when the ice moves forward, the features will be destroyed. Glacier ice moves by gravity from higher elevation on land toward the ocean, implying that the ice margin's grounding line must back-step for every formed rung. This can only happen if mass is lost at a regular pace. The precise ice dynamics of this regular mass loss that is paced by tide is not resolved and presents a challenge for the ice-modeling community. Although the mechanical details are yet to be characterized, Dowdeswell *et al.* have used the idea that the ocean tide-paces the formation of the rungs to convert the distances between the rungs to a retreat rate of the ice sheet.

Perhaps most importantly, Dowdeswell *et al.* demonstrate the immense value of

high-resolution seafloor mapping in unraveling the complex history of glacial dynamics. Only fractions of the seafloor in the hard-to-access ice-covered polar regions are mapped, and much is left to discover and learn. Scientists working on submarine glacial landforms have experienced a breakthrough in seafloor mapping capabilities similar to what their colleagues working in the terrestrial realm achieved when high-resolution terrain models of the land surface became available through airborne and satellite technology. Indeed, Dowdeswell *et al.* used the latest geophysical mapping technology mounted on an unmanned mini-submarine to survey the seafloor. Nonetheless, the pace of mapping the oceans, specifically in remote areas, is orders of magnitude slower because of the logistical difficulties and the fact that the ocean is in the way. ■

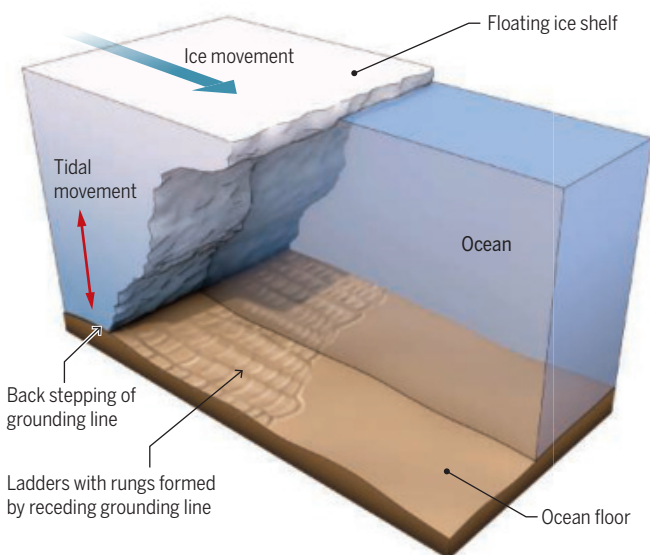
#### REFERENCES AND NOTES

1. J. A. Dowdeswell *et al.*, *Science* **368**, 1020 (2020).
2. E. Rignot, J. Mouginot, M. Morlighem, H. Seroussi, B. Scheuchl, *Geophys. Res. Lett.* **41**, 3502 (2014).
3. E. Erdmann, *Geol. Foren. Stockh. Forh.* **11**, 73 (1889).
4. S. Björck, *Quat. Int.* **27**, 19 (1995).
5. M. Jakobsson *et al.*, *Geology* **39**, 691 (2011).
6. A. G. C. Graham *et al.*, *J. Geophys. Res. Earth Surf.* **118**, 1356 (2013).
7. R. Lien, A. Solheim, A. Elverhoi, K. Rokoengen, *Polar Res.* **7**, 43 (1989).
8. K. Andreassen, M. C. M. Winsborrow, L. R. Bjarnadóttir, D. C. Rührer, *Quat. Sci. Rev.* **92**, 246 (2014).

10.1126/science.abc3583

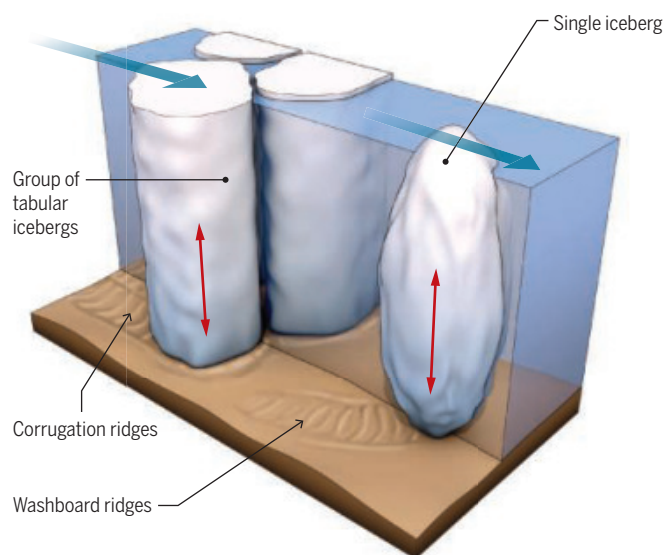
## Unraveling glacial dynamics

Seafloor patterns can reveal grounded ice margin (left), iceberg (right), and under ice (not shown) scenarios.



### Ladders with rungs

Ridges form when ice settles during low tide. The ice margin is lifted during the next high tide, loses mass from calving and melting, and settles 20 to 25 m further inland to form a ridge during the next low tide. If the ice sheet has a protruding ice keel that extends into a cavity below the grounded ice, it may form a different pattern (corrugation ridges).



### Corrugation and washboard ridges

These patterns are created by icebergs moving individually or in a group. When the ice is moved up and down by the ocean tide, sediment ridges are squeezed out at their trailing edges.

# Catching up to nature's ribosomes

Flow chemistry enables total chemical synthesis of proteins without solution-phase ligation

By **Caroline Proulx**

**C**hemical protein synthesis allows the systematic incorporation of one or more unnatural amino acids at precise locations along a protein backbone that enable structure-function relationship studies (1, 2). However, solid-phase peptide synthesis (SPPS) (3) is usually limited to peptides of 50 residues, and as a result, chemical protein synthesis requires native chemical ligation (NCL) (4) reactions for the chemoselective coupling of unprotected peptide fragments in solution. This combined multistep approach typically requires the synthesis and sequential ligation of at least three peptide fragments to access proteins, a process that remains relatively laborious. On page 980 of this issue, Hartrampf *et al.* (5) chemically synthesized single-domain proteins in hours. They circumvent the use of solution-phase chemistry by carefully optimizing iterative amino acid couplings on a solid support using a flow-chemistry setup (see the figure).

The introduction of SPPS in the 1960s (3) revolutionized peptide sciences. The attachment of the carboxyl-terminal amino acid to an insoluble polymeric support allowed each reaction to be done with excess reagents that could be easily washed off through simple filtration, a technique that earned Bruce Merrifield the Nobel Prize in Chemistry in 1984. Because there are no purifications steps in between each amino acid coupling and deprotection reactions performed on a solid support, near-quantitative yields are required for each monomer addition cycle to enable the synthesis and purification of proteins. Common by-products that have plagued peptide syntheses have included those arising from deletions, truncations, aspartimide formation, and amino acid epimerizations. Each unwanted reaction yields material that is often difficult or impossible to separate from the desired product with high-performance liquid chromatography purification methods.

Although much progress has been made to address these challenges (6), peptide sequence lengths that can be routinely accessed with traditional SPPS approaches fall well below the lengths of entire protein

sequences. This limitation has required the development and use of postsynthetic ligation methods. However, a wide variety of unnatural amino acids can be incorporated using this approach. Alternatively, incorporation of unnatural amino acids into proteins can be done through genetic code expansion in biological systems instead (7), albeit with differences in substrate scope.

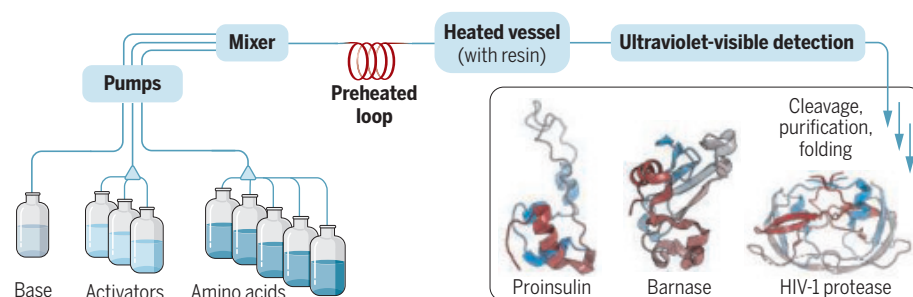
In a previous study from this team, Mijalis *et al.* reported automated fast-flow peptide synthesis (AFPS) procedures that substantially accelerated the process and improves the synthesis of difficult peptide sequences (8). Notably, their AFPS system has shortened the amino acid addition

protocol for total chemical protein synthesis by AFPS. Comparative analyses with proteins produced by biological expression validated that the synthetic proteins obtained in this study exhibited similar structure and function.

Overall, in addition to its impressive speed, this new technique leads to a three-fold increase in peptide size limit achievable by AFPS techniques. This advance should facilitate future protein synthesis endeavors and influence multiple fields of research. Coupling AFPS technology with existing NCL methods could deliver >300-residue proteins after a single ligation reaction. Moreover, it is easy to imagine

## Fast-flow automated protein synthesis

Hartrampf *et al.* optimized concentration, flow rate, reagents, additives, and temperature to minimize unwanted by-products in peptide synthesis. The peptide lengths are in the range of those of single-domain proteins.



cycle to less than 1 min, and convenient inline ultraviolet-visible monitoring has allowed quantitative analysis of the fluorenylmethoxycarbonyl (Fmoc) deprotection reactions. This feature offers the marked advantage of identifying problematic coupling steps rapidly and consistently throughout the synthesis, versus the time-consuming manual analyses typically used.

In the present study, Hartrampf *et al.* have methodically optimized the parameters of their AFPS setup, including concentration, flow rate, reagents, additives, and temperature, to surmount the difficult task of reducing by-products sufficiently to enable protein synthesis (5). They established particular sets of optimal conditions for each amino acid incorporation by first using the 30-residue glucagon-like peptide-1 as a test. They then applied their optimized procedure to the synthesis of nine different proteins, thus establishing a generalized

similar optimization efforts for a wide variety of unnatural amino acid residues, expanding their utility far beyond their current scope and potentially yielding all-unnatural protein-mimetic material that is inaccessible by biological methods. In that respect, it will not only catch up to but surpass ribosome capabilities. ■

## REFERENCES AND NOTES

1. S. B. H. Kent, *Chem. Soc. Rev.* **38**, 338 (2009).
2. V. Agouridas *et al.*, *Chem. Rev.* **119**, 7328 (2019).
3. R. B. Merrifield, *J. Am. Chem. Soc.* **85**, 2149 (1963).
4. P. E. Dawson, T. W. Muir, I. Clark-Lewis, S. B. Kent, *Science* **266**, 776 (1994).
5. N. Hartrampf *et al.*, *Science* **368**, 980 (2020).
6. R. Behrendt, P. White, J. Offer, *J. Pept. Sci.* **22**, 4 (2016).
7. L. Wang, P. G. Schultz, *Angew. Chem. Int. Ed.* **44**, 34 (2004).
8. A. J. Mijalis *et al.*, *Nat. Chem. Biol.* **13**, 464 (2017).

## ACKNOWLEDGMENTS

The author gratefully acknowledges North Carolina State University for startup support.

10.1126/science.abb9711

Department of Chemistry, North Carolina State University, Raleigh, NC 27695-8204, USA. Email: cproulx@ncsu.edu

## CORONAVIRUS

# The search for a COVID-19 animal model

A comparison of SARS-CoV-2 replication, transmission, and disease in mice to monkeys

By **Seema S. Lakdawala**<sup>1</sup> and  
**Vineet D. Menachery**<sup>2</sup>

**A**s the pandemic caused by severe acute respiratory syndrome-coronavirus 2 (SARS-CoV-2) continues to cause worldwide upheaval, scientists are racing to find appropriate animal models to study the coronavirus disease 2019 (COVID-19) attributed to the virus. The optimal animal model will depend on the scientific question. On page 1016 of this issue, Shi *et al.* (1) describe severe viral burden and airborne transmission of SARS-CoV-2 between cats and ferrets, highlighting an important animal model for SARS-CoV-2 transmission. Additionally, on page 1012 of this issue, Rockx *et al.* (2) found that young and aged cynomolgus macaques infected with SARS-CoV-2 shed virus in the upper and lower respiratory tract, but failed to develop severe clinical symptoms. These animal models offer distinct platforms to ask specific questions about SARS-CoV-2 infection, induction of disease, and transmission.

Humans with COVID-19 display a wide range of disease symptoms, from asymptomatic to severe pneumonia (3). Translating data from a single animal model to the varied disease outcomes in humans is not only challenging, but potentially misleading. Studies examining the efficacy of vaccines and antiviral drugs traditionally use models of severe disease, which may not mimic the common pathology in the majority of COVID-19 patients and could limit understanding of other important questions, including infection dynamics and transmission. Previous work on other emerging coronaviruses, such as Middle East respiratory syndrome-coronavirus (MERS-CoV) and SARS-CoV-1, have included mice, hamsters, ferrets, monkeys, and camels as animal models (4). Although mice are the preferred research animal model because of their cost, reproduction rate, and wealth of reagents available for

studying this species, early reports indicate that they are unsuitable for SARS-CoV-2 infection, likely due to receptor incompatibility (5). Therefore, transgenic mice that express the human angiotensin-converting enzyme 2 (hACE2), which is the host cell receptor for SARS-CoV-2 entry, will be useful to examine COVID-19 (5–7). Preliminary work with hACE2 mice demonstrates susceptibility but limited disease severity (8) (see the table).

Shi *et al.* administered a large dose of SARS-CoV-2 intranasally to a wide range of animals—ferrets, cats, dogs, pigs, chickens, and ducks—to test replication, pathogenesis, and transmission. The virus replicated

a combined intranasal and intratracheal administration shed virus in the upper and lower respiratory tract, but clinical symptoms were mild. Similarly, Gao *et al.* (9) tested the efficacy of an inactivated vaccine in rhesus macaques. In this study, vaccination with inactivated SARS-CoV-2 produced antibodies against the viral spike protein and nucleoprotein in mice, rats, and macaques. Macaques vaccinated with 3 or 6 µg of inactivated virus in alum were challenged 22 days later and demonstrated reduced viral RNA in nasal and anal swabs.

Together, these studies, along with preliminary studies in hamsters (10), suggest that there are only a handful of susceptible

## Searching for the best animal model to study COVID-19

Comparison of currently available animal models for SARS-CoV-2 infection and COVID-19.

| ANIMAL MODEL        | UPPER RESPIRATORY TRACT* | LOWER RESPIRATORY TRACT† | FECES/FECAL SWAB | CONTACT TRANSMISSION | AIRBORNE TRANSMISSION | WEIGHT LOSS | SOURCE  |
|---------------------|--------------------------|--------------------------|------------------|----------------------|-----------------------|-------------|---------|
| Cat (6 to 9 months) | Y‡                       | N                        | Y                | NR                   | Y (33%)               | NR          | (1)     |
| Chicken             | N                        | N                        | NR               | N                    | NR                    | NR          | (1)     |
| Dog                 | N                        | N                        | Y                | N                    | NR                    | NR          | (1)     |
| Duck                | N                        | N                        | NR               | N                    | NR                    | NR          | (1)     |
| Ferret              | Y‡                       | Y§                       | Y                | Y (100%)             | Y (30%)               | NR          | (1, 14) |
| hACE2 mouse         | NR                       | Y‡                       | Y‡               | NR                   | NR                    | Y           | (8)     |
| Hamster             | Y‡                       | Y‡                       | Y‡               | Y (100%)             | NR                    | Y           | (10)    |
| Kitten              | Y‡                       | Y‡                       | NR               | NR                   | Y (33%)               | NR          | (1)     |
| Macaque             | Y                        | Y                        | NR               | NR                   | NR                    | N           | (2, 9)  |
| Pig                 | N                        | N                        | NR               | N                    | NR                    | NR          | (1)     |

\* Includes nasal washes, nasal swabs, nasal turbinate, soft palate, trachea. † Includes lung sections. ‡ Denotes detection of infectious virus.

§ Infectious titer in the ferret lung was only reported in (14). COVID-19, coronavirus disease 2019; hACE2, human angiotensin-converting enzyme 2; NR, not reported; SARS-CoV-2, severe acute respiratory syndrome-coronavirus 2.

efficiently in the upper respiratory tract of cats and ferrets, suggesting that these animals are permissive to SARS-CoV-2. However, no severe clinical symptoms such as weight loss or respiratory distress were noted in ferrets or cats. In the other models, virus was not detected in nasal or rectal swabs, with the exception of two dogs in which SARS-CoV-2 RNA was detected in rectal swabs and the animals produced antibodies against the virus. These data suggest that pigs, chickens, and ducks are not permissive to SARS-CoV-2 infection.

Rockx *et al.* found that cynomolgus macaques infected with SARS-CoV-2 using

SARS-CoV-2 animal models (hamsters, ferrets, cats, and nonhuman primates). Susceptibility is likely driven by either binding affinity to the host ACE2 receptor or by differences in host protease activity on the spike protein, both key factors in coronavirus cell entry (11). In addition to release of infectious virus in the respiratory tract, viral RNA was found in rectal swabs of cats, ferrets, and macaques (1, 2), which is consistent with initial clinical observations of patients with COVID-19 (12) and suggests a potential role for the fecal-oral transmission route.

Epidemiological data have clearly de-

<sup>1</sup>Department of Microbiology and Molecular Genetics, Center for Vaccine Research, University of Pittsburgh School of Medicine, Pittsburgh, PA, USA. <sup>2</sup>Department of Microbiology and Immunology, Institute for Human Infection and Immunity, World Reference Center for Emerging Viruses and Arboviruses, University of Texas Medical Branch at Galveston, Galveston, TX, USA. Email: lakdawala@pitt.edu; vimenach@utmb.edu

fined that COVID-19 has a higher case fatality rate in individuals over 60 years of age (3). Yet, most in vivo research models use young, healthy animals. Models that recapitulate this aging phenotype would be incredibly useful to examine the underlying biology behind this phenomenon. To address this, Shi *et al.* examined COVID-19 symptoms in kittens versus cats aged 6 to 9 months, but found the opposite phenotype. COVID-19 was more severe in kittens; one kitten died on day 3 after infection and had a larger viral distribution compared to older cats. This variation in viral dissemination in kittens may be reminiscent of the vast tissue tropism and variation in disease severity exhibited by SARS-CoV-2 in humans (12). By contrast, Rockx *et al.* tested SARS-CoV-2 in young and aged macaques and did not observe any age-dependent differences. Of note, the virus is not consistently lethal in any of the animals tested thus far, nor does SARS-CoV-2 infection in these animals recapitulate the severe clinical symptoms observed in humans. As these animal models continue to be developed, attention should be paid to the role of age and other health conditions; these factors may be critical parameters that are necessary to fully evaluate human disease.

Transmission of viruses between people, either through contact (direct or indirect) or virus-containing aerosols, is a key determinant of viral disease burden globally. An important aspect of the SARS-CoV-2 pandemic, and previous influenza pandemics, is efficient airborne transmission of the virus. Airborne transmission can include a wide range of aerosol sizes. At close contact ranges, the exposure to large and small aerosols containing viruses is high. Shi *et al.* examined airborne transmission of SARS-CoV-2 between kittens and aged cats and observed that in both scenarios, the virus could transmit through the air to 33% of naïve recipient cats or kittens. In these studies, animals were separated by perforated barriers that limit physical contact but allow for air to be shared between the experimentally infected donor and the susceptible recipient. Studies of influenza virus transmission have indicated that viral replication in the upper respiratory tract, and specifically the soft palate, play an important role in airborne transmission (13). Shi *et al.* found that SARS-CoV-2 replicated in the soft palate of cats, kittens, and ferrets. Although ferret transmission was not examined in this study, a report suggested a similar airborne transmission rate of 30% for SARS-CoV-2 in ferrets (14). No contact transmission between dogs and other animals (pigs, ducks, and chickens) was observed (1).

The transmission of SARS-CoV-2 between cats highlights the susceptibility of this animal model to infection. Consistent with this observation, transmission of SARS-CoV-2 from humans to tigers was recently documented, as was virus spread among big cat units in the Bronx Zoo (15). On the basis of data from Shi *et al.*, infected cats appear asymptomatic, so infections in cats may go undetected. Additional studies are needed into the seroprevalence of SARS-CoV-2-specific antibodies in cats and identification of coronaviruses from this animal source to ascertain the potential for cats to be an intermediate host for SARS-CoV-2.

As the pursuit of SARS-CoV-2 vaccines and antivirals surges on, animal models play the most important role to determine the effectiveness of potential therapeutic strategies. The available studies suggest that hamsters, ferrets, and cats may serve as attractive alternatives to nonhuman primate and transgenic mouse studies. Because hamsters and transgenic mice display the most severe clinical symptoms, such as weight loss, they may provide robust small-animal models for studying efficacy of various vaccine platforms. By contrast, cats and ferrets may provide a useful model system for studying transmissibility of the virus and the effectiveness of antivirals to limit spread. With robust reduction in viral load as presented by Gao *et al.* (9), nonhuman primates may offer the most relevant model to assess vaccine and antiviral effectiveness before rapid deployment to humans. Therefore, continued evaluation of mice to nonhuman primate models will provide critical data on the animals best suited to study the many open questions about COVID-19. ■

#### REFERENCES AND NOTES

1. J. Shi *et al.*, *Science* **368**, 1016 (2020).
2. B. Rockx *et al.*, *Science* **368**, 1012 (2020).
3. Z. Wu, J. M. McGoogan, *JAMA* **323**, 1239 (2020).
4. L. M. Gretebeck *et al.*, *Curr. Opin. Virol.* **13**, 123 (2015).
5. P. Zhou *et al.*, *Nature* **579**, 270 (2020).
6. P. B. McCray Jr. *et al.*, *J. Virol.* **81**, 813 (2007).
7. V. D. Menachery *et al.*, *Proc. Natl. Acad. Sci. U.S.A.* **113**, 3048 (2016).
8. L. Bao *et al.*, *bioRxiv* 10.1101/2020.02.07.939389 (2020).
9. Q. Gao *et al.*, *Science* 10.1126/science.abc1932 (2020).
10. S. F. Sia *et al.*, *Research Square* 10.21203/rs.3.rs-20774/v1 (2020).
11. V. D. Menachery *et al.*, *J. Virol.* **94**, (2020).
12. Y. Chen *et al.*, *J. Med. Virol.* 10.1002/jmv.25825 (2020).
13. S. S. Lakdawala *et al.*, *Nature* **526**, 122 (2015).
14. Y. I. Kim *et al.*, *Cell Host Microbe* **20**, 30187 (2020).
15. N. Daly, "Seven more big cats test positive for coronavirus at Bronx Zoo," *National Geographic*, 22 April 2020.

#### ACKNOWLEDGMENTS

The authors are funded by NIH CEIRS HHSN272201400007C (S.S.L.) and R00 AG049092 (V.D.M.).

10.1126/science.abc6141

#### IMMUNOLOGY

## Killer cells add fire to fuel immunotherapy

Cytotoxic lymphocytes induce inflammatory target cell death, amplifying antitumor immunity

By Christopher J. Nicolai and David H. Raulet

Cytotoxic lymphocytes, including natural killer (NK) cells and cytotoxic T lymphocytes (CTLs or CD8<sup>+</sup> T cells), mediate antiviral and antitumoral immunity. Target cell killing by CTLs and NK cells is primarily mediated through the release of cytotoxic granules that contain serine proteases called granzymes and a pore-forming protein, perforin. Perforin delivers granzyme B (GZMB) into target cells, where it initiates apoptosis, a noninflammatory form of programmed cell death (1, 2). On page 965 of this issue, Zhou *et al.* (3) report their discovery of a new mechanism of cytotoxicity in which granzyme A (GZMA), delivered to certain target cells by NK cells and CTLs, activates gasdermin B (GSDMB), a pore-forming protein, which causes a proinflammatory form of cell death called pyroptosis (4). Expression of GSDMB by mouse tumor cells conferred better tumor control in response to immune checkpoint therapy.

Programmed cell death can occur through a variety of pathways that result in distinct biological outcomes. The best studied programmed cell death pathway is apoptosis, in which cytoplasmic and nuclear material condense into membrane-bound fragments, called apoptotic bodies, which are phagocytosed and destroyed by macrophages (2). Cell death through apoptosis is considered noninflammatory and is necessary for organismal development and homeostasis. By contrast, pyroptosis ("fiery death") is a proinflammatory form of cell death, usually activated by multiprotein oligomers called inflammasomes, which are triggered by a variety of stimuli. Inflammasomes activate inflammatory caspase-1, -4, -5, or -11, leading to lytic cell death and the release of proinflammatory

Department of Molecular and Cell Biology,  
University of California, Berkeley, Berkeley, CA, USA.  
Email: raulet@berkeley.edu

molecules, such as the cytokines interleukin-1 $\beta$  (IL-1 $\beta$ ) and IL-18, and eicosanoids (4, 5). Two pivotal studies identified gasdermin D (GSDMD) as a target of inflammatory caspases and the key executor of pyroptosis (6, 7). Upon cleavage, the amino-terminal domain of GSDMD oligomerizes to form pores in the cell membrane, leading to cell permeabilization and cytokine release. GSDMD is one of a family of gasdermin proteins (8) that have pore-forming domains but differ in the proteases that activate them. The roles of some members of the gasdermin family are unknown.

Zhou *et al.* provide compelling evidence that cytolysis by CTLs and NK cells is sometimes pyroptotic instead of apoptotic. In addition to GZMB, granules released by cytotoxic lymphocytes contain GZMA, which directly cleaves GSDMB in the cytosol, un-

to amplify. The results support the view that cytotoxic lymphocytes both kill target cells and in some cases activate additional inflammatory signals through pyroptosis that amplify the immune response.

GSDMB was more frequently expressed in human tumors that arose in mucosal and gastric tissues than in other types of tumors, although less often than in corresponding normal tissues, possibly reflecting selective loss of GSDMB in advanced cancers. In some types of human cancer, notably bladder carcinoma and skin cutaneous melanoma, there was a correlation between GSDMB expression and higher patient survival, although GSDMB expression in renal clear cell carcinomas was associated with lower patient survival.

Pyroptotic killing induced by cytotoxic lymphocytes has been observed previously,

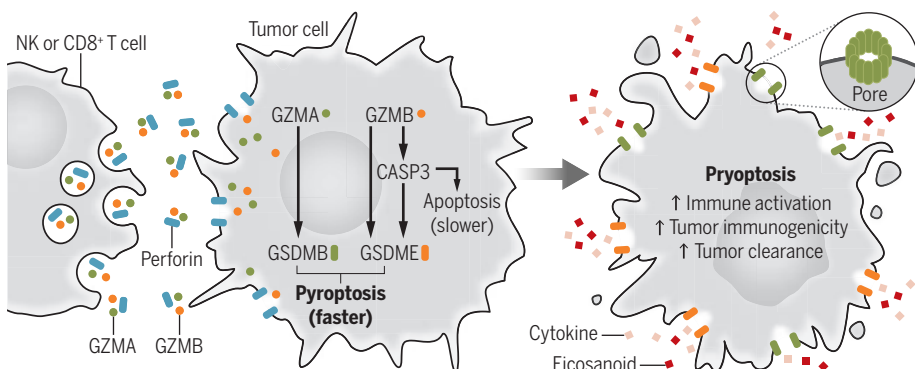
after CAR-T cell treatments in mouse models. The authors reported that GSDME-dependent pyroptosis was induced only when the T cells encountered the strong activating signals mediated by CAR engagement with CD19 and not through typical T cell antigen receptor-mediated signaling. Furthermore, another study showed that introducing nanoparticles containing active GSDMA into tumor cells mobilizes powerful antitumor T cell responses (11). It was shown that IL-1 $\beta$ , and to a lesser extent IL-18, were necessary for this amplified antitumor response.

Together with the study of Zhou *et al.*, these studies suggest that pyroptosis is a common outcome of encounters between cytotoxic lymphocytes and susceptible target cells and that pyroptosis provides a feed-forward mechanism to amplify cellular immunity and tumor rejection (see the figure). These studies do not yet provide a detailed understanding of how pyroptosis amplifies the antitumor response. Inflammatory signaling coupled with the release of target cell antigens are likely important, but the relevant inflammatory signals remain poorly defined. In one case, IL-1 $\beta$  and possibly IL-18 were shown to play a role in pyroptosis-induced immune enhancement (11), whereas another report argued that IL-1 $\beta$  plays no role (9). If IL-1 $\beta$  and/or IL-18 are important, it remains unclear exactly how they mediate their amplifying effects.

Moreover, it is not clear how the cytokines are elaborated in these circumstances. In inflammasome-induced pyroptosis, “priming” of cells by pattern-recognition receptors (which recognize pathogens) is often required for synthesis of pro-IL-1 $\beta$  and pro-IL-18, and the cytokines are processed by caspases to generate the active forms (5). How priming might occur in tumor cells is unclear, but activation of stimulator of interferon genes (STING; a sensor of cytoplasmic DNA) is an intriguing possibility (12). Although much remains to be learned, these findings require a revision of how cell-mediated cytotoxicity occurs and its consequences. ■

## Pyroptosis amplifies cellular immunity

Granzyme B (GZMB) and GZMA released by cytotoxic lymphocytes [natural killer (NK) and CD8+ T cells] penetrate target cells with the help of perforin. Recent evidence reveals that GZMA directly cleaves gasdermin B (GSDMB), whereas GSDME can be activated directly by GZMB but also indirectly by caspase 3 (CASP3). Activation of GSDMB or GSDME initiates pyroptosis, which promotes inflammation that amplifies cellular immunity.



leashing its amino-terminal pore-forming domain and initiating pyroptosis. Because this can be faster than apoptosis, cells that expressed GSDMB underwent pyroptosis rather than apoptosis. GSDMB expression was rare in a large panel of human tumor cell lines, but its expression could be induced in ~30% of the lines upon stimulation with cytokines, especially interferon- $\gamma$  (IFN- $\gamma$ ), a pleiotropic cytokine secreted by activated lymphocytes, including CTLs and NK cells. Mice do not express a GSDMB homolog yet still express GZMA. Mice bearing tumors engineered to express GSDMB showed greater tumor rejection than did mice bearing GSDMB-deficient tumors when combined with anti-programmed cell death protein 1 (PD-1) immunotherapy. These findings suggest that PD-1 blockade was necessary to unleash antitumor immune responses that GZMA-dependent GSDMB activation helped

although mediated by other gasdermin family members. For example, GZMB from NK cells directly cleaved and activated GSDME in target cells and concomitantly activated caspase 3, which also activates GSDME (9). Cleaved GSDME initiated pyroptosis and amplified immune infiltration of mouse mammary tumors grafted in mice, macrophage phagocytosis of tumor cells, and tumor rejection. Disruption of the *Gsdme* gene in mouse tumor cell lines resulted in faster-growing tumors and reduced survival in vivo, building on previous evidence that GSDME is a tumor suppressor that is frequently mutated or repressed in tumors.

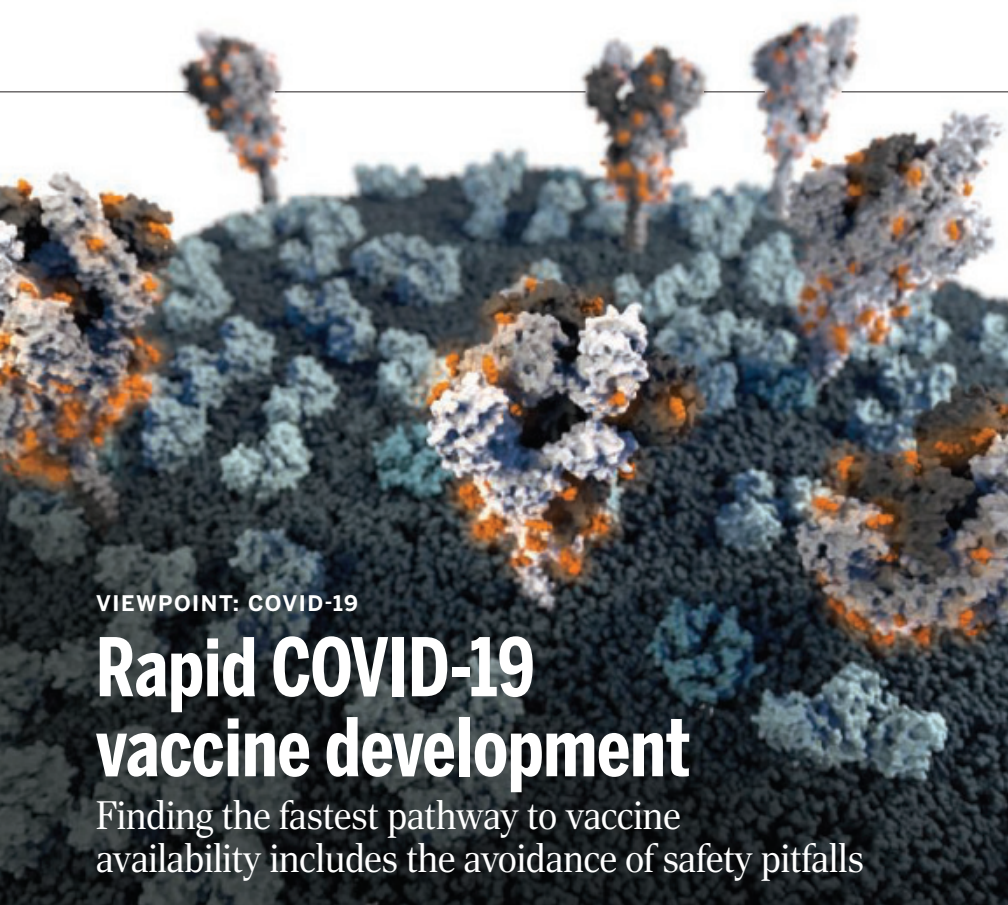
Killing of human CD19<sup>+</sup> leukemia cells in vitro by CD19-targeting chimeric-antigen receptor (CAR) T cells initiates tumor cell pyroptosis (10). In this case, pyroptosis was associated with systemic inflammation, known as cytokine release syndrome,

## REFERENCES AND NOTES

1. Voskoboinik *et al.*, *Nat. Rev. Immunol.* **15**, 388 (2015).
2. J. F. Kerr *et al.*, *Br. J. Cancer* **26**, 239 (1972).
3. Z. Zhou *et al.*, *Science* **368**, eaaz7548 (2020).
4. T. Bergsbaken *et al.*, *Nat. Rev. Microbiol.* **7**, 99 (2009).
5. K. Schroder, J. Tschoopp, *Cell* **140**, 821 (2010).
6. J. Shi *et al.*, *Nature* **526**, 660 (2015).
7. N. Kayagaki *et al.*, *Nature* **526**, 666 (2015).
8. P. Broz *et al.*, *Nat. Rev. Immunol.* **20**, 143 (2020).
9. Z. Zhang *et al.*, *Nature* **579**, 415 (2020).
10. Y. Liu *et al.*, *Sci. Immunol.* **5**, eaax7969 (2020).
11. Q. Wang *et al.*, *Nature* **579**, 421 (2020).
12. S. S. Ho *et al.*, *Immunity* **44**, 1177 (2016).

## ACKNOWLEDGMENTS

We thank R. Vance, K. Deets, and A. Tubbs for helpful comments.



VIEWPOINT: COVID-19

# Rapid COVID-19 vaccine development

Finding the fastest pathway to vaccine availability includes the avoidance of safety pitfalls

By **Barney S. Graham**

**R**apid development of a vaccine to prevent coronavirus disease 2019 (COVID-19) is a global imperative, and defining the stakes and potential hurdles is critical because regulatory and medical decisions are based on benefit:risk calculations. The ability of viruses to achieve pandemic spread is diminished by establishing higher levels of community (herd) immunity, and a key question is whether protection against severe acute respiratory syndrome-coronavirus 2 (SARS-CoV-2) will happen by widespread deployment of an effective vaccine or by repeated waves of infection over the next few years until ~60 to 70% of people develop immunity. Because the human population is naïve to SARS-CoV-2, the consequences of repeated epidemics will be unacceptably high mortality, severe economic disruption, and major adjustments to our way of life. Therefore, the benefit of developing an effective vaccine is very high, and even greater if it can be deployed in time to prevent repeated or continuous epidemics.

Vaccine development is usually measured in decades, so having access to approved vaccines available for large-scale distribution before the end of 2020 or even 2021

would be unprecedented. However, new manufacturing platforms, structure-based antigen design, computational biology, protein engineering, and gene synthesis have provided the tools to now make vaccines with speed and precision. Antiviral vaccines can be classified into two broad categories. Gene-based vaccines deliver gene sequences that encode protein antigens that are produced by host cells. These include live-virus vaccines, recombinant vaccine vectors, or nucleic acid vaccines. Protein-based vaccines include whole-inactivated virus, individual viral proteins or subdomains, or viral proteins assembled as particles, all of which are manufactured in vitro. Recombinant vaccine vectors and nucleic acid vaccines are best suited for speed because they can be more easily adapted to platform manufacturing technologies in which upstream supply chains and downstream processes are the same for each product. Precision is achieved by knowing the atomic structure of the vaccine antigen and preserving the epitopes targeted by the vaccine.

For any vaccine intended to generate antibody-mediated immunity, delivering a conformationally correct protein is critical. The CoV spike protein is displayed on the virus surface and carries out viral entry. It accomplishes this by undergoing a massive rearrangement that pulls the virus and cell membranes together and fuses them. Therefore, spike is a dynamic and metastable protein that has two major conformational

The trimeric spike protein is the primary target for vaccine-induced antibodies intended to block virus attachment to the human angiotensin-converting enzyme 2 (ACE2) receptor.

states, prefusion and postfusion. Displaying this antigen so that it maintains the surface contours and chemistry of the original native prefusion spike protein will preserve the epitopes required for eliciting high-quality neutralizing antibody responses. The vaccine formulation and delivery can also be crafted to influence T cell functions and response patterns. Gene-based delivery can induce CD8<sup>+</sup> T cells and generally drive a CD4<sup>+</sup> T helper 1 cell (T<sub>H</sub>1)-type immune response, which has favorable antiviral properties. Adjuvants not only can be used to improve the magnitude and durability of antibody responses induced by protein-based vaccines but can also influence T cell-derived cytokine patterns and thus modulate immune responses.

Safety is a primary goal for vaccines that are given to otherwise healthy people, and there is a risk that vaccination could make subsequent SARS-CoV-2 infection more severe. This has happened before with vaccines based on whole-inactivated virus formulated in alum for a coronavirus of cats and for another unrelated respiratory virus in children. There are two different syndromes previously associated with vaccine-enhanced disease (see the table). One is antibody-dependent enhancement (ADE) (1) and the other is vaccine-associated enhanced respiratory disease (VAERD) (2). ADE is an Fc (the tail end of an antibody)-mediated enhancement of infection typically associated with flaviviruses, such as dengue virus (3). ADE is measured in vitro on cells that express Fc receptors (FcRs) either naturally or by transfection. The ADE mechanism involves increased binding efficiency of virus-antibody complexes to FcR-bearing cells, which triggers viral entry. This is more likely to occur when vaccine-induced antibody fails to effectively neutralize the virus because of insufficient concentration or affinity or the wrong specificity.

ADE has been described for feline infectious peritonitis virus (FIPV), a coronavirus that targets macrophages for infection (tropism) and causes a systemic vasculitis-like disease (4). Antibody-mediated disease enhancement was demonstrated after infection in cats that were previously vaccinated with alum-adjuvanted inactivated virus. Although SARS-CoV-2 cellular tropism has not been completely defined, it is a respiratory virus, and consistent with coronaviruses that cause Middle East respiratory syndrome (MERS-CoV) and SARS (SARS-CoV-1), infection of respiratory epithelium results in a very different pathogenesis than the macrophage-tropic FIPV. ADE was shown to occur for SARS-

Vaccine Research Center, National Institute of Allergy and Infectious Diseases, National Institutes of Health, Bethesda, MD, USA. Email: bgraham@mail.nih.gov

CoV-1 in vitro in an FcR-bearing human B cell lymphoma cell line and based on detection of viral gene fragments by polymerase chain reaction (PCR). However, there is no experimental data in vivo showing that this type of antibody-mediated entry is relevant to the pathophysiology of respiratory coronaviruses like SARS-CoV-1, and even in vitro, no infectious virus was produced, suggesting an abortive replication cycle in myeloid cells (5).

VAERD is a distinct clinical syndrome that occurred in young children in the 1960s when whole-inactivated virus vaccines for measles and respiratory syncytial virus (RSV) were tested (6, 7). Immunizing with limiting doses of RSV antigen, especially with conformationally incorrect antigens, can result in two major types of immunological phenomenon that correlate with enhanced respiratory disease (ERD). One is a relatively high ratio of binding antibody to neutralizing antibody. Having a large amount of antibody that binds, but does not neutralize, virus in the presence of a high viral load could potentially result in immune complex deposition

clearance. Therefore, avoiding T<sub>H</sub>2-biased immune responses may be important, especially in young infants with small airways that can be easily obstructed. In the youngest cohort of children who received the FI-RSV vaccine, 80% of those infected required hospitalization compared with 5% of placebo recipients (7). In the lung histopathology of the two children who died, there was an abundant polymorphonuclear leukocyte response in lungs that included eosinophils. This is consistent with findings in animal models of T<sub>H</sub>2-biased CD4<sup>+</sup> T cell responses associated with FI-RSV and VAERD (11).

Similar T cell and cytokine response patterns have been shown in mice, cotton rats, cattle, and nonhuman primate models of RSV immunized with whole-inactivated virus formulated with alum (12). In almost all the examples of VAERD demonstrated in humans for RSV and measles, and in animals for SARS (13), the vaccine antigen was whole-inactivated virus. There are caveats to the animal experiments because the allergic inflammation phenomenon can also be elic-

T<sub>H</sub>2-biased immune responses. Using limiting dilutions of vaccines and examining lung pathology in animals with breakthrough infection after challenge should also help gauge the likelihood of aberrant pathology in vaccinated humans.

Defining the immunological parameters of VAERD in animal models of RSV delayed extensive industry involvement in vaccine development by ~30 years. Although the potential risk of vaccine-induced antibody or T cell responses leading to adverse responses to natural SARS-CoV-2 infection should be carefully evaluated, there is also a risk of delaying clinical trials in favor of prolonged evaluation of vaccines in animal models that do not fully recapitulate the pathogenesis of disease in humans. In the midst of a pandemic, it is reasonable to require certain qualities in candidate vaccines as described above and to start phase 1 clinical trials based on preliminary immunogenicity in animals and expanded trials based on human immunogenicity and evidence of protection in animal models. Justifying expansion to thousands of subjects in efficacy trials (that is, phase 2 and 3 trials) could include additional evidence of vaccine safety in animals immunized with limiting doses of vaccine and breakthrough infections after SARS-CoV-2 challenge. Judicious evaluation of candidate vaccines in healthy adults in parallel with vaccine studies in animal models and coincident process development to scale-up production capacity provides a path forward with minimal risk to human subjects and the potential for enormous benefit through accelerated COVID-19 vaccine availability. ■

Potential risks associated with vaccine development for COVID-19

Antibodies that bind virus without neutralizing infectivity can cause disease through increased viral replication or formation of immune complexes that deposit in tissue and activate complement pathways associated with inflammation. T helper 2 cell (T<sub>H</sub>2)-biased responses have also been associated with ineffective vaccines that lead to enhanced disease after subsequent infection. Antibody-dependent enhancement (ADE) of viral replication has occurred in viruses with innate macrophage tropism. Virus-antibody immune complexes and T<sub>H</sub>2-biased responses can both occur in vaccine-associated enhanced respiratory disease (VAERD).

|            | Antibody-mediated  |  | T cell-mediated  |
|------------|--|--|--|
|            | ADE  | VAERD  | VAERD  |
| Mechanism  | Fc-mediated increase in viral entry                                      | Immune complex formation and complement deposition | T <sub>H</sub> 2-biased immune response                            |
| Effectors  | Macrophage activation and inflammatory cytokines                         | Complement activation and inflammatory cytokines   | Allergic inflammation and T <sub>H</sub> 2 cytokines               |
| Mitigation | Conformationally correct antigens and high-quality neutralizing antibody |  | T <sub>H</sub> 1-biasing immunization and CD8 <sup>+</sup> T cells |

and complement activation. This was demonstrated in the small airways of infants during the formalin-inactivated (FI) RSV vaccine trial in 1966 and contributed to inflammation and airway obstruction (8). A similar phenomenon occurred after measles infection of Rhesus macaques that were immunized with whole-inactivated measles virus vaccine (9). The other observation is that immunization with whole-inactivated virus vaccines followed by RSV infection can result in allergic inflammation (10). Responses that accentuate production of the cytokines interleukin-4 (IL-4), IL-5, and IL-13 result in increased mucus production, eosinophil recruitment, airway hyperresponsiveness, and attenuated cytolytic T cell activity, collectively known as T<sub>H</sub>2 immune responses. These events potentiate airway dysfunction and delay viral

ited by using the same cell line and media to grow the vaccine virus and challenge virus. Cellular components and media additives can cause sensitization to those proteins even without viral antigens present (14). There are ways to mitigate the risks of vaccine-enhanced disease syndromes informed by prior work on RSV vaccines that should be considered for COVID-19 vaccine development (15). It will be important to demonstrate the potential for vaccine efficacy in early-phase clinical studies by measuring the induction of neutralizing antibodies and in animal models by demonstrating protection against virus replication and disease. Equally important will be using conformationally correct antigens to elicit high-quality, functionally relevant antibody and to avoid induction of non-neutralizing antibody and

REFERENCES AND NOTES

1. J. R. Mascola et al., *AIDS Res. Hum. Retroviruses* **9**, 1175 (1993).  
2. F. P. Polack, *Pediatr. Res.* **62**, 111 (2007).  
3. K. A. Dowd, T. C. Pierson, *Virology* **411**, 306 (2011).  
4. C. W. Olsen, W. V. Corapi, C. K. Ngichabe, J. D. Baines, F. W. Scott, *J. Virol.* **66**, 956 (1992).  
5. M. Jaume et al., *J. Virol.* **85**, 10582 (2011).  
6. V. A. Fulginiti, J. J. Eller, A. W. Downie, C. H. Kempe, *JAMA* **202**, 1075 (1967).  
7. H. W. Kim et al., *Am. J. Epidemiol.* **89**, 422 (1969).  
8. F. P. Polack et al., *J. Exp. Med.* **196**, 859 (2002).  
9. F. P. Polack, S. J. Hoffman, G. Crujeiras, D. E. Griffin, *Nat. Med.* **9**, 1209 (2003).  
10. B. S. Graham et al., *J. Immunol.* **151**, 2032 (1993).  
11. T. J. Ruckwardt, K. M. Morabito, B. S. Graham, *Immunity* **51**, 429 (2019).  
12. A. Muralidharan, C. Li, L. Wang, X. Li, *Expert Rev. Vaccines* **16**, 351 (2017).  
13. M. Bolles et al., *J. Virol.* **85**, 12201 (2011).  
14. C. A. Shaw et al., *Vaccine* **31**, 306 (2013).  
15. S. K. Browne, J. A. Beeler, J. N. Roberts, *Vaccine* **38**, 101 (2020).

ACKNOWLEDGMENTS

Thanks to J. Mascola, K. Morabito, K. Corbett, K. Bok, R. Seder, and M. Kanekiyo for helpful comments and discussions. This work was supported by intramural funding from the National Institute of Allergy and Infectious Diseases, NIH. The author is an inventor on patent applications that involve coronavirus vaccines and monoclonal antibodies.

# RETROSPECTIVE

# Eleanor Margaret Burbidge (1919–2020)

Astronomer, astrophysicist, and champion of gender equality

By Alec Boksenberg

**W**orld-celebrated observational astronomer and astrophysicist Eleanor Margaret Burbidge (known as Margaret) died on 5 April at age 100. Margaret was a brilliant researcher, innovator, leader, and inspiration to others. She greatly advanced knowledge of the properties of stars and distant galaxies and, most famously, demonstrated with colleagues how almost all elements are fabricated from hydrogen within stars. By both practice and example, she was a force for gender equality in science and antidiscrimination in all forms. She served as the first female director of key scientific bodies and institutions in the United States and the United Kingdom.

Margaret was born in 1919 in Davenport, England. By the age of 12, she was consuming substantial books on astronomy. She graduated from University College London (UCL) in 1939 with a degree in astronomy with concentrations in mathematics and physics. Particularly attracted by the physical complexity of stars, Margaret enrolled as a graduate student at UCL while looking after the telescope instruments of the University of London Observatory at Mill Hill. During World War II, she worked on spectroscopic stellar research, taking advantage of the unusually dark skies created by blackouts and often sheltering from nearby German bomb blasts. She finished her Ph.D. in astronomy and astrophysics in 1943 and published her first scientific paper in 1946. In 1947, she met her husband to be, Geoffrey Burbidge, when he enrolled in the physics Ph.D. program at UCL. They married in 1948, soon after she inspired him to turn to astrophysics by inviting him to the observatory where she had become acting director.

They moved in 1950 to the United States in search of telescopes and sites superior to those in the United Kingdom. In response to her first job application, Margaret received a letter saying the position was not open to women. In 1951, she was welcomed by the University of Chicago's Yerkes Observatory in Wisconsin. Later, she applied to observe at

the Mount Wilson Observatory in California but was denied, so Geoffrey applied instead. Margaret succeeded in using the observatory through subterfuge—she posed as Geoffrey's assistant, whereas the reverse was true.

On an extended visit to the Institute of Astronomy in Cambridge, England, in 1955 to 1956, Margaret—who had already made many substantial observational discoveries—played a crucial role in the intensive work that produced one of the most important discoveries in the history of astrophysical research to this day. Along with Geoffrey, physicist William Fowler, and astrophysicist Fred Hoyle, Margaret demonstrated in extraordinary breadth and depth that the bulk of all elements in the Universe were synthesized within stars through progressive stages of nuclear fusion and final outburst.



Along with Fred Hoyle and Geoffrey, Margaret favored the steady-state theory of the Universe, which postulates that the Universe is constantly generating new matter to counter its own expansion, as opposed to the Big Bang theory, which states that there was a definite beginning. She contributed evidence for the steady-state theory through her observations, although her important work on the then-mysterious fast-moving quasars (now recognized to be distant galaxies powered by immense central black holes) suggested a different explanation. A chance discovery by others led to wide acceptance of the Big Bang theory, but Margaret's persistent radical work should be celebrated as revolutionary thinking that spurred efforts toward further observations and inspired new theories to progress to a conclusion.

Margaret was well known for her work opposing professional discrimination against

women. Perhaps remembering the cunning strategy required to conduct her own early observatory work, she often advised women to be relentless in finding alternative routes when something obstructed their path to a goal. In 1971, she declined the American Astronomical Society's influential Annie Jump Cannon Award, given exclusively to women, because she felt that it was itself discriminatory. She held many top leadership and administrative posts, including director of the Royal Greenwich Observatory in the United Kingdom from 1973 to 1975, president of the American Astronomical Society from 1976 to 1978, and president of the American Association for the Advancement of Science (the publisher of *Science*) in 1983. From 1979 to 1988, she was the first director of the Center for Astrophysics and Space

Sciences at the University of California, San Diego, where she worked from 1962 until her retirement. She was inducted into the Women's Museum of California Hall of Fame in 2003. Asteroid (5490) Burbidge was named after her.

I got to know Margaret through small scientific social gatherings in Cambridge and London, at which we exposed, explored, and debated ideas, sometimes vehemently but always in good humor. Margaret was calm, soft-spoken, and polite. Once, while discussing the Hubble Space Telescope Faint Object Spectrograph that she had helped develop, she showed me an old photographic record of a faint spectrum she had obtained from the ground. At first, I could see nothing on it except for a very faint, grainy haze. Then, with a broad smile, she tilted the photograph on its long side, visually condensing the image vertically and bringing the spectrum well into view. We both laughed at how creative thinking could provide clarity.

Throughout Margaret's life, she showed that in what was (and remains) a so-called man's world, women can and should be recognized for their brilliance and rise to the greatest heights of achievement and fame. Margaret did so with graciousness, humanity, and a drive to help others along the way. She made a difference not only to her field but to all scientists who can look to her as an example of persisting despite obstacles. ■

Institute of Astronomy, University of Cambridge, Cambridge, UK. Email: boksy@ast.cam.ac.uk

10.1126/science.abc6555



## VACCINATION: COVID-19

# A strategic approach to COVID-19 vaccine R&D

A public-private partnership and platform for harmonized clinical trials aims to accelerate licensure and distribution

By **Lawrence Corey**<sup>1,2</sup>, **John R. Mascola**<sup>3</sup>,  
**Anthony S. Fauci**<sup>4</sup>, **Francis S. Collins**<sup>5</sup>

**T**here is an unprecedented need to manufacture and distribute enough safe and effective vaccine to immunize an extraordinarily large number of individuals in order to protect the entire global community from the continued threat of morbidity and mortality from severe acute respiratory syndrome-coronavirus 2 (SARS-CoV-2). The global need for vaccine and the wide geographic diversity of the pandemic require more than one effective vaccine approach. Collaboration will be essential among biotechnology and pharma-

ceutical companies, many of which are bringing forward a variety of vaccine approaches (1). The full development pathway for an effective vaccine for SARS-CoV-2 will require that industry, government, and academia collaborate in unprecedented ways, each adding their individual strengths. We discuss one such collaborative program that has recently emerged: the ACTIV (Accelerating COVID-19 Therapeutic Interventions and Vaccines) public-private partnership. Spearheaded by the U.S. National Institutes of Health (NIH), this effort brings together the strengths of all sectors at this time of global urgency. We further discuss a collaborative platform for conducting harmonized, randomized controlled vaccine efficacy trials. This mechanism aims to generate essential safety and efficacy data for several candidate vaccines in parallel, so as to accelerate the licensure and distribution of multiple vaccine platforms and vaccines to protect against COVID-19 (coronavirus disease 2019).

We currently know little about what constitutes a protective immune response

against COVID-19. Data from SARS-CoV-1 patients as well as recently infected SARS-CoV-2 patients document relatively high levels of immune responses after infection, especially antibody responses to the surface (spike) protein that mediates entry into host cells. However, in vivo data on the type or level of immunity required to protect from subsequent re-infection, and the likely duration of that protection, are currently unknown. In animal models of SARS-CoV-1, immunization with recombinant subunit proteins and viral- and nucleic acid-vectored vaccines, as well as passive transfer of neutralizing antibodies to the spike protein, have been shown to be protective against experimental infection (2, 3). Endpoints vary from protection of infection to modification of viral replication and disease. These data bring optimism that a highly immunogenic vaccine will elicit the magnitude and quality of antibody responses required for protection. The role that T cell immunity plays in preventing acquisition or amelioration of early disease, either in animal challenge models or in human coronavirus disease, is unclear (4); this constitutes another reason why a diversity of vaccine approaches must be pursued.

A high degree of safety is a primary goal for any widely used vaccine, and there is theoretical risk that vaccination could make subsequent SARS-CoV-2 infection more severe. This has been reported for feline coronaviruses and has been observed in some vaccine-challenge animal models of SARS-CoV-1 (5). These preclinical data suggest that the syndrome of vaccine-associated enhanced respi-

<sup>1</sup>Vaccine and Infectious Disease Division, Fred Hutchinson Cancer Research Center, Seattle, WA 98109, USA.

<sup>2</sup>Departments of Medicine and Lab Medicine, University of Washington, Seattle, WA 98195, USA. <sup>3</sup>Vaccine Research Center, National Institute of Allergy and Infectious Diseases, National Institutes of Health, Bethesda, MD 20892, USA. <sup>4</sup>National Institute of Allergy and Infectious Diseases, National Institutes of Health, Bethesda, MD 20892, USA. <sup>5</sup>National Institutes of Health, Bethesda, MD 20892, USA. Email: afauci@niaid.nih.gov

ratory disease results from a combination of poorly protective antibodies that produce immune complex deposition together with a T helper cell 2 ( $T_H2$ )-biased immune response. The potential mechanism behind vaccine-induced immune enhancement and the means to minimize this risk have recently been reviewed (6). It will be important to construct conformationally correct antigens to elicit functionally effective antibodies—a lesson learned from vaccine-induced enhanced lower respiratory illness among infants receiving a formalin-inactivated respiratory syncytial virus (RSV) vaccine. Animal models of SARS-CoV-2 infection are currently being developed, and these models can be used to better understand the immune responses associated with protection (7).

### CLINICAL AND IMMUNOLOGICAL ENDPOINTS

The primary endpoint for defining the effectiveness of a COVID vaccine also requires discussion. The two most commonly mentioned are (i) protection from infection as defined by seroconversion, and (ii) prevention of clinically symptomatic disease, especially amelioration of disease severity, including the frequency of disease requiring high-intensity medical care with some assessment of a decrease in hospitalization. This requires the close evaluation of the effect of vaccination on the severity of COVID-19 disease in a wide variety of epidemiological and medical settings among both younger and elderly populations as well as underserved minorities. All of these issues need to be evaluated in the context of these initial efficacy trials. Achieving these endpoints could also be associated with reduced transmissibility on a population basis.

Primary endpoints that involve reduction of disease require greater numbers of enrollees into trials, given that asymptomatic infection is estimated to be 20 to 40% of total cases of COVID-19 (8). Initial efficacy trials may then require a large initial enrollment, with ongoing monitoring of both serologic and clinical endpoints. A major challenge leading to a degree of complexity in developing clinical trial protocols for serological endpoints is the lack of precise knowledge of incidence rates (9). A critical requirement for such a multi-trial strategy is the establishment of independent laboratories with similar or identical validated serologic assays to provide a harmonizing bridge between multiple vaccine products and multiple vaccine efficacy trials. The use of these laboratories for each clinical trial, or the sharing of critical specimens from a trial, should be required. Parameters that would distinguish the immune response resulting from vaccination versus from infection are under intense in-

vestigation, and there is an immediate need to develop assays to address this issue.

Efficacy trials need to be evaluated for both benefit and harm. The likelihood of SARS-CoV-2 reexposure is much higher than that of SARS-CoV-1, which has disappeared from community circulation, and hence longer-term evaluation of potential enhancement with reexposure is needed. This requirement does not preclude licensure based on the endpoints outlined above; however, it does indicate that more prolonged follow-up of the initial vaccine cohorts should be undertaken. The durability of clinical and serologic endpoints will also need to be explored, as waning of immunity is common with human coronavirus infections (10). Coronaviruses have a single-stranded RNA genome with a relatively high mutation rate. Although there has been some genetic drift during the evolution of the SARS-CoV-2 epidemic, major alterations in the spike protein are not extensive to date, especially in the regions thought to be important for neutralization; this enables cautious optimism that vaccines designed now will be effective against circulating strains 6 to 12 months in the future (11).

The possibility of performing controlled human challenge trials, in which a small number of volunteers are vaccinated and subsequently challenged with SARS-CoV-2, has been suggested. Such experiments, if designed to define potential immune correlates or winnow out less effective vaccine approaches, may have utility. However, this approach has shortcomings with respect to pathophysiology and safety (12). Although the risk of severe disease or death in young healthy individuals from COVID-19 is quite low, it is not zero, and we do not yet have proven effective therapies for COVID-19 to rescue volunteers with complications from such a challenge. It is likely that a SARS-CoV-2 challenge strain will, by design, cause mild illness in most volunteers and thus may not recapitulate the pulmonary pathophysiology seen in some patients. Moreover, partial efficacy in young healthy adults does not predict similar effectiveness among older adults with major cofactors associated with COVID-19 disease, nor would it prove reduction of transmissibility to major susceptibility groups. Whether such experiments may be worthy of pursuit or would have a beneficial impact on timelines for vaccine development needs careful evaluation by an independent panel of ethicists, clinical trialists, and experts on vaccine development.

### VACCINE PLATFORMS

It is encouraging that vaccine development efforts have moved swiftly, and several major vaccine platforms are moving toward clinical evaluation. These include traditional recom-

binant protein, replicating and nonreplicating viral vectors, and nucleic acid DNA and mRNA approaches. Each of these vaccine platforms has advantages and limitations. Important characteristics include speed and flexibility of manufacture, safety and reactogenicity, the profile of humoral and cellular immunogenicity, durability of immunity, scale and cost of manufacturing, vaccine stability, and cold chain requirements. No single vaccine or vaccine platform alone is likely to meet the global need, and so a strategic approach to the multi-pronged endeavor is absolutely critical.

Several companies are developing nucleic acid-based vaccines, including Moderna, BioNTech/Pfizer, CureVac (mRNA-based), and Inovio (DNA-based). DNA- and mRNA-based vaccines can be generated quickly on the basis of viral sequence, which allows a rapid pathway to the clinic (13, 14). Currently, optimal immunogenicity of DNA requires an electroporation or an injector delivery device to facilitate DNA entry into cells. mRNA vaccines use lipid nanoparticles to protect and deliver the mRNA and effectively adjuvant the immunogen. The scalability of these lipid nanoparticles and their temperature stability are issues that need to be addressed. Although there is a wide body of early-phase clinical experience with nucleic acid vaccines, none are licensed for widespread usage. As such, the path forward is filled with optimism, but some uncertainty remains, requiring rapid assessment of these products' immunogenicity and safety while addressing the lack of commercial experience with them.

Traditional recombinant protein technology can be used to express the spike protein (e.g., Sanofi, Novavax), and although the time to establish cell lines needed for manufacturing is longer than for nucleic acid vaccines, there is a robust commercial experience with protein and protein particle vaccines, including licensed vaccines for hepatitis B, human papillomavirus, varicella zoster, and influenza. Protein vaccines will require a potent adjuvant, which can be critical for inducing a predominantly  $T_H1$ -type immune response; however, the availability of certain adjuvants may be limited. Viral vector vaccines encode the viral gene of interest into one of several well-characterized vectors, including adenovirus (Ad) and vesicular stomatitis virus (VSV). The replication-defective adenovirus 26 (rAd26), recently shown to be safe and immunogenic in preventing Ebola virus infection (15), is being developed by Janssen Pharmaceuticals for COVID-19. This platform has the potential to be manufactured at large scale. Preexisting immunity to the specific viral vector can attenuate immunogenicity, and this needs to be addressed in early-stage trials. A recombinant chimpanzee

Ad vector (ChAdOx1), developed by the University of Oxford and AstraZeneca, has also entered clinical trials. Similar versions of ChAd vaccine products have been tested in prior clinical trials and shown to be safe and immunogenic. The VSV vector vaccine platform is replication-competent and thus induces a robust, likely durable immune response with a single dose. A licensed VSV Ebola vaccine made by Merck is highly effective after a single dose, although its reactogenicity may be limiting in some populations. These diverse approaches provide the potential for scalable production required for widespread population use.

### STRATEGIC COLLABORATIONS

Under the ACTIV public-private partnership, NIH has partnered with its sister agencies in the Department of Health and Human Services, including the Food and Drug Ad-

(DSMB) should be used so that the regulatory framework for the entire enterprise is coordinated and the regulatory agencies and the public can make objective assessment of the effect sizes between approaches. As vaccine candidates are poised to enter phase 1, the collective planning for phase 3 must be undertaken. Although much of this focus is on trials in the United States, the COVID-19 Prevention Networks established under the ACTIV program have a global focus, and coordination with the World Health Organization, Coalition for Epidemic Preparedness Innovations, and other global philanthropic partners must also occur.

Harmonized master protocols will be needed to enable transparent evaluation of the relative effectiveness of each vaccine approach. This harmonization can best be achieved through public-private partnerships such as ACTIV, in which government-

dent statisticians having access to cross-trial data in real time, and centralized immune monitoring laboratories. These innovations in the process of vaccine development are required to achieve the rapid development of the platform technologies entering clinical trials. Global effort, global cooperation, and transparency are needed to maximize the speed, veracity, and decision-making required to deliver scientific advances to the global population in a timely fashion. Models for all of these programs exist, and rapid implementation of these ideas is essential if we are to succeed in the timelines required to return us to pre-COVID-19 social interactions.

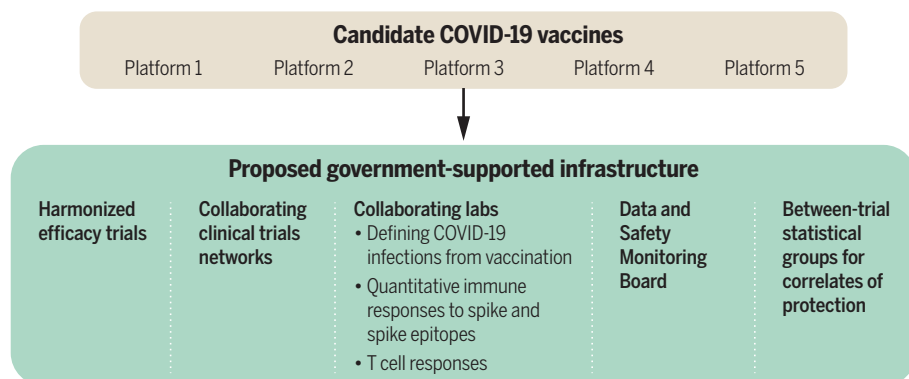
### SCALE UP

The ability to manufacture hundreds of millions to billions of doses of vaccine requires the vaccine-manufacturing capacity of the entire world. Although new technologies and factories can be developed to sustain production, there is an immediate need to fund the necessary biomanufacturing infrastructure, including the fill/finish steps that provide vialled vaccine products for distribution. Cost, distribution system, cold chain requirements, and delivery of widespread coverage are all potential constriction points in the eventual delivery of vaccines to individuals and communities. All of these issues require global cooperation among organizations involved in health care delivery and economics.

To return to a semblance of previous normality, the development of SARS-CoV-2 vaccines is an absolute necessity. To achieve this goal, all the resources in the public, private, and philanthropic sectors need to participate in a strategic manner. The ACTIV public-private partnership and collaborative harmonized efficacy trials are enabling models to achieve our common goal. ■

## The ACTIV model for SARS-CoV-2 vaccine development

The necessary partners in the public-private partnership are based on nonidentical but harmonized efficacy trials associated with collaborating clinical trials networks and laboratories, a common Data and Safety Monitoring Board, and an independent statistical group to determine correlates of protection.



ministration, Centers for Disease Control and Prevention, and Biomedical Advanced Research and Development Authority; other U.S. government departments including the Departments of Defense and Veterans Affairs; the European Medicines Agency; and representatives from academia, philanthropic organizations, more than 15 biopharmaceutical companies, and the Foundation for NIH. This forum allows for discussions and consensus on vaccine trial designs, rapid data sharing, and close collaborations between the public and private sectors to rapidly and efficiently conduct vaccine efficacy studies. There is an emerging consensus that vaccine trials need to either use common independent laboratories or contribute samples and data for the purpose of generating surrogate markers that ultimately speed licensure and an overall comparison of efficacy. A common Institutional Review Board as well as a common cross-trial Data and Safety Monitoring Board

supported central laboratories and independent biostatisticians serve as key resources for efficacy trials, thereby providing a standardized way to assess the relative immune responses of different types of vaccines (see the figure). Such laboratories enhance the ability to define correlates of protection, which would speed licensure for all vaccines as well as define populations that will achieve protective immunity. Data should be shared among companies and be provided to independent statistical evaluation, allowing the early evaluation of a potential surrogate marker of protection, which would markedly speed licensure and distribution. Such data can only be obtained from harmonization and collaboration early on, during the planning of efficacy trials and the implementation of the collaboration described in the figure: the use of collaborating clinical trial sites, the monitoring of these efficacy trials through a common DSMB, indepen-

### REFERENCES AND NOTES

1. N. Lurie, M. Saville, R. Hatchett, J. Halton, *N. Engl. J. Med.* 10.1056/NEJMp2005630 (2020).
2. J. ter Meulen *et al.*, *Lancet* **363**, 2139 (2004).
3. H. Bisht *et al.*, *Proc. Natl. Acad. Sci. U.S.A.* **101**, 6641 (2004).
4. J. Huang *et al.*, *Vaccine* **25**, 6981 (2007).
5. M. Bolles *et al.*, *J. Virol.* **85**, 12201 (2011).
6. B. S. Graham, *Science* **368**, 945 (2020).
7. B. Rockx *et al.*, *Science* **368**, eabb7314 (2020).
8. T. M. McMichael *et al.*, *N. Engl. J. Med.* 10.1056/NEJMoa2005412 (2020).
9. S. M. Kissler, C. Tedijanto, E. Goldstein, Y. H. Grad, M. Lipsitch, *Science* **368**, 860 (2020).
10. W. Liu *et al.*, *J. Infect. Dis.* **193**, 792 (2006).
11. T. Bedford *et al.*, medRxiv 2020.04.02.20051417 [preprint], 16 April 2020.
12. S. K. Shah *et al.*, *Science* **368**, 832 (2020).
13. K. A. Dowd *et al.*, *Science* **354**, 237 (2016).
14. N. Pardi *et al.*, *Nature* **543**, 248 (2017).
15. I. D. Milligan *et al.*, *JAMA* **315**, 1610 (2016).

### ACKNOWLEDGMENTS

We thank C. Dieffenbach and E. Erbeling for insightful discussion and comments, and M. Miner for editorial assistance.

Published online 11 May 2020  
10.1126/science.abc5312

# Ethics and governance for digital disease surveillance

The question is not whether to use new data sources but how

By **Michelle M. Mello**<sup>1,2</sup> and **C. Jason Wang**<sup>1,3</sup>

**D**igital epidemiology—the use of data generated outside the public health system for disease surveillance—has been in use for more than a quarter century [see supplementary materials (SM)]. But several countries have taken digital epidemiology to the next level in responding to COVID-19. Focusing on core public health functions of case detection, contact tracing, and isolation and quarantine, we explore ethical concerns raised by digital technologies and new data sources in public health surveillance during epidemics. For example, some have voiced concern that trust and participation in such approaches may be unevenly distributed across society; others have raised privacy concerns. Yet counterbalancing such concerns is the argument that “sometimes it is unethical *not* to use available data” (1); some trade-offs may be not only ethically justifiable but ethically obligatory. The question is not whether to use new data sources—such as cellphones, wearables, video surveillance, social media, internet searches and news, and crowd-sourced symptom self-reports—but how.

## INNOVATIONS AGAINST COVID-19

Some efforts involve escalations of existing techniques of digital epidemiology—for example, using cellphone signals and social media data to map the spread of the virus—whereas other, more innovative initiatives focus on implementing public health measures such as isolation and quarantine.

## Disease modeling and forecasting using machine learning and artificial intelligence

There is growing potential to use machine learning and big data to forecast disease spread and prioritize people for testing or limitations on movement. One controversial application during the COVID-19 outbreak has been the Chinese government’s require-

ment that citizens in more than 200 cities in stall an Alipay app on their smartphones that assigns a risk code to each person indicating the extent to which they are permitted to move around the community (see SM). The coding algorithm reportedly incorporates information on time spent at risky locations and frequency of contact with other people. Public dissatisfaction with the app arose from lack of transparency about the reasons

## Whether to implement, how to implement

### What is the alternative?

Whether to adopt a digital surveillance measure should be evaluated by referencing the counterfactual. What would be used instead of the technology, and is that more or less desirable?

### Least burdensome alternative

For its use to be justified, a digital technology should be judged the least burdensome alternative that would accomplish the public health objective.

### Public oversight

Oversight must include members of the public; focus on particular uses of the data, not just data transfers; and promote trustworthy, transparent, and convincing justifications for the decisions taken.

### Correcting mistakes

Processes through which potential errors can be challenged in the courts may be modified, involving longer waits, less robust hearings, and reduced access to counsel. Proving mistakes can be difficult where a decision has been driven by an algorithm whose logic may not be transparent.

### Inequities and bias

Inequities persist in people’s access to the internet and cellphones. Even among those having access, disparities exist in who uses these technologies. These disparities risk creating bias in new data sets.

people were classified into particular groups and mismatch with individuals’ own beliefs about their risk level. Yet algorithmic classification and prioritization of individuals or localities may offer an alternative to haphazard rollout of social distancing orders and COVID-19 testing.

## Leveraging and linking large datasets for case identification

Governments have massive troves of citizens’ personal data at their disposal that can be used to identify persons at increased risk of infection and prioritize them for investigation by health officials. The Taiwanese government linked immigration and customs data on travelers (in batch files, after deleting irrelevant travel history) to National Health Insurance data on hospital and clinic visits to identify individuals whose symptoms could be due to contracting the novel coronavirus during travel to an affected area (2). That information was shared with health care providers so that they could use it to make decisions during patient visits, such as asking for additional history of present illness and ordering a COVID-19 test.

## Risk-based border security

Taiwan developed an interesting alternative to blanket travel restrictions: individualized risk assessment. Travelers scan a QR code using their smartphone, which leads to an online travel declaration form that asks for travel history and flight information, symptoms of fever or respiratory infection, and contact information in Taiwan. On the basis of their health and travel information, travelers are either sent a pass by text, asked to do home quarantine for 14 days, or instructed to self-isolate at home for 14 days (2).

## Electronic monitoring of quarantined and isolated individuals

New Zealand, Thailand, and Taiwan use cellphone location data to monitor movement of persons subject to quarantine or isolation orders. In Taiwan, for example, violators can receive heavy fines or be ordered into facilities, but the government first messages individuals to instruct them to return home and asks local police to check on them (2). China, Poland, and Russia have gone further, using facial recognition software to monitor compliance with orders (see SM). Such measures, although intrusive, help reduce the need for labor-intensive, in-person monitoring. Deidentified location data from cellphones and social media apps can also be used to monitor population-level adherence to social distancing orders (see SM).

Digital technologies are also useful for supporting confined individuals. Remote monitoring through smartphones improves

<sup>1</sup>Center for Health Policy/Primary Care and Outcomes Research, Department of Medicine, Stanford University School of Medicine, Stanford, CA, USA. <sup>2</sup>Stanford Law School, Stanford, CA, USA. <sup>3</sup>Department of Pediatrics and Center for Policy, Outcomes and Prevention, Stanford University School of Medicine, Stanford, CA, USA. Email: mmello@law.stanford.edu

the prospects for isolating and quarantining people at home rather than in facilities. People's temperatures can be transmitted by wearables, digital thermometers, or video, and health workers can regularly check on people's needs without exposing themselves to the risk of transmission. Communities, too, can mobilize to assist those confined at home, as is occurring in the United States through the neighborhood social networking app NextDoor.

### Enhanced contact tracing

Serious doubts have been raised about whether traditional methods of contact tracing alone can arrest the COVID-19 epidemic. Adding algorithmic contact tracing through a cellphone app or operating system is proposed to reduce transmission of the virus through instantaneous notification of contacts (see SM) (3). A real-world experiment with such an approach is under way in Singapore, where in March 2020 the government requested that citizens install a government-developed smartphone app called TraceTogether. The app uses Bluetooth technology to exchange identifier numbers with the phones of other TraceTogether users within 6 feet of the user, sharing data with the government only if the user becomes subject to contact tracing because of a COVID-19 diagnosis (see SM). As of late April 2020, similar apps have been rolled out in nearly 30 countries, and a high-profile effort by Google and Apple to develop standards is under way (4).

The Israeli government has gone farther than Singapore, making use of infected persons' cellphone location data on an involuntary basis. Its approach sends texts to persons who come into contact with known COVID-19 cases to inform them that they must immediately quarantine themselves for 14 days (5). South Korea, too, has opted to use geolocation data without seeking consent. It publicly posts information on where infected persons traveled in the days before their diagnosis based on cellphone location data, credit card records, and surveillance video (5). No names are included, but individuals' age, nationality, and sex are. Taiwan used itineraries of passengers who disembarked the Diamond Princess cruise ship to send text alerts to people residing in areas the passengers visited, asking them to self-monitor and notify officials of any symptoms. The recipient list was compiled by using mobile phone base station positioning.

### ETHICAL ISSUES RAISED

Ethical issues raised by digital epidemiology center on a core tension: these new uses of people's data can involve both personal and social harms, but so does failing to harness the enormous power of data to arrest epidemics.

### Respecting privacy

Many epidemiologic uses of new data sources do not implicate informational privacy to a greater extent than current commercial and research practices—although some people may feel greater disquiet about governments using their data than they do companies or academics. Other uses involve larger potential intrusions on privacy. Using cellphone location and text data, in particular, goes beyond what citizens of democratic nations are accustomed to. Everyday uses of public and private data are typically not conducted with personal identifiers attached. Moreover, except for use by law enforcement, data are not ordinarily used for purposes of tracking down and imposing consequences on the subjects of the data. Contact tracing of the kind being carried out in Israel, by contrast, involves immediately imposing public health orders on those traced.

### Respecting autonomy

Respect for individuals' autonomy generally requires asking them for permission to access their personal information and use it in particular ways. Informed consent is a bedrock principle of research ethics and medical care and is expressed—albeit weakly—in Terms and Conditions agreements for use of websites and apps, which ask users to agree to the company's planned uses of their data. The consent issue has particular salience for contact tracing through cellphone records because at least three alternative regimes—opt in, opt out, and mandatory—are possible, and different countries have made different choices.

### Equity concerns

Use of new data sources can improve representation of some populations in epidemiologic analysis, including people who are underrepresented in data from laboratories and health care providers because they cannot or do not access care. Nevertheless, inequities persist across the globe in people's access to the internet and cellphones. Even in areas with access, disparities exist in who uses these technologies (see SM). These disparities risk creating bias in new data sets.

### Minimizing the risk of error

The risk that governments will make errors in identifying areas and individuals at high risk of disease infection is heightened when using new data because of three factors: scope, speed, and sources. First, the use of large datasets means that a much greater number of people are under review than would ordinarily be the case; errors in even a small percentage of cases translate into large numbers of people affected. Second, the pressure to develop and roll out apps and al-

gorithms quickly during an emergency may mean compromises on testing and validation. But erroneously flagging individuals or areas can involve serious social and economic burdens, such as stay-at-home orders and business closures. Mistakes also undermine trust and waste limited public health resources (6). Third, the sources of information in some new datasets will be less reliable than traditional disease reporters. Particularly given the spread of misinformation about disease outbreaks through social media, the need to validate data derived from internet news, search data, and social media posts is acute. Self-reports of perceived symptoms, too, may be inaccurate or incomplete and are not easy to corroborate (see SM).

Correcting mistakes can pose special challenges during public health emergencies, underscoring the importance of taking steps up front to minimize the risk of error. Ordinary processes through which citizens and businesses can challenge public health orders in the courts may be modified, involving longer waits, less robust hearings, and reduced access to counsel. Proving mistakes can also be difficult when a decision has been driven by an algorithm because algorithmic logic is often not transparent.

### Accountability

A key question is how to ensure that companies and governments conducting and using epidemiologic analyses of new data sources are accountable for what they do. Democratic processes ordinarily help ensure that policymaking is reasonably transparent, the public has opportunities for input, and irresponsible officials can be removed. But many initiatives during COVID-19 have been undertaken by countries without strong democratic traditions and free-speech protections. Even in the United States, technological solutions are being pursued by small groups of officials and tech company leaders working outside ordinary channels and public view. The need to make decisions quickly may justify such processes but increases concerns about responsible practices.

The potential for misappropriation of data collected and methods developed for disease surveillance looms large. After all, the same approaches that can be used for case identification and contact tracing can be used to identify and track a government's political opponents (5). Such fears undercut trust in what public health officials are trying to do, and without public trust and participation, many key strategies for fighting infectious disease cannot succeed.

### POLICY RECOMMENDATIONS

Two principles should serve as lodestars when considering the ethics of digital surveil-

lance during pandemics. First, the wisdom of adopting a digital surveillance measure should be evaluated not in the abstract but by reference to the counterfactual. What would be used instead of the technology, and is that more or less desirable? The counterfactual for COVID-19 involves mass shelter-at-home and business closure orders, which impose serious liberty and economic deprivations and are, in most areas, completely nonconsensual. Digital surveillance offers the prospect of expediting the lifting of such orders and minimizing their use in future outbreaks (3). It may have particular value for vulnerable groups such as the elderly and persons with chronic illness who may otherwise remain confined after others are released.

The second principle is that for its use to be justified, a digital technology should be judged the least burdensome alternative that would accomplish the public health objective (7, 8). This principle has long driven thinking in public health ethics and law. For disease outbreaks, what constitutes the least restrictive alternative depends on the available public health resources, evidence concerning what behaviors people will engage in without coercive public health orders, features of the pathogen's transmissibility, and the stage of the epidemic. Even if such a weighing points toward the imposition of digital surveillance, the least restrictive alternative principle can help minimize privacy intrusions—for example, through data minimization (identifying the narrowest possible set of data elements, especially identifiable ones, and the minimum duration and scope of use required to achieve the objective) (8). We consider applications of these two principles to particular technologies with value in combating the novel coronavirus and similar pathogens.

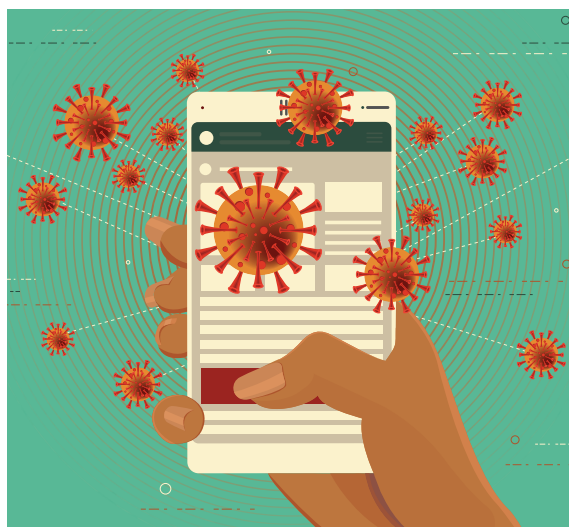
### Using algorithms in disease modeling and risk classifications

The use of artificial intelligence techniques for disease forecasting raises minimal ethical concerns if it uses individually deidentified data. But using personally identifiable information in algorithms that assign risk scores or categories to individuals, such as in the case of the Alipay app, must be considered more seriously because of the social consequences attached to these determinations. Here, the main concerns are the usual ones about algorithmic bias and error, and solutions offered for such problems in other contexts are applicable. These include making code and datasets publicly accessible and subject to peer review and continuing to refine the model as additional data become available. Additional safeguards should include creating mecha-

nisms for individuals to challenge algorithmic classifications, making classifications time limited, and using classifications to support recommendations rather than legal restrictions on individuals' movement.

### Using electronic monitoring to support confined persons

Wider use of electronic monitoring to support individuals under confinement orders (isolation, quarantine, or shelter at home) should be pursued. It is aligned with both public health goals (because supported individuals are more likely to be able to stay home) and the principles of solidarity and reciprocity, which recognize societal obligations to support those called on to sacrifice liberty to prevent harm to others. Electronic monitoring is less intrusive than in-person visits by public health workers, safer for workers, and easier to scale, enabling officials



to reach more people. For diseases that are only transmissible when the infected person is symptomatic, virtually observed symptom checks may speed individuals' release from confinement by quickly ascertaining when they no longer present a danger to others. Public health officials should move quickly to expand use of virtual check-ins with persons confined at home, prioritizing those most likely to need assistance because of infection status, membership in a vulnerable group, and lack of social supports.

### Using electronic monitoring to enforce restrictions on movement

The use of electronic monitoring to enforce confinement orders and travel restrictions is more problematic. In the United States, for example, the Supreme Court has held that a judicial warrant must be obtained, after showing probable cause to believe a person violated the law, to search private cellphone

records for law-enforcement purposes (see SM). It is unclear how courts would apply that precedent to enforcement of public health orders, but violation of some such orders is a crime.

Electronic monitoring by use of cellphone Bluetooth data, bracelets, or video cameras would likely be more effective in detecting public health order violations than current methods, which rely on police detection or police response to complaints. The question is whether more enforcement is better. The benefits of stringently enforcing mass shelter-at-home orders are not entirely clear, and the potential for strict enforcement—particularly through electronic eyes—to undermine trust in government and stoke resistance is troublesome.

The principles of the least restrictive alternative and proportionality (7) will be helpful in determining whether to use electronic enforcement for public health orders in future disease outbreaks. There is a strong argument in favor of monitoring bracelets for persons who present a high risk of harm to others if officials have a reasonable suspicion that they will not comply with home isolation. It is less restrictive than the likely alternative for such individuals: confining them in secure facilities. Even in this context, electronic monitoring should not immediately trigger law-enforcement action; rather, the first intervention should be outreach by public health officials. They should seek to understand the reasons for a person's noncompliance, which may include misunderstanding of the order or inability to satisfy basic needs such as food and health care.

The justification for electronic enforcement attenuates as the gravity of potential harm and likelihood of noncompliance shifts. For these reasons, population-wide shelter-at-home orders present a weak case for using electronic surveillance for individual enforcement purposes. However, using electronic data to understand the extent of compliance at the population level—as is now being done by using deidentified cellphone data to measure travel distances from home—is well justified. Such information involves little or no privacy intrusion and has helped public health officers understand whether they need to issue clarifications of what is permitted and prohibited, tighten social distancing orders further, or provide additional economic and social supports to enable people to stay home.

### Using cellphone data for contact tracing

For COVID-19, the arguments for using cellphone Bluetooth data for contact tracing are

compelling. Because the virus is transmissible through casual contact for at least a few days before onset of symptoms, people are unlikely to be able to recall all those they may have exposed. Even if they could, the number of public health workers needed to perform contact tracing grossly exceeds the available supply. The most likely counterfactual is failure, or inability to fight the epidemic without longer-term social distancing orders. Digital contact tracing offers an effective, less burdensome alternative that is proportional to the threat. Not everyone has smartphones, but using the technology can conserve scarce human resources for working with those who do not.

Should the technology be installed on a mandatory, opt-out, or opt-in basis? The best available evidence suggests that for pathogens with characteristics similar to COVID-19, an opt-out regime is the least restrictive alternative. Research using UK data suggests that COVID-19 could be suppressed if 80% of smartphone users (56% of the overall population, assuming 70% smartphone penetrance) use the app (9). In a survey of U.S. smartphone users, about 40% said they would definitely opt in to a contact tracing app, and just under 70% said definitely or probably (figures were slightly higher for UK users) (10); another survey found much lower opt-in rates among U.S. smartphone users (17% definitely, 32% probably) (11). These numbers fall short of the mark, especially because human inertia will mean some who are willing in theory do not actually install the app. In Singapore—a small nation with fairly high tolerance for government involvement in citizens' lives—only about 20% of smartphone users have installed the TraceTogether app (12).

Thus, although some endorse an opt-in system (3), and legislation proposed in the U.S. would codify that approach (see SM), the available evidence justifies a consent regime that impinges further on individual autonomy. Bolstering the argument in favor of opt out is that users are offered reciprocal benefits: notification if they come into contact with someone dangerous and assistance in protecting friends and family whom they may have endangered.

Although some bioethicists argue that nonconsensual collection of identifiable contact data may be justified for COVID-19 to prevent harm to others (8), opt out is ethically preferable to mandatory use and likely to be sufficient. This setup uses choice architecture to allow those with strong preferences to act on them while not conflating philosophical objections with simple inertia. Studies of electronic health record sharing have found that people tend to stick with the default choice: Only 2 to 5% opt out of health information exchange (13). Although opt outs

from smartphone data sharing may be higher owing to lower trust in government (10), opt out should be tried and evaluated before moving to mandatory use. Opt-out rates can be minimized if public health officials and technology companies collaborate to distribute plain-language FAQs that clearly explain how the data will be collected and used and what benefits there are for users.

Some propose, as an alternative, that contact tracing technology should be mandatory but have a “privacy-protecting” design in which the government receives a list of cases and a list of exposed persons but no information that permits association of particular cases and contacts (14). Such proposals are antithetical to effective epidemiology because they preclude use of the data to track the geographic spread of a pathogen. Use of identifiable data by governments should be carefully limited but must be permitted. TraceTogether operationalizes the least restrictive alternative principle by transmitting users' data to officials only if an individual becomes infected, and then only in specified ways. Executing binding data-use agreements can further ensure data minimization, and experts have articulated several provisions that ought to be included (15). Among these must be the exit strategy—plans for terminating the use of data and destroying data when the public health need for them ends (see SM).

### PROCESS RECOMMENDATIONS

When any of these technologies are implemented, it should be through a thoughtful and transparent process. We endorse prior calls for an oversight process by a body that includes members of the public and focuses on particular uses of the data, not just data transfers (3, 8), and for “trustworthy public communication...providing transparent and convincing justifications for the decisions taken” (7) (see SM). South Korea and Taiwan's examples illustrate that diligent transparency can cultivate high levels of trust in the government's strategy (2) (see SM).

But such approaches are far from guaranteed. For example, the situation in the United States leaves much to be desired. A group of technology companies convened by the White House to discuss potential uses of technology to combat COVID-19 has no evident agenda, public or stakeholder group representation, or set of guiding principles. Ethicists and legal experts do not appear to be involved. No processes (for example, adaptation of the notice-and-comment period used for administrative rule-making) have been created for the public to give input. Proposed uses of technology have percolated up through scattered media reports but not through official channels. Communiques from companies working on these technologies are short

on details about how government would be involved. No mechanisms are in place for oversight of tech companies as they pursue this work. The news media and watchdog organizations will continue to be important mechanisms for accountability, but effective oversight requires access to full information about what will be done, how, and why.

Sturdy oversight structures are not easy to stand up in the middle of an emergency. Work will be needed after the COVID-19 threat fades to ensure that we are better prepared next time. For example, federal health agencies could commission a report from the U.S. National Academies of Sciences, Engineering and Medicine recommending rules of the road for digital surveillance in pandemics, and modifications could be made to state and federal privacy and emergency powers laws to facilitate its implementation.

There has been much talk of harnessing the power and ingenuity of the tech sector to fight disease outbreaks, but “harnessing” implies carefully placed constraints and firm direction by a driver. We have yet to craft that yoke. ■

### REFERENCES AND NOTES

1. D. J. Hand, *Big Data* **6**, 176 (2018).
2. C. J. Wang, C. Y. Ng, R. H. Brook, *JAMA* **10.1001/jama.2020.3151** (2020).
3. L. Ferretti *et al.*, *Science* **368**, eabb6936 (2020).
4. Top10VPN, COVID-19 digital rights tracker, 28 April 2020; [www.top10vpn.com/research/investigations/covid-19-digital-rights-tracker](http://www.top10vpn.com/research/investigations/covid-19-digital-rights-tracker)
5. S. Hendrix, R. Eglash, *Washington Post*, 19 March 2020.
6. E. Vayena *et al.*, *PLoS Comput. Biol.* **11**, e1003904 (2015).
7. Nuffield Council on Bioethics, Ethical Considerations in Responding to the COVID-19 Pandemic (Nuffield Council on Bioethics, 2020); [www.nuffieldbioethics.org/assets/pdfs/Ethical-considerations-in-responding-to-the-COVID-19-pandemic.pdf](http://www.nuffieldbioethics.org/assets/pdfs/Ethical-considerations-in-responding-to-the-COVID-19-pandemic.pdf)
8. Nuffield Council on Bioethics, Guide to the Ethics of Surveillance and Quarantine for Novel Coronavirus (Nuffield Council on Bioethics, 2020); [www.nuffieldbioethics.org/assets/pdfs/Guide-to-the-ethics-of-surveillance-and-quarantine-for-novel-coronavirus.pdf](http://www.nuffieldbioethics.org/assets/pdfs/Guide-to-the-ethics-of-surveillance-and-quarantine-for-novel-coronavirus.pdf)
9. R. Hinch *et al.*, Effective configurations of a digital contact tracing app: a report to NHSX (16 April 2020); <https://045.medsci.org.uk/files/files/report-effective-app-configurations.pdf>
10. S. Altmann *et al.*, Acceptability of app-based contact tracing for COVID-19: Cross-country survey evidence (4 May 2020); <https://osf.io/6bn47/?pid=7vgq9>
11. *Washington Post*/University of Maryland, National poll, 21 to 26 April 2020 (5 May 2020); <https://wapo.st/3frcv3v>
12. Z. Doffman, *Forbes* (12 April 2020); <https://bit.ly35EQjyx>
13. M. M. Mello, J. Adler-Milstein, K. L. Ding, L. Savage, *Milbank Q.* **96**, 110 (2018).
14. C. Canca, *Medium*, 10 April 2020; <https://bit.ly/2YJmewn>
15. Z. Emanuel *et al.*, “A national and state plan to end the coronavirus crisis” (Center for American Progress, 2020); [www.americanprogress.org/issues/healthcare/news/2020/04/03/482613/national-state-plan-end-coronavirus-crisis](http://www.americanprogress.org/issues/healthcare/news/2020/04/03/482613/national-state-plan-end-coronavirus-crisis)

### ACKNOWLEDGMENTS

The authors are grateful to C.-M. Chen, I.-M. Parrig, J.-H. Chuang, and H.-W. Jyan for generously sharing information about measures adopted in Taiwan and to G. Lo and G. Wilson for research assistance.

### SUPPLEMENTARY MATERIALS

[science.sciencemag.org/content/368/6494/951/suppl/DC1](http://science.sciencemag.org/content/368/6494/951/suppl/DC1)

Published online 11 May 2020

10.1126/science.abb9045

sciencemag.org **SCIENCE**



Sentient species, such as elephants, deserve rights, some argue, while less complex creatures do not.

BOOKS *et al.*

## POLICY

# Revisiting rights in an ever-evolving world

Data and genetic privacy join proposed privileges for nonhumans, robots, and nature

By **Dov Greenbaum**

**T**he *Coming Good Society* offers a cursory overview of the state of human rights in an age of emerging technologies. More accessible narrative than academic treatise, this enjoyable read examines how changing norms create opportunities to expand the scope of universal protections and rights. Authors William F. Schulz, former executive director of Amnesty International USA, and Sushma Raman, executive director of the Harvard Kennedy School Carr Center for Human Rights Policy, look to their own experiences and extensive professional encounters to support their arguments in the book's eight short but substantive chapters.

Rights reflect our consensus of what is or ought to be in a good society. As such, human rights are in constant flux, evolving and sometimes devolving as social and political norms change, societies adapt, and discoveries and advancing technologies change worldviews. Rights are also transactional claims that create duties and obligations of the powerful to the less powerful. They promote civility, deter

oppression, and provide a sense of dignity to groups within these penumbras.

In the book's third chapter, Schulz and Raman consider new rights to which they believe we are all entitled, in the form of improved privacy protections. They ground these rights in ideals of autonomy and control, as corporations seek to learn more about us and to use that information to manipulate our behavior. The authors propose the widespread implementation of rights already granted—recently and prominently—to Europeans through the General Data Protection Regulation. These include the right to be forgotten (i.e., the right to have negative personal data erased from internet search results). Schulz and Raman also advocate using algorithm transparency requirements to limit the biases that are often unintentionally encoded into those algorithms, which reflect the “presumptions and predictions of their makers.”

The authors continue their discussion of emerging privacy concerns in the book's fourth chapter, which examines how privacy should be accorded to our genetic information. Here, they address the ownership of

DNA, the rights of parents and children in reproductive scenarios involving genetic engineering, and the challenges presented by animal-human chimeras. Science-literate readers might find this chapter a bit underwhelming, as it is written to be accessible to a broad audience.

The book's fifth chapter suggests that rights could be employed to protect vulnerable groups suffering under corrupt leadership, which, while generally illegal, is frequently tolerated, often at the expense of the poor and powerless. Notably, the authors argue for a right to be free from corruption rather than the right to good governance, as they see corruption as much broader than an abuse of authority. They include, for example, financial rules that intensify the unfair distribution of wealth.

A recurring theme in the book is that of competing rights. For example, some advocates have proposed that same-sex couples should be guaranteed the right to access surrogacy services, but such a right could challenge the rights and autonomy of surrogate mothers, an often-oppressed group who are potential victims of trafficking and exploitation. Schulz and Raman also describe antagonistic interactions between competing rights groups, for example, between some women's rights advocates and groups promoting the rights of nonbinary individuals. The authors suggest that “the inclusion of newly established rights need not vitiate the old.”

The book closes with a discussion of the possible extension of human rights to nonhumans, including animals, robots, and nature. These chapters provide an excellent

overview of current discussions but offer little in the way of novel and provocative rights. Here also, the authors are forced to make distinctions between those animals, robots, and natural resources that ought to be granted rights and those that should not, owing to conflicting needs and demands. Such distinctions are sometimes rational, as in the case of the rights of obligate carnivores over their prey, and at other times seemingly arbitrary, as when Schulz and Raman suggest

valuing the survival of native species over invasive ones that were introduced to a habitat through no fault of their own. One is left wondering whether these proposed divisions will one day seem as problematic and discriminatory as others the authors argue against elsewhere in the book. ■



**The Coming Good Society**  
William F. Schulz  
and Sushma Raman  
Harvard University Press,  
2020. 328 pp.

The reviewer is at Zvi Meitar Institute for Legal Implications of Emerging Technologies, Herzliya, Israel, and the Department of Molecular Biophysics and Biochemistry, Yale University, New Haven, CT, USA. Email: dov.greenbaum@idc.ac.il

10.1126/science.abc0163

## CLIMATE POLICY

# The will to act when the data are dire

Then and now, American politicians have failed to heed scientific warnings

By Erika Lorraine Milam

In the face of a dire planetary prognosis, American politicians in the 1980s faced a simple question: Act now, or wait and see? These are the same options available to anyone presented with an uncertain future, whether rising levels of atmospheric carbon dioxide, a cyst that might turn cancerous, or scattered cases of an infectious disease that could explode into a pandemic. *Losing Earth* focuses on the first of these, but as I read the book—under a stay-at-home order in New Jersey owing to the spread of coronavirus disease 2019—Nathaniel Rich's frustration resonated with my own. Why, he asks, did American politicians fail to act when scientists agreed that there was a real and present danger?

In 1951, environmentalist Rachel Carson had noted that the growing season in the subarctic regions was longer, growth rings on trees were fatter, and cod were migrating farther north. "The long trend is toward a warmer earth," she wrote (1).

In 1975, anthropologist Margaret Mead convened a symposium calling attention to the endangered atmosphere. Arguing that the issue would need to be addressed on a planetary scale, she called for more research, especially scientific models of the likely future that could guide action in the present.

Rich observes that by 1979, scientists had assembled the essential pieces of the climate warming puzzle. By the end of the next decade, evidence regarding the future of the planet was incontrovertible: Increased levels of carbon dioxide in the atmosphere were causing the planet to warm. Models warned of a litany of dangers: rising sea levels, the abandonment of coastal cities, widespread droughts, and shifting agricultural belts. These issues, Rich notes, were understood to be environmental in nature and political in impact.

The book's two main characters—Rafe Pomerance and James Hansen—move through its pages like characters from a Frederick Forsyth novel: cool, competent, unfussy, and at odds with a world that underappreciates their hard-won expertise. Pomerance was "not a scientist" but a stooping six-foot-

four environmental policy analyst with horn-rimmed glasses and a mustache. Hansen had majored in math and physics but dreamed of baseball. He helped create computer models of carbon circulation on a planetary scale and worked with Jule Charney to produce a report that predicted that the planet would warm by 3°C in the next century (2). Pomerance scrutinized the evidence, read between the lines, and started calling politicians.

They might have succeeded in convincing those in power of the need to curb the world's fossil fuel dependency were it not for President Ronald Reagan's investment in fossil fuels and unrelenting war on environmentalism throughout the 1980s, followed by President George H. W. Bush's 1989 appointment of John Sununu as White House Chief of staff. If Pomerance and Hansen are the book's heroes, Sununu is the archvillain.

Ever since Mead's 1975 conference, Rich posits, Sununu had interpreted claims of global warming as an excuse to bridle economic progress and enact authoritarian global solutions to a problem whose existence he doubted. Pomerance and Hansen could not convince Sununu otherwise, and when given the opportunity to steer the country's policy away from reckoning with climate change, Sununu took it. (He remains skeptical of global warming to this day.)

Rich's tight focus on the lives of a handful of men allows him to frame science and politics as mirror worlds—Hansen and Pomerance never quite grokking the power dynamics

## Losing Earth: A Recent History

Nathaniel Rich  
Farrar, Straus and Giroux,  
2019. 224 pp.



of politics and Sununu handily rejecting the logic of science. More broadly, Rich suggests that many Americans found it difficult to appreciate the connection between actions in the present and long-term effects, the lag between cause and effect exacerbated by our species's tolerance for self-delusion.

Rich's description of the politicians' inaction when presented with robust scientific evidence now feels prescient. Yet from the perspective of a world beset by the social, political, and health impacts of a novel coronavirus, I found myself searching the book for the key relations that characterize the causal space between personal choices and a cultural zeitgeist. It was not until the epilogue that Rich turned his attention to the powerful dynamics of funding in science, attempts of the fossil fuel industry to manipulate the optics of knowledge for a broader public, and the disproportionate effects of climate change according to demographics and geography. ■

## REFERENCES AND NOTES

1. R. Carson, *The Sea Around Us* (Oxford Univ. Press, 1951).
2. National Research Council, *Carbon Dioxide and Climate: A Scientific Assessment* (The National Academies Press, 1979); <https://doi.org/10.17226/12181>.

10.1126/science.abc6191



Fertility rates and other indicators of human progress have declined.

## PODCAST

### Slowdown: The End of the Great Acceleration—and Why It's Good for the Planet, the Economy, and Our Lives

Danny Dorling  
Yale University Press, 2020. 400 pp.

Even before the pandemic brought many institutions to an abrupt standstill, a number of indicators—from fertility rates to GDP growth—suggested that human progress has slowed in recent decades. This week on the *Science* podcast, geographer Danny Dorling reveals why this might not be such a bad thing.

[sciencemag.org/podcasts](https://sciencemag.org/podcasts)

10.1126/science.abc6198

The reviewer is at the Department of History, Princeton University, Princeton, NJ 08544, USA.  
Email: [emilam@princeton.edu](mailto:emilam@princeton.edu)



## LETTERS

Unnecessary restrictions on blood donors should be removed to maximize the blood and plasma available for use.

Edited by Jennifer Sills

## Ease restrictions on U.S. blood donations

With a vaccine for coronavirus disease 2019 (COVID-19) likely more than a year away, we must identify effective therapies for patients now. One promising approach is the use of plasma from patients who have recovered from COVID-19 (1, 2). To facilitate this strategy, the U.S. Food and Drug Administration (FDA) recently revised some of the restrictions on blood donation, including a decrease in deferral time for men who have sex with men (MSM) to 3 months (3). This is a positive change to an outdated guideline, but it does not go far enough.

In 1983, the FDA indefinitely barred all MSM from donating blood for fear of transmitting human immunodeficiency virus (HIV) and hepatitis B/C by transfusion. In 2015, the lifetime ban was changed to 12 months from last sexual contact (4). Today, the risk of contracting HIV or hepatitis B/C through transfusion is less than 1 in 2 million, and the incidence is substantially lower (5). This success is due to advances in screening, not to banning MSM from donating blood. The false-negative rates of modern HIV nucleic acid tests fall around 0.05%. The window between infection and detection has dropped to 9 days (5, 6). Despite this improvement, the FDA continues to exclude otherwise healthy MSM through arguably discriminatory policy. Although a step forward from the 12-month policy, a deferral period of 3 full months is not necessary to protect patients (7, 8).

Moreover, this revised policy may not meaningfully increase the donor pool, given that waiting until 3 months after sexual contact amounts to a lifetime blood donation ban for many men.

The demand for healthy blood and convalescent plasma will accelerate as COVID-19 infects more Americans. To address the acute shortage (9), the deferral period should be decreased to 2 weeks, after which we can reliably screen for HIV. More granular deferrals could also be introduced. Instead of a blanket discriminatory ban on MSM blood donations, we could evaluate donors based on concrete risky behaviors, such as having unprotected sex with multiple sexual partners or sharing needles. Alternatively, we could inactivate pathogenic DNA and RNA with intercalating molecules such as amotosalen, which European blood centers already do routinely (10, 11). Coupled with robust testing and screening, these approaches will exclude fewer healthy donors while still minimizing the risk of transfusion-transmitted HIV.

The FDA's policies must be grounded in science. Safely lifting the restrictions on blood donations has the potential to save millions of lives in a normal year (12). Now, plasma may play a crucial role in treating patients suffering from COVID-19. We cannot afford to turn away HIV-negative blood with lifesaving antibodies just because the donor is gay or bisexual.

Chirag Vasavda<sup>1\*</sup>, Byron K. Ho<sup>2</sup>, Solomon H. Snyder<sup>1</sup>

<sup>1</sup>The Solomon H. Snyder Department of Neuroscience, Johns Hopkins University School of Medicine, Baltimore, MD 21205, USA. <sup>2</sup>Department of Dermatology, Johns Hopkins University School of Medicine, Baltimore, MD 21205, USA.

\*Corresponding author. Email: cvasavda@jhmi.edu

## REFERENCES AND NOTES

1. A. Casadevall, L.-A. Pirofski, *J. Clin. Invest.* **130**, 1545 (2020).
2. C. Shen *et al.*, *JAMA* **323**, 1582 (2020).
3. P. Marks, "Coronavirus (COVID-19) update: FDA provides updated guidance to address the urgent need for blood during the pandemic" (FDA, 2020); [www.fda.gov/news-events/press-announcements/coronavirus-covid-19-update-fda-provides-updated-guidance-address-urgent-need-blood-during-pandemic](http://www.fda.gov/news-events/press-announcements/coronavirus-covid-19-update-fda-provides-updated-guidance-address-urgent-need-blood-during-pandemic).
4. FDA, "Revised recommendations for reducing the risk of Human Immunodeficiency Virus transmission by blood and blood products" (2020); [www.fda.gov/regulatory-information/search-fda-guidance-documents/revised-recommendations-reducing-risk-human-immunodeficiency-virus-transmission-blood-and-blood](http://www.fda.gov/regulatory-information/search-fda-guidance-documents/revised-recommendations-reducing-risk-human-immunodeficiency-virus-transmission-blood-and-blood).
5. S. Zou, S. L. Stramer, R. Y. Dodd, *Transfus. Med. Rev.* **26**, 119 (2012).
6. M. Busch, K. Watanabe, J. Smith, S. Hermansen, R. Thomson, *Transfusion* **40**, 585 (2000).
7. E. DeBuck, T. Dieltjens, V. Compennolle, P. Vandekerckhove, *PLoS One* **10**, e0122523 (2015).
8. B. R. Sturrock, S. Mucklow, *Clin. Med.* **18**, 304 (2018).
9. J. Stephenson, "Canceled blood drives, social distancing cause nationwide blood shortages," *JAMA Health Forum* (2020).
10. L. Lin *et al.*, *Transfusion* **45**, 580 (2005).
11. J. Irsch, L. Lin, *Transfus. Med. Hemother.* **38**, 19 (2011).
12. A. J. Miyashita, G. J. Gates, *Effects of Lifting Blood Donation Bans on Men Who Have Sex with Men* (Williams Institute, 2014).

10.1126/science.abc2322

## The precarious position of postdocs during COVID-19

Postdoctoral researchers play a crucial role in many research groups, serving as mentors, teachers, and leaders as they develop their skills and prepare for scientific careers (1). However, the coronavirus disease 2019 (COVID-19) crisis has put funding and support for postdoc positions at risk, threatening to upend the career paths available to these junior scientists.

Even in normal times, postdoctoral positions provide little job security (2, 3). Most postdocs are employed on yearly contracts, and the availability of research funds is highly variable (1). Postdocs receive little institutional support in comparison to undergraduates, graduate students, and faculty. The positions often do not provide access to affordable health care or child care, career counseling or resources, paid sick leave, or employee and student benefits such as alumni network membership or union representation (1, 2, 4–7). Before the pandemic, an ongoing national discussion among postdocs was taking place to address the benefits of collective bargaining and unionization, as many feel the working conditions and terms of employment are substandard or outright nonexistent (1, 3, 8). For 2 to 3 years (and sometimes much longer), postdocs tolerate these subpar conditions in hopes of using their experience to propel them into full-time jobs as professors or researchers outside academia (2).

However, the economic crisis resulting from COVID-19 stay-at-home orders has spurred a growing list of universities to implement hiring freezes and cancel new faculty hires (9, 10). This lowers the chances that postdocs can obtain coveted full-time positions. Meanwhile, experimental work has all but ground to a halt, visas are expiring with little clarity about the prospect of extensions, and continued funding has become uncertain, jeopardizing the time-sensitive research that postdocs are conducting during their short contracts.

Although many institutions have granted some form of pandemic relief to other members of the academic community, postdocs have been overlooked (11, 12). To protect the future and diversity of the scientific pipeline, universities and research institutes must take immediate action to retain these vital junior scientists. Institutions should implement programs to prolong fellowship positions (12), similar to stop-the-clock policies available to tenure-track faculty, and vigorously advocate for federal-level extensions to visa programs. They should also offer temporary assistance to help vulnerable postdocs cope with current child care and health care challenges.

M. Arslan Ahmed, Amir H. Behbahani\*, Adrian Brückner, Caroline J. Charpentier, Livia H. Morais, Stewart Mallory, Allan-Hermann Pool  
California Institute of Technology, Pasadena, CA 91125, USA.

\*Corresponding author. Email: amirhb@caltech.edu

#### REFERENCES AND NOTES

1. S. C. McConnell *et al.*, *eLife* **7**, e40189 (2018).
2. S. Kahl, D. K. Ginther, *Nat. Biotechnol.* **35**, 90 (2017).
3. H. Sauerermann, M. Roach, *Science* **352**, 663 (2016).
4. M. Alun *et al.*, *Nat. Ecol. Evol.* **10**, 1038/s41559-020-1178-6 (2020).
5. C. Woolston, *Nature* **565**, 125 (2019).
6. K. Spratt, "Affordable child care for postdocs: One institution's solution," *Science* (2000).
7. M. Kristoffersen, "Postdocs struggle with child care costs," *Yale News* (2020).
8. B. D. Weitzner, "Why I'm pushing for a postdoc union," *Science* (2017).
9. K. Kelsky, "The professor is in: Stranded on the academic job market this year?," *The Chronicle of Higher Education* (2020).
10. M. T. Nietzel, "College furloughs have begun," *Forbes* (2020).
11. N. Gott, "UC Berkeley students receive emergency aid as part of federal coronavirus relief bill," *The Daily Californian* (2020).
12. Ed Markey, United States Senator for Massachusetts, Press Release, "Senators Markey and Tillis lead 31 senators in calling for \$26 billion in next coronavirus relief package to support research workforce" (2020).

#### COMPETING INTERESTS

All authors are board members of the California Institute of Technology (Caltech) Postdoctoral Association (CPA). The views expressed herein do not in any way represent the view of other members of the CPA board, postdoctoral individuals at Caltech, or Caltech.

10.1126/science.abc5143

## Sumatran rhinoceros on the brink of extinction

The Sumatran rhinoceros (*Dicerorhinus sumatrensis*), the closest living relative to the extinct woolly rhino, has been on decline for about a million years (1), but it is now at risk of imminent extinction. According to the International Union for Conservation of Nature Red List, the Sumatran rhino is Critically Endangered (2). In just 20 years, the species population has decreased from 250 to just 80 animals. Since the recent death of the last Sumatran rhino in Malaysia (3), all remaining individuals live in one of four subpopulations in Indonesia (2, 4). The current population is not sustainable without the help of breeding programs.

The main reason for the Sumatran rhino's population collapse is poaching driven by the Asian black market of traditional medicine, where a kilo of rhino horn can sell at around US\$65,000 (5, 6). In addition, human activities such as deforestation fragment the rhino's habitats (4). If these human activities continue, the rhino population will likely go extinct by 2030 (7).

In addition to curtailing these harmful activities, capture, relocation, and breeding programs are now critical to prevent population collapse and avoid harmful mutations leading to diseases that reduce the reproductive capacity of the Sumatran rhinos (8, 9). The breeding programs managed by the World Association of Zoos and Aquariums (10) may be able to provide conservation programs with new individuals to increase genetic diversity. However, these strategies must take into account that Sumatran rhinos do not thrive or breed well in captivity or outside their ecosystem (11). Breeding

programs should urgently be established in the rhino's natural habitat and include both natural and artificial insemination as well as embryo technologies, as has been tried for the northern white rhino (12). We must devote time and resources to ensure that the remaining 80 Sumatran rhinos are not the last.

Su Shiung Lam<sup>1,2</sup>, Nyuk Ling Ma<sup>2,1</sup>, Wanxi Peng<sup>1</sup>, Christian Sonne<sup>3,1\*</sup>

<sup>1</sup>Henan Agricultural University, Zhengzhou, China.

<sup>2</sup>Universiti Malaysia Terengganu, Terengganu, Malaysia.

<sup>3</sup>Aarhus University, Roskilde, Denmark.

\*Corresponding author. Email: cs@bios.au.dk

#### REFERENCES AND NOTES

1. H. L. Mays *et al.*, *Curr. Biol.* **28**, 70 (2018).
2. N. J. van Strien *et al.*, *Dicerorhinus sumatrensis* (The IUCN Red List of Threatened Species, 2008).
3. J. Bittel, "Last Sumatran rhino in Malaysia dies," *National Geographic* (2019).
4. International Rhino Foundation, Sumatran rhino (<https://rhinos.org/species/sumatran-rhino/>).
5. H. H. T. Prins, B. Okita-Ouma, *Science* **340**, 1167 (2013).
6. L. Neme, "Despite ban, rhino horn flooding black markets across China," *National Geographic* (2017).
7. W. J. Ripple *et al.*, *Sci. Adv.* **1**, e1400103 (2015).
8. International Rhino Foundation, Sumatran rhino rescue (<https://rhinos.org/sumatranrhinorecue/>).
9. N. E. Schaffer *et al.*, *J. Threat. Taxa* **12**, 15279 (2020).
10. World Association of Zoos and Aquariums, Conservation Breeding Programmes ([www.waza.org/priorities/conservation/conservation-breeding-programmes/](http://www.waza.org/priorities/conservation/conservation-breeding-programmes/)).
11. J. Hance, "When it comes to captive breeding, not all Sumatran rhinos are equal," *Mongabay* (2019).
12. E. Callaway, *Nature* **533**, 20 (2016).

10.1126/science.abc2202

#### TECHNICAL COMMENT ABSTRACTS

Comment on "High-surface-area corundum by mechanochemically induced phase transformation of boehmite"

Jiangong Li, Sanxu Pu, Wenbin Cao, Lu Li, Ruiyun Guo

Amrute *et al.* (Reports, 25 October 2019, p. 485) claimed that no methods were able to produce high-purity  $\alpha$ -Al<sub>2</sub>O<sub>3</sub> with surface areas greater than 100 m<sup>2</sup> g<sup>-1</sup>, even though much higher surface areas up to 253 m<sup>2</sup> g<sup>-1</sup> have been reported. Moreover, the materials they obtained could be porous aggregates and may not be 13-nm nanoparticles, as claimed.

Full text: [dx.doi.org/10.1126/science.abb0142](https://doi.org/10.1126/science.abb0142)

Response to Comment on "High-surface-area corundum by mechanochemically induced phase transformation of boehmite"

Amol P. Amrute, Zbigniew Łodziana, Hannah Schreyer, Claudia Weidenthaler, Ferdi Schüth  
Li *et al.* commented that our report claims that methods reported thus far cannot enable the production of high-purity corundum with surface areas greater than 100 m<sup>2</sup> g<sup>-1</sup>, and that our obtained material could be porous aggregates rather than nanoparticles. We disagree with both of these suggestions.

Full text: [dx.doi.org/10.1126/science.abb0948](https://doi.org/10.1126/science.abb0948)



## AAAS NEWS & NOTES

Students present their talents as they pitch their innovations at the third annual HBCU Making & Innovation Showcase in Washington, D.C., in February 2020.

# Diverse students display inventions at HBCU showcase

Innovators from historically black institutions address challenges being faced by their communities

By **Andrea Korte**

A social media platform for online education, a smart cane that warns visually impaired users of objects along their path, and a mobile app that connects customers to restaurants eager to distribute surplus food were just a few of the inventions that student innovators from historically black colleges and universities displayed at a recent showcase.

The American Association for the Advancement of Science, with support from the National Science Foundation, hosted the third annual HBCU Making & Innovation Showcase in February 2020 in Washington, D.C. The event, held in conjunction with AAAS's and NSF's Emerging Researchers National Conference, brought together 80 students and faculty members from HBCUs for 2 days of interactive workshops and training on invention and entrepreneurship. The conference culminated with 18 teams of undergraduate and graduate students from 13 colleges and universities pitching their innovations.

"Entrepreneurial thinking and an invention mindset are critical to address the challenges that affect communities around the world, and in our own backyards," said Neela White, a project director in AAAS's Diversity, Equity, and Inclusion program. "As we look at the shifting demographics in the country, we must be intentional about ensuring that innovation ecosystems are fully inclusive."

The showcase was inspired by a similar effort held during the White House's 2015 National Week of Making, which celebrated the maker movement: individuals and groups harnessing technology and creativity to turn their innovative ideas into reality. Quincy Brown, a AAAS STEM program director at the time, proposed the HBCU Making & Innovation Showcase to the National Science Foundation in 2017 and hosted the first showcase in 2018.

"The showcase is designed to provide an opportunity for students to display the talent and innovation already at HBCUs, show how these students are addressing challenges specific to their communities, heighten the awareness of the individuals and resources that support an inclusive innovation ecosystem, and further develop students' skills," White said.

Each of the teams created an innovative solution to a problem in its community related to one of 17 United Nations Sustainable Development Goals, which include quality education, clean water and sanitation, affordable and clean energy, and "no poverty." The teams designed and built prototypes to address a pressing challenge in their community. Each participant then filmed a video of their prototype to demonstrate and pitch their solutions to expert judges, who selected the top three projects at the showcase.

The winning team—Nicolette Barrieffe, a student at Clark Atlanta University, and Stephen Seymour and Leoul Tilahun, both from Morehouse College—tackled the U.N. goal of climate action with a network of communication devices intended for use in disasters and other emergency situations. The Guardian Network allows individuals to report their status when internet connectivity and cellular services are not available using long-range communication networks. The network also features a dashboard to allow emergency operators and first responders to keep track of those in need and allocate assistance.

The February presentation by Barrieffe, Seymour, and Tilahun was not the first time they took part in the showcase. The trio competed in the showcase's inaugural competition in 2018 as first-year college students, placing second.

"Based on their success, they wanted to do bigger and better projects," said Ayodeji Oyesanya, who served as the team's faculty adviser in 2018 and 2020. Oyesanya runs the Morehouse College

## AAAS NEWS & NOTES

MakerSpace Exploration Center and advised five teams participating in this year's showcase.

In the break between showcases, Seymour and Barriffe co-founded MakeWay, a student organization dedicated to designing innovative projects that now counts more than 60 members. "This year, I got the gang back together," said Seymour. "But now of course, you see the world in a different way. Our perspectives are more matured and developed."

"The trio returned to the showcase determined to win," noted Oyesanya, and they achieved their goal.

As an adviser, Oyesanya seeks to encourage students to solve problems on their own. "I find it remarkable how these students can make such wonderful projects and such creative projects and innovative projects with what could be perceived as limited resources," he said. "Because we are an HBCU, we don't have the resources and the million-dollar budget of a lot of predominantly white institutions. But these students have learned not to allow that to stagnate them and to still be able to compete with any of these schools in the country."

Added White, "I was blown away by the talent of all of the students, by the level of knowledge they brought and how much more they were willing to absorb. It was just really great."

White was also impressed with how strongly students connected with the sustainability themes to inform their projects. "They are driven by social good; they are driven by wanting to do something good for their region, for the global well-being," she said.

"Our number one goal whenever we work on a project is that it's culturally relevant," said Barriffe. When Seymour's family was affected by Hurricane Dorian, which hit the Bahamas in 2019, the team realized that emergency communications would be an important place to focus their efforts, she said.

In addition to the competition, students and faculty attending the showcase took part in workshops on subjects such as technology transfer, the business of entrepreneurship, and career pathways in the innovation sector.

Another session focused on collaboration and teamwork in innovation.

"It's really hard to make new things happen when you're by yourself," said Diana Yousef, who, along with her business partner Huda Elasaad, spoke during a session titled "The Power of Teams: From Invention to Entrepreneurship."

Yousef and Elasaad are the chief executive officer and chief technology officer, respectively, of change:WATER Labs, which has developed a new type of toilet for use in places lacking sanitation infrastructure. Their "iThrone" uses a waste-evaporating material and a urine-powered bio-battery to dehydrate human waste as a way to replace flushing in places with no sewage plumbing.

The pair were also the first ever to be selected together as co-ambassadors for the AAAS-Lemelson Invention Ambassadors Program, which seeks to increase understanding of the critical role of invention in improving quality of life and to encourage a new and diverse generation of inventors.

During the showcase, Yousef and Elasaad emphasized to participants that working with a team allows everyone to contribute their strength. Yousef trained as a lab scientist and holds an MBA, while Elasaad is a water system engineer. As the pair traversed the innovation-to-market pathway, they brought varied abilities to the effort. "We cover different parts of that journey," said Yousef. "We have these different skill sets that all come together, and it makes it all possible."

Yousef later reflected on her experiences as a woman and daughter of immigrants in the innovation sphere.



Nicolette Barriffe and Stephen Seymour explain their winning innovations.

"There's definitely a lot of discounting that happens," she said. "To see what AAAS and this initiative are doing to promote serious innovators and scientists who don't look like the scientists that everybody imagines is really amazing."

Knowing the importance of seeing oneself represented in a community, White made sure the event featured speakers from a diverse range of backgrounds, including minorities, women, and HBCU graduates who are now leaders in tech and entrepreneurship. "It was very relatable for all of the students," White said.

Participants also had the opportunity to be inspired by each other.

"I learned a lot from my peers, especially those who have been seasoned with years of experience," said Barriffe. "It's definitely powerful, especially as a woman of color in STEM."

Under the leadership of AAAS STEM Program Director Iris R. Wagstaff, the current principal investigator of the NSF grant that supports the showcase, new strategic partnerships and collaborations have been formed, expanding the showcase and providing additional resources and training to students. Social media and online platforms also extend the showcase experience.

The conversation continues online with the newly launched Emerging Researchers National Conference in STEM LinkedIn community for participants of the ERN conference and HBCU Making & Innovation Showcase, White said. The online platform means that tech and innovation leaders can reach a much broader cross section of students, including those whose ideas might not yet be fully fledged to take part in a showcase, she noted. Yet, the community has already become a hub for resource-sharing, regular online workshops, and ongoing conversation for students unable to convene in person.

Innovation, after all, is an ongoing, iterative process, White said, adding that students who attended the 2020 showcase were "very eager to go back to their campuses and continue working on these innovations."

The students from the winning team also plan to continue pursuing innovation and entrepreneurship.

Seymour, for instance, is concerned that the Bahamas—his home country—and the broader Caribbean region lack STEM education resources. "There's a huge demand for it," said Seymour, adding that he hopes to get involved with "finding ways to push the envelope on how we utilize our resources" to encourage students to explore STEM disciplines from an early age. Focusing on the social capacity of innovation is another factor driving his interest.

"Sometimes the greatest ideas are just the ones that have the impact," Seymour said. "If you can't really help or change someone's way of living, how impactful is that?"

# RESEARCH

## IN SCIENCE JOURNALS

Edited by Michael Funk

### EVOLUTIONARY BIOLOGY

#### Primate kin recognition

**K**in selection, the selection of behaviors that benefit kin, is key to social and cooperative behavior. Primates can recognize kin through heritable facial traits. The question is whether this behavior is incidental from shared genes or if it is instead subject to selection. Charpentier *et al.* studied the behavior of mandrills, nonhuman primates that live in enormous groups composed of matriline, in which daughters stay with the mother

and sons disperse. Using sophisticated artificial intelligence, they graded facial resemblances and correlated them with the social interactions of maternal and paternal half-siblings. The authors found evidence of selection for kin recognition and discuss differences between maternal and paternal half-siblings and the intricacies resulting from different social settings and the selective forces involved. —ABR *Sci. Adv.* 10.1126/sciadv.aba3274 (2020).

Recognition of kin influences the social interactions of mandrills (shown), social primates that form large groups.

### SEPARATIONS

#### Zeolites that prefer alkynes

Alkenes such as ethylene and propene must be separated from alkynes before they can be converted in polymers. Drawbacks in current methods, such as hydrogenation of alkynes producing unwanted alkanes, has spurred interest in sorption separation methods. Zeolites have generally been inefficient, given the similar sizes and volatilities of the molecules. Chai *et al.* incorporated atomically dispersed divalent transition metal cations into faujasite zeolite and found that the nickel-containing analog efficiently removed alkynes from

olefins through chemoselective binding at open nickel(II) sites. At ambient conditions in the presence of water and carbon dioxide, the zeolites retained separation selectivities of 100 and 92, respectively, for acetylene over ethylene and propyne over propylene for 10 adsorption-desorption cycles. —PDS

*Science*, this issue p. 1002

### CORONAVIRUS

#### Alternative hosts and model animals

The severe acute respiratory syndrome-coronavirus 2 (SARS-CoV-2) pandemic may have originated in bats, but how

it made its way into humans is unknown. Because of its zoonotic origins, SARS-CoV-2 is unlikely to exclusively infect humans, so it would be valuable to have an animal model for drug and vaccine development. Shi *et al.* tested ferrets, as well as livestock and companion animals of humans, for their susceptibility to SARS-CoV-2 (see the Perspective by Lakdawala and Menachery). The authors found that SARS-CoV-2 infects the upper respiratory tracts of ferrets but is poorly transmissible between individuals. In cats, the virus replicated in the nose and throat and caused inflammatory pathology deeper in the respiratory tract, and airborne transmission did occur between

pairs of cats. Dogs appeared not to support viral replication well and had low susceptibility to the virus, and pigs, chickens, and ducks were not susceptible to SARS-CoV-2. —CA

*Science*, this issue p. 1016;  
see also p. 942

### BLOOD-BRAIN BARRIER

#### Transport vehicle for CNS therapeutics

Delivering therapeutics to the brain is complicated by the presence of the blood-brain barrier. Kariolis *et al.* and Ullman *et al.* developed a transport vehicle (TV) for central nervous system (CNS) delivery of therapeutics

and tested it in mice and monkeys. The TV was obtained by binding an antibody fragment of the human immunoglobulin G1 to the transferrin receptor expressed in brain endothelial cells. Fusing the TV to the anti- $\beta$ -secretase antibody resulted in high expression of the antibody in the CNS in mice and monkeys. In a mouse model of lysosomal storage disorder, peripheral delivery of iduronate 2-sulfatase fused to the TV had therapeutic effects. The TV might be effective for delivering therapeutics in neurological disorders. —MM

*Sci. Transl. Med.* **12**, eaay1359, eaay1163 (2020).

## OCEAN CIRCULATION

### Changing forces in midstream

The intensity and frequency of the strongest cyclones east of Taiwan have increased over the past several decades as the climate has warmed. Zhang *et al.* found that one result of this trend has been the strengthening of Kuroshio current transport off the coast of Japan. The Kuroshio, like its Atlantic counterpart the Gulf Stream, is a surface current that moves huge volumes of warm water from low latitudes to high ones. As strong Pacific cyclones have become stronger, they have increased the amount of energy contained in cyclonic mesoscale ocean eddies and decreased that of anticyclonic ones. This in turn has increased the transfer of energy to the Kuroshio as eddies move into the current, providing a feedback between



Tropical cyclones, such as Typhoon Maria in 2018, seen in a satellite image, appear to be strengthening the Kuroshio current in the North Pacific.

climate warming and ocean heat transport. —HJS

*Science*, this issue p. 988

## ORGANIC CHEMISTRY

### Stitching alkynes into bryostatin 3

The bryostatin family of marine natural products has been explored for a wide variety of pharmaceutical applications but remains challenging to source. The general structure comprises a macrocycle that contains three smaller, six-membered rings. Bryostatin 3 is distinguished by the added complexity of a fourth, fused lactone ring. Trost *et al.* report a convergent synthesis of this complex molecule, taking advantage of alkyne coupling reactions to stitch together three main fragments and asymmetric dihydroxylation and propargylation reactions to set stereochemistry. —JSY

*Science*, this issue p. 1007

## CANCER

### Profiling tumor bacteria

Bacteria are well-known residents in human tumors, but whether their presence is advantageous to the tumors or to the bacteria themselves has been unclear. As an initial step toward addressing this question, Nejman *et al.* produced an exhaustive catalog of the bacteria present in more than 1500 human tumors representing seven different tumor types (see the Perspective by Atreya and Turnbaugh). They found that the bacteria within tumors were localized within both cancer cells and immune cells and that the bacterial composition varied according to tumor type. Certain biologically plausible associations were identified. For example, breast cancer subtypes characterized by increased oxidative stress were enriched in bacteria that produce mycothiol, which can detoxify reactive oxygen species. —PAK

*Science*, this issue p. 973; see also p. 938

## IN OTHER JOURNALS

Edited by **Caroline Ash**  
and **Jesse Smith**



Color-enhanced transmission electron micrograph of a single-celled green alga *Chlamydomonas reinhardtii*

## BIOLOGICAL MEMBRANES

### Dissecting uneven complex distribution

Eukaryotic cells contain heterogeneous membranes that vary in curvature, lipid and protein composition, and cellular context. Filling in molecular details for such cellular structures is a great challenge for structural biologists. Wietrzynski *et al.* used in situ cryo-electron tomography to capture views of the native thylakoid membranes of the single-celled green alga *Chlamydomonas reinhardtii*. Advances in data collection and processing permitted identification of specific membrane-associated complexes such as photosystems I and II, adenosine triphosphate synthase, and thylakoid-associated ribosomes. Two-dimensional projections of the membrane surface revealed a sharp compositional transition between appressed membranes (those that directly face another membrane) and nonappressed membranes. This technique should enable study of how these membranes are organized at both the cellular and molecular levels and how they react to different light conditions. —MAF

*eLife* **9**, e53740 (2020).

## MEDICAL GENETICS

### Genetic variant takes the pressure off

The identification of rare genetic variants that protect carriers from a specific disease can provide a launch point for studies of disease biology and therapy. In a search for genes that affect

the risk of developing the common eye disease glaucoma, Tanigawa *et al.* examined data from more than 500,000 individuals represented in UK and Finnish biobanks. They found that missense and nonsense variants in *ANGPTL7*, the gene encoding angiopoietin-related protein 7, which is a member of

a protein family implicated in angiogenesis, were associated with lower intraocular pressure and reduced risk of glaucoma, including a variant that reduced risk by 34%. Consistent with a role in glaucoma, ANGPTL7 is expressed in the trabecular meshwork, a tissue that drains fluid (aqueous humor) from the eye. —PAK

*PLOS Genet.* **16**, e1008682 (2020).

## IMMUNOLOGY

### Commensals produce a gut reaction

Commensal bacteria in the small intestine are known to help shape immune responses. Less well understood is whether the microbiota residing in the stomach are similarly immunoregulatory. Satoh-Takayama *et al.* report that commensal bacteria can indeed regulate group 2 innate lymphoid cell (ILC2) homeostasis in the stomach. Furthermore, *Helicobacter pylori*, a pathogen responsible for gastritis and gastric cancer in humans, rapidly induces stomach ILC2 proliferation and activation in mice in an interleukin-7 (IL-7)– and IL-33–dependent manner. IL-5 production by ILC2 triggers B cell secretion of immunoglobulin A, which plays a role in *H. pylori* containment. ILC2 and commensal bacteria in the stomach may therefore serve as targets for various gastrointestinal disorders. —STS

*Immunity* **52**, 635 (2020).

## NEUROSCIENCE

### Dopamine circuits facilitate fear learning

To ensure survival, powerful mechanisms of pain sensation and fear learning have evolved in animals. One important fear-learning center is the amygdala of the mammalian brain. Dopamine neurons in the midbrain ventral tegmental area (VTA) project into several brain regions, including the amygdala. Using in vivo optogenetics and optrode recordings, as well as

anatomic circuit tracing and cFos imaging, Tang *et al.* studied the role of this dopamine pathway in the formation of fear memory. The authors found that a few VTA dopamine neurons projecting into the mouse amygdala were activated when a mild shock was administered to the animal's foot. Dopamine release thus facilitates the formation of a fear memory. —PRS

*J. Neurosci.* **40**, 3969 (2020).

## ORGANIC CHEMISTRY

### Epoxidizing arenes

Although the metabolism of aromatic rings often involves epoxide formation, this reaction has proven challenging to translate into applications in synthetic chemistry. Siddiqi *et*

*al.* now report a straightforward sequential protocol for arene epoxidation: A photochemical cycloaddition with a triazoline reagent first dearomatizes the arene and then a manganese catalyst introduces the oxygen in the epoxide ring. Oxidative removal of the triazoline completes the process. Minor modification of the conditions for benzenes also cleanly produced ring-expanded oxepines from naphthalene and quinoline reactants. —JSY

*J. Am. Chem. Soc.* **10.1021/jacs.0c02724** (2020).

## PHYSICS

### Tuning the Chern number

The material  $\text{MnBi}_2\text{Te}_4$  is an antiferromagnet that can, in

thin-film form, support interesting topological states. Ge *et al.* investigated the transport properties of  $\text{MnBi}_2\text{Te}_4$  films 7 to 10 layers thick in the presence of a magnetic field. The authors showed that the films were in the so-called Chern insulator state, exhibiting quantized conductance that could not be explained by the ordinary quantum Hall effect. The thinner, seven-layer samples had a Chern number of 1, whereas the 9- and 10-layer samples were in an even more exotic state with a Chern number of 2. The tuning of the Chern number with sample thickness was also supported by numerical calculations. —JS

*Natl. Sci. Rev.* **10.1093/nsr/nwaa089** (2020).

## GRASSLAND

### Move the fences

The sensitive alpine meadow and steppe systems of the Tibetan Plateau have experienced serious degradation over the past half-century. To restore these habitats, an extensive system of wire fences has been erected across the region; some have been in place for 30 years. Fences can protect plants from immediate grazing by livestock, but they limit connectivity for other organisms, interrupt trophic dynamics, and artificially divide landscapes. Sun *et al.* used a large-scale meta-analysis to determine whether these fences have been effective for restoration, how they affect wildlife, and what effect they have on human populations on the basis of interviews with local herders. Fences that had been in place for short to medium periods of time were able to increase aboveground vegetative biomass for both meadows and steppe. However, long-term fencing decreased plant growth and diversity, with negative ecosystem impacts. In addition, fences inhibited the movement of three focal mammal species—Tibetan gazelles, yaks, and donkeys—which increased their grazing impact on unfenced regions. The herders perceived fences as not only preventing their ability to use traditional grazing practices but also as being ineffective overall. Fences can be useful tools but only when they are transitional and impermanent. —SNV

*Sci. Bull.* **10.1016/j.scib.2020.04.035** (2020).



The high-altitude grasslands of Tibet have become badly degraded, but fencing out key grazers, such as these Tibetan antelopes, is not a long-term solution.

## REVIEW SUMMARY

## FOREST ECOLOGY

# Pervasive shifts in forest dynamics in a changing world

Nate G. McDowell\*, Craig D. Allen, Kristina Anderson-Teixeira, Brian H. Aukema, Ben Bond-Lamberty, Louise Chini, James S. Clark, Michael Dietze, Charlotte Grossiord, Adam Hanbury-Brown, George C. Hurtt, Robert B. Jackson, Daniel J. Johnson, Lara Kueppers, Jeremy W. Lichstein, Kiona Ogle, Benjamin Poulter, Thomas A. M. Pugh, Rupert Seidl, Monica G. Turner, Maria Uriarte, Anthony P. Walker, Chonggang Xu

**BACKGROUND:** Forest dynamics arise from the interplay of chronic drivers and transient disturbances with the demographic processes of recruitment, growth, and mortality. The resulting trajectories of vegetation development drive the biomass and species composition of terrestrial ecosystems. Forest dynamics are changing because of anthropogenic-driven exacerbation of chronic drivers, such as rising temperature and CO<sub>2</sub>, and increasing transient disturbances, including wildfire, drought, windthrow, biotic attack, and land-use change. There are widespread observations of increasing tree mortality due to changing climate and land use, as well as observations of growth stimulation of younger forests due to CO<sub>2</sub> fertilization. These antagonistic processes are co-occurring globally, leaving the fate of future forests uncertain. We examine the implications of changing forest demography and its drivers for both future forest management and forecasting impacts of global climate forcing.

**ADVANCES:** We reviewed the literature of forest demographic responses to chronic drivers and transient disturbances to generate hy-

potheses on future trajectories of these factors and their subsequent impacts on vegetation dynamics, with a focus on forested ecosystems. We complemented this review with analyses of global land-use change and disturbance datasets to independently evaluate the implications of changing drivers and disturbances on global-scale tree demographics. Ongoing changes in environmental drivers and disturbance regimes are consistently increasing mortality and forcing forests toward shorter-statured and younger stands, reducing potential carbon storage. Acclimation, adaptation, and migration may partially mitigate these effects. These increased forest impacts are due to natural disturbances (e.g., wildfire, drought, windthrow, insect or pathogen outbreaks) and land-use change, both of which are predicted to increase in magnitude in the future. Atmospherically derived estimates of the terrestrial carbon sink and remote sensing data indicate that tree growth and potentially recruitment may have increased globally in the 20th century, but the growth of this carbon sink has slowed. Variability in growth stimulation due to CO<sub>2</sub> fertilization is evident globally, with observations

and experiments suggesting that forests benefit from CO<sub>2</sub> primarily in early stages of secondary succession. Furthermore, increased tree growth typically requires sufficient water and nutrients to take advantage of rising CO<sub>2</sub>. Collectively, the evidence reveals that it is highly likely that tree mortality rates will continue to increase, whereas recruitment and growth will respond to changing drivers in a spatially and temporally variable manner. The net impact will be a reduction in forest canopy cover and biomass.

**OUTLOOK:** Pervasive shifts in forest vegetation dynamics are already occurring and are likely to accelerate under future global changes, with consequences for biodiversity and climate forcing. This conclusion is robust with respect to the abundant literature evidence and our global assessment of historical demographic changes, but it also forms the basis for hypotheses

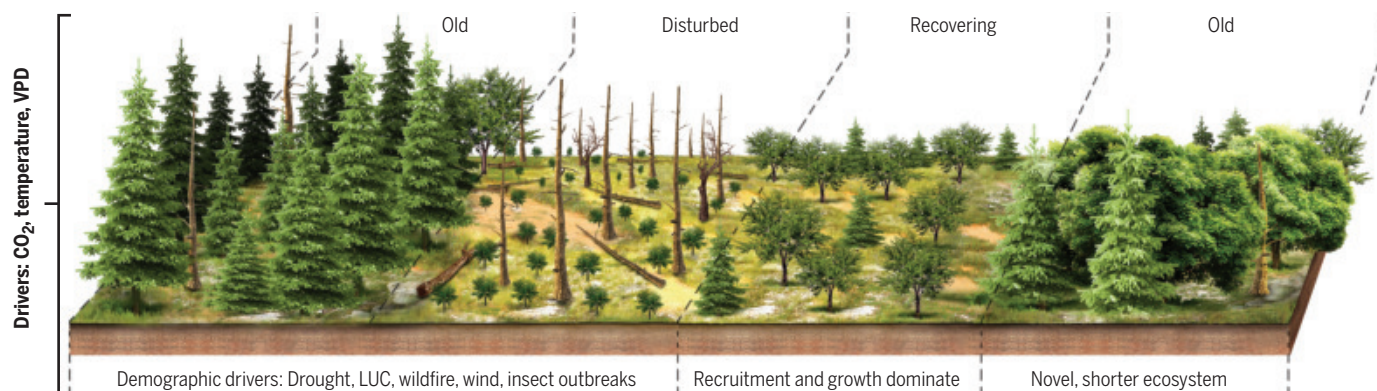
## ON OUR WEBSITE

Read the full article at <https://dx.doi.org/10.1126/science.aaz9463>

regarding the patterns and processes underlying the shifts in forest dynamics. These hypotheses will be directly testable using emerging terrestrial and satellite-based observation networks. The existing evidence and newly made observations provide a critical test of Earth system models that continue to improve in their ability to simulate forest dynamics and resulting climate forcing. Ultimately, forest managers and natural resource policies must confront the consequences of changing climate and disturbance regimes to ensure sustainable forests and accrue their associated benefits. ■

The list of author affiliations is available in the full article online.

\*Corresponding author. Email: [nate.mcdowell@pnsl.gov](mailto:nate.mcdowell@pnsl.gov)  
Cite this article as N. G. McDowell *et al.*, *Science* 368, eaaz9463 (2020). DOI: 10.1126/science.aaz9463



**A conceptual diagram of the components of forest dynamics and the disturbances that drive them.** In the far-left panel, a mature ecosystem is responsive primarily to localized mortality, and the primary drivers of demography are chronically changing variables such as CO<sub>2</sub>, temperature, and vapor pressure deficit (VPD). In the next panel, the system is disturbed by fire, insect outbreak, or another large-scale perturbation that removes most of the overstory trees,

and species adapted to rapid postdisturbance recruitment become established. In the third panel, recruitment and growth dominate demographic processes, with mortality increasing over time as competition leads to self-thinning. In the last panel, a mature ecosystem is dominated by species that have replaced the original community in response to chronic environmental changes, leading to a novel ecosystem.

## RESEARCH ARTICLE SUMMARY

## IMMUNOLOGY

# Granzyme A from cytotoxic lymphocytes cleaves GSDMB to trigger pyroptosis in target cells

Zhiwei Zhou\*, Huabin He\*, Kun Wang, Xuyan Shi, Yupeng Wang, Ya Su, Yao Wang, Da Li, Wang Liu, Yongliang Zhang, Lianjun Shen, Weidong Han, Lin Shen, Jingjin Ding, Feng Shao†

**INTRODUCTION:** In cellular immunity, cytotoxic T lymphocytes (CTLs) and natural killer (NK) cells use perforin to deliver serine protease granzymes into target cells to kill them. Gasdermins are pore-forming proteins that execute pyroptosis, a form of proinflammatory cell death. Gasdermin D (GSDMD) is cleaved by caspase-1/4/5/11 upon inflammasome activation, releasing the pore-forming domain for plasma membrane disruption. Gasdermin E (GSDME) is similarly cleaved by caspase-3, converting apoptosis to pyroptosis. The functional mechanism for other gasdermins is unknown.

**RATIONALE:** The view that granzymes induce target-cell apoptosis was proposed two decades ago, when apoptosis was thought to be the

dominant form of programmed cell death and assays to ascertain apoptosis were insufficiently accurate. Furthermore, granzyme cytotoxicity was only assessed in a few cell types. Discovery of the gasdermin family, which are true cell death executors, has altered our understanding of programmed cell death. In this work, we explored whether members of the gasdermin family might respond to granzymes and induce pyroptosis.

**RESULTS:** The expression of gasdermin B (GSDMB) but no other gasdermins in human embryonic kidney (HEK) 293T cells induced pyroptotic killing by NK cells, accompanied by an interdomain cleavage of GSDMB. These processes were blocked by inhibiting the perforin–granzyme pathway. In vitro profiling

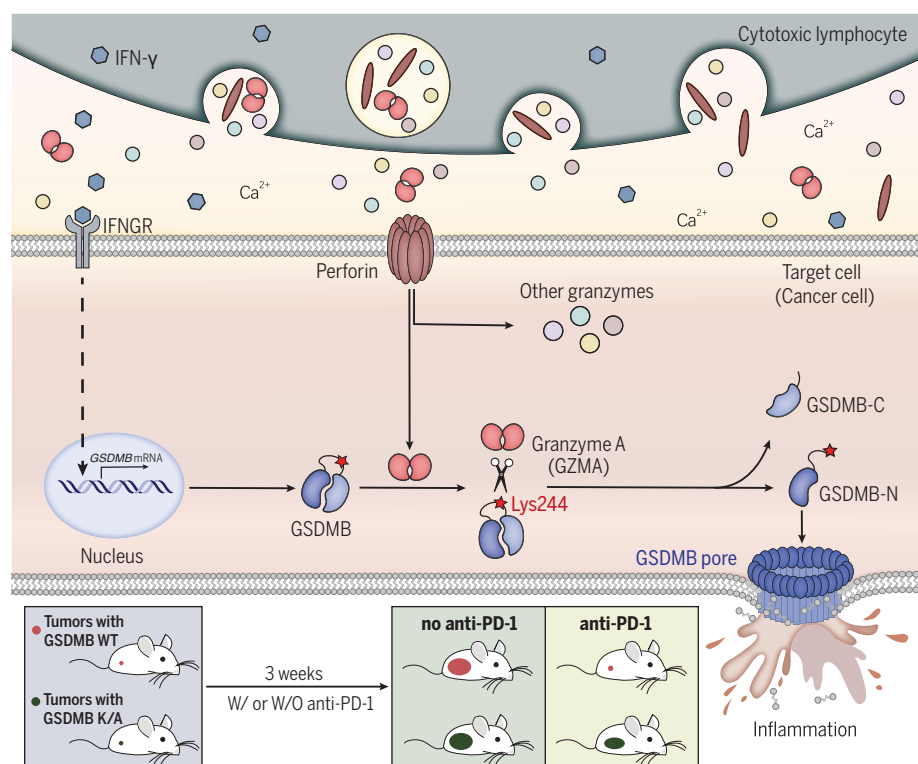
of all five human granzymes identified granzyme A (GZMA), which readily cleaved GSDMB, predominantly at Lys<sup>244</sup> within the interdomain linker. This cleavage unmasked the pore-forming activity of GSDMB. GZMA, delivered into GSDMB-reconstituted cells by electroporation or perforin,

## ON OUR WEBSITE

Read the full article at <https://dx.doi.org/10.1126/science.aaz7548>

induced extensive pyroptosis with interdomain cleavage of GSDMB. These effects were diminished by a K229A/K244A (KK/AA) mutation of GSDMB [in which lysine (K) was replaced by alanine (A) at positions 229 and 244, respectively]. In cells normally undergoing apoptosis upon GZMA delivery, the additional expression of GZMA-cleavable GSDMB converted apoptosis into pyroptosis. Pyroptotic killing by NK cells was blocked by both the KK/AA mutation and a knockdown of *GZMA* expression. Among 39 cell lines, three, including the esophageal carcinoma (OE19 cells), expressed GSDMB and underwent pyroptosis upon GZMA delivery. Knockout experiments revealed that pyroptosis in OE19 cells required the interdomain cleavage of GSDMB. Furthermore, GSDMB expression was up-regulated by interferon- $\gamma$  (IFN- $\gamma$ ). Approximately one-third of GSDMB-negative cell lines showed IFN- $\gamma$ -induced GSDMB expression. IFN- $\gamma$  promoted GZMA- or NK cell-induced pyroptosis in several target cells. Primary T cells, including anti-CD19 chimeric-antigen receptor (CAR) T cells and NY-ESO-1-specific T cell receptor (TCR)-engineered T cells (TCR T cells), also induced pyroptosis in GSDMB-reconstituted cells through cleavage of GSDMB by GZMA. Introducing GZMA-cleavable GSDMB into mouse cancer cells promoted tumor clearance in mice. *GSDMB* was highly expressed in certain tissues, particularly digestive tract epithelia, including the derived tumors. GSDMB appeared to be silenced in gastric and esophageal cancers. The Cancer Genome Atlas database recorded a strong positive correlation between *GSDMB* expression and patient survival for bladder carcinoma and skin cutaneous melanoma.

**CONCLUSION:** GZMA from cytotoxic lymphocytes cleaves and activates GSDMB to induce target cell pyroptosis. This immune effector mechanism promotes CTL-mediated tumor clearance in mice. High GSDMB expression in the digestive system suggests the importance of GSDMB-mediated immunity in these tissues and will guide immunotherapy for related cancers. Our findings suggest that substrates such as gasdermins, rather than their upstream proteases, determine the nature of cell death. ■



**GZMA from cytotoxic lymphocytes cleaves GSDMB in target cells, predominantly at Lys<sup>244</sup> within the interdomain linker.** The cleavage allows GSDMB pore-forming domain (GSDMB-N) to perforate plasma membrane and induce pyroptosis. Expression of GSDMB wild type (WT) but not its GZMA-resistant K/A mutant in mouse cancer cells promotes cytotoxic T lymphocyte-mediated tumor clearance when the inhibitory checkpoint is blocked by antibody to programmed cell death 1 (PD-1). IFNGR, IFN- $\gamma$  receptor.

The list of author affiliations is available in the full article online.

\*These authors contributed equally to this work.

†Corresponding author. Email: [shaofeng@nibs.ac.cn](mailto:shaofeng@nibs.ac.cn)

Cite this article as Z. Zhou et al., *Science* 368, eaaz7548 (2020). DOI: 10.1126/science.aaz7548

## RESEARCH ARTICLE SUMMARY

## MAGNETISM

## Self-induced spin glass state in elemental and crystalline neodymium

Umut Kamber, Anders Bergman, Andreas Eich, Diana Iuşan, Manuel Steinbrecher, Nadine Hauptmann, Lars Nordström, Mikhail I. Katsnelson, Daniel Wegner\*, Olle Eriksson, Alexander A. Khajetoorians\*

**INTRODUCTION:** Spin glasses are one of the more intriguing, but least understood, magnetic states of matter. In stark contrast to ordered magnets, spin glasses form a state characterized by seemingly random and uncorrelated magnetic patterns lacking long-range order. The distinguishing feature of spin glasses is aging: The magnetic state depends on its history, which is driven by multiple time scales. Despite decades of theoretical developments, there is still no clear understanding about when spin glass behavior arises. It is commonly believed that disorder is a key ingredient, in addition to competing magnetic interactions, as exhibited by the textbook example of dilute magnetic alloys.

**RATIONALE:** Despite more than 50 years of investigation, there is still no consensus on the magnetic ground state of the element neodymium (Nd). Below the Néel temperature, previous experiments reported the onset of static spin spirals with different periodicities, or so-called “multi- $Q$  states,” as well as evidence of additional phase transitions. Although these observations illustrate the complexity in this material, it is not well understood how the multiplicity of these  $Q$  states depends on tem-

perature and the exchange landscape of the material and which real-space magnetic interactions cause the multi- $Q$  states.

**RESULTS:** We show that single-crystalline elemental Nd exhibits unconventional spin glass behavior well described by the recently proposed concept of self-induced spin glassiness. Traditional spin glasses, such as the hallmark metallic alloy Cu-Mn, are based on competing interactions and disorder. By contrast, self-induced spin glasses can be created solely by competing interactions without strong disorder, for example, in systems with long-range magnetic interactions. We studied Nd by growing ultraclean, epitaxial thick islands and films, both of which were representative of bulk Nd. Using spin-polarized scanning tunneling microscopy, magnetic images of the surface revealed strong, local, noncollinear magnetic order at the atomic scale with a multiplicity of  $Q$  states and no long-range order (left). We quantified the role of defects on the glassiness, showing that cleaner samples led to more pronounced glassy behavior exemplified by the increased mixing of distinct  $Q$  states. The spatially dependent  $Q$  states were defined by

a spectral distribution of degenerate magnetic wave vectors (right), which varied spatially and with time. Harnessing ab initio and atomic spin dynamics calculations, we quantified the magnetic interactions, which illustrated strongly competing, distance-dependent interactions intricately linked to the crystal structure of

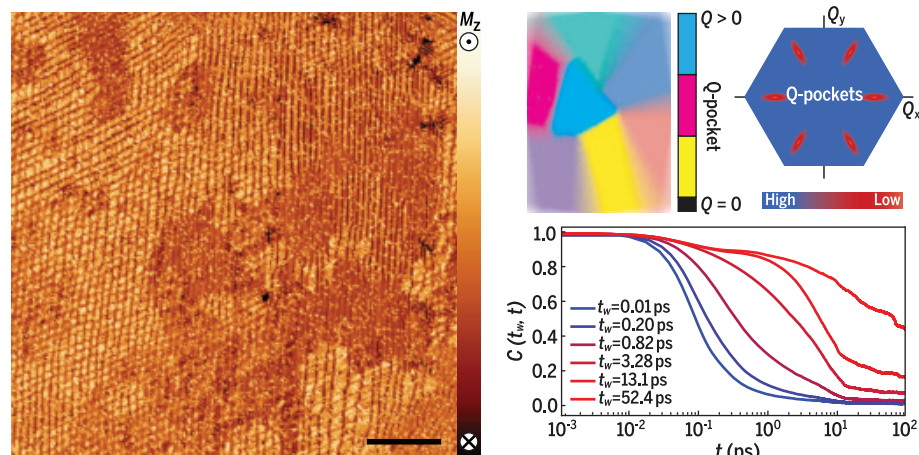
Nd. Moreover, the resultant energy landscape illustrates many favorable  $Q$  states, showing that glassiness in Nd results from the conditions required for self-induced spin glasses.

## ON OUR WEBSITE

Read the full article at <https://dx.doi.org/10.1126/science.aay6757>

When probing the response to applied magnetic fields and temperature, we observed the existence of multiple time scales reminiscent of aging in traditional spin glass materials. The calculated autocorrelation function, a mean-field picture of the aging dynamics, also showed aging behavior reminiscent of traditional spin glasses (bottom). Experiments also showed that the aging dynamics were strongly dependent on the underlying value of  $Q$ , leading to behavior reminiscent of the concept of dynamic heterogeneity observed in structural glasses. In this way, the energy landscape can be described by a rugged, multiwell potential composed of degenerate  $Q$  states. Unlike traditional spin glasses, competing interactions in Nd are driven by its electronic and the structural properties, which lead to self-induced glassiness.

**CONCLUSION:** Our findings not only suggest that glassy behavior can be found in elements with crystalline order, but also unravel the decades-long debate about the magnetic behavior of Nd. The coexistence of short-range order exhibited by degenerate  $Q$  states and aging dynamics manifested by multiple time scales provides the first experimental confirmation of self-induced glassiness. The existence of strong local  $Q$  order and the  $Q$ -dependent dynamics may imply that multiple but select time scales exist, resulting from a rugged, multiwell landscape, when compared with traditional spin glasses. This provides a new platform with which to explore dynamic heterogeneity in a spin glass material. It remains to be understood what is particularly special about the crystal structure and electronic properties in Nd, and this will necessitate a deeper theoretical understanding of the role of electron correlation effects, as well as the interplay between spin and orbital degrees of freedom. The example here expands our views on magnetic states of matter, inviting further research into aging behavior in magnetic systems. ■



**Spin- $Q$  glass.** (Left) Real-space magnetization image with spin-polarized scanning tunneling microscopy at  $T = 1.3$  K of thick films of Nd(0001). The surface shows multi- $Q$  states but no long-range order. (Right) Sketch of spin- $Q$  glass in both real and reciprocal spaces, with color illustrating the distribution of  $Q$  states in real space derived from flat pockets in  $Q$ -space. (Bottom) Calculated autocorrelation function for Nd with increasing waiting time ( $t_w$ ) illustrating aging behavior.

The list of author affiliations is available in the full article online.

\*Corresponding author. Email: [d.wegner@science.ru.nl](mailto:d.wegner@science.ru.nl) (D.W.); [a.khajetoorians@science.ru.nl](mailto:a.khajetoorians@science.ru.nl) (A.A.K.)

Cite this article as U. Kamber *et al.*, *Science* 368, eaay6757 (2020). DOI: 10.1126/science.aay6757

## RESEARCH ARTICLES

## INVASIVE SPECIES

# Biotic interactions drive ecosystem responses to exotic plant invaders

L. P. Waller<sup>1\*</sup>, W. J. Allen<sup>2</sup>, B. I. P. Barratt<sup>3,4</sup>, L. M. Condon<sup>1</sup>, F. M. França<sup>5,6</sup>, J. E. Hunt<sup>7</sup>, N. Koele<sup>7</sup>, K. H. Orwin<sup>7</sup>, G. S. Steel<sup>2</sup>, J. M. Tylanakis<sup>2</sup>, S. A. Wakelin<sup>8</sup>, I. A. Dickie<sup>2\*</sup>

Ecosystem process rates typically increase after plant invasion, but the extent to which this is driven by (i) changes in productivity, (ii) exotic species' traits, or (iii) novel (non-coevolved) biotic interactions has never been quantified. We created communities varying in exotic plant dominance, plant traits, soil biota, and invertebrate herbivores and measured indicators of carbon cycling. Interactions with soil biota and herbivores were the strongest drivers of exotic plant effects, particularly on measures of soil carbon turnover. Moreover, plant traits related to growth and nutrient acquisition explained differences in the ways that exotic plants interacted with novel biota compared with natives. We conclude that novel biological interactions with exotic species are a more important driver of ecosystem transformation than was previously recognized.

Introductions of exotic plants are transforming Earth's ecosystems and altering the way in which they cycle carbon (C) (1–7). Successful exotic species can modify C-cycling through several potential inter-related mechanisms, most notably by increases to community productivity driving higher amounts of biomass returned to soil (2) and different traits of exotics compared with native species driving a higher proportion of high-quality biomass to soil (1, 5, 8). Much less attention has focused on how altered biotic interactions in an exotic species' new range may affect C-cycling. It is well known that organisms above and belowground such as plants, soil biota, and invertebrate herbivores mediate ecosystem processes related to C-cycling and that exotic plants often differ in their interactions with new biota where there is no shared co-evolutionary history (i.e., novel) (5–7, 9). Thus, a third potential mechanism is that differences in the ways that exotics interact with novel organisms in recipient communities explain changes to C-cycling. However, the relative importance of, and interactions among, these three mechanisms are unknown; most studies have focused on systems invaded by species with high productivity, making it impossible to separate the impacts of community biomass increases from other mechanisms.

Both predictive understanding and applied management of C stocks require these three nonmutually exclusive hypothesized mechanisms to be disentangled. Here, we resolve this gap in knowledge with a multifactor, multi-response experiment aimed at partitioning the drivers of exotic impacts on ecosystem functions related to C-cycling.

We established 160 experimental ecosystems (mesocosms); manipulated interactions among plants, soil biota, and invertebrate herbivores

in a fully factorial design; and measured how the traits and biomass of exotic species and biotic interactions affected ecosystem properties and processes (10) (Fig. 1A). Each mesocosm was grown in a 125-L pot (575-mm diameter; Fig. 1B) and comprised one of 20 individual, eight-species plant communities (table S1) varying orthogonally in the proportion of exotic and woody shrub and/or tree species (0 to 100% and 0 to 63%, respectively). These plants were taken from a pool of 20 exotic and 19 native and/or endemic New Zealand plant species (table S2). Soil biota were manipulated using a modified plant–soil feedback approach (11). Each plant species was grown in monoculture in 10-L pots containing field-collected soil for 9 to 10 months (for soil collection details, see table S3), allowing the conditioning of typical associated soil biota for each of the plant species (Fig. 1C). We created “home” soils by taking the conditioned soil from each of the eight representative species in a mesocosm and mixing it together to create a single inoculum. Each home soil mixture was also used as an “away” soil in a different mesocosm that did not contain any of the representative plants in that inoculum (table S4). These soils were intended to increase the relative biomass in inocula of specialized and preferred interaction partners of the resident (or nonresident) plant species, including but not limited to bacteria, fungi, oomycetes, and nematodes. Invertebrate insect herbivore populations were added into half of the mesocosms with home soils and

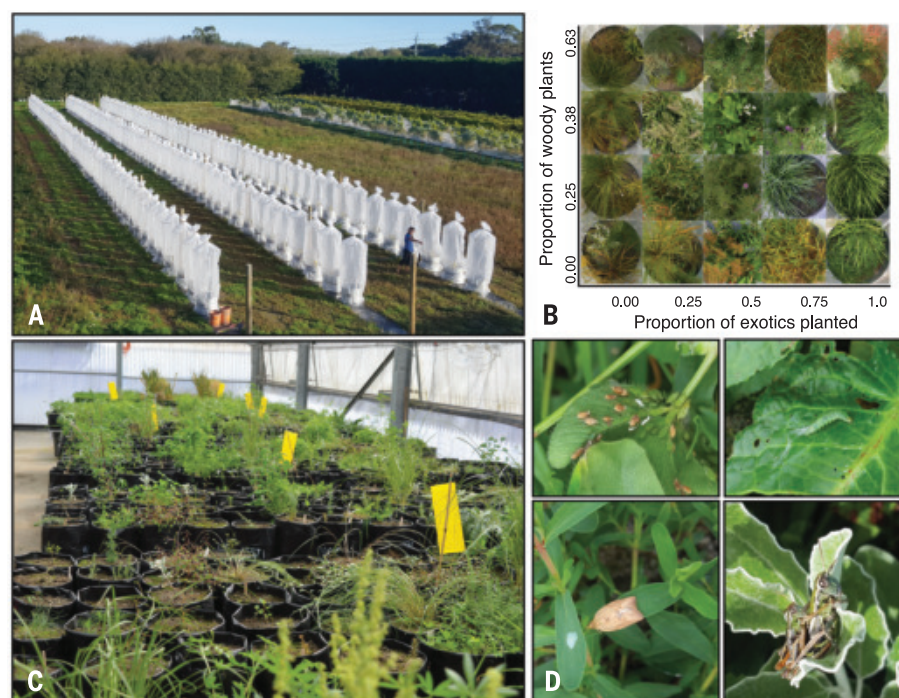


**Fig. 1. Details of the experiment.** (A) Aerial view and (B) orthogonal design of the 20 communities. (C) Plants grown in the initial soil-conditioning stage. (D) Four of the 20 herbivores established in the mesocosms.

<sup>1</sup>Bio-Protection Research Centre, Lincoln University, Lincoln 7647, New Zealand. <sup>2</sup>Bio-Protection Research Centre, School of Biological Sciences, University of Canterbury, Christchurch 8041, New Zealand. <sup>3</sup>AgResearch, Invermay Research Centre, Mosgiel 9092, New Zealand. <sup>4</sup>Department of Botany, University of Otago, Dunedin 9016, New Zealand. <sup>5</sup>Lancaster Environment Centre, Lancaster University, Lancaster LA1 4YQ, UK. <sup>6</sup>Embrapa Amazônia Oriental, Belém 66095-100, Brazil. <sup>7</sup>Manaaki Whenua Landcare Research, Lincoln 7640, New Zealand. <sup>8</sup>Scion, Christchurch 8011, New Zealand.

\*Corresponding author. Email: laurenwallergmail.com (L.P.W.); Ian.Dickie@canterbury.ac.nz (I.A.D.)

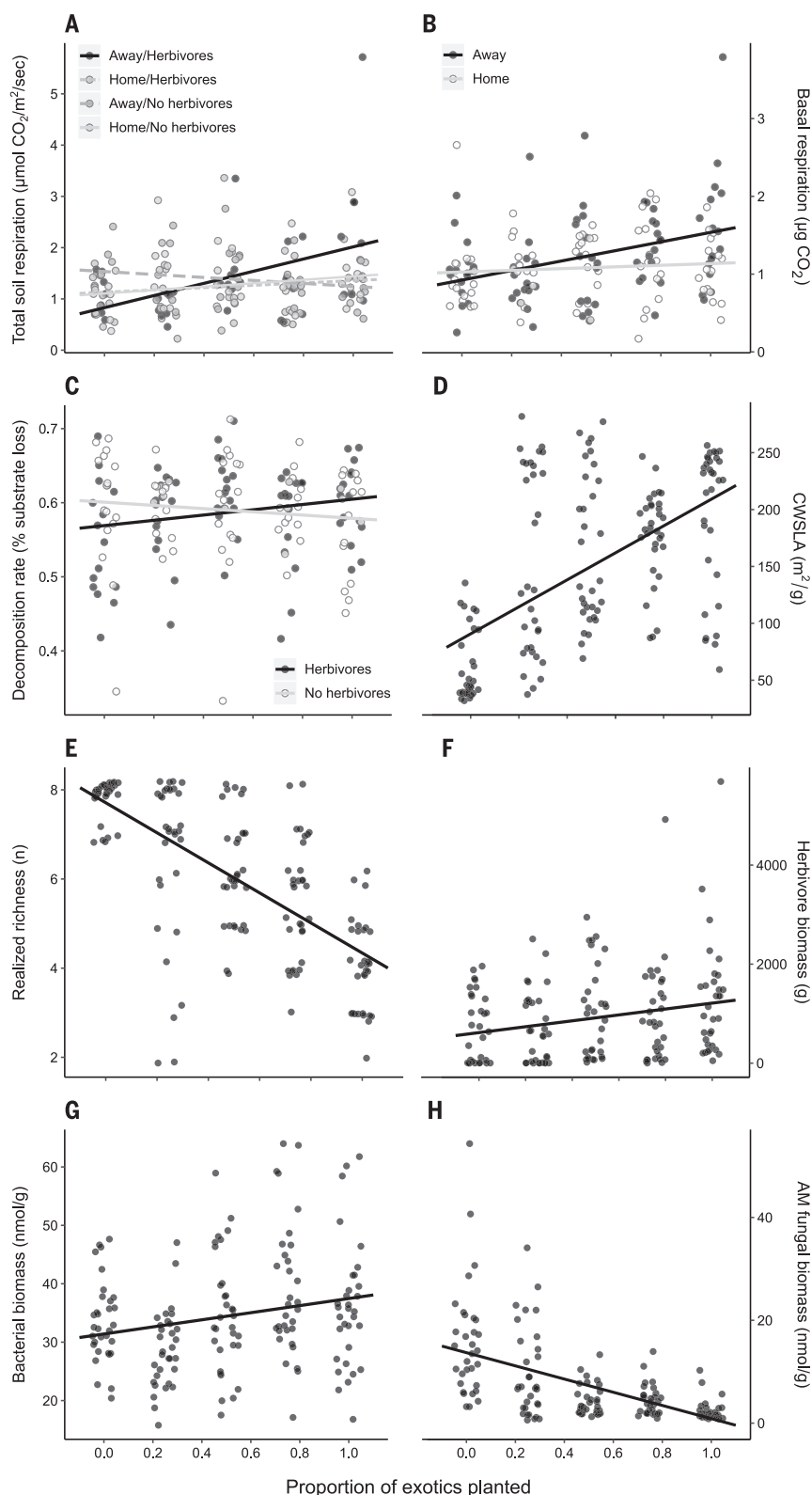


**Fig. 2. Relationship between exotic plants and ecosystem properties.** (A) Total soil respiration. (B) Basal respiration. (C) Decomposition rate. (D) Community-weighted SLA. (E) Realized plant richness. (F) Herbivore biomass. (G) Bacterial biomass and (H) AMF biomass as a function of proportion of exotics planted and our imposed biotic treatments. Only significant predictors are shown; nonsignificant predictors were removed from the full model based on Akaike information criterion (AIC) selection. Regression lines represent the output of the best-fitting mixed model.

half with away soils. Thirteen invertebrate herbivore species (hereafter simply referred to as “herbivores”) introduced into the mesocosms successfully established, along with seven self-colonizing species, totaling 20 species in all (table S5). All mesocosms were sealed with mesh cages (15% shade factor) designed to retain added herbivores and exclude others from entering (Fig. 1, A and D).

In each mesocosm, we measured distinct ecosystem properties and processes that are relevant to C-cycling dynamics (12): above- and belowground biomass; total in situ soil respiration ( $R_T$ ); basal respiration ( $R_B$ , a measure of soil microbial activity); microbial biomass ( $R_{St}$ , measured as substrate-induced respiration); decomposition (rate of standardized substrate mass loss); soil organic matter; nitrogen (N) availability; herbivore biomass; arbuscular mycorrhizal fungi (AMF) biomass and other fungal biomass [using neutral lipid fatty acid (NLFA) and phospholipid fatty acid (PLFA) biomarkers, respectively]; and bacterial biomass (using PLFA). We measured plant traits representative of fundamental plant life history strategies (13): specific leaf area (SLA), specific root length (SRL), fine-root production, the rate of above- and belowground growth [net primary productivity (NPP)], and the rate of increase in plant height between two sampling periods. We also collected leaf N content ( $N_{mass}$ ) data from an external database where available (table S2). SLA is an easily measured trait that correlates positively with relative growth rate (13) and nutrient use efficiency (14) and can directly influence soil C-cycling (15). Root traits such as SRL can directly affect interactions belowground with soil biota that drive changes to ecosystem processes (16). SLA and SRL were measured for each species separately and then scaled to the community level by calculating community-weighted mean trait values using plant biomass from each mesocosm (10). We incorporated more N-fixing exotic species into our communities compared with native species because N-fixers are more common among the New Zealand exotic flora compared with the native flora, and we would expect N-fixing and non-N-fixing exotics to differ in their effects on ecosystem properties (2). Likewise, we might expect differences between herbaceous versus woody species in their impact on functioning (2), so we included a woody gradient orthogonal to proportion exotic.

We used linear mixed-effects models to test our hypothesis that measured ecosystem properties were affected by our treatments, with the proportion of exotic plants in a community, soil and herbivore treatments, interactions among these factors, and plant effect traits (i.e., SLA, weighted by community biomass) as covariates. We used piecewise structural equation modeling (SEM) to explore how exotic species and their traits directly and indirectly

(through modifying herbivore biomass, soil microbes, and soil nutrients) influenced C-cycling. To draw the causal links between exotic plant dominance (defined here as a higher richness of exotic compared with native plants), plant traits, herbivores, and soil microbiota to our ecosystem functions in the SEM, we modeled our dependent variables as a function of the experimental responses measured in the mesocosms. We measured SLA and SRL from plants outside of the mesocosms to capture effect traits (17) that were broadly representative of the life history strategies of our plant species but not the plastic responses to our treatments. Thus, even though we weighted trait values by biomass of each plant in the mesocosms, the community-weighted SLA and

SRL values used in the hypothesized models and the SEM may over- or underestimate the response of these traits. Finally, to partition the effects of N-fixing exotic species versus non-N-fixing exotics from different plant functional groups, we included the realized proportion of woody and herbaceous N-fixing and non-N-fixing exotic plants into the SEM.

### Altered biotic interactions are the strongest drivers of ecosystem functions

Biotic interactions (herbivory and home and/or away soil treatments) modified the impact of exotic species on measures of soil C-cycling (i.e., respiration and decomposition). The presence of herbivores and away soil doubled in situ soil respiration rates in exotic-dominated

communities compared with corresponding native communities ( $R_T$ ~proportion exotic\*soil origin\*herbivore,  $\chi^2 = 10.41$ ,  $p < 0.001$ ; Fig. 2A). Reduced abundance of species-specific soil biota (away soil) in exotic-dominated communities increased soil microbial respiration by 1.5 times compared with the same communities grown in soils cultured to contain more specialist biota ( $R_B$ ~proportion exotic\*soil origin,  $\chi^2 = 4.77$ ,  $p < 0.03$ ; Fig. 2B). Soil C:N ratios were also lower in away soils under exotic plants (C:N~proportion exotic\*soil,  $\chi^2 = 3.87$ ,  $p < 0.05$ ). Higher proportions of N-fixing plant biomass also explained increases in basal respiration in exotic-dominated communities (Figs. 3 and 4). Herbivore feeding on exotic plants correlated positively with decomposition rates (decomposition~proportion exotic\*herbivore,  $\chi^2 = 4.29$ ,  $p < 0.04$ ; Fig. 2C). These results underpin the need to explicitly include biological interactions in C-cycling models to improve predictions of ecosystem and global C budgets.

### Ecosystem effects by exotic plants are mediated by leaf traits, not increases to community biomass

Exotic species had 1.8 times higher mean SLA (SLA~plant provenance,  $\chi^2 = 44.64$ ,  $p < 0.001$ ; fig. S3), grew taller 2.5 times faster (height~plant provenance,  $\chi^2 = 49.42$ ,  $p < 0.0001$ ), had 2 times higher leaf N ( $N_{mass}$ ~plant provenance,  $\chi^2 = 5.05$ ,  $p < 0.02$ ), and assimilated twice as much C into tissues compared with native plants ( $NPP_{shoots}$ ~plant provenance,  $\chi^2 = 5.24$ ,  $p < 0.02$ ;  $NPP_{roots}$ ~plant provenance,  $\chi^2 = 3.61$ ,  $p = 0.057$ ), congruent with traits of exotic plants worldwide (8). Root traits (SRL, average diameter of fine roots and the proportion of fine roots), however, did not differ between native and exotic species (SRL~plant provenance,  $\chi^2 = 0.25$ ,  $p = 0.62$ ; average diameter,  $\chi^2 = 0.32$ ,  $p = 0.57$ ; fine roots,  $\chi^2 = 0.05$ ,  $p = 0.82$ ). Exotic plants also increased mean leaf trait values at the community level, because the community-weighted mean SLA (CWSLA) increased with the proportion of exotics in the community (CWSLA~proportion exotic,  $\chi^2 = 12.64$ ,  $p < 0.001$ ; Fig. 2D). High SLA is indicative of a suite of traits allowing for faster growth (13), potentially explaining the larger biomass and faster growth of exotic compared with native plants.

Exotic invaders can increase community biomass as a function of higher resource acquisition (18) and resource use efficiency (19), stronger competitive ability [(20); but not always, see (21) for exceptions], and ability to reach high abundance (22). In our experiment, exotic plants were indeed larger and more competitive than native plants, as evidenced by double the per capita plant biomass (per capita plant biomass~plant provenance,  $\chi^2 = 7.66$ ,  $p < 0.006$ ; fig. S1) and a drop in total plant richness as the proportion of planted

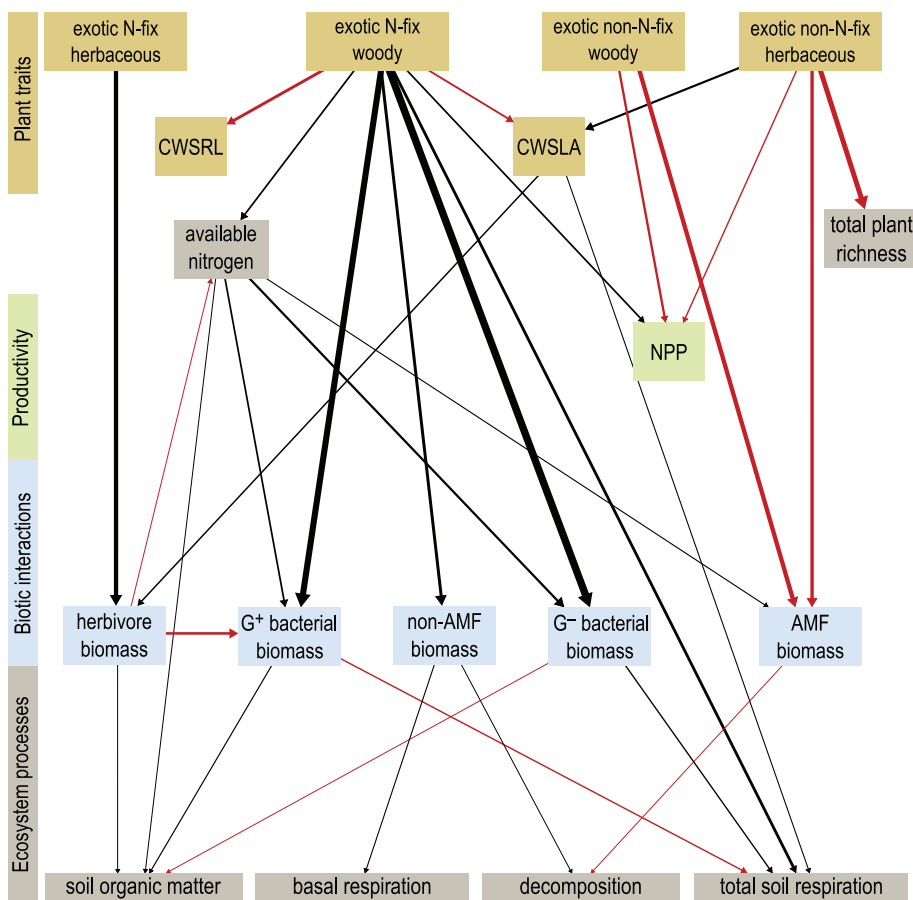


**Fig. 3. Piecewise structural equation model showing the inferred direct and indirect effects of exotic plant richness, traits and biotic interactions on indicators of ecosystem function.** Plant traits (yellow boxes) are the realized proportional richness of exotic N-fixing and non-N-fixing woody and herbaceous plants, CWSLA, and community-weighted SRL (CWSRL). Productivity (green boxes) is measured as NPP, the rate of plant biomass produced over the course of the experiment; Biotic interactions (blue boxes) include AMF biomass, non-AMF biomass, herbivore biomass, and Gram-positive ( $G^+$ ) and Gram-negative ( $G^-$ ) bacterial biomass. Ecosystem processes (gray boxes) are the total plant richness, available N, decomposition, soil organic matter, basal respiration, and total in situ respiration. A priori hypothesized models can be found in table S6. Black arrows indicate significant factors associated with positive effects on response variables and red arrows indicate negative effects. Only significant predictors are shown; nonsignificant predictors were removed from the full model on the basis of AIC selection. Arrow width corresponds to absolute values of relative effect sizes, which can be found, along with standardized coefficients and  $p$  values for each path, in table S7.

exotic species increased (plant richness~proportion exotic,  $\chi^2 = 47.36$ ,  $p < 0.001$ ; Fig. 2E), likely through competitive exclusion. Although species richness declined along the exotic gradient, exotic plants compensated for this loss with increased per capita biomass, resulting in no net change in total community biomass production along the exotic gradient (mesocosm biomass~proportion exotic,  $\chi^2 = 0.01$ ,  $p = 0.92$ ; fig. S2). This result, combined with the lack of direct links from NPP to ecosystem functions in the SEM (Fig. 3), suggests that the effects of exotic plant biomass on ecosystem functions were likely caused by differences in traits, leading to changes in the mean quality of plant inputs. In other words, the total quantity of biomass was the same whether communities were 100% native or 100% exotic. What differed was the relative proportion of high-quality material, which was higher in exotic-dominated communities.

Exotic plants and plants with higher SLA also supported a greater herbivore biomass (herbivore biomass~plant provenance,  $\chi^2 = 26.07$ ,  $p < 0.001$ ; Fig. 3 and fig. 5), a result similar to that of a previous study conducted with naturally occurring herbivores (23). Faster-growing plants with high SLA typically have tissues with proportionately lower structural

carbohydrates and, as such, are more readily mineralizable by herbivores and soil biota (13, 24). Indeed, exotic-dominated communities accumulated more herbivores (herbivore biomass~proportion exotic,  $\chi^2 = 16.49$ ,  $p < 0.001$ ; Fig. 2F), and this was partly driven by the higher mean SLA of these communities (Fig. 3).

#### Herbivore accumulation on exotic plants explains heightened decomposition rates

Previous reports have shown increases in decomposition rates as high as 117% after exotic invasion, whereas others have shown decreases [for review, see (2)]. Here, decomposition rates increased only in exotic communities in which herbivores were also present (Fig. 2C). This relationship was likely driven by the higher nutritional quality of exotic compared with native plants, with consumed biomass returned to soil by herbivores more rapidly and in a more readily mineralizable form (24). Exotic plants were more palatable, as indicated by their higher SLA, leaf N, and growth rates (24). Further, N-fixing woody and non-N-fixing herbaceous exotics had higher rates of growth despite high herbivore feeding (Fig. 3), indicating that exotics may compensate for damaged tissues more readily. Although it

is not unusual for plant-herbivore interactions to increase decomposition when herbivores feed on more palatable plants (24, 25), the accumulation of herbivores on exotic plants (particularly on non-N-fixing herbaceous exotics; Fig. 3), coupled with the high regrowth capacity of those plants, likely explains increased decomposition rates in mesocosms with a high proportion of exotic plants and herbivores added. Accumulation of successful biocontrol arthropods aimed at reducing exotic plant biomass may have similar effects in communities where they have been introduced. Our findings clarify previous idiosyncrasies from studies focused on exotic plant effects on decomposition (2), showing that exotic plants increase decomposition rates, but only when herbivores are present and able to accumulate.

#### Changes to C-cycling by exotic plants develops through multiple pathways

Basal and in situ respiration rates were elevated when exotic plants interacted with novel soil biota and insect herbivores. This result emerges from multiple potential pathways, the first by alteration of two bacterial taxonomic groups indicative of different C-cycling strategies. Exotic-dominated communities were associated with elevated bacterial biomass (bacterial biomass~proportion exotic,  $\chi^2 = 7.54$ ,  $p < 0.006$ ; Fig. 2G), particularly where N-fixing woody species were present (Fig. 3) and in communities with high mean SLA (bacterial biomass~CWSLA,  $\chi^2 = 4.62$ ,  $p < 0.03$ ). Herbivores depressed bacterial biomass overall (bacterial biomass~herbivore,  $\chi^2 = 13.06$ ,  $p < 0.001$ ; fig. S6), but also reduced the relative proportion of Gram-positive bacteria (fig. S7A), many of which are oligotrophic taxa using slow enzymatic pathways to break down recalcitrant C sources, compared with Gram-negative bacteria (often copiotrophic), which are associated with more rapid utilization of plant-based labile C sources (26–28) (Fig. 3). Aboveground herbivory can also change exudation profiles and increase plant C allocation belowground into roots (29). Thus, by increasing the amount of labile C available to soil microbes through exudates (28), herbivores may have shifted the functional attributes of the bacterial community toward those associated with the more rapid breakdown of short-term pools.

#### Decomposition is faster where non-N-fixing exotic plants reduce AMF

A second pathway by which exotic plants can increase soil C loss is through their reduced interactions with AMF. AMF biomass in soil decreased with exotic dominance (AMF~proportion exotic:  $\chi^2 = 46.27$ ,  $p < 0.001$ ; Fig. 2H) and a greater proportion of non-N-fixing plants (Fig. 3). Communities with lower AMF biomass

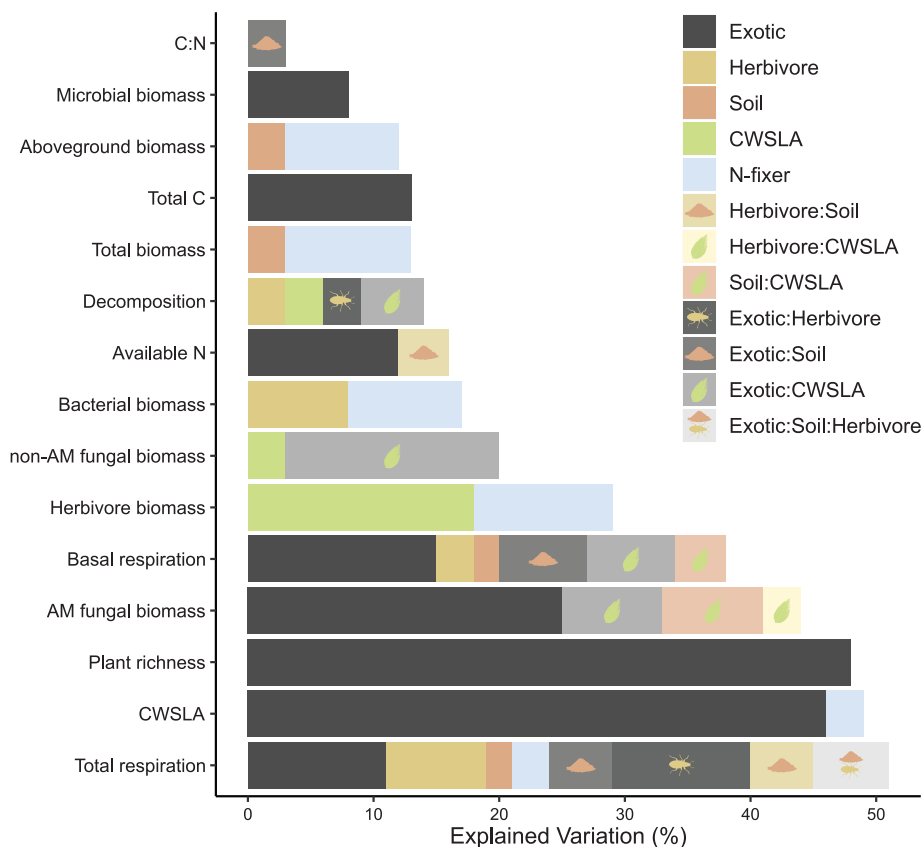


**Fig. 4. Variance partitioned among treatments from hypothesized models.** Bars show the percentage of variation explained by each treatment and their interactions (indicated with a colon in the key) on our measured ecosystem properties.

were associated with faster rates of decomposition (Fig. 3). AMF can stabilize organic matter in soil (30) by rapidly assimilating plant C into extensive intra- and extraradical hyphal structures (31), but much of this hyphal biomass may reside in soil as recalcitrant material and increase aggregate stabilization in soil (32). Non-AMF plants exude more labile C into soil (33, 34), which can increase mineralization of soil organic matter by cooccurring microbes (30, 33, 34). Indeed, suppression of AMF has accelerated soil respiration in previous studies (35). By contrast, ectomycorrhizal plants stimulate C mineralization in soils (33). However, we did not observe increases in C turnover in communities with ectomycorrhizal plants, likely because communities containing these species typically contained only a single ectomycorrhizal individual and made up a relatively small proportion of biomass (~6% where they occurred).

Although AMF are ubiquitous and associate with most land plants, there is wide variation in the degree to which plants invest in AMF (36), which may be species specific (36) and differ depending on provenance (37) or environmental conditions (38). A meta-analysis has shown that native plants have lower AMF colonization when grown near or after exotic plants, but provenance did not predict differences in AMF abundance among exotic plants (37). Here, exotic non-N-fixing plants caused the biggest declines in plant richness (Fig. 3), which may have reduced the availability of potentially better hosts for AMF. N-fixing plants did not reduce AMF biomass, likely reflecting their high reliance on AMF to meet the high phosphorus demand of N fixation (39). AMF were also strongly reduced by non-N-fixing woody plants (Fig. 3), possibly reflective of suppression by ectomycorrhizal plants and associated fungi (40). Finally, direct suppression of AMF hyphae has been observed in soils with a high abundance of Gram-negative bacteria (41), which were elevated in our exotic-dominated communities. Thus, increases in potentially antagonistic bacteria or other biota may explain the concomitant reductions in AMF biomass in exotic-dominated communities, or reduced biomass may reflect lower investment in AMF by the exotic plants grown here. AMF can buffer C emissions as long as decomposition rates remain low (42, 43), suggesting that decreases in AMF biomass under exotic plants represents another avenue by which C dynamics shift after invasion.

Increased microbial respiration rates in exotic-dominated communities grown in soils with depressed levels of species-specific soil biota (i.e., away soils) (Fig. 2B) were also likely driven by functional changes to bacterial communities. Plants grown in soils including species-specific soil biota (i.e., home soils) had a higher proportion of Gram-positive

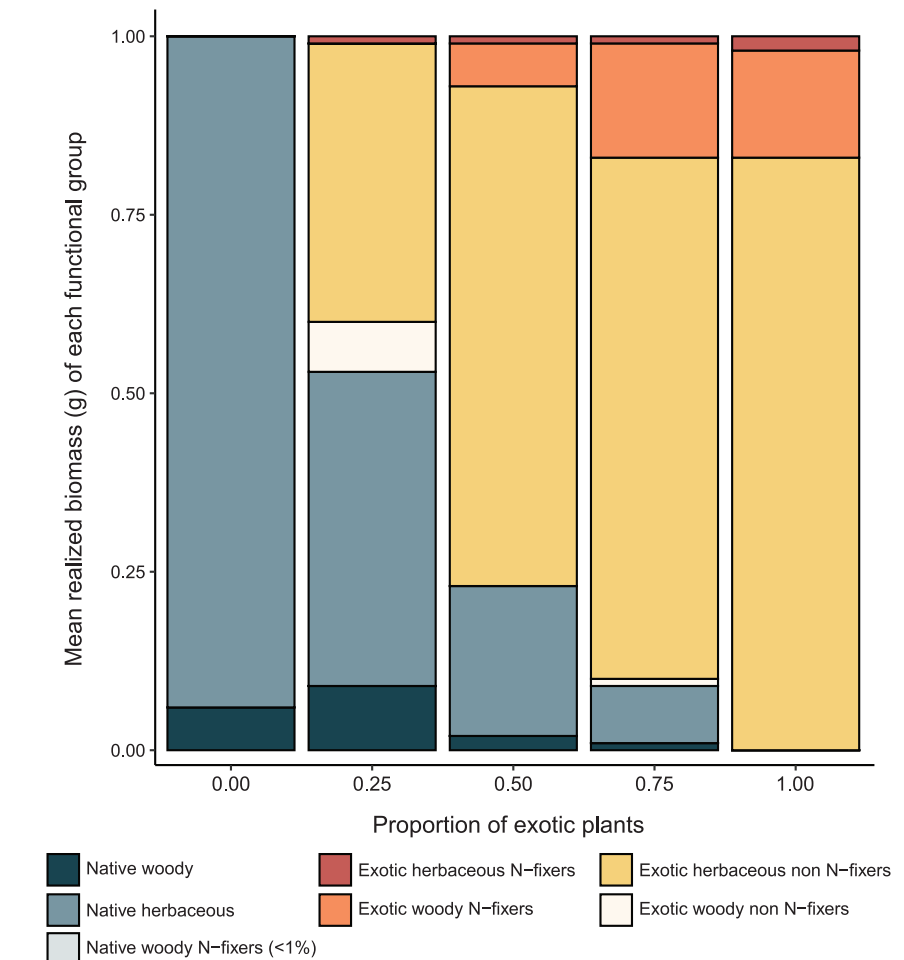


**Fig. 5. Mean proportion of plant biomass realized relative to proportion planted by provenance and functional group.** Bars represent the mean realized proportion of biomass for exotic and native plants of each plant functional group and provenance along the planted exotic gradient.

bacteria (Gram-positive bacteria~soil,  $\chi^2 = 3.94$ ,  $p < 0.047$ ; fig. S7B), a predominantly oligotrophic group containing many important, often specialized plant pathogens and recalcitrant litter specialists (27). Although we cannot determine whether soil biota were beneficial or harmful to plants, community-level reductions in plant biomass in home soil support the notion of more highly specialized pathogen loads or poor-quality mutualists (mesocosm plant biomass~soil,  $\chi^2 = 8.80$ ,  $p < 0.003$ ; Fig. 4 and fig. S4). Regardless of their effects on live plants, oligotrophic taxa often have slower growth and respiratory loss rates (27, 28) and may have slowed respiratory losses in home soils. In fact, increases in Gram-positive bacteria were associated with higher soil organic matter (Fig. 3), likely explaining the higher C:N in home soils. By contrast, the higher basal respiration rates in away soils likely reflect the relatively rapid breakdown of labile plant material by more prevalent copiotrophic taxa. This provides a temporal aspect to invasion effects on C dy-

namics. If home soils (containing more specialist soil biota) represent more established invasions and away soils newer invasions (containing no specialist soil biota), then we can expect faster turnover of recently assimilated C in new invasions, shifting to slower turnover and greater storage of longer-term C pools over time as specialist bacteria increase in abundance.

Our results could inform projects aimed at using nature-based solutions to fight climate change, such as the Trillion Trees Program ([www.trilliontrees.org/](http://www.trilliontrees.org/)). Fast-growing exotic plants may be ideally suited for plantings when the goal is to sequester C aboveground, but exotic plants may have more variable effects belowground compared with native plants. Currently, N-fixing trees from the genus *Acacia* are among the most commonly planted plantation trees globally (44). Results from our experiment, which included *A. dealbata*, suggest that these types of trees may indeed increase soil C stocks, particularly in soils previously occupied by those species (i.e., home soils).

through their positive effects on oligotrophic, specialist soil biota. However, these gains may be reduced over time through respiration associated with increases in copiotrophic taxa such as those that we have observed (Fig. 3), particularly in new or frequently harvested plantations. Our results also suggest that soil C stability may vary depending on whether exotic plants accumulate herbivores and/or fungal saprotrophs regardless of woodiness.

The pathways by which N-fixing versus non-N-fixing exotics affect ecosystem properties related to C-cycling appear to differ, and their relative effects differed between woody and herbaceous plants. N-fixing woody exotics disproportionately affected ecosystem functions relative to their proportional biomass in communities (Fig. 5), which has also been observed in other systems (45). Despite their low richness, the five exotic N-fixing woody species with high survival drove the biggest increases in fungal and bacterial biomass (Fig. 3), likely explaining much of the increased microbial respiration rates along the exotic gradient (Fig. 3). Non-N-fixing species contributed to significant decreases in AMF biomass, which may be driven by their exploitative life history strategies [i.e., fast growth (46) and high SLA; Figs. 2 and 3]. Herbaceous N-fixing exotics had no detectable effects in their communities, whereas non-N-fixing woody species had few (but strong) effects, perhaps because these species did not reach maturity, whereas many of the herbaceous plants grew quite large and usually flowered. Thus, exotic effects on ecosystem functions consistently result from differences in the way that they interact with other organisms in their environment compared with their native counterparts. Our experiment reveals multiple pathways through which these effects occur, influenced in different ways by various plant traits, including leaf traits, plant functional group (i.e., woody or herbaceous, N-fixing or not), and their typical microbial associations.

Taken together, these results suggest that shifts in fungal and bacterial function in exotic-dominated communities with herbivores and more generalist soil biota may underpin increased respiration rates through more rapid microbial mineralization of organic matter. Soil organic matter is primarily derived from plants and developed and turned over through interactions among soil microbiota (47), the abiotic environment (48), and living plant root exudates (49), which can differ substantially depending on plant composition (50). Indeed, our analyses indicate that it is not simply the large increases in exotic plant biomass that drive changes to C-cycling, but also differences in the types of inputs compared with natives. Exotic N-fixers drive increases in faster-cycling bacterial taxa, whereas high-quality exotic leaf tissues promote biomass of herbivores that

reduce slower-cycling relative to faster-cycling taxa (Fig. 3 and fig. S7).

Understanding the factors regulating ecosystem responses in invaded ecosystems is complicated by the myriad of factors that influence C gains and losses. Our manipulative experiment showed strong interdependence among three leading hypotheses used to explain drivers of exotic plant impacts on ecosystem properties related to C-cycling. Exotic plants, which make up the greatest proportion of biomass in many invaded communities, have traits (e.g., high SLA and  $N_{mass}$ ) that influence the way that they interact with herbivores and soil biota to drive ecosystem properties. Our results show that exotic and native plants differ in common bacterial and fungal pathways of C storage and release, and these differences are driven by trait differences such as SLA, woodiness, and the ability to fix N. Exotic plants, particularly woody species that fix N, increase bacterial and non-AMF biomass associated with storage and breakdown of C pools. By contrast, non-N-fixing exotic herbs substantially reduce AMF biomass, which accelerates soil C loss compared with communities dominated by native plants. In addition to their effects on fungi and bacteria, herbaceous exotic plants increase herbivore biomass, which we linked to increases in decomposition, an indicator of C-cycling. Our study provides an unprecedented community-scale understanding of how the transformation of ecosystems by exotic species depends on complex species interactions, emphasizing the need for whole-ecosystem approaches.

## REFERENCES AND NOTES

- J. G. Ehrenfeld, *Ecosystems* (N. Y.) **6**, 503–523 (2003).
- C. Liao et al., *New Phytol.* **177**, 706–714 (2008).
- D. A. Peltzer, R. B. Allen, G. M. Lovett, D. Whitehead, D. A. Wardle, *Glob. Change Biol.* **16**, 732–746 (2010).
- J. G. Ehrenfeld, *Annu. Rev. Ecol. Evol. Syst.* **41**, 59–80 (2010).
- W. H. van der Putten, J. N. Klironomos, D. A. Wardle, *ISME J.* **1**, 28–37 (2007).
- B. E. Wolfe, J. N. Klironomos, *Bioscience* **55**, 477–487 (2005).
- M. E. Rout, R. M. Callaway, *Science* **324**, 734–735 (2009).
- M. van Kleunen, E. Weber, M. Fischer, *Ecol. Lett.* **13**, 235–245 (2010).
- A. A. Agrawal et al., *Ecology* **86**, 2979–2989 (2005).
- See the supplementary materials and methods.
- J. D. Bever, K. M. Westover, J. Antonovics, *J. Ecol.* **85**, 561–573 (1997).
- C. A. Johnston et al., *Front. Ecol. Environ.* **2**, 522–528 (2004).
- I. J. Wright et al., *Nature* **428**, 821–827 (2004).
- H. Poorter, J. R. Evans, *Oecologia* **116**, 26–37 (1998).
- E. Laliberté, J. M. Tylianakis, *Ecology* **93**, 145–155 (2012).
- R. D. Bardgett, L. Mommer, F. T. De Vries, *Trends Ecol. Evol.* **29**, 692–699 (2014).
- K. N. Suding et al., *Glob. Change Biol.* **14**, 1125–1140 (2008).
- M. Tamura, N. Tharayil, *New Phytol.* **203**, 110–124 (2014).
- J. L. Funk, P. M. Vitousek, *Nature* **446**, 1079–1081 (2007).
- J. M. Levine et al., *Proc. Biol. Sci.* **270**, 775–781 (2003).
- C. C. Daehler, *Annu. Rev. Ecol. Evol. Syst.* **34**, 183–211 (2003).
- M. Vilà et al., *Ecol. Lett.* **14**, 702–708 (2011).
- A. A. Agrawal, P. M. Kotanen, *Ecol. Lett.* **6**, 712–715 (2003).

- D. J. Augustine, S. J. McNaughton, *J. Wildl. Manage.* **62**, 1165–1183 (1998).
- D. A. Wardle et al., *Science* **304**, 1629–1633 (2004).
- C. Kramer, G. Gleixner, *Soil Biol. Biochem.* **40**, 425–433 (2008).
- N. Fierer, M. A. Bradford, R. B. Jackson, *Ecology* **88**, 1354–1364 (2007).
- N. Farin et al., *Soil Biol. Biochem.* **128**, 111–114 (2019).
- J. N. Holland, W. Cheng, D. A. Crossley Jr., *Oecologia* **107**, 87–94 (1996).
- D. L. Jones, A. Hodge, Y. Kuzyakov, *New Phytol.* **163**, 459–480 (2004).
- P. L. Staddon, C. B. Ramsey, N. Ostle, P. Ineson, A. H. Fitter, *Science* **300**, 1138–1140 (2003).
- Y. G. Zhu, R. M. Miller, *Trends Plant Sci.* **8**, 407–409 (2003).
- R. P. Phillips, T. J. Fahey, *Ecology* **87**, 1302–1313 (2006).
- E. R. Brzostek, D. Dragoni, Z. A. Brown, R. P. Phillips, *New Phytol.* **206**, 1274–1282 (2015).
- B. Zhang et al., *Sci. Rep.* **6**, 19990 (2016).
- G. W. Wilson, D. C. Hartnett, *Am. J. Bot.* **85**, 1732–1738 (1998).
- R. A. Bunn, P. W. Ramsey, Y. Lekberg, *J. Ecol.* **103**, 1547–1556 (2015).
- N. C. Johnson, J. H. Graham, F. A. Smith, *New Phytol.* **135**, 575–585 (1997).
- P. Bonfante, I.-A. Anca, *Annu. Rev. Microbiol.* **63**, 363–383 (2009).
- K. M. Becklin, M. L. Pallo, C. Galen, *J. Ecol.* **100**, 343–351 (2012).
- N. B. Svenningsson et al., *ISME J.* **12**, 1296–1307 (2018).
- E. F. Leifheit, E. Verbruggen, M. C. Rillig, *Soil Biol. Biochem.* **81**, 323–328 (2015).
- E. Verbruggen, J. Jansa, E. C. Hammer, M. C. Rillig, *J. Ecol.* **104**, 261–269 (2015).
- M. Dodet, C. Collet, *Biol. Invasions* **14**, 1765–1778 (2012).
- J. M. Craine, W. G. Lee, S. Walker, “The context of plant invasions in New Zealand: Evolutionary history and novel niches” in *Biological Invasions in New Zealand* (Springer, 2006), pp. 167–177.
- L. Koziol, J. D. Bever, *Ecology* **96**, 1768–1774 (2015).
- D. W. Hopkins, E. G. Gregorich, *Biol. Div. Func. Soil* **2005**, 57–80 (2005).
- J. F. Dormaar, *Biol. Fertil. Soils* **10**, 121–126 (1990).
- J. A. Bird, D. J. Herman, M. K. Firestone, *Soil Biol. Biochem.* **43**, 718–725 (2011).
- F. Z. Haichar et al., *ISME J.* **2**, 1221–1230 (2008).
- L. P. Waller et al., Data for: Biotic interactions drive ecosystem responses to exotic plant invaders, *Dryad* (2020); <https://doi.org/10.5061/dryad.wwp2gm5gb>.

## ACKNOWLEDGMENTS

We thank D. Wardle and E. T. Kiers for valuable comments and J. Allen, N. Allen, A. Barrington, G. Boitt, J. Breitmeyer, J. Bufford, J. Burson, D. Conder, R. Cresswell, D. Dash, L. Dickie, B. Fairbrass, C. Ferguson, B. Ganley, T. Glare, A. Holyoake, D. Jack, C. Johns, J. Johns, E. Jones, B. Kwan, S. Larsen, H. Lea, I. Luxford, F. Martoni, L. Meachen, A. McKinnon, G. McSweeney, M. O’Callaghan, A. Puértolas, B. Richards, S. Richardson, H. Ridgeway, R. Scott, M.-R. Shadboit, K. Slattery, R. Vardy, R. Wainer, D. Waller, M. Waller, A. Wakelin, and S. Wilson for technical support. **Funding:** This research was primarily supported by Tertiary Education Commission funding to the BioProtection Research Centre. **Author contributions:** Conceptualization: W.J.A., L.M.C., I.A.D., J.M.T., L.P.W.; Funding acquisition: B.I.P.B., L.M.C., I.A.D., J.M.T., S.A.W.; Investigation: W.J.A., F.M.F., J.E.H., N.K., K.H.O., G.S.S., L.P.W.; Data analysis: W.J.A., I.A.D., J.M.T., L.P.W.; Supervision: B.I.P.B., L.M.C., I.A.D., J.M.T.; Writing original draft: L.P.W.; Writing, review, and editing: all authors. **Competing interests:** The authors declare no competing interests. **Data and materials availability:** The data reported here have been deposited in Dryad (51).

## SUPPLEMENTARY MATERIALS

[science.sciencemag.org/content/368/6494/967/suppl/DC1](https://science.sciencemag.org/content/368/6494/967/suppl/DC1)  
Materials and Methods

Figs. S1 to S7  
Tables S1 to S7  
References (52–67)

2 December 2019; accepted 20 April 2020  
10.1126/science.aba2225

## CANCER

# The human tumor microbiome is composed of tumor type-specific intracellular bacteria

Deborah Nejman<sup>1\*</sup>, Ilana Livvyatan<sup>1,2\*</sup>, Garold Fuks<sup>3\*</sup>, Nancy Gavert<sup>1</sup>, Yaara Zwang<sup>1</sup>, Leore T. Geller<sup>1</sup>, Aviva Rotter-Maskowitz<sup>1</sup>, Roi Weiser<sup>4,5</sup>, Giuseppe Malle<sup>1</sup>, Elinor Gigi<sup>1</sup>, Arnon Meltser<sup>1</sup>, Gavin M. Douglas<sup>6</sup>, Iris Kamer<sup>7</sup>, Vancheswaran Gopalakrishnan<sup>8†</sup>, Tali Dadosh<sup>9</sup>, Smadar Levin-Zaidman<sup>9</sup>, Sofia Avnet<sup>10</sup>, Tehila Atlan<sup>11</sup>, Zachary A. Cooper<sup>12</sup>, Reetakshi Arora<sup>8</sup>, Alexandria P. Cogdill<sup>13</sup>, Md Abdul Wadud Khan<sup>8</sup>, Gabriel Ologun<sup>8</sup>, Yuval Bussi<sup>1,2,14</sup>, Adina Weinberger<sup>1,2</sup>, Maya Lotan-Pompan<sup>1,2</sup>, Ofra Golani<sup>15</sup>, Gili Perry<sup>16</sup>, Merav Rokah<sup>17</sup>, Keren Bahar-Shany<sup>16</sup>, Elisa A. Rozeman<sup>18</sup>, Christian U. Blank<sup>18</sup>, Anat Ronai<sup>19</sup>, Ron Shaoul<sup>19</sup>, Amnon Amit<sup>20,21</sup>, Tatiana Dorfman<sup>22,23</sup>, Ran Kremer<sup>24</sup>, Zvi R. Cohen<sup>5,25</sup>, Sagi Harnov<sup>5,26</sup>, Tali Siegal<sup>27</sup>, Einav Yehuda-Shnaidman<sup>28</sup>, Einav Nili Gal-Yam<sup>29</sup>, Hagit Shapira<sup>28</sup>, Nicola Baldini<sup>10,30</sup>, Morgan G. I. Langille<sup>6,31</sup>, Alon Ben-Nun<sup>5,17</sup>, Bella Kaufman<sup>5,7</sup>, Aviram Nissan<sup>32</sup>, Talia Golan<sup>5,7</sup>, Maya Dadiani<sup>16</sup>, Keren Levanon<sup>5,16</sup>, Jair Bar<sup>5,7</sup>, Shlomit Yust-Katz<sup>5,27</sup>, Iris Barshack<sup>5,33</sup>, Daniel S. Peeper<sup>34</sup>, Dan J. Raz<sup>35</sup>, Eran Segal<sup>1,2</sup>, Jennifer A. Wargo<sup>8,13</sup>, Judith Sandbank<sup>28</sup>, Noam Shental<sup>36‡</sup>, Ravid Straussman<sup>1‡§</sup>

Bacteria were first detected in human tumors more than 100 years ago, but the characterization of the tumor microbiome has remained challenging because of its low biomass. We undertook a comprehensive analysis of the tumor microbiome, studying 1526 tumors and their adjacent normal tissues across seven cancer types, including breast, lung, ovary, pancreas, melanoma, bone, and brain tumors. We found that each tumor type has a distinct microbiome composition and that breast cancer has a particularly rich and diverse microbiome. The intratumor bacteria are mostly intracellular and are present in both cancer and immune cells. We also noted correlations between intratumor bacteria or their predicted functions with tumor types and subtypes, patients' smoking status, and the response to immunotherapy.

**M**ore than 16% of cancer incidence worldwide has been attributed to infectious agents (*1*). Intratumor bacteria have been reported in many tumor types (*2–19*), but these bacteria have not been characterized in a comprehensive manner (*20*). The gut microbiome has been shown to have multiple effects on tumor biology, such as the transformation process, tumor progression, and the response to anticancer therapies including immunotherapy (*21–29*). Thus, characterization of the tumor microbiome may be an essential step in unraveling the effects that tumor bacteria have on different cancer hallmarks.

## Bacterial DNA, RNA, and lipopolysaccharide are present in many human solid tumors

Because the tumor microbiome has a relatively low biomass, contamination of the tumor

samples with bacteria or bacterial DNA can be problematic (*30, 31*). Therefore, it is critical to include multiple measures to avoid, or at least detect, any possible contamination in the process of profiling the tumor microbiome (supplementary note) (*32, 33*). For next-generation sequencing applications, it is also important to use mechanical tissue shearing in the DNA isolation protocol to ensure the complete recovery of DNA from within the cell wall of Gram-positive bacteria—a step not included in most standard DNA isolation protocols (*6, 7*). To characterize and visualize intratumor bacteria, we applied an extensive combination of methods to a large cohort of solid human tumor samples to detect bacterial DNA, RNA, and bacterial outer membrane or cell wall components.

We focused on seven solid tumor types that represent either common cancer types or cancer

types for which the tumor microbiome is largely unknown, such as melanoma, bone, and brain tumors (Fig. 1A). To address laboratory-borne contaminants, we introduced 643 negative controls that were processed with the samples, including 437 DNA extraction controls and 206 polymerase chain reaction (PCR) no-template controls (NTCs). To address contamination that might have occurred before the samples reached our laboratory, we also included 168 paraffin-only samples taken from the margins of the paraffin blocks (without tissue) that were used in the study (Fig. 1A).

Overall, we profiled 1010 tumor samples and 516 normal samples, including normal adjacent tissues (NATs) from the same patients (Fig. 1A and table S1). In the case of ovarian cancer, our normal samples came from the ovaries or uteruses of the patients or from normal fallopian tube fimbria of unmatched healthy subjects (tables S1 and S2). To quantify bacterial DNA, we used a real-time quantitative PCR (qPCR) assay with universal primers 967F and 1064R specific for the bacterial ribosomal 16S gene [16S rDNA (ribosomal DNA)] (*34*). Levels of bacterial DNA in all tumor types were significantly higher than those found in both DNA extraction and paraffin controls (Fig. 1B; *P* value  $<10^{-10}$  for each tumor type, Wilcoxon rank sum test). We found that different cancer types vary in the proportion of tumors that are positive for bacterial DNA, ranging from only 14.3% in melanoma to >60% in breast, pancreatic, and bone tumors. Bacterial DNA was also detected in solid tumors that have no direct connection with the external environment, such as ovarian cancer, glioblastoma multiforme (GBM), and bone cancer.

To validate the presence of bacteria in human tumors, we stained >400 additional tumors (not related to the 1526 samples described above), representing six of our seven profiled tumor types, for the presence of bacteria. We conducted immunohistochemistry (IHC) using antibodies against bacterial lipopolysaccharide (LPS) and lipoteichoic acid (LTA) to detect Gram-negative and Gram-positive bacteria, respectively (*35, 36*). We also used RNA fluorescence in situ hybridization (FISH), with a

<sup>1</sup>Department of Molecular Cell Biology, Weizmann Institute of Science, Rehovot, Israel. <sup>2</sup>Department of Computer Science and Applied Mathematics, Weizmann Institute of Science, Rehovot, Israel.

<sup>3</sup>Department of Physics of Complex Systems, Weizmann Institute of Science, Rehovot, Israel. <sup>4</sup>Division of Surgery, Tel-Aviv Sourasky Medical Center, Tel-Aviv, Israel. <sup>5</sup>Sackler Faculty of Medicine, Tel-Aviv University, Tel-Aviv, Israel. <sup>6</sup>Department of Microbiology and Immunology, Dalhousie University, Halifax, NS, Canada. <sup>7</sup>Institute of Oncology, Sheba Medical Center, Ramat Gan, Israel.

<sup>8</sup>Department of Surgical Oncology, The University of Texas MD Anderson Cancer Center, Houston, TX, USA. <sup>9</sup>Department of Chemical Research Support, Weizmann Institute of Science, Rehovot, Israel.

<sup>10</sup>Orthopaedic Pathophysiology and Regenerative Unit, IRCCS Istituto Ortopedico Rizzoli, Bologna, Italy. <sup>11</sup>Department of Bioinformatics, Jerusalem College of Technology, Jerusalem, Israel.

<sup>12</sup>Translational Medicine, Oncology R&D, AstraZeneca, Gaithersburg, MD, USA. <sup>13</sup>Department of Genomic Medicine, The University of Texas MD Anderson Cancer Center, Houston, TX, USA. <sup>14</sup>Department of Biomolecular Sciences, Weizmann Institute of Science, Rehovot, Israel.

<sup>15</sup>Department of Life Sciences Core Facilities, Weizmann Institute of Science, Rehovot, Israel. <sup>16</sup>Cancer Research Center, Sheba Medical Center, Ramat Gan, Israel. <sup>17</sup>Department of Thoracic Surgery, Sheba Medical Center, Ramat Gan, Israel.

<sup>18</sup>Department of Medical Oncology and Division of Molecular Oncology and Immunology, Netherlands Cancer Institute, Amsterdam, Netherlands. <sup>19</sup>Pediatric Gastroenterology Institute, Rambam Medical Center, Haifa, Israel. <sup>20</sup>Faculty of Medicine, Technion-Israel Institute of Technology, Haifa, Israel.

<sup>21</sup>Department of Obstetrics and Gynecology, Rambam Health Care Campus, Haifa, Israel. <sup>22</sup>Division of General Surgery, Rambam Health Care Campus, Haifa, Israel. <sup>23</sup>Ambulatory and Breast Surgery Service, Rambam Health Care Campus, Haifa, Israel.

<sup>24</sup>Department of Thoracic Surgery, Rambam Health Care Campus, Haifa, Israel. <sup>25</sup>Department of Neurosurgery, Sheba Medical Center, Ramat Gan, Israel. <sup>26</sup>Department of Neurosurgery, Rabin Medical Center, Beilinson Hospital, Petach Tikva, Israel.

<sup>27</sup>Neuro-Oncology Unit, Rabin Medical Center, Beilinson Hospital, Petach Tikva, Israel. <sup>28</sup>Institute of Pathology, Megalab, Maccabi Healthcare Services, Rehovot, Israel.

<sup>29</sup>Breast Oncology Institute, Sheba Medical Center, Ramat Gan, Israel. <sup>30</sup>Department of Biomedical and Neuromotor Sciences, University of Bologna, Bologna, Italy. <sup>31</sup>Department of Pharmacology, Dalhousie University, Halifax, NS, Canada. <sup>32</sup>Department of Surgical Oncology (Surgery C), Sheba Medical Center, Ramat Gan, Israel.

<sup>33</sup>Department of Pathology, Sheba Medical Center, Ramat Gan, Israel. <sup>34</sup>Division of Molecular Oncology & Immunology, Netherlands Cancer Institute, Amsterdam, Netherlands. <sup>35</sup>Division of Thoracic Surgery, City of Hope Medical Center, Duarte, CA, USA. <sup>36</sup>Department of Mathematics and Computer Science, The Open University of Israel, Ra'anana, Israel.

\*These authors contributed equally to this work. †Present address: AstraZeneca, Gaithersburg, MD, USA. ‡These authors contributed equally to this work.

§Corresponding author. Email: ravidst@weizmann.ac.il

universal probe against bacterial 16S ribosomal RNA (rRNA), to detect bacterial RNA in these tumors (37). To control for nonspecific staining, IHC-negative controls (no primary antibody) and FISH-negative controls (nonspecific complement probe) were also applied to the samples (figs. S1 and S2). Bacterial LPS and 16S rRNA were frequently detected in all tumor types (Fig. 1C) and demonstrated a similar spatial distribution (Fig. 1D and fig. S3). LTA was detected mainly in melanomas and was largely absent in other tumor types.

Generally, more tumors were found to be positive for bacteria using visualization methods than by using qPCR. This disparity may be because of some limitation in the sensitivity of our qPCR assay, or it might be caused by our strict cutoff for confirming a sample as positive.

**Intratumor bacteria are mostly intracellular and are present in both cancer and immune cells**

Pathological examination of tumor cores indicated that LPS and bacterial 16S rRNA were

localized mainly in cancer cells and immune cells (Fig. 2A and fig. S4). In cancer cells, bacterial 16S rRNA was detected mostly in the cytoplasm, whereas LPS staining was associated with both the cytoplasm and the nucleus (Fig. 2B and fig. S5). CD45-positive leukocytes generally exhibited a stronger cytoplasmic bacterial staining by 16S rRNA staining than that exhibited by cancer cells (Fig. 2C and fig. S6A). LTA-positive bacteria were almost exclusively found in macrophages, as detected by hematoxylin and eosin (H&E) staining and verified by immunofluorescence (IF) for CD68 (Fig. 2D and fig. S6B). LTA was rarely detected in cancer cells or in CD45+/CD68– immune cells (Fig. 2). Although the intensity of bacterial LPS and LTA staining was very strong in CD45+/CD68+ cells, bacterial 16S rRNA was only rarely found in macrophages by FISH (Fig. 2, A and D, and figs. S4 and S6). This discrepancy may reflect macrophage ingestion of bacterial components rather than live bacteria, or it may result from the accumulation of LPS and LTA in macrophages long after the bacteria have been phagocytized and processed by the macrophages. It has been previously demonstrated that the processing of bacterial LPS by macrophages is very slow; therefore, LPS can be found in these cells months after the bacteria were ingested and processed (38).

To further verify the presence of bacteria inside cancer cells, we performed correlative light and electron microscopy (CLEM) (39, 40) on four human breast tumors that were positive for bacterial LPS and 16S rRNA (fig. S7). Combined LPS fluorescence staining and transmission electron microscopy (TEM) imaging of the same cells clearly demonstrated the intracellular localization of bacteria in all four tumors (Fig. 2E and fig. S7). In many cases, the bacteria were found in close proximity to the nuclear membrane. Because we did not detect intranuclear bacteria by TEM, we suspect that the appearance of LPS nuclear localization in some tumors represents the staining of cytoplasmic perinuclear bacteria.

Whereas bacterial 16S rRNA FISH staining appeared as a diffused signal inside cells, typical bacterial rods or cocci were only rarely detected (in 3 of 426 cores). This observation, combined with the fact that no cell wall polymer LTA was detected in cancer cells—despite the detection of many Gram-positive bacteria in human tumors by 16S rDNA sequencing—suggests that bacteria in tumor cells may have altered their envelope, perhaps leading to a cell wall-deficient state, akin to L-forms (41). Cell wall-deficient bacteria are known to be found exclusively inside cells, where their morphology transforms into less-defined structures of highly variable sizes and shapes (42, 43). Our TEM images also suggest that many of the

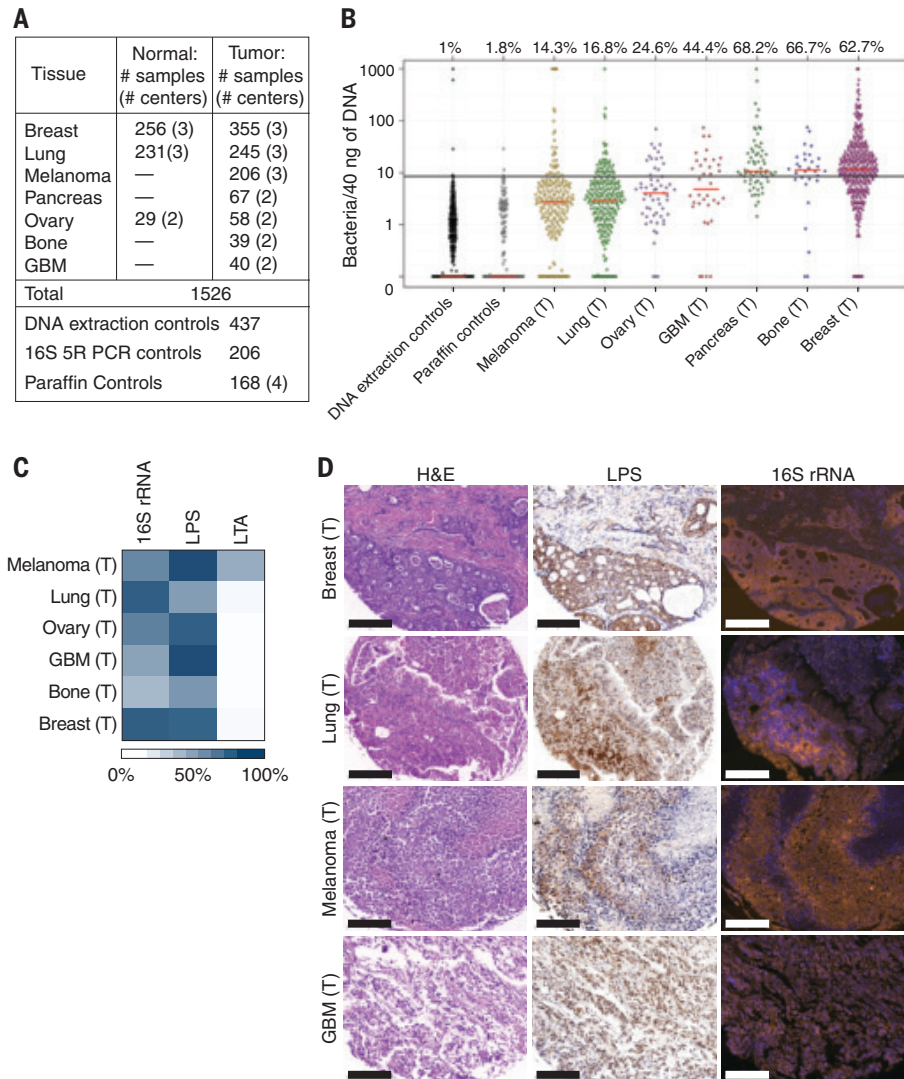


**Fig. 1. Bacterial components are detected in human tumors.** (A) Number of human samples analyzed in the study. Normal samples include both normal tissue samples and normal adjacent tissue (NAT) to tumor samples, as detailed in table S1. Dashes indicate data not available. GBM, glioblastoma multiforme. (B) The presence of bacterial DNA in human tumors was assessed by bacterial 16S rDNA qPCR. A calibration curve, generated by spiking bacterial DNA into human DNA, was used to estimate bacterial load, which was then normalized against batch-specific qPCR NTCs. Values were floored to 0.1. Red bars represent the median. The proportion of samples of each cancer type that had more bacteria than the 99th percentile of the DNA extraction control samples (black bar) is depicted above each cancer type. (C) Heatmap representing the proportion of tumors that stained positively for 16S rRNA, LPS, or LTA.  $n = 40$  to 101 tissue cores per tumor type. (D) Consecutive slices from four human tumor types were stained with H&E, anti-LPS antibody (LPS), or with FISH probes against bacterial 16S rRNA. Scale bars, 200  $\mu$ m. The letter (T) indicates samples originating from tumors.

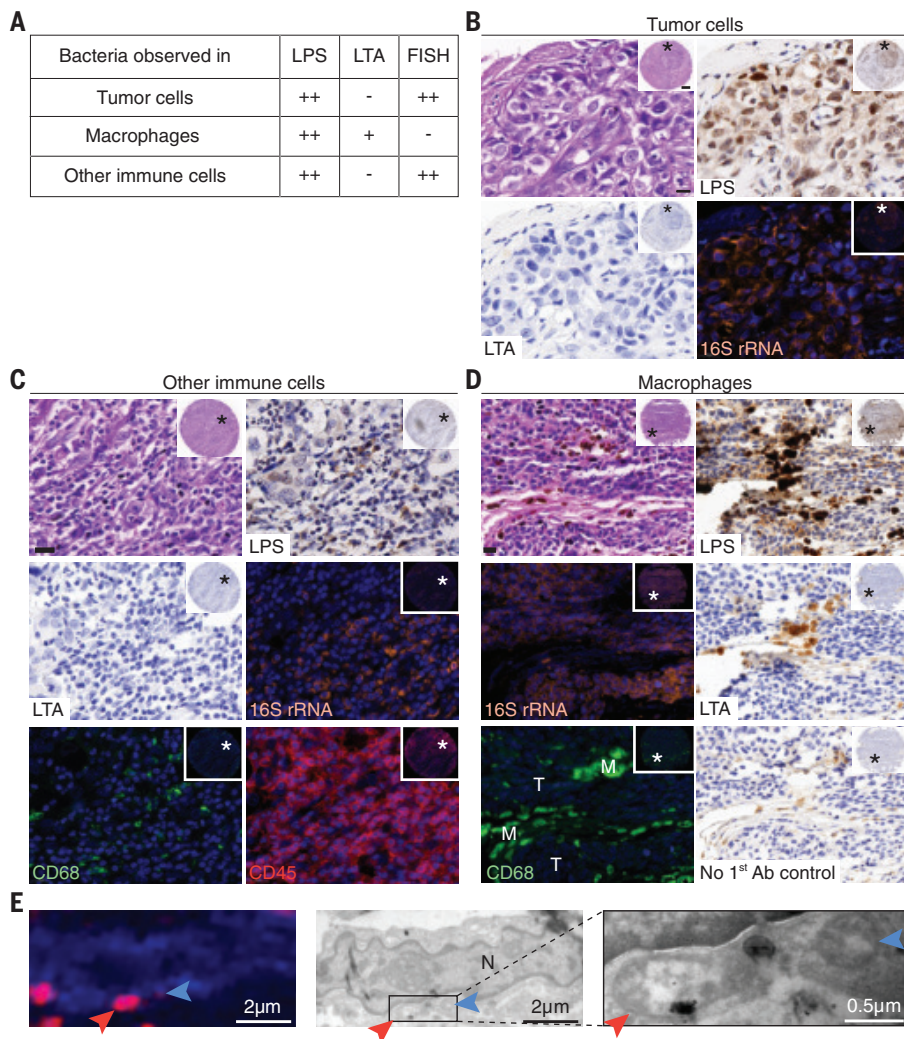


**Fig. 2. Intratumor bacteria are found inside both cancer and immune cells.** (A) Summary of the staining patterns of LPS, LTA, and bacterial 16S rRNA in different cell types across 459, 427, and 354 tumor cores, respectively. CD45+/CD68+ cells are referred to as macrophages; CD45+/CD68- cells are referred to as other immune cells. (B to D) Representative cores are shown demonstrating the different staining patterns in human tumors. Asterisks mark the region that was selected for higher magnification. (B) Bacterial LPS and 16S rRNA are demonstrated in breast cancer cells. (C) Bacterial LPS and 16S rRNA are demonstrated in CD45+/CD68- cells of a highly inflamed breast tumor. (D) A melanoma tumor demonstrating typical staining of macrophage-associated bacteria (M), with positive LPS and LTA staining but no 16S rRNA staining. Nearby tumor cells (T) show the typical LPS and 16S rRNA staining, with negative LTA staining. Each inset demonstrates a low magnification of the entire core. Scale bars in high-magnification images, 20  $\mu$ m. (E) CLEM demonstrates intracellular bacteria in human breast cancer. IF image shows DAPI in blue and LPS in red. Two bacteria are marked with arrows. TEM images of the same cell are shown in grayscale. High-magnification image of the boxed area is shown on the right. The letter N marks the cell nucleus.

intracellular bacteria lack a cell wall (Fig. 2E and fig. S7).

### The microbiome of breast tumors is richer and more diverse than that of other tumor types

To characterize the intratumor microbiome, we developed a multiplexed 16S rDNA sequencing protocol that amplifies five short regions along the 16S rRNA gene: the 5R 16S rDNA sequencing method (Fig. 3A). By amplifying 68% of the bacterial 16S rRNA gene

using short amplicons, this method increases the coverage and resolution of the detection of bacterial species compared with the widely used V4 or V3-V4 amplification (fig. S8). Moreover, it can be applied to partially degraded DNA originating from formalin-fixed paraffin-embedded tumors. Reads from 1526 samples and 811 negative controls (DNA extraction controls, 16S 5R PCR controls, and paraffin controls) were computationally combined into long amplicons, using Short Multiple Regions

Framework (SMURF) (44) and the Greengenes database as a reference. To improve taxonomic assignment, we used the Ribosomal Database Project (RDP) classifier to augment the Greengenes database by assigning a species-level taxonomy to 380,000 bacterial 16S rRNA sequences that originally lacked such taxonomy (45) (table S3 and materials and methods). Thirty-nine samples and 10 controls that had fewer than 1000 normalized reads were discarded from further analysis (materials and methods).

Overall, we detected 9190 bacterial species across the different tumor or normal tissue types (Fig. 3B and table S2). Because some of these species may represent contamination of the samples, we applied a strict set of six filters to control for potential sources of contamination. To account for the most frequent general contaminants, filter 1 removed 167 bacterial species that were detected in >7.5% of our DNA extraction and NTC negative control samples or in the paraffin controls. This threshold demarcates the transition between most of the species that are absent or very rarely present in controls and the species that appear much more commonly in controls (fig. S9). We then applied three filters to control for batch effects that originate from DNA extraction, PCR amplification, or sequencing lane using hundreds of negative controls as a background for laboratory-borne contamination (filters 2 to 4). Filters 5 and 6 were added to control for contamination that might have been introduced to the samples before their processing in the laboratory. Filter 5 uses paraffin-only samples (without tissue) from the margins of the same paraffin blocks that were used in the study to control for contamination in the process of preparing and storing the paraffin blocks. Lastly, to account for other potential sources of medical center-specific contamination, filter 6 excluded bacteria that were not significantly enriched in a specific tumor type across multiple medical centers. Only bacteria that passed all six filters in a specific cancer type or its NAT were considered to be hits that are present in this cancer or NAT condition (Fig. 3B, table S4, materials and methods, and supplementary note).

We found that breast tumors had a richer and more diverse microbiome than all other tumor types tested ( $P$  value  $<10^{-15}$  for each tumor type, Wilcoxon rank sum test; Fig. 3, C and D, and figs. S10 and S11). An average of 16.4 bacterial species were detected in any single breast tumor sample, whereas the average was <9 in all other tumor types ( $P$  value  $<10^{-17}$  for each tumor type, Wilcoxon rank sum test; Fig. 3E and fig. S11). We also found that bacterial load and richness were higher in the breast tumor samples than those found in normal breast samples from healthy subjects.

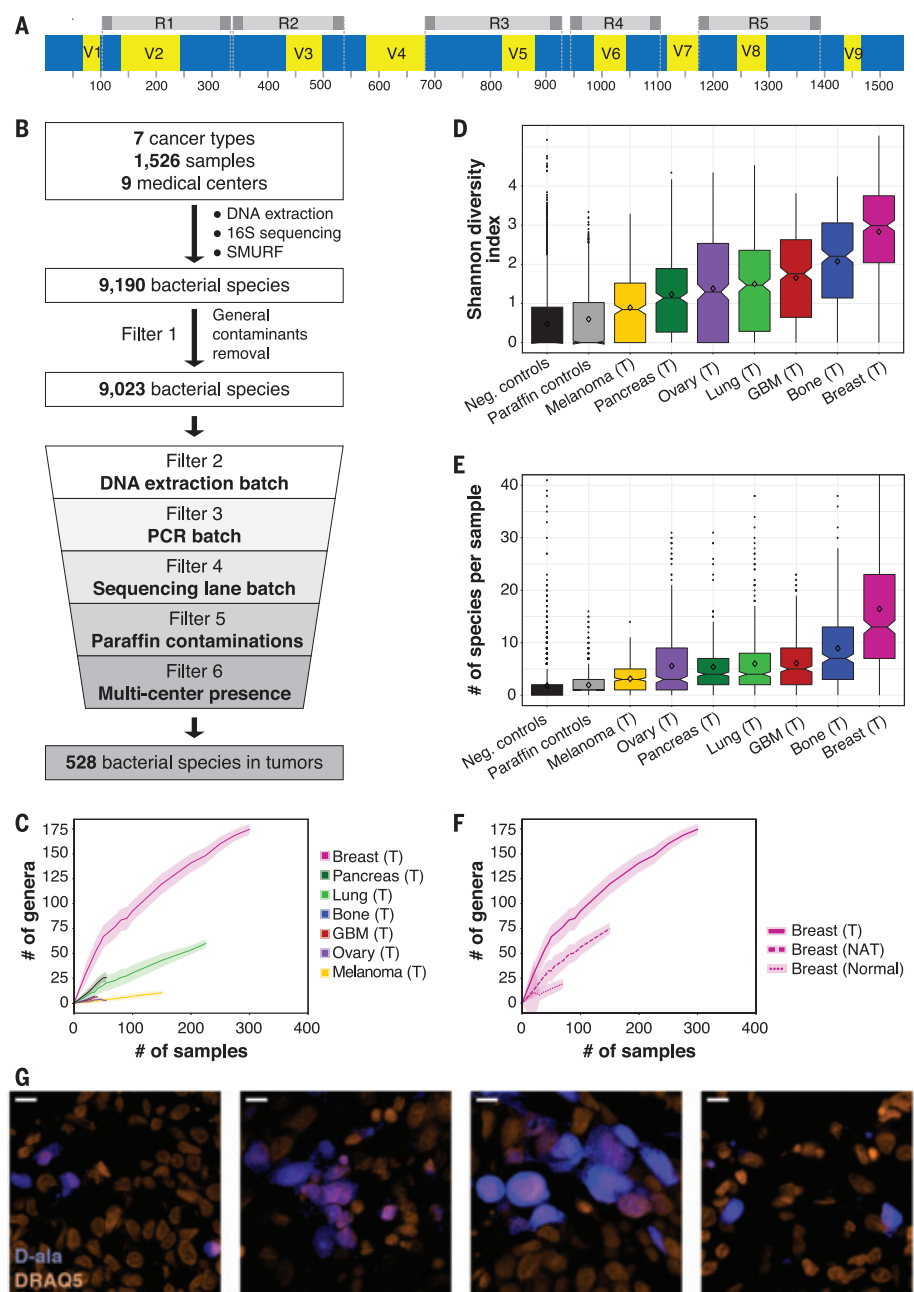


**Fig. 3. The microbiome of breast tumors is richer and more diverse than that of other tumor types.**

(A) Graphic representation of the bacterial 16S rRNA gene with its conserved (blue) and variable (yellow) regions. The sequence from *Escherichia coli* K-12 substrain MG1655 was used as a reference sequence. The five amplicons of the multiplexed 5R PCR method are depicted in gray. (B) Schematic representation of the analysis pipeline applied to 16S rDNA sequencing data. (C) Rarefaction plots showing the number of bacterial genera that passed all filters in the different tumor types per number of tumor samples that were selected for the analysis. Light color shading represents confidence intervals based on 100 random subsamplings for each number of tumor samples that was analyzed. (D) Box blot of Shannon diversity indexes of all samples, segregated by tumor type. Neg., negative. (E) Box blot of the numbers of bacterial species present in each tumor. For (D) and (E), values were calculated on rarefied data of 40 samples per tumor type, with 10 iterations. For each iteration, only bacteria that passed all filters in any of the tumor types were included in the analysis. (F) Rarefaction plots for the number of bacterial genera that passed all filters in breast tumor, breast NAT, and breast normal samples. Light color shading represents confidence intervals based on 100 random subsamplings for each number of samples that was analyzed. (G) Fluorescent images from four human breast tumors that were cultured ex vivo with fluorescently labeled D-alanine for 2 hours (blue). Nuclei were stained with DRAQ5 (orange). Scale bars, 10  $\mu$ m.

Tumor-adjacent normal breast tissue had an intermediate bacterial load and richness, between those of the breast tumor and normal samples (Fig. 3F and fig. S12). In contrast, we did not find a higher bacterial load in lung and ovarian tumors compared with their tumor-adjacent normal tissues (fig. S12).

To determine whether live bacteria are present in human tumors, we collected fresh breast tumor samples from five women undergoing breast surgery. All tissues were gently dissociated in sterile conditions, plated on 35 types of agar growth media, and incubated in both aerobic and anaerobic conditions, representing a broad span of growth conditions to accommodate a high diversity of bacteria (table S5) (46). In agreement with the positive staining of these tumors for LPS and 16S rRNA FISH (fig. S13), >1000 colonies were grown per tumor from four of the tumors, and 37 colonies were grown from one tumor. In contrast, applying the same steps of tissue dissociation and culturing protocol to five full sets of negative control plates (350 plates) using only phosphate-buffered saline (PBS) yielded only five colonies in total. Whole-genome sequencing of 474 representative colonies from all five tumors demonstrated that they represented 37 different bacterial species, 11 of which (29.7%) are bacteria that were previously detected as hits in our breast tumor cohort (table S5). Fifteen isolated species (40.5%) were detected in our breast tumor cohort but did not pass all filters. For 105 of the colonies, we could not identify the bacteria at the species level (table S5 and materials and methods). Overall, these results show that live bacteria from three main phyla—Proteobacteria, Firmicutes, and Actinobacteria—can be found in breast tumors.

To further validate the presence of live, metabolically active bacteria in human tumors, we cultured slices from four freshly resected human breast tumors ex vivo in the presence of fluorescently labeled D-alanine or dimethyl sulfoxide (DMSO) control. Although D-alanine is used by bacteria to generate peptidoglycan, an essential component of the bacterial cell wall, it is not used by mammalian cells (fig. S14) (47). We detected intracellular labeling in all four tumors, which supports the hypothesis that the tumors harbor live intracellular bacteria (Fig. 3G).

#### Different tumor types have distinct microbial compositions

Using a single sequencing methodology and platform for the characterization of the microbiome in multiple tumor types enabled us to directly compare the microbiomes of these tumors. Comparison of the beta-diversity between all pairs of samples within a given

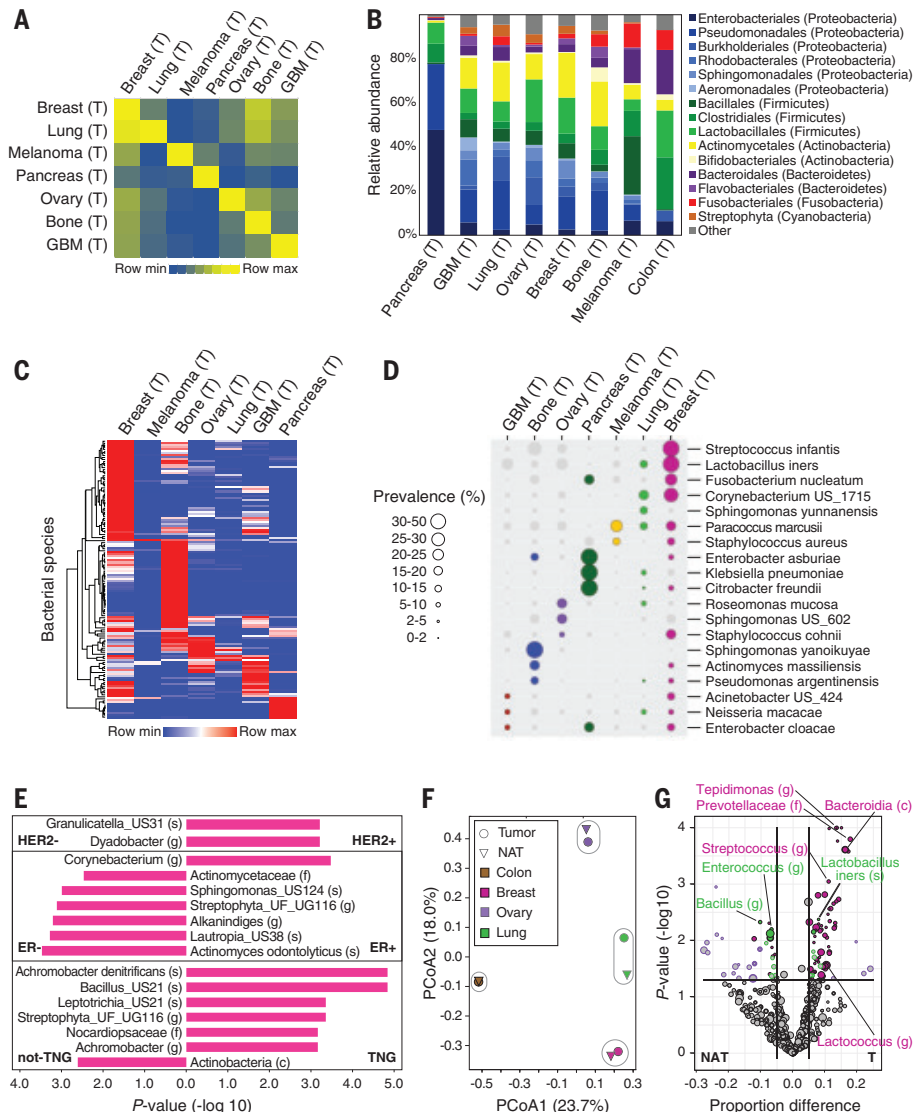


**Fig. 4. Different tumor types have distinct microbial compositions.** (A) Jaccard similarity indexes were computed on the basis of profiles of bacterial species that passed all filters in tumors ( $n = 528$ ) between all possible pairs of samples. The heatmap presents the average of all indexes between sample pairs from any two cancer types. (B) Distribution of order-level phylotypes across different tumor types. Relative abundances were calculated by summing up the reads of species that passed all filters in the different tumor types and belong to the same order. Orders are colored according to their associated phylum. (C) Unsupervised hierarchical clustering of the prevalence of 137 bacteria species that were hits in one of the tumor types and are present in 10% or more of the samples in at least one of the tumor types. (D) The prevalence of 19 bacteria from (C), displayed across the different tumor types. Only bacteria that are a hit in a given tumor type are represented with colored circles. Circle size indicates the prevalence level in samples. US, unknown species. (E) Bacterial taxa with a significant differential prevalence between different breast tumor subtypes are presented in a bar plot.  $P$  values were calculated using a two-sample proportion  $z$  test to compare between HER2+ ( $n = 61$ ) and HER2- ( $n = 247$ ), ER+ ( $n = 270$ ) and ER- ( $n = 49$ ), or triple negative (TNG) ( $n = 36$ ) and non-TNG ( $n = 284$ ) breast tumors. The direction of the bars indicates the enrichment direction. All bacteria presented had a false discovery rate (FDR)-corrected  $Q$  value  $< 0.25$ . US, unknown species; UG, unknown genus; UF, unknown family; (s), species; (g), genus; (f), family; (c), class. (F) Principal coordinate analysis (PCoA) biplot on the Jaccard similarity indexes between bacterial species profiles of the different tissue types. Only bacteria that passed all filters for the specific tissue type were considered. Tumor types and their normal tissue are grouped. (G) Volcano plot demonstrating the differential prevalence of bacteria between tumors (T) and their NAT in breast, lung, and ovary samples. A two-sample proportion  $z$  test was used to calculate the  $P$  values. Sizes of dots reflect phylotype levels, gradually increasing from species to phylum. Bacteria are colored according to the tumor type (breast, pink; lung, green; and ovary, purple) if they passed significance thresholds (effect size  $> 5\%$ ,  $P$  value  $< 0.05$ , and FDR-corrected  $Q$  value  $< 0.25$ ).

tumor type and across different tumor types revealed that the microbiomes of tumors of the same type tend to be more similar to each other than they are to the microbiomes of other tumor types (Fig. 4A and fig. S15). The distribution of order-level phylotypes revealed marked changes between the bacterial composition of the different tumor types (Fig. 4B and fig. S16). We added 22 colorectal tumors from one medical center to our cohort to help relate some of our findings to the known colorectal cancer microbiome (table S2) (11, 12). Consistent with previous reports, bacteria belonging to the Firmicutes and Bacteroidetes phyla were the most abundant species in colorectal tumors (Fig. 4B) (10). In contrast, Proteobacteria dominated the microbiome of pancreatic cancer, similarly to the normal duodenal microbiome makeup (16, 17, 48, 49). This may reflect a retrograde bacterial migration from the duodenum, to which the pancreatic duct opens, as we have previously reported (16). Although species belonging to the Proteobacteria and Firmicutes phyla accounted for most of the detected bacterial sequences in all cancer types, the Proteobacteria to Firmicutes (P/F) ratio appears to vary between tumor types (Fig. 4B). We also detected taxa of the Actinobacteria phylum, including the Corynebacteriaceae and Micrococcaceae families, mostly in nongastrointestinal tumors (Fig. 4B and fig. S16). These observations are in agreement with previous reports describing the microbiome of breast, lung, and ovarian cancer (2, 4, 6, 9, 14, 15, 18).

A tumor-type distinctive microbiome composition was also apparent at the species level. Unsupervised clustering of the most prevalent intratumor bacterial species ( $n = 137$  species) demonstrated that many of these species are enriched in certain tumor types (Fig. 4, C and D, and fig. S17). *Fusobacterium nucleatum*, previously reported to be enriched in colorectal tumors, was also a hit in our breast and pancreatic tumor cohorts (fig. S17). We also observed a distinct microbiome across subtypes of the same tumor type. For example, when comparing different subtypes of breast cancer according to their estrogen receptor (ER), progesterone receptor (PR), and HER2 status, we found multiple bacterial taxa whose prevalence was different between the subtypes (Fig. 4E and table S6). Lastly, although the overall microbial composition of the different tumor types was relatively similar to their NAT microbiome (Fig. 4F), we also detected bacteria with a different prevalence in tumors and in their NAT (Fig. 4G and table S7). Consistent with our observation that bacterial load and richness of breast tumors are higher than those in breast NAT (Fig. 3F and fig. S12), we found many bacteria that are significantly enriched in breast tumors compared with their NAT (Fig. 4G).

Metabolic functions encoded by intratumor bacteria are associated with clinical features of certain tumor subtypes

Our results demonstrate that intratumor bacteria span a wide spectrum of the bacterial kingdom. To investigate the functional activities of intratumor bacteria, we used the PICRUST2 tool (50–52) to map the 16S sequences to the genes and pathways that these bacterial species may harbor (fig. S18 and tables S8 and S9). Unsupervised clustering analysis of 287 predicted metabolic MetaCyc pathways that showed the greatest variability between the tumor types revealed that certain microbiome metabolic pathways were relatively specific to certain tumor types (Fig. 5A). We found a few tumor type-specific enrichments of bacterial pathways that can degrade metabolites known to be enriched in these same tumor types (table S10). For example, degradation of hydroxyprolines by bacteria (MetaCyc PWY-5159) was enriched in bone

tumors (effect size 14.6%,  $P$  value  $<0.01$ , proportion test). Bone collagen is a main source of hydroxyproline, and many bone pathologies, like bone tumors, have been shown to result in elevated hydroxyproline levels (53). In the case of lung cancer, MetaCyc pathways responsible for the degradation of chemicals in cigarette smoke, such as toluene, acrylonitrile, and aminobenzoates (TOLUENE-DEG-2-OH-PWY, P344-PWY, and PWY-6077), were significantly enriched in bacteria found in lung tumors compared with other tumor types (effect size 8.4, 8, and 7.2%,  $P$  value  $<0.001$  for all, proportion test). The enrichment for bacteria with the predicted capability to degrade cigarette smoke metabolites in lung tumors may suggest that high levels of these metabolites create a preferred niche for bacteria that can use these metabolites. To confirm this hypothesis, we compared the bacterial functions found in non-small cell lung cancers (NSCLCs) of 100 current

smokers with those in NSCLCs of 43 people who had never smoked (never-smokers). We found that 17 of the 49 MetaCyc pathways that were significantly enriched in tumors of current smokers were pathways that degrade chemicals found in cigarette smoke, such as nicotine, anthranilate, toluene, and phenol (Fig. 5B, blue circles, and table S11). We also found eight MetaCyc pathways related to the biosynthesis of metabolites that can be used by plants—for example, for the biosynthesis of glycine, a key intermediate in plant photorespiration (Fig. 5B, red circles, and table S11). We speculate that some plant-associated bacteria, or their DNA, are present in cigarette tobacco and are thus enriched in the lung tumors of smokers. To determine which bacteria contribute to the MetaCyc pathways that are enriched in the lung tumors of current smokers, we compared the proportion of all bacterial taxa found in

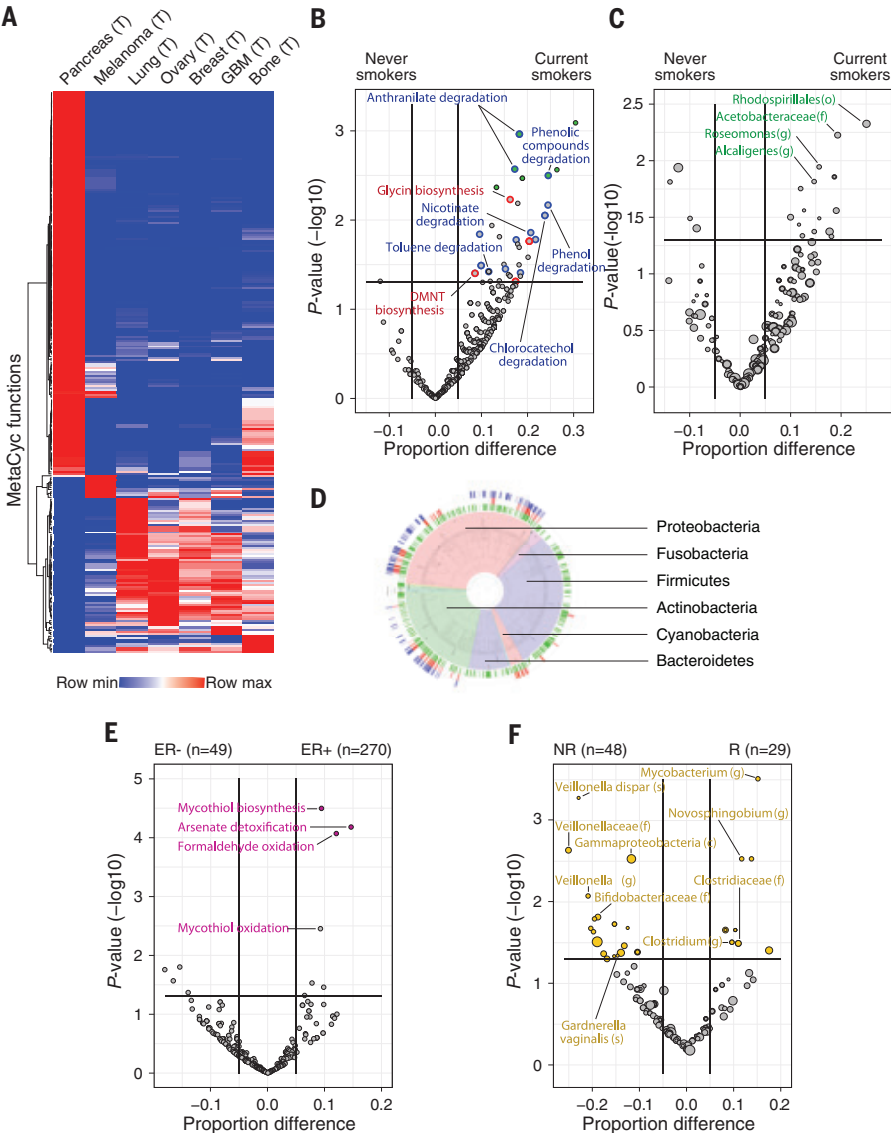


**Fig. 5. Predicted bacterial metabolic functions are associated with clinical features.** (A) Heatmap demonstrating unsupervised hierarchical clustering of the frequencies of 287 MetaCyc pathways across the different tumor types. Only pathways that are abundant (frequency  $>10\%$  in at least one tumor type) and variable (standard deviation divided by the average of frequencies  $>0.4$ ) were included (table S10). (B and C) Volcano plots demonstrating bacterial MetaCyc pathways (B) and taxa (C) that are enriched in lung tumors from smokers ( $n = 100$ ) versus never-smokers ( $n = 43$ ). Effect size represents the difference in the proportion between the groups. A two-sample proportion z test was used to calculate the  $P$  values. Green filled circles indicate pathways with FDR-corrected  $Q$  values  $<0.25$ . Degrading pathways of smoke chemicals are indicated by blue circles in (B); plant-related metabolic pathways are indicated by red circles in (B). (o), order. (D) Taxonomy wheel plot of bacterial species that contributed to degradation of cigarette smoke metabolites (blue ring) and to the biosynthesis of plant metabolites functions (red ring) are indicated on the phylogenetic tree, along with all bacteria that are hits in lung tumors (green ring). (E) Volcano plot demonstrating enriched bacterial MetaCyc functions in ER+ versus ER- breast tumors. A two-sample proportion z test was used to calculate the  $P$  values. Colored circles indicate pathways with FDR-corrected  $Q$  values  $<0.25$ . (F) Volcano plot demonstrating the bacterial taxa enriched in melanoma patients who responded (R) to immune checkpoint inhibitors (ICI) versus nonresponders (NR). A binomial test was used to calculate the  $P$  values for the enrichment or depletion of bacterial taxa in the responder cohort versus the non-responder cohort. The size of dots reflects phylo-type levels, gradually increasing from species to phylum. Colored circles indicate taxa with FDR-corrected  $Q$  values  $<0.25$ .

lung tumors of current smokers ( $n = 100$ ) with those in the tumors of never-smokers ( $n = 43$ ). We found that most of the enriched taxa in the lung tumors of smokers belong to the Proteobacteria phylum. However, none of these bacteria reached significance after correction for multiple-hypothesis testing (Fig. 5C and table S12), which indicates that there was no homogeneous population of species conferring this functionality across samples. We reasoned that, although bacterial ecology differs between tumors, there is a shared functional signal related to the specific environment within the lungs of smokers. We were able to demonstrate that a very large number of heterogeneous bacteria contribute to the degradation functions of cigarette smoke metabolites and the biosynthesis of plant metabolites (Fig. 5D). Bacteria expressing these functions are found mainly in the Proteobacteria, Actinobacteria, and Cyanobacteria phyla, and they are depleted from the Firmicutes phylum (Fig. 5D).

We also found selective enrichment of bacterial functions in certain tumor subtypes. For example, multiple MetaCyc pathways were enriched in bacteria from 270 ER+ breast tumors compared with 49 ER– breast tumors (Fig. 5E and table S13). The most significantly enriched pathways in bacteria within ER+ breast tumors were arsenate detoxification and mycothiol biosynthesis. Arsenic is a Group 1 carcinogen that can increase the risk of breast cancer (54) and has been shown to induce expression of the estrogen receptor in human breast cancer (55). Mycothiol is used by bacteria to detoxify reactive oxygen species (56). Because ER+ breast tumors are known to have increased oxidative stress compared with ER– tumors (57), we hypothesize that bacteria with the ability to synthesize mycothiol can better survive in the ER+ tumor microenvironment. We also found enrichment of bacterial functions when comparing breast tumor with NAT samples (table S14). For example, enzymes related to anaerobic respiration were enriched in bacteria from breast cancer versus NAT. Overall, our analysis of MetaCyc pathways suggests a connection between the functions of bacteria present in the tumor and their tumor microenvironment.

Lastly, as our IF staining suggests (Fig. 2), bacteria can be found inside CD45+ immune cells, which indicates that they might influence or reflect the immune state of the tumor microenvironment. To determine whether a specific intratumor microbial signature is correlated with the response to immunotherapy, we compared metastatic melanomas from patients who responded to immune checkpoint inhibitors (ICI) ( $n = 29$ ) with those from patients who did not respond ( $n = 48$ ). Although we did not find significant changes in the load of bacteria between responders and nonresponders to ICI, we did find multiple taxa that

were differentially more ( $n = 18$ ) or less ( $n = 28$ ) abundant in the melanomas of responders compared with nonresponders (Fig. 5F, fig. S19, and table S15). Taxa that were more abundant in tumors of responders included *Clostridium*, whereas *Gardnerella vaginalis* was more abundant in tumors of nonresponders. Notably, this is in line with differential abundances of taxa in the gut microbiome of melanoma patients responding to ICI (23–25).

## Discussion

In the present study, we characterized the microbiome of 1526 samples from seven human tumor types. We took multiple measures to minimize and control for contamination (supplementary note) and used our 5R multiplexed bacterial 16S rDNA PCR sequencing technique to gain species-level resolution.

The exploration of multiple tumor types with a single platform allowed us to compare different tumor types and uncover cancer type-specific microbial signatures. This is consistent with a recent publication that demonstrated that reexamination of whole-genome and whole-transcriptome sequencing data from The Cancer Genome Atlas (TCGA) for microbial sequences identified associations between different cancer types and specific microbiota (19). Extending our analysis to the functional level demonstrated that, despite a very large variation in taxa levels, certain tumor environments are enriched for common, relevant bacterial functional traits. This observation is somewhat analogous to the relative stability of the human gut microbiome functions compared with its microbial taxa (58, 59). Using multiple visualization methods and culturomics, we were able to validate the presence of bacteria in the tumors and demonstrate their intracellular localization in both cancer and immune cells.

Our data do not establish whether intratumor bacteria play a causal role in the development of cancer or whether their presence simply reflects infections of established tumors (60, 61). As tumors develop, their disorganized, leaky vasculature may allow circulating bacteria to enter, and the immunosuppressed environment may provide a refuge for them (61, 62). Intratumor bacteria may also arise from the NAT, which can explain the high similarity we found between the tumor microbiome and its NAT microbiome. Whether or not bacteria play a causal role in tumorigenesis, it is of interest to further explore the effects that intratumor bacteria may have on different phenotypes of cancer cells and on the immune system and its interactions with tumor cells. Just as manipulation of the gut microbiome has been shown to affect the response of tumors to immune-checkpoint blockade therapy (23–25, 28), we speculate that manipulation of the tumor microbiome may also affect tumor

immunity and the response to immune therapy. Thus, better understanding of these effects may pave the way for novel treatment options for cancer patients.

## REFERENCES AND NOTES

- C. de Martel et al., *Lancet Oncol.* **13**, 607–615 (2012).
- C. Xuan et al., *PLOS ONE* **9**, e83744 (2014).
- K. J. Thompson et al., *PLOS ONE* **12**, e0188873 (2017).
- S. Banerjee et al., *Front. Microbiol.* **9**, 951 (2018).
- L. Costantini et al., *Sci. Rep.* **8**, 16893 (2018).
- K. L. Greathouse et al., *Genome Biol.* **19**, 123 (2018).
- B. A. Peters et al., *Cancer Epidemiol. Biomark. Prev.* **28**, 731–740 (2019).
- P. Apostolou et al., *J. Cardiothorac. Surg.* **6**, 137 (2011).
- S. Banerjee et al., *Oncotarget* **8**, 36225–36245 (2017).
- Z. Gao, B. Guo, R. Gao, Q. Zhu, H. Qin, *Front. Microbiol.* **6**, 20 (2015).
- M. Castellari et al., *Genome Res.* **22**, 299–306 (2012).
- A. D. Kostic et al., *Genome Res.* **22**, 292–298 (2012).
- K. S. Stefanou et al., *Prostate* **68**, 306–320 (2008).
- C. Urbaniak et al., *Appl. Environ. Microbiol.* **82**, 5039–5048 (2016).
- C. Urbaniak et al., *Appl. Environ. Microbiol.* **80**, 3007–3014 (2014).
- L. T. Geller et al., *Science* **357**, 1156–1160 (2017).
- S. Pushalkar et al., *Cancer Discov.* **8**, 403–416 (2018).
- G. Yu et al., *Genome Biol.* **17**, 163 (2016).
- G. D. Poore et al., *Nature* **579**, 567–574 (2020).
- B. Goodman, H. Gardner, *J. Pathol.* **244**, 667–676 (2018).
- S. H. Wong et al., *Gastroenterology* **153**, 1621–1633.e6 (2017).
- A. D. Kostic et al., *Cell Host Microbe* **14**, 207–215 (2013).
- V. Gopalakrishnan et al., *Science* **359**, 97–103 (2018).
- V. Matson et al., *Science* **359**, 104–108 (2018).
- B. Routy et al., *Science* **359**, 91–97 (2018).
- S. Viaud et al., *Science* **342**, 971–976 (2013).
- N. Iida et al., *Science* **342**, 967–970 (2013).
- B. A. Helmink, M. A. W. Khan, A. Hermann, V. Gopalakrishnan, J. A. Wargo, *Nat. Med.* **25**, 377–388 (2019).
- M. R. Rutkowski et al., *Cancer Cell* **27**, 27–40 (2015).
- S. J. Salter et al., *BMC Biol.* **12**, 87 (2014).
- R. Eisenhofer et al., *Trends Microbiol.* **27**, 105–117 (2019).
- N. M. Davis, D. M. Proctor, S. P. Holmes, D. A. Relman, B. J. Callahan, *Microbiome* **6**, 226 (2018).
- M. C. de Goffau et al., *Nature* **572**, 329–334 (2019).
- M. L. Sogin et al., *Proc. Natl. Acad. Sci. U.S.A.* **103**, 12115–12120 (2006).
- C. R. H. Raetz, C. Whitfield, *Annu. Rev. Biochem.* **71**, 635–700 (2002).
- W. Fischer, in *New Comprehensive Biochemistry*, vol. 27, J.-M. Ghuyssen, R. Hakenbeck, Eds. (Elsevier, 1994), pp. 199–215.
- R. I. Amann et al., *Appl. Environ. Microbiol.* **56**, 1919–1925 (1990).
- C. Forestier, E. Moreno, J. Pizarro-Cerdá, J. P. Gorvel, *J. Immunol.* **162**, 6784–6791 (1999).
- K. T. Tokuyasu, *J. Microsc.* **143**, 139–149 (1986).
- A. Abada, S. Levin-Zaidman, Z. Porat, T. Dadosh, Z. Elazar, *Proc. Natl. Acad. Sci. U.S.A.* **114**, 12749–12754 (2017).
- E. Klieneberger-Nobel, *J. Gen. Microbiol.* **3**, 434–443 (1949).
- J. Errington, *Open Biol.* **3**, 120143 (2013).
- J. Errington, *Biochem. Soc. Trans.* **45**, 287–295 (2017).
- G. Fuks et al., *Microbiome* **6**, 17 (2018).
- T. Z. DeSantis et al., *Appl. Environ. Microbiol.* **72**, 5069–5072 (2006).
- J. T. Lau et al., *Genome Med.* **8**, 72 (2016).
- M. S. Siegrist et al., *ACS Chem. Biol.* **8**, 500–505 (2013).
- G. Ou et al., *Am. J. Gastroenterol.* **104**, 3058–3067 (2009).
- E. Nistal et al., *Inflamm. Bowel Dis.* **18**, 649–656 (2012).
- G. M. Douglas et al., PICRUSt2: An improved and extensible approach for metagenome inference. *bioRxiv* 672295 [Preprint]. 15 June 2019. [www.biorxiv.org/content/10.1101/672295v1](https://www.biorxiv.org/content/10.1101/672295v1).
- Y. Ye, T. G. Doak, *PLOS Comput. Biol.* **5**, e1000465 (2009).
- S. Louca, M. Doebeli, *Bioinformatics* **34**, 1053–1055 (2018).
- M. Nakagawa, Y. Sugiura, T. Oshima, G. Kajino, H. Hirako, *Nagoya J. Med. Sci.* **29**, 345–367 (1967).
- N. Khanjani, A.-B. Jafarnejad, L. Tavakkoli, *Rev. Environ. Health* **32**, 267–277 (2017).
- J. Du et al., *PLOS ONE* **7**, e35957 (2012).
- A. M. Reyes et al., *Antioxid. Redox Signal.* **28**, 487–504 (2018).

57. P. Karihtala, S. Kauppila, Y. Soini, Arja-Jukkola-Vuorinen, *BMC Cancer* **11**, 262 (2011).
58. Human Microbiome Project Consortium, *Nature* **486**, 207–214 (2012).
59. A. Eng, E. Borenstein, *Microbiome* **6**, 45 (2018).
60. J. L. Pope, S. Tomkovich, Y. Yang, C. Jobin, *Transl. Res.* **179**, 139–154 (2017).
61. J. Cummins, M. Tangney, *Infect. Agent. Cancer* **8**, 11 (2013).
62. C. K. Baban, M. Cronin, D. O'Hanlon, G. C. O'Sullivan, M. Tangney, *Bioeng. Bugs* **1**, 385–394 (2010).
63. N. Shental, NoamShental/5R: First release, April 2020, version v1.0, Zenodo (2020); <http://doi.org/10.5281/zenodo.3740525>.
64. I. Liviyatan, iliviyatan/TMB: TMB for Science publication, version science\_pub, Zenodo (2020); <http://doi.org/10.5281/zenodo.3740536>.

## ACKNOWLEDGMENTS

We thank all members of the Straussman laboratory as well as E. Elinav, D. Douek, U. Gophna, and R. Kolter for fruitful discussions. **Funding:** R.St. is funded by the Israel Science Foundation (grant no. 2044/17), the Binational Science Foundation (grant no. 2013332), the European Research Council (ERC) under the European Union's Horizon 2020 research and innovation program (grant agreement no. 818086), the Fabrikant-Morse Families Research Fund for Humanity, the Chantal d'Adesky Scheinberg Research Fund, the Moross Integrated Cancer Center, the Rising Tide Foundation, the International Collaboration Grant from the Jacki and Bruce Barron Cancer Research Scholars' Program, and a partnership of the Israel Cancer Research Fund and City of Hope (COH), as supported by The Harvey L. Miller Family Foundation. R.St. is the incumbent of the Roel C. Buck Career Development Chair. N.S. is funded by the Ministry of Science, Technology and Space, Israel (grant no. 3-11174). Research reported in this publication included work performed in the COH Pathology Research Services Core supported by the National Cancer Institute of the National Institutes of Health under award no. P30CA033572. The content is solely the responsibility of the authors and does not necessarily represent the official views of the National Institutes of Health. A.P.C. is supported by the Cancer Prevention and Research Institute of Texas Research Training Program (RP170067). **Author contributions:** D.N., I.L., G.F., N.S., and R.St. conceived and initiated the project and performed most of the data analysis. I.L., G.F., and O.G. wrote data analysis code. D.N., N.G., and Y.Z. performed staining experiments. D.N., L.T.G., and A.R.-M. generated sequencing data. R.W. and N.G. performed the culturomics experiments. A.W., M.L.-P., Y.B., L.T.G., A.R.-M., E.G., A.M., and E.S. contributed to the culturomics experiment. G.M.D., M.G.I.L., and I.L. were responsible for transforming bacterial species into functions using PICRUSt 2. I.L. and T.A. generated GraPhlAn analysis. T.Da. and S.L.-Z. performed CLEM experiments. R.St., D.N., I.L., and N.S. wrote the initial manuscript. G.F., N.G., and Y.Z. helped with preparations of the manuscript. J.S., I.K., V.G., S.A., G.P., M.R., Z.A.C., R.A., A.P.C., M.A.W.K., G.O., K.B.-S., S.H., T.S., E.A.R., C.U.B., A.R., R.Sh., A.A., T.Do., R.K., Z.R.C., E.N.G.-Y., E.Y.-S., H.S., N.B., A.B.-N., B.K., A.N., T.G., M.D., K.L., J.B., S.Y.-K., I.B., D.S.P., R.W., J.A.W., and D.J.R. provided patient samples. J.S. and G.M. helped with pathological analysis. R.St. supervised the project. **Competing interests:** R.St. received a grant from Merck EMD Serono and is a paid adviser to Biomica and BiomX. R.St., N.S., D.N., I.L., and G.F. are inventors on a U.S. provisional patent application (63/005,540) submitted by Yeda Research and Development, the Weizmann Institute of Science. J.A.W. and V.G. are inventors on a U.S. patent application (PCT/US17/53,717) submitted by the University of Texas MD Anderson Cancer Center that covers methods to enhance immune checkpoint blockade responses by modulating the microbiome. J.A.W. reports compensation for speaker's bureau and honoraria from Immedex, Dava Oncology, Omniprex, Illumina, Gilead, PeerView, Physician Education Resource, MedImmune, and Bristol-Myers Squibb. J.A.W. serves as a consultant and advisory board member for Roche/Genentech, Novartis, AstraZeneca, GlaxoSmithKline, Bristol-Myers Squibb, Merck, Biothera Pharmaceuticals, and Microbiome DX. J.A.W. also receives research support from GlaxoSmithKline, Roche/Genentech, Bristol-Myers Squibb, and Novartis. **Data and materials availability:** Breast and colon samples from Sheba; melanoma samples from the Netherlands Cancer Institute–Antoni van Leeuwenhoekziekenhuis (NKI-AVL); and lung, breast, ovary, and GBM samples from the Israeli Biorepository Network for Research (MIDGAM) are available from R.St. under material transfer agreements with the Weizmann Institute. All processed data are available in the manuscript or the supplementary materials. The software package for applying SMURF using the 5R primers is available at Zenodo (63). The implementation code for the

16S sequencing analysis pipeline with filters can be found at Zenodo (64). Bacterial 16S sequencing data are available from the National Center for Biotechnology Information BioProject database under accession no. PRJNA624822.

## SUPPLEMENTARY MATERIALS

science.sciencemag.org/content/368/6494/973/suppl/DC1  
Supplementary Note  
Materials and Methods

Figs. S1 to S19  
Tables S1 to S15  
References (65–76)  
MDAR Reproducibility Checklist

29 July 2019; resubmitted 22 January 2020  
Accepted 14 April 2020  
10.1126/science.aay9189

## PEPTIDE SYNTHESIS

# Synthesis of proteins by automated flow chemistry

N. Hartrampf<sup>1\*</sup>, A. Saebi<sup>1†</sup>, M. Poskus<sup>1‡</sup>, Z. P. Gates<sup>1‡</sup>, A. J. Callahan<sup>1</sup>, A. E. Cowfer<sup>1</sup>, S. Hanna<sup>1</sup>, S. Antilla<sup>1,2</sup>, C. K. Schissel<sup>1</sup>, A. J. Quartararo<sup>1</sup>, X. Ye<sup>1</sup>, A. J. Mijalis<sup>1§</sup>, M. D. Simon<sup>1¶</sup>, A. Loas<sup>1</sup>, S. Liu<sup>1#</sup>, C. Jessen<sup>3</sup>, T. E. Nielsen<sup>3</sup>, B. L. Pentelute<sup>1,\*\*\*</sup>

Ribosomes can produce proteins in minutes and are largely constrained to proteinogenic amino acids. Here, we report highly efficient chemistry matched with an automated fast-flow instrument for the direct manufacturing of peptide chains up to 164 amino acids long over 327 consecutive reactions. The machine is rapid: Peptide chain elongation is complete in hours. We demonstrate the utility of this approach by the chemical synthesis of nine different protein chains that represent enzymes, structural units, and regulatory factors. After purification and folding, the synthetic materials display biophysical and enzymatic properties comparable to the biologically expressed proteins. High-fidelity automated flow chemistry is an alternative for producing single-domain proteins without the ribosome.

**M**echanical pumps, valves, solid supports, and computers have transformed the way we perform chemical reactions. Continuous, multistep flow technology has enabled routine access to small molecules ranging from pharmaceutical ingredients to natural products and bulk commodities (1). Advantages of flow synthesis over batch methods are in-line spectroscopic monitoring, efficient mixing, and precise control over the reaction parameters (2). Translating these capabilities to the total chemical synthesis of peptides and proteins will provide rapid access to an expanded chemical space.

Protein production is an essential part of research in academia and industry and can be accomplished by biological methods or chemical synthesis. Most proteins are obtained by biological expression, a process that largely lim-

its their chemical composition to the canonical proteinogenic amino acids (3). Advances in genetic code expansion have allowed for the incorporation of up to two unnatural amino acids in the structures of native proteins (4). By contrast, chemical synthesis offers unmatched flexibility when incorporation of multiple unnatural amino acids, posttranslational modifications, or artificial backbones is desired (3). Synthetic proteins have become accessible with a combination of solid-phase and ligation methodologies. Yet, total chemical synthesis of proteins remains highly labor intensive.

Solid-phase peptide synthesis (SPPS) is the foundation of chemical peptide and protein production (5). Despite decades of optimization, peptides longer than 50 amino acids are difficult to synthesize with standard SPPS instrumentation, owing in large part to generation of by-products from deletion, truncation, and aggregation of the growing chains (6, 7). It was not until the development of native chemical ligation (NCL) that chemical synthesis of protein chains became practical (8). Despite the efforts dedicated to improving NCL techniques (9), a major bottleneck resides in the absence of a routine, widely applicable protocol to access the requisite peptide fragments (10, 11). We set out to address this problem by developing a reliable method to synthesize long peptides and protein chains using flow chemistry.

Flow-based SPPS is gaining momentum owing to its advantageous features—for example, control over physical parameters and greatly reduced formation of side products (12–14). Studies carried out as early as 1970

<sup>1</sup>Department of Chemistry, Massachusetts Institute of Technology, 77 Massachusetts Avenue, Cambridge, MA 02139, USA. <sup>2</sup>Department of Materials Science and Engineering, Massachusetts Institute of Technology, 77 Massachusetts Avenue, Cambridge, MA 02139, USA.

<sup>3</sup>Novo Nordisk A/S, Novo Nordisk Park, DK-2760 Måløv, Denmark.

\*Present address: Department of Chemistry, University of Zurich, Winterthurerstrasse 190, 8057 Zurich, Switzerland.

†These authors contributed equally to this work.

‡Present address: p53Lab, Agency for Science, Technology and Research (A\*STAR), 8A Biomedical Grove, Singapore 138648, Singapore.

§Present address: Department of Genetics, Harvard Medical School, 77 Avenue Louis Pasteur, Boston, MA 02115, USA.

¶Present address: Ginkgo Bioworks, 27 Drydock Avenue, Boston, MA 02210, USA.

#Present address: Department of Chemistry, East China Normal University, 3663 North Zhongshan Road, Shanghai 200062, China.

\*\*\*Corresponding author. Email: blp@mit.edu



found that automation and high fidelity of peptide synthesis could be achieved by containing the solid support in a reactor and operating it as a fixed bed (15, 16). Instead of complex systems for liquid handling to dispense reagents and wash the resin, high-performance liquid chromatography (HPLC) pumps were used to continuously deliver reagents, establishing the principles of peptide synthesis in flow. Inspired by this early work, over the past 5 years we developed rapid, automated fast-flow peptide synthesis (AFPS) instrumentation that incorporates amino acid residues in as little as 40 s at temperatures up to 90°C (17–19).

Even though prior work by us and others on flow-based SPPS considerably reduced the total synthesis time, the potential of flow chemistry to enable synthesis of peptide chains in

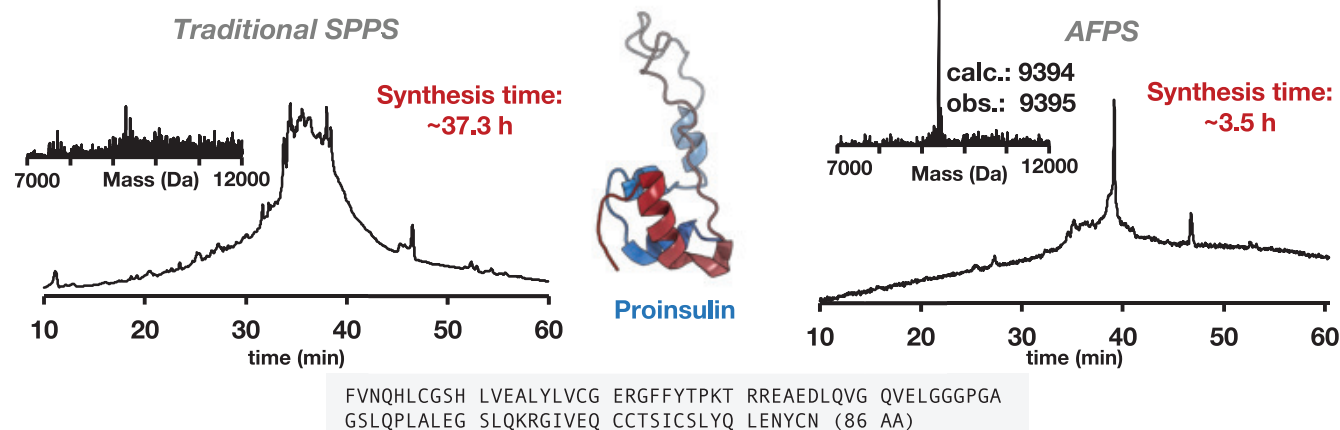
the range of single-domain proteins has not been fully realized (17–23). We set out to optimize our AFPS technology to meet this challenge (19). We report here a routine protocol that allows for stepwise chemical total synthesis of peptide chains exceeding 50 amino acids in length, with a cycle time of ~2.5 min per amino acid (Fig. 1A). The optimized protocol was built on a collection of analytical data acquired with an AFPS system and delivers products with high fidelity and of high chiral purity. Using this protocol, single-domain protein chains ranging from barstar (90 amino acids) to sortase A<sub>59–206</sub> (sortase A\*, 164 amino acids) were synthesized in 3.5 to 6.5 hours. To demonstrate production of functional proteins, these sequences were folded, and their biophysical properties and enzymatic activities were determined. The time scale of chemical

protein synthesis is on par with that of recombinant expression and therefore offers a practical alternative to biochemical methods while opening up the chemical space beyond canonical amino acids.

### Rapid screening of reaction variables for AFPS protocol development

We chose to first optimize coupling efficiency and later investigate possible side reactions induced by the optimized coupling conditions. On a benchmark AFPS instrument previously developed in our laboratory (17, 19), reagents are mixed, heated, and delivered onto a pre-tempered solid support using three HPLC pumps. In-line ultraviolet-visible (UV-vis) detection of the reactor eluent is used to monitor removal of the N-terminal protecting group after each coupling cycle. Indirectly, this

## A Traditional SPPS vs. AFPS, analytical data for crude proinsulin



## B Traditional SPPS vs. AFPS, analytical data for crude HIV-1 protease

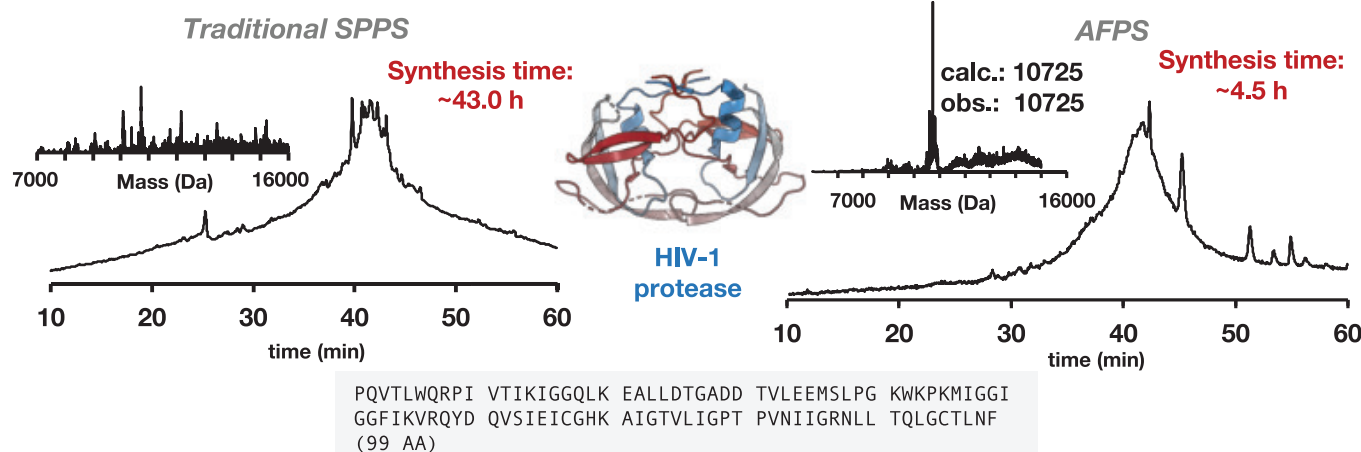


**Fig. 2. Synthesis of proinsulin and HIV-1 protease demonstrates the advantage of AFPS over traditional SPPS methods.** (A and B) Analytical HPLC data of the crude proinsulin (A) and HIV-1 protease (B) are presented as the main chromatographic traces with absorbance detection at 214 nm (additional details in the SM). Deconvoluted masses are displayed in the insets. Analytical data for the synthesis of crude protein chain using SPPS on a commercially available synthesizer at 70°C with total cycle times of 26 min per amino acid and

40 equivalents of amino acid for each coupling are displayed on the left; analytical data for the synthesis of crude protein chain using AFPS at 90°C with 60 equivalents of amino acid for each coupling are displayed on the right. PDB 2KQP (proinsulin) (58) and 2JE4 (HIV-1 protease dimer with inhibitor, not identical to the sequence synthesized) (30) were used. Crude material of higher quality was obtained in the case of HIV-1 protease by substitution of Cys and Met residues, as described in SM section 5. AA, amino acids.

information reports on the efficiency of the preceding coupling step.

We first optimized general parameters, including flow rate, reaction solvent, reagent concentration, temperature, and coupling agents (Fig. 1B and tables S1 to S7). Modifications to our original AFPS protocol included increasing reagent concentrations to 0.4 M (24), the use of amine-free *N,N*-dimethylformamide (DMF), and an increase in temperature to 85° to 90°C for reagent activation and coupling. The performance of different activators for the coupling step was also investigated, identifying the azabenzotriazol-reagents PyAOP [(7-azabenzotriazol-1-yloxy)tripyrrolidinophosphonium hexafluorophosphate] and HATU (hexafluorophosphate azabenzotriazole tetramethyl uranium) as optimal.

Automated collection and analysis of data combined with the synthesis parameters allowed for optimization of residue-specific coupling conditions. By comparing data on amino acid deprotections, we were able to gain information on coupling efficiency for all canonical amino acids and generated a general amino acid-specific recipe (tables S8 and S9). Analytical comparison of the products obtained for glucagon-like peptide-1 (GLP-1) is illustrative of the improvement in crude peptide quality achieved with the optimized synthesis conditions (Fig. 1B).

We aimed to suppress aspartimide formation, a major side reaction in SPPS and AFPS. Because increased temperature leads to more aspartimide formation, various deprotection bases, additives, and aspartic acid protecting groups were screened to minimize this unwanted side reaction (25, 26). We found that milder deprotection bases [i.e., piperazine and 1-hydroxybenzotriazole (HOBt) with piperidine] and bulky aspartic acid protecting groups [i.e., *O*-3-methylpent-3-yl (OMpe)] decreased the level of aspartimide formation (fig. S3 and table S10). The most effective strategies, however, were the addition of formic acid as a piperidine additive and backbone protection with dimethoxybenzyl glycine. Formic acid (2% stock solution in 40:60 v/v piperidine:DMF) was therefore used as an additive for deprotection, and backbone protection was applied for collagen and fibroblast growth factor 1 (FGF1) syntheses.

We confirmed retention of chirality for amino acids at high risk of epimerization (i.e., cysteine and histidine) in a final optimization step (figs. S4 to S9) (27). The influence of temperature, time, and activating agent, as well as different side-chain protecting groups were screened (Fig. 1, C and D) (17). For both amino acids, epimerization increases with activation time and temperature. The choice of protecting group proved to be critical for histidine. Ultimately, activation of Fmoc-Cys(Trt)-OH and Fmoc-His(Boc)-OH with PyAOP with a shorter

time at 60°C resulted in <2% D-epimer formation (Fmoc, fluorenylmethoxycarbonyl; Trt, trityl; Boc, *tert*-butoxycarbonyl). Next, we determined that the amount of epimerization under these optimized conditions does not increase over multiple coupling cycles (Fig. 1E). The amount of D-isomer did not change over 100 amino acid couplings executed after manual capping of the N-terminus, indicating that epimerization of cysteine and histidine only occurs during the activation step. Implementation of these conditions allowed us to solidify the general AFPS protocol, which was then applied to the production of sequences exceeding 50 amino acids [table S11 and supplementary materials (SM) section 3.10].

### Optimized AFPS outperforms traditional synthesis methods

We investigated if our optimized AFPS conditions could facilitate the synthesis of longer sequences using proinsulin (86 amino acids) and human immunodeficiency virus-1 (HIV-1) protease (99 amino acids) as test sequences. The total synthesis of human proinsulin was previously reported using NCL of three peptide fragments individually prepared by SPPS (28). HIV-1 protease was previously prepared using stepwise and chemical ligation routes under Boc-SPPS conditions (29, 30). Using our standard AFPS protocol, the syntheses of proinsulin and HIV-1 protease were completed in 3.5 and 4.5 hours, respectively. HPLC purification yielded 2.2 mg (1%) of purified proinsulin and 5.3 mg (1%) of purified HIV-1 protease.

A comparison between AFPS and standard batch SPPS syntheses on commercially available synthesizers at room temperature, 70°C, and 90°C indicated substantially improved synthetic outcome for the optimized AFPS protocol (Fig. 2 and SM section 4). On each instrument, machine-specific, optimized conditions were used to achieve the best synthesis outcome. For HIV-1 protease and proinsulin, AFPS yielded the desired product as the major species along with minor by-products of similar weight, as determined by analytical HPLC and liquid chromatography-mass spectrometry (LC-MS). By contrast, synthesis on commercially available peptide synthesizers took approximately five times longer and resulted in a complex compound mixture. AFPS therefore offers a substantial improvement when directly compared with traditional SPPS methods, both with respect to time and performance.

### Optimized AFPS enables routine access to single-domain protein chains

To demonstrate general applicability of our AFPS protocol, the synthesis of additional protein chains ranging from ~70 to ~170 amino acids was performed (Fig. 3A and SM section 5). These sequences were chosen to enable com-

parison with literature data. We chose not only historically relevant targets for drug discovery, such as HIV-1 protease and murine double minute 2 (MDM2) (31, 32), but also proteins that serve as therapeutics themselves, such as FGF1 and proinsulin (33, 34). Barstar, barnase, lysozyme, MDM2, and sortase A\* allowed for a direct comparison of recombinant and synthetic proteins. The ability of AFPS technology to rapidly and simultaneously incorporate noncanonical amino acids in greater number and of greater diversity than biological methods was tested by synthesizing derivatives of barnase and HIV-1 protease containing site-directed mutations. In the case of barnase, we incorporated *p*-bromophenylalanine at a site previously investigated for mutational tolerance (35). Then, we produced synthetic HIV-1 protease in which two methionine and one cysteine residues were replaced as previously described with norleucine and aminobutyric acid, respectively (Fig. 3B), to avoid potential oxidation side products and increase synthetic efficiency (30). All sequences were successfully synthesized in 3.5 to 6.5 hours.

The desired protein was the main product in every synthesis, and HPLC purification yielded milligram quantities of product. Isolated yields after HPLC purification ranged from 2.2 to 19.0 mg (1 to 5%), a sufficient amount of material for folding and evaluation of tertiary structure and biological function (Fig. 3B and SM section 5). In conclusion, optimized AFPS allows for the routine stepwise chemical synthesis of peptide chains of up to ~170 amino acids and therefore substantially decreases time and labor associated with the chemical production of single-domain proteins.

### The structure and function of folded synthetic proteins are comparable to recombinant samples

Determining the purity of long synthetic peptides is challenging because of difficulties associated with identification and quantification of by-products by standard analytical techniques. In a physiological environment, the native folded structure of a globular protein, which gives rise to its distinctive biological activity, is determined by its amino acid sequence (36). As a consequence, the tertiary structure of a protein can be used as a measure of the chemical integrity of the primary amino acid sequence (37).

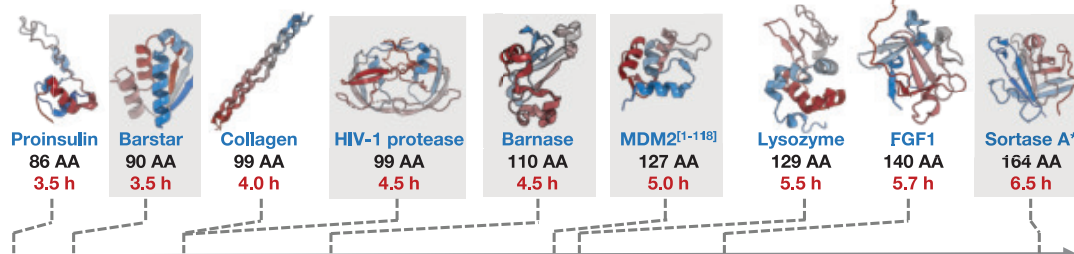
We folded and purified selected synthetic proteins by size exclusion chromatography and ion exchange chromatography and characterized their tertiary structure with biophysical and functional assays, alongside recombinant protein standards. Our goal was to demonstrate the fidelity of our AFPS protocol in delivering synthetic proteins of defined covalent structure and high chiral integrity. To this aim, we thoroughly characterized barnase and further

investigated barstar, sortase A\*, MDM2, and HIV-1 protease. Folding of the synthetic proteins was case-specific and was achieved either by following a literature protocol or by screening various conditions.

Chemical denaturation is diagnostic for assessing structural integrity and stability of synthetic proteins. The globular protein barnase, a bacterial ribonuclease (RNase) isolated from *Bacillus amyloliquefaciens*, is a model system

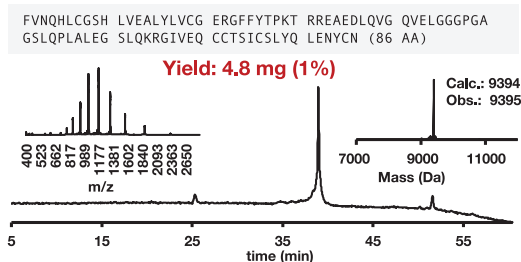
to investigate protein folding, denaturation, and binding to its inhibitor protein barstar (Fig. 4A) (38, 39). The primary structures of synthetic and recombinant barnase were indistinguishable by LC-MS and HPLC methods

## A Single domain proteins synthesized using AFPS

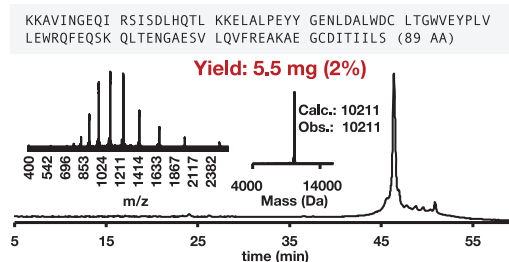


## B Analytical data

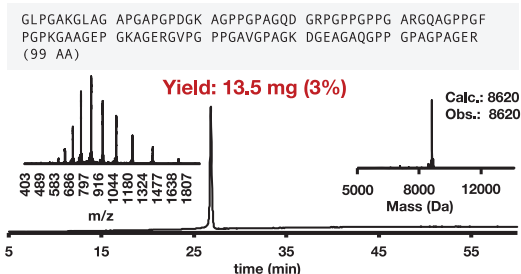
### Proinsulin



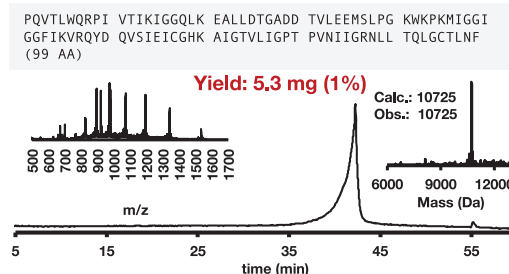
### Barstar



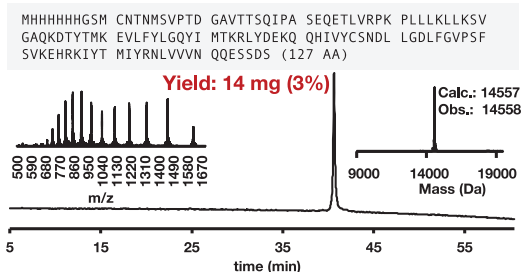
### Collagen



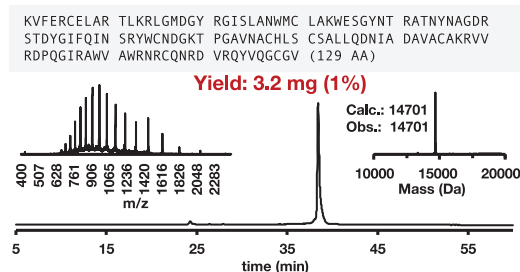
### HIV-1 protease



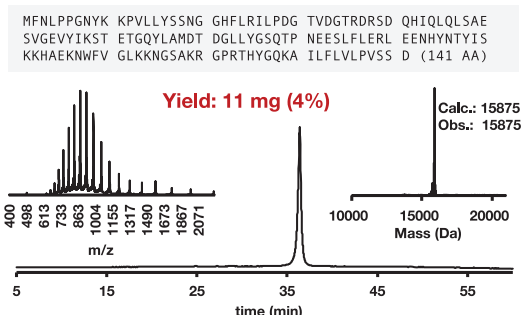
### MDM2[1-118]



### Lysozyme



### FGF1



### Sortase A\*

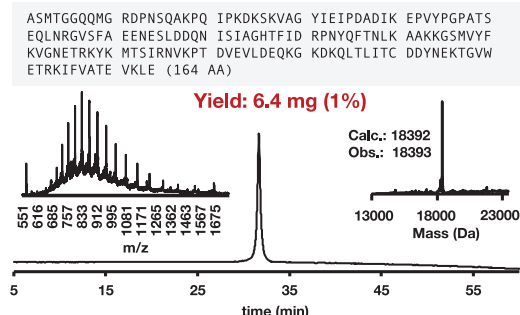


## Fig. 3. AFPS enables high-fidelity production of long amino acid sequences in hours.

(A) Sequences produced using an AFPS instrument. Sequences highlighted in gray were folded and purified, and their structure and biological activity were evaluated. All sequences were synthesized using the same standard recipe. PDB 1AY7 (barstar) (59), 2KQP (proinsulin) (58), 1CGD (collagen) (60), 2JE4 (HIV-1 protease dimer with inhibitor) (30), 1BRS (barnase) (57), 3G03 (MDM2) (61), 2NWD (lysozyme) (62), 4Q9G (FGF1) (63), and 2KID (sortase A) (64) were used. (B) Analytical data for the purified sequences of proinsulin, barstar, collagen, HIV-1 protease, MDM2<sup>[1-118]</sup>, lysozyme, FGF1, and sortase A\*. For all cases, analytical HPLC data of the purified protein chains are presented as the main chromatographic trace with absorbance detection at 214 nm. The gradient for analytical HPLC was 5 to 65% B. A linear gradient of acetonitrile with 0.08% trifluoroacetic acid (TFA) added (solvent B) in water with 0.1% TFA added (solvent A) was used in all cases. Electrospray ionization (ESI) mass spectrum (upper left) and deconvoluted mass spectrum (upper right) are also shown in each case. Both spectra were obtained by summation of the entire LC peak; additional details on purification and analytical methods are in the SM section 5.

(Fig. 4B). We used a chemical denaturation fluorometric assay as a readout for the integrity of the tertiary structure (Fig. 4C). In this assay, tryptophan fluorescence was used to monitor the folding equilibrium, as the concentration of urea was varied. Synthetic

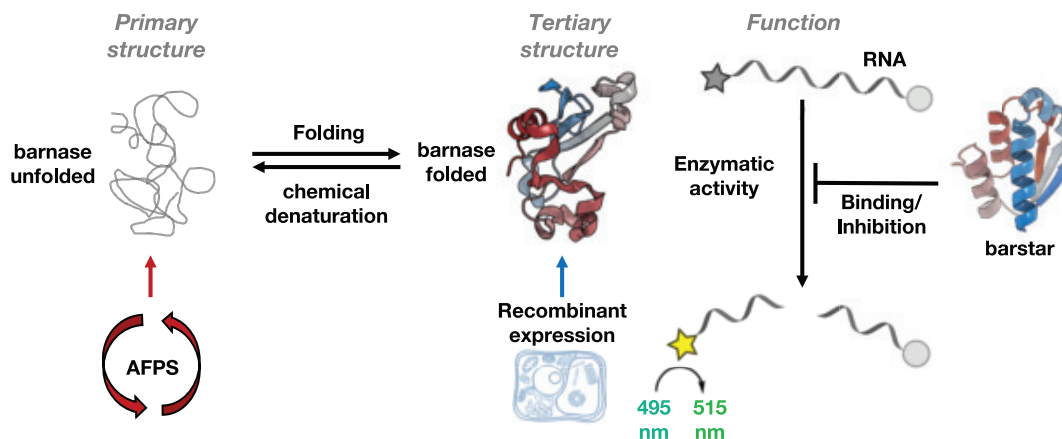
barnase exhibited a transition midpoint (the concentration at which half of the sample is unfolded,  $[D]_{50\%}$ ) that compared well to both the authentic recombinant sample and literature value  $\{[D]_{50\%, \text{synthetic}} = 4.68 \pm 0.06 \text{ M}; [D]_{50\%, \text{recombinant}} = 4.63 \pm 0.04 \text{ M (mean} \pm \text{SE)}\}$ ;

$[D]_{50\%, \text{literature}} = 4.57 \text{ M}\}$  (39). More importantly, the  $m$  values obtained in the experiment, which describe the slope of the unfolding transition and are a sensitive measure of structural homogeneity, were similar  $[m_{\text{synthetic}} = 1.82 \pm 0.25 \text{ kcal mol}^{-1} \text{ M}^{-1}; m_{\text{recombinant}} = 1.88 \pm$

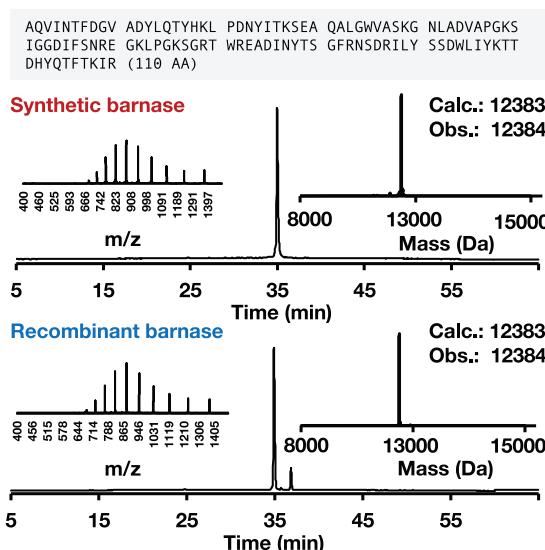
**Fig. 4. Synthetic barnase and synthetic barstar fold into the native tertiary structure and display enzymatic activity comparable to recombinant samples.**

(A) Conceptual overview of production and analysis methods. (B) Comparison of primary structures obtained from AFPS and recombinant expression. For both cases, analytical HPLC data of the purified barnase are presented as the main chromatographic trace with absorbance detection at 214 nm (additional details in the SM). ESI mass spectrum and deconvoluted mass spectrum of the purified peptide samples are displayed in the upper-left and the upper-right insets, respectively. Both spectra were obtained by summation over the entire LC peak in the chromatogram. (C) Structural evaluation of barnase in a chemical denaturation assay using urea as denaturant performed in triplicate; results are reported as mean  $\pm$  SE. Error bars on the graph indicate SE. (D) Quantitative enzymatic activity assay performed in triplicate; error bars are not displayed for clarity. Details are outlined in the SM.  $k_{\text{cat}}/K_M$  values are reported as mean  $\pm$  SE. (E) Barnase inhibition and binding assay using recombinant and synthetic barstar. 3.4 nM barnase was used in all conditions. Details are outlined in the SM. PDB 1BRS (barnase) (57) and 1AY7 (barstar) (59) were used.

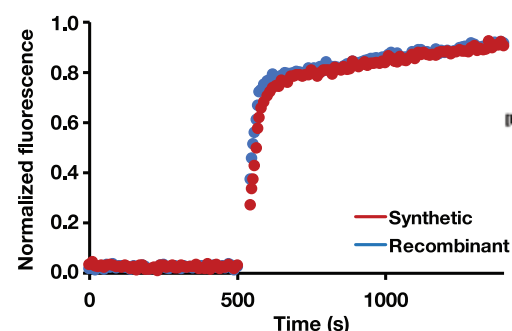
#### A Production, structure and function of barnase



#### B Analysis of primary structure

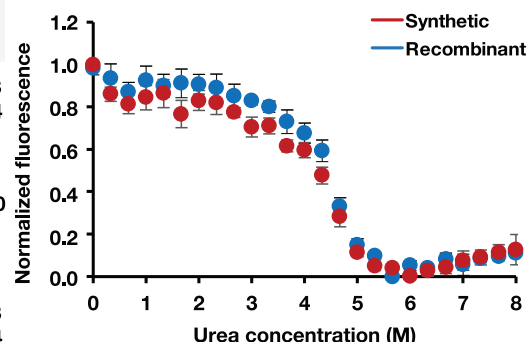


#### D Fluorogenic activity assay



**Synth. barnase:**  $k_{\text{cat}}/K_M = (7.6 \pm 0.2) \times 10^6 \text{ M}^{-1} \text{ s}^{-1}$   
**Rec. barnase:**  $k_{\text{cat}}/K_M = (9.0 \pm 0.3) \times 10^6 \text{ M}^{-1} \text{ s}^{-1}$   
**Literature:**  $k_{\text{cat}}/K_M = (1.3 \pm 0.4) \times 10^7 \text{ M}^{-1} \text{ s}^{-1}$

#### C Chemical denaturation of synthetic barnase



**Synth. barnase:**  $m = 1.82 \pm 0.25 \text{ kcal mol}^{-1} \text{ M}^{-1}$   
 $[D]_{50\%} = 4.68 \pm 0.06 \text{ M}$   
**Rec. barnase:**  $m = 1.88 \pm 0.21 \text{ kcal mol}^{-1} \text{ M}^{-1}$   
 $[D]_{50\%} = 4.63 \pm 0.04 \text{ M}$   
**Literature:**  $m = 2.06 \text{ kcal mol}^{-1} \text{ M}^{-1}$   
 $[D]_{50\%} = 4.57 \text{ M}$

#### E Barstar inhibits barnase activity

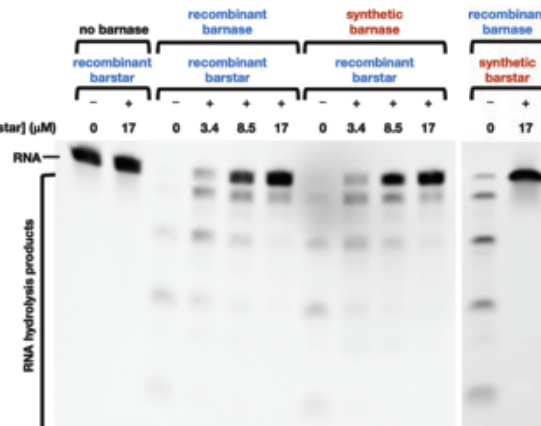
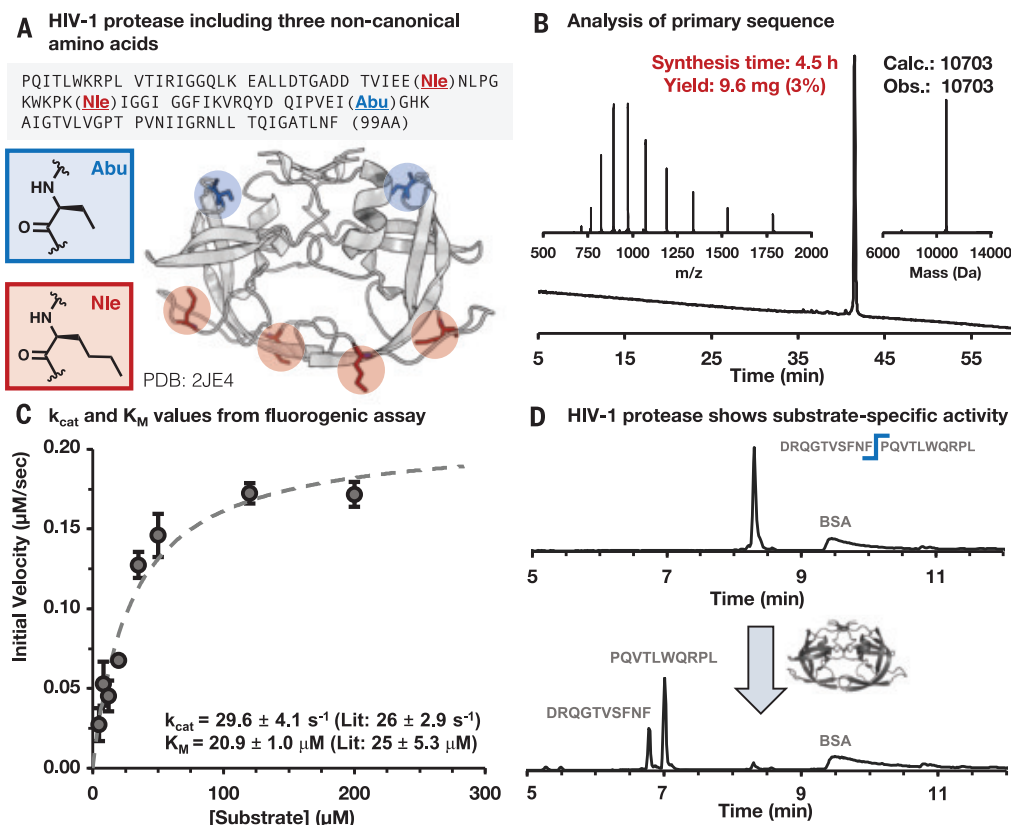


**Fig. 5. Synthetic HIV-1 protease containing three noncanonical amino acids folds into the native dimer structure and displays enzymatic activity and substrate specificity comparable to literature samples. (A)** Crystal structure of HIV-1 protease dimer with highlighted noncanonical amino acids aminobutyric acid (Abu, blue) and norleucine (Nle, red). PDB 2JE4 (HIV-1 protease dimer with inhibitor) (30) was used. **(B)** Primary structure obtained from AFPS. Analytical HPLC data of the purified HIV-1 protease is presented as the main chromatographic trace with absorbance detection at 214 nm (additional details in the SM). ESI mass spectrum and deconvoluted mass spectrum of the purified sample are displayed in the upper-left and the upper-right insets, respectively. Both spectra were obtained by summation over the entire LC peak in the chromatogram. **(C)** Quantitative enzymatic activity assay performed in triplicate for the determination of  $k_{cat}$  and  $K_M$  values. Results are reported as mean  $\pm$  SE. Error bars on the graph indicate SE. Lit., literature. **(D)** Qualitative substrate specificity assay with model substrate p12nt, in which HIV-1 protease exclusively cleaves at a single Phe-Pro site whereas bovine serum albumin (BSA) stays intact; details are outlined in the SM.



0.21 kcal mol<sup>-1</sup> M<sup>-1</sup> (mean  $\pm$  SE);  $m_{\text{literature}} = 2.06$  kcal mol<sup>-1</sup> M<sup>-1</sup>] (39). If the synthetic protein were microheterogeneous (e.g., contained a distribution of isomers or deletion coproducts), then the apparent  $m$  value may be altered owing to the distribution of  $[D]_{50\%}$  values represented within the mixture. Therefore, because the synthetic sample exhibited an  $m$  value within the error of the recombinant sample, we concluded that microheterogeneity was negligible.

Enzymatic assays show comparable activity of synthetic proteins obtained by AFPS and their recombinant equivalents. Enzymatic catalysis is sensitive to minor changes in the enzyme's tertiary structure, for which even single point mutations can have a major impact (40, 41). We evaluated the native activity of three synthetic variants of well-studied enzymes: barnase, HIV-1 protease, and sortase A\*. Barnase catalyzes hydrolysis at diribonucleotide GpN sites. Its specific activity can be measured by monitoring hydrolysis of a DNA-RNA hybrid containing a Förster resonance energy transfer fluorophore pair (42). The enzymatic efficiency of synthetic barnase was  $k_{cat}/K_M = (7.6 \pm 0.2) \times 10^6$  M<sup>-1</sup> s<sup>-1</sup> (mean  $\pm$  SE), which is comparable to that of recombinant barnase [ $k_{cat}/K_M = (9.0 \pm 0.3) \times 10^6$  M<sup>-1</sup> s<sup>-1</sup> (mean  $\pm$  SE)] determined using the same assay (Fig. 4D).

The primary structure of HIV-1 protease was confirmed by LC-MS and HPLC methods (Fig. 5B). HIV-1 protease hydrolyzes the peptides of HIV, and using a fluorogenic peptide allows for quantification of its proteolytic activity (43). Synthetic HIV-1 protease displays a Michaelis constant of  $K_M = 20.9 \pm 1.0$   $\mu$ M (mean  $\pm$  SE) and a turnover number of  $k_{cat} = 29.6 \pm 4.1$  s<sup>-1</sup> (mean  $\pm$  SE), close to literature values published for a similar synthetic sample obtained by SPPS (Fig. 5C) (30). Incubation of the synthetic protease with a model substrate peptide results in wild type-like specificity with exclusive cleavage at a single Phe-Pro site (Fig. 5D) (29).

Sortase A<sub>59–206</sub> is a transpeptidase produced by Gram-positive bacteria that catalyzes a cell wall sorting reaction at a threonine-glycine bond in the LPXTG motif (Leu-Pro-X-Thr-Gly, where X is any amino acid) (44). We synthesized the 164-amino acid-long sortase A\* variant (P94S/D160N/K196T; P, Pro; S, Ser; D, Asp; N, Asn; K, Lys; T, Thr) to allow for direct comparison to a recombinant standard (45, 46). At a concentration of 0.01 mg/ml, synthetic sortase A\* led to 47% product formation by LC-MS within 24 hours (starting from 0.2 mg/ml GGGGGLY and AQUALPETGEE as test substrates; G, Gly; L, Leu; Y, Tyr; A, Ala; Q, Gln; E, Glu) (fig. S23). This conversion value is com-

parable to that determined for the recombinant protein (50% product formation within 24 hours). Enzymatic activity assays of synthetic proteins accessed by AFPS therefore confirmed both the high substrate specificity and comparable activity to recombinant enzymes and literature values.

Binding studies of synthetic MDM2 and barnase confirmed specific affinities for their respective substrates. Barnase binds selectively and with high affinity to its inhibitor barstar. In a gel-based assay, recombinant barstar inhibited RNase activity of synthetic and recombinant barnase in a concentration-dependent manner (Fig. 4E) (47). In addition, synthetic barstar obtained with AFPS performed comparably to recombinant barstar. To quantify binding of a synthetic protein to a known ligand, we also characterized the N-terminal binding domain of MDM2<sup>[1–118]</sup> (32). The binding of MDM2 to p53 is a key interaction in multiple pathways up-regulated in cancer (48, 49). We folded milligram quantities of synthetic MDM2<sup>[1–118]</sup> and characterized its binding to immobilized p53<sup>[14–29]</sup> using biolayer interferometry (figs. S24 and S25). Synthetic MDM2<sup>[1–118]</sup> displayed an affinity toward p53 [dissociation constant ( $K_d$ ) = 6.25  $\mu$ M] comparable to the literature value ( $K_d$  = 5.45  $\mu$ M) obtained under the same folding conditions.

## Discussion

The optimized AFPS protocol demonstrates advantages of flow chemistry over common batch methods, yielding peptide chains more than three times longer than previously accessible by routine standard SPPS (6). An improvement to existing flow protocols was achieved by rapid screening of variables in a reproducible reaction setup. Even though in this study AFPS yields superior results over traditional SPPS methods in terms of total synthesis time and crude product quality, general challenges associated with peptide synthesis, such as low atom economy and the use of DMF as a solvent, remain unsolved. A potentially limiting feature of our setup is synthesis scale. The capacity of the reactor used in our study allows up to 200 mg of resin with a loading of 0.49 mmol/g. Increased production output can be achieved by incorporating a larger reactor in the current system, but such a modification will likely require specific optimization, toward which we performed preliminary investigations (19). Since we implemented AFPS, we have produced more than 5000 peptides and automatically collected in-line analysis data for all syntheses. Moving forward, this extensive, high-quality dataset could be leveraged to further improve peptide synthesis in flow using machine learning and other computational methods. Ultimately, we intend for this report to serve as a blueprint for the automated flow synthesis of other biopolymers and artificial sequence-defined polymers (50).

A robust, widely available routine method for chemical production of proteins is poised to have a strong impact on chemical biology and the development of new therapeutics. Our advances provide a viable solution to reliably assemble long linear peptide chains, shifting the focus in the field of chemical protein synthesis to improving folding protocols and, most importantly, applications. Combined with chemical ligation, rapid stepwise production of single-domain proteins by AFPS technology will extend the practical applications of total chemical synthesis to the majority of human proteins (those with a mass of up to ~30 kDa) (10, 51). In this respect, we envisage adapting to our AFPS protocol the incorporation of peptide hydrazides for thioester-based ligation, an approach previously achieved with manual flow instrumentation (52). Additional research avenues opened by our method include rapid access to mirror-image proteins, posttranslationally modified proteins, and de novo-designed, abiotic proteins. Introduction of noncanonical amino acids as point mutations in native proteins will make accessible variants with considerably altered biological function, for example, catalytic activity (53, 54). Finally, AFPS has the potential to enable on-demand production of time-sensitive and potentially life-saving personalized medicine,

such as for enzyme replacement therapy or neoantigen cancer vaccines (55, 56).

## REFERENCES AND NOTES

1. J. Britton, C. L. Raston, *Chem. Soc. Rev.* **46**, 1250–1271 (2017).
2. D. Webb, T. F. Jamison, *Chem. Sci.* **1**, 675–680 (2010).
3. S. Bondalapati, M. Jbara, A. Brik, *Nat. Chem.* **8**, 407–418 (2016).
4. J. W. Chin, *Nature* **550**, 53–60 (2017).
5. R. B. Merrifield, *J. Am. Chem. Soc.* **85**, 2149–2154 (1963).
6. S. B. H. Kent, *Chem. Soc. Rev.* **38**, 338–351 (2009).
7. A. A. Zompra, A. S. Galanis, O. Werbitzky, F. Albericio, *Future Med. Chem.* **1**, 361–377 (2009).
8. P. E. Dawson, T. W. Muir, I. Clark-Lewis, S. B. Kent, *Science* **266**, 776–779 (1994).
9. V. Agouridas et al., *Chem. Rev.* **119**, 7328–7443 (2019).
10. P. E. Dawson, S. B. H. Kent, *Annu. Rev. Biochem.* **69**, 923–960 (2000).
11. A. El-Faham, F. Albericio, *Chem. Rev.* **111**, 6557–6602 (2011).
12. N. Ahmed, *Chem. Biol. Drug Des.* **91**, 647–650 (2018).
13. C. P. Gordon, *Org. Biomol. Chem.* **16**, 180–196 (2018).
14. A. J. Mijalis, A. Steinauer, A. Schepartz, B. L. Pentelute, in *Flow Chemistry in Organic Synthesis* (Georg Thieme Verlag, Stuttgart, 2018), pp. 381–398.
15. E. Bayer, G. Jun, I. Halász, I. Sebastian, *Tetrahedron Lett.* **11**, 4503–4505 (1970).
16. T. J. Lukas, M. B. Prystowsky, B. W. Erickson, *Proc. Natl. Acad. Sci. U.S.A.* **78**, 2791–2795 (1981).
17. A. J. Mijalis et al., *Nat. Chem. Biol.* **13**, 464–466 (2017).
18. S. K. Mong, A. A. Vinogradov, M. D. Simon, B. L. Pentelute, *ChemBioChem* **15**, 721–733 (2014).
19. M. D. Simon, “Fast flow biopolymer synthesis,” thesis, Massachusetts Institute of Technology, Cambridge, MA (2017).
20. S. Fuse, Y. Otake, H. Nakamura, *Chem. Asian J.* **13**, 3818–3832 (2018).
21. S. Fuse, Y. Mifune, T. Takahashi, *Angew. Chem. Int. Ed.* **53**, 851–855 (2014).
22. L. K. Spare, V. Laude, D. G. Harman, J. R. Aldrich-Wright, C. P. Gordon, *React. Chem. Eng.* **3**, 875–882 (2018).
23. E. T. Sletten, M. Nuño, D. Guthrie, P. H. Seeberger, *Chem. Commun.* **55**, 14598–14601 (2019).
24. M. Schnölzer, P. Alewood, A. Jones, D. Alewood, S. B. H. Kent, *Int. J. Pept. Protein Res.* **40**, 180–193 (1992).
25. T. Michels, R. Dölling, U. Haberkorn, W. Mier, *Org. Lett.* **14**, 5218–5221 (2012).
26. M. Mergler, F. Dick, B. Sax, P. Weiler, T. Vorherr, *J. Pept. Sci.* **9**, 36–46 (2003).
27. S. A. Palasek, Z. J. Cox, J. M. Collins, *J. Pept. Sci.* **13**, 143–148 (2007).
28. S. Luisier, M. Avital-Shmilovici, M. A. Weiss, S. B. H. Kent, *Chem. Commun.* **46**, 8177–8179 (2010).
29. J. Schneider, S. B. H. Kent, *Cell* **54**, 363–368 (1988).
30. E. C. B. Johnson et al., *J. Am. Chem. Soc.* **129**, 11480–11490 (2007).
31. A. Brik, C.-H. Wong, *Org. Biomol. Chem.* **1**, 5–14 (2003).
32. J. D. Oliner et al., *Nature* **362**, 857–860 (1993).
33. D. Bresson et al., *J. Clin. Invest.* **116**, 1371–1381 (2006).
34. E. Gasser, C. P. Moutos, M. Downes, R. M. Evans, *Nat. Rev. Endocrinol.* **13**, 599–609 (2017).
35. L. Serrano, J. T. Kellis Jr., P. Cann, A. Matouschek, A. R. Fersht, *J. Mol. Biol.* **224**, 783–804 (1992).
36. C. B. Anfinsen, *Science* **181**, 223–230 (1973).
37. S. B. Kent, P. F. Alewood, *Curr. Opin. Chem. Biol.* **22**, viii–xi (2014).
38. R. W. Hartley, *Trends Biochem. Sci.* **14**, 450–454 (1989).
39. J. T. Kellis Jr., K. Nyberg, A. R. Fersht, *Biochemistry* **28**, 4914–4922 (1989).
40. J. R. Knowles, *Science* **236**, 1252–1258 (1987).
41. U. Arnold et al., *J. Am. Chem. Soc.* **125**, 7500–7501 (2003).
42. B. R. Kelemen et al., *Nucleic Acids Res.* **27**, 3696–3701 (1999).
43. M. V. Toth, G. R. Marshall, *Int. J. Pept. Protein Res.* **36**, 544–550 (1990).
44. H. Ton-That, G. Liu, S. K. Mazmanian, K. F. Faull, O. Schneewind, *Proc. Natl. Acad. Sci. U.S.A.* **96**, 12424–12429 (1999).
45. J. J. Ling, R. L. Polcarpo, A. E. Rabideau, X. Liao, B. L. Pentelute, *J. Am. Chem. Soc.* **134**, 10749–10752 (2012).
46. R. L. Polcarpo et al., *Angew. Chem. Int. Ed.* **53**, 9203–9208 (2014).
47. A. A. Vinogradov, E. D. Evans, B. L. Pentelute, *Chem. Sci.* **6**, 2997–3002 (2015).
48. F. Touti, Z. P. Gates, A. Bandyopadhyay, G. Lautrette, B. L. Pentelute, *Nat. Chem. Biol.* **15**, 410–418 (2019).

49. P. Chène, *Mol. Cancer Res.* **2**, 20–28 (2004).
50. J.-F. Lutz, M. Ouchi, D. R. Liu, M. Sawamoto, *Science* **341**, 1238149 (2013).
51. S. J. Wheellan, A. Marchler-Bauer, S. H. Bryant, *Bioinformatics* **16**, 613–618 (2000).
52. M. D. Simon et al., *ChemBioChem* **15**, 713–720 (2014).
53. J. C. Li, T. Liu, Y. Wang, A. P. Mehta, P. G. Schultz, *J. Am. Chem. Soc.* **140**, 15997–16000 (2018).
54. H. Xiao et al., *Proc. Natl. Acad. Sci. U.S.A.* **112**, 6961–6966 (2015).
55. R. J. Desnick, E. H. Schuchman, *Nat. Rev. Genet.* **3**, 954–966 (2002).
56. N. L. Truex et al., *Sci. Rep.* **10**, 723 (2020).
57. A. M. Buckle, G. Schreiber, A. R. Fersht, *Biochemistry* **33**, 8878–8889 (1994).
58. Y. Yang et al., *J. Biol. Chem.* **285**, 7847–7851 (2010).
59. J. Sevcik, L. Urbanikova, Z. Dauter, K. S. Wilson, *Acta Crystallogr. D Biol. Crystallogr.* **54**, 954–963 (1998).
60. J. Bella, B. Brodsky, H. M. Berman, *Structure* **3**, 893–906 (1995).
61. A. Czarna et al., *Cell Cycle* **8**, 1176–1184 (2009).
62. T. Durek, V. Y. Torbeev, S. B. H. Kent, *Proc. Natl. Acad. Sci. U.S.A.* **104**, 4846–4851 (2007).
63. X. Xia, L. M. Longo, M. Blaber, *J. Pharm. Sci.* **104**, 566–576 (2015).
64. N. Suree et al., *J. Biol. Chem.* **284**, 24465–24477 (2009).
65. A. J. Mijalis, amijalis/afps-integration: AFPS-analysis: Code used to extract and analyze data from AFPS synthesis files. Zenodo (2020).

## ACKNOWLEDGMENTS

We thank T. F. Jamison, H. U. Stilz, L. F. Iversen, K. Little, and D. Lundsgaard for productive discussions and administrative support. We acknowledge the participants of the 26th American Peptide Symposium and the 8th Chemical Protein Synthesis Meeting, especially P. E. Dawson, R. T. Raines, and S. B. H. Kent, for helpful discussions and for suggesting additional experiments. We also thank E. D. Evans, F. W. W. Hartrampf, and R. L. Holden for careful proofreading of the manuscript. We are grateful to N. L. Truex for providing recombinant sortase A\*. Finally, we acknowledge C. M. T. Hartrampf for designing Fig. 1A. **Funding:** Financial support for this project was provided by Novo Nordisk A.S., A.E.C., and C.K.S. gratefully acknowledge support from the National Science Foundation Graduate Research Fellowship under grant no. 1122374; A.E.C. is additionally supported by an MIT Dean of Science Fellowship. **Author contributions:** N.H., T.E.N., and B.L.P. conceptualized the research; N.H., M.P., A.J.M., and S.L. optimized synthesis conditions; A.J.M. provided the software for UV data analysis, and M.D.S. built the AFPS used in this report; M.P., A.J.C., and C.J. performed comparison of AFPS with traditional SPPS methods; N.H., A.S., M.P., A.J.C., A.E.C., S.H., S.A., C.K.S., and A.J.Q. synthesized, purified, and analyzed protein samples; N.H., Z.P.G., and B.L.P. conceptualized folding and biological evaluation of the synthetic proteins; N.H., A.S., M.P., Z.P.G., A.J.C., and X.Y. performed biological evaluation and expression of recombinant proteins; N.H., Z.P.G., A.L., and B.L.P. wrote the manuscript with input of all coauthors. **Competing interests:** B.L.P. is a cofounder of Amide Technologies and Resolute Bio. Both companies focus on the development of protein and peptide therapeutics. A.J.M. and M.D.S. hold equity in Amide Technologies. The following authors are inventors on patents and patent applications related to the technology described: A.J.M., M.D.S., and B.L.P. are co-inventors on U.S. patent application 20170081358A1 (23 March 2017) describing methods and systems for solid-phase peptide synthesis; M.D.S. and B.L.P. are co-inventors on U.S. patents 9,868,759 (16 January 2018), 9,695,214 (4 July 2017), and 9,169,287 (27 October 2015) describing solid-phase peptide synthesis processes and associated systems. **Data and materials availability:** Code for analysis of the UV-vis traces obtained from the AFPS instrument is available in a GitHub repository (65). All data are available in the main text or the supplementary materials.

## SUPPLEMENTARY MATERIALS

science.sciencemag.org/content/368/6494/980/suppl/DC1  
Materials and Methods  
Supplementary Text  
Figs. S1 to S25  
Tables S1 to S14  
References (66–71)  
MDAR Reproducibility Checklist

10 February 2020; accepted 30 March 2020  
10.1126/science.abb2491

## OCEAN CIRCULATION

# Strengthening of the Kuroshio current by intensifying tropical cyclones

Yu Zhang<sup>1\*</sup>, Zhengguang Zhang<sup>1</sup>, Dake Chen<sup>2,3</sup>, Bo Qiu<sup>4</sup>, Wei Wang<sup>1</sup>

A positive feedback mechanism between tropical cyclones (TCs) and climate warming can be seen by examining TC-induced energy and potential vorticity (PV) changes of oceanic geostrophic eddies. We found that substantial dissipation of eddies, with a strong bias toward dissipation of anticyclonic eddies, is directly linked to TC activity. East of Taiwan, where TCs show a remarkable intensifying trend in recent decades, the ocean exhibits a corresponding upward trend of positive PV anomalies. Carried westward by eddies, increasing numbers of positive PV anomalies impinge on the Kuroshio current, causing the mean current to accelerate downstream. This acts in opposition to decreasing basin-scale wind stress and has a potentially important warming impact on the extratropical ocean and climate.

In a warming climate, very intense tropical cyclones (TCs; categories 4 and 5 on the Saffir-Simpson scale) are becoming more intense and frequent, as proposed by theoretical and modeling studies (1–4) and supported by observations (5, 6). This behavior raises the question of what feedbacks can be induced by TC changes on climate. Much prior work has been focused on TCs' interaction with the quiescent upper ocean. For example, the decay of cold ocean wakes produced by storm-driven mixing causes net heating of the upper ocean and has been suggested to have important effects on global climate (7, 8). The ocean is anything but quiescent or uniform, though, and is full of dynamical structures of different scales. Among them, rotating structures with spatial scales of order O (10 to 100 km), temporal scales of order O (100 days), and vertical extents of 1000 m or more, usually referred to as mesoscale eddies, are the most ubiquitous and energetic; they play an essential role in transporting material and energy, and they modulate large-scale ocean circulation (9–11).

Because mesoscale eddies are ubiquitous, their encounters with TCs are not rare. By modulating subsurface density as well as thermal conditions, these synoptic-scale structures have been found to greatly affect the evolution of a storm's strength, posing a big challenge for operational prediction of TC intensity (12–15). Meanwhile, TCs can also have a large impact on eddies through more than one mechanism and in different or opposite ways. For example, in central areas of TCs,

strong and positive wind stress curl dominates, producing divergent surface currents, forcing cool water upward from below, and elevating isopycnals as much as 100 m, in the same sense as the circulation of cyclonic eddies and the associated upward displacements of isopycnals. Hence, oceanic cyclonic eddies can be enhanced or generated (16–18) while their mirror images, anticyclonic eddies, can be weakened. In outer regions of TCs, the wind stress curl is negative and very weak. Although the effects are to strengthen anticyclonic eddies yet weaken cyclonic eddies, opposite to those inside TCs' cores, the amplitudes are much reduced. In the meantime, at the smallest scale satisfying geostrophy, mesoscale eddies are always close to geostrophic balance. If this balance is disturbed through processes such as the shoaling of isopycnals by strong storms, the flow will adjust itself back to a state of geostrophic balance. This process, known as geostrophic adjustment, was first considered

by Rossby in 1938 (19) and has since been investigated in a variety of contexts both linear and nonlinear (20–23). Common to all those studies is that the flows in question hold less energy at their end states than they do initially, and energy is dispersed in the form of inertial gravity waves (19, 24). It is therefore anticipated that eddies under the influence of strong storms may be perturbed and subsequently undertake adjustment processes that attenuate them (25).

Evidence continues to mount that both mechanisms described above exist, working together to reduce the strength of anticyclonic eddies but acting against each other in changing cyclonic eddies. Which process dominates, and what overall influence the TCs exert on an underlying eddy field, remains unclear. To this end, a survey of eddies' lifetime evolution—in particular, immediately after their meeting with TCs—is necessary. The advent of satellite altimetry has enabled global and synoptic mapping of eddies with prominent surface signatures (26). The later combination of data from two altimeters has provided a time-series record of global maps of ocean eddies at high spatial and temporal resolutions [DT-2014 daily “two-sat merged” gridded product provided by archiving, validation, and interpretation of satellite oceanographic data (AVISO) (27)]. On the basis of that record, an eddy-tracking data archive was constructed, providing at daily frequency the center, amplitude, polarity, radius, and rotational velocity for those eddies identified and tracked by altimetry (28). In addition, Argo floats have provided depth profiles of temperature and salinity, from which eddies' vertical structures can be extracted (29). Taking advantage of both AVISO and Argo data, a law for the universal structure of eddies was uncovered (30), making it possible

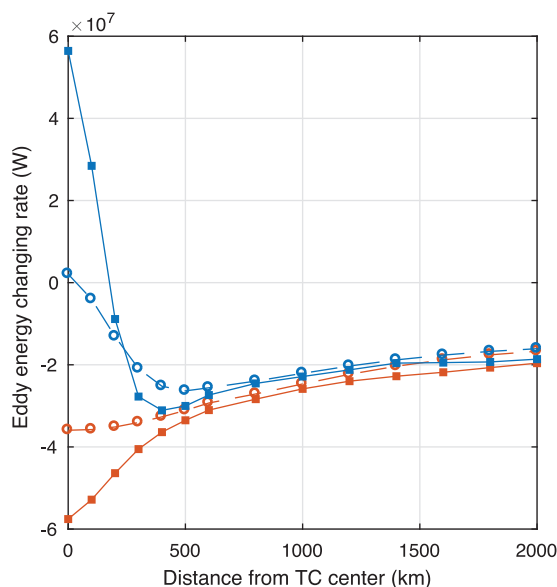


**Fig. 1. Changing rate of eddy energy versus distance from TC center.**

Mean changing rate of eddies' total energy is plotted against radial distance, averaged over 15 days after passing of TCs, for anticyclonic eddies (red curves) and cyclonic eddies (blue curves). Curves with circles are for all TCs in the western North Pacific Ocean between 1993 and 2014; those with squares are for more intense winds with speed greater than 40 m s<sup>-1</sup>.

<sup>1</sup>Physical Oceanography Laboratory/CIMST, Ocean University of China and Qingdao National Laboratory for Marine Science and Technology, Qingdao, P. R. China. <sup>2</sup>State Key Laboratory of Satellite Ocean Environment Dynamics, Second Institute of Oceanography, Ministry of Natural Resources, Hangzhou, P. R. China. <sup>3</sup>Southern Marine Science and Engineering Guangdong Laboratory (Zhuhai), Zhuhai, P. R. China. <sup>4</sup>Department of Oceanography, University of Hawai'i at Manoa, Honolulu, HI, USA.

\*Corresponding author. Email: yuz@ouc.edu.cn

to accurately infer an eddy's three-dimensional structure from its surface signal. Using 20 years of these datasets in combination with TC observations in the western North Pacific, we carried out an analysis of the evolution of three-dimensional eddy energy and potential vorticity fields with a special focus on storm effects. [Potential vorticity (PV) is a dynamically conserved quantity depicting the tendency of a rotating fluid to spin.] Our results indicate that the interaction with TCs can introduce an important, newly recognized feature of the eddy field, which, together with the strengthening trend of TCs in a warming climate, has potentially strong influence on large-scale ocean circulation and climate.

### Eddy response to TCs

Figure 1 shows the results of a survey of the rates of energy change of eddies during the 15-day period after their encounters with TCs in the western North Pacific Ocean (see supplementary materials). The rate of change depends on factors including storm wind speed, eddy polarity, and the radial distance,  $r$ , between an eddy and the storm's center at the time of meeting.

Cyclonic and anticyclonic eddies show obvious differences with little asymmetry about the storm track (see supplementary materials), especially under strong winds. Anticyclonic eddies that have passed within ~1000 km of the storm center generally experience substantial

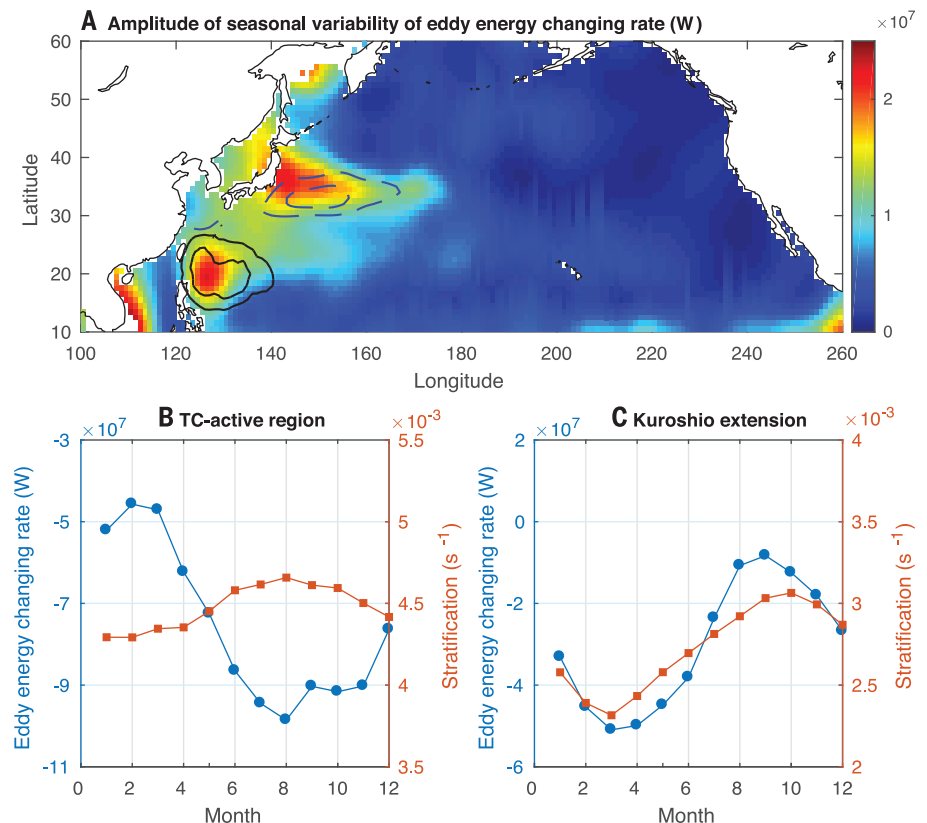
weakening afterward. On average, the energy decay rate declines from the storm center monotonically outward, asymptotically approaching the background dissipation level that is weaker than the central maximum value by a factor of 2 to 3 (red curves in Fig. 1). Cyclonic eddies' responses, although close to those of anticyclonic eddies' responses farther away from the storm, exhibit a tendency to strengthen progressively as they approach the storms' centers (blue curves in Fig. 1). Thus, TCs not only cause the entire eddy field to decay substantially more quickly than otherwise might have occurred but also make cyclonic eddies relatively stronger than anticyclonic eddies.

As seasonal phenomena, TCs develop mostly during the months of June through November, with peak activity occurring usually in late summer (31). If TCs' effect is dominant in driving eddy dissipation, the year-round energy evolution of eddies should exhibit similar seasonality.

In the North Pacific Ocean, only two areas demonstrate strong seasonal variation of the decay rates of eddies (Fig. 2A), and both are near the western boundary: One located at 20° to 30°N and 120° to 130°E, east of Taiwan, coincides with the region of the strongest TC activity (solid contours in Fig. 2A); the other one is located in the Kuroshio Extension. Both regions are prominent for vigorous eddy fields, but they differ from each other in two important aspects. First, their energetic eddy fields have different origins. In the Kuroshio Extension

region, a high eddy kinetic energy level arises from the meandering of the current itself (32), while along latitudes around 25°N, eddies are generated in the shearing flows between the eastward Subtropical Counter Current located in the 18° to 25°N band and the underlying westward North Equatorial Current (33). After generation, these eddies propagate mainly westward at speeds of a few centimeters per second, evolve as they move, enter and pass through the region of strong TC activity, and finally collide with the Kuroshio before they disappear (32). Second, seasonal variations of the eddies' decay rates in the two regions have different origins. In the TC-active region, the seasonal variation of the decay rate is in phase with that of TC activity (Fig. 2B), and so is the difference of decay rates between anticyclonic and cyclonic eddies (see supplementary materials). Both pieces of evidence indicate TCs' vital role in causing eddy dissipation. In the Kuroshio Extension region, the seasonal variation of the decay rate is almost 180° out of phase with that in the south, being strong in winter and spring but weak in summer and autumn (Fig. 2C). A closer look at different factors contributing to eddies' energy evolution reveals that the seasonality of the decay rate in this area is primarily due to the seasonally varying ocean stratification. Following the seasonal variation of solar irradiance, the buoyancy flux across the air-sea interface changes, as does the stratification in the ocean interior, which,

**Fig. 2. Seasonal variation of eddy energy changing rate.** (A) Seasonal variation amplitude of eddy energy changing rate in the North Pacific Ocean (color scale). TC intensity, defined as annual accumulated power input of TCs to the ocean,  $\sum v^3$  (where  $v$  is the local instantaneous wind speed from the Best Track Dataset of Tropical Cyclones), is shown as solid contours. Seasonal variation amplitudes of oceanic stratification are shown as dashed contours. See supplementary materials for details. (B and C) Seasonal variation of eddy energy changing rate (blue) as compared with seasonal variation of oceanic stratification (red) in the TC-active region (120° to 130°E, 20° to 30°N) (B) and the Kuroshio Extension region (C). A 3-month running mean smoothing was applied to the time series.



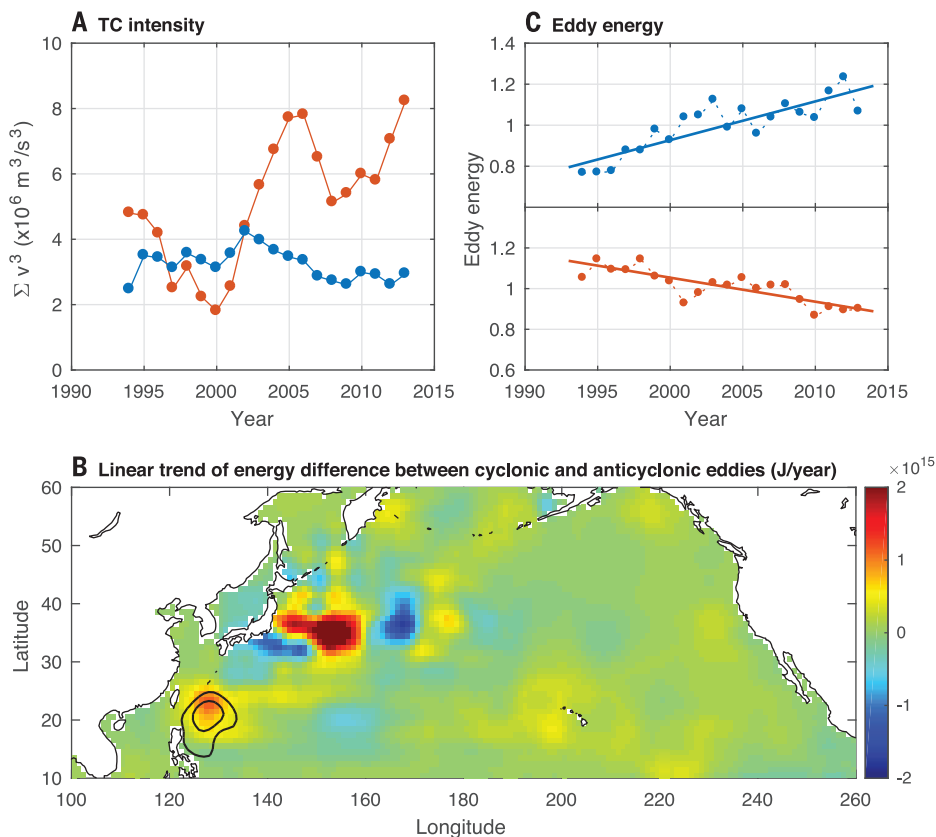


**Fig. 3. Time series of TC intensity and energy difference between cyclonic eddies and anticyclonic eddies.** (A) Time series of TC intensity, defined as annual accumulated power input in the TC-active area with winds below  $40 \text{ m s}^{-1}$  (blue) and above  $40 \text{ m s}^{-1}$  (red), from 1993 to 2014. (B) Linear trend of energy difference between cyclonic eddies and anticyclonic eddies in the North Pacific Ocean (color scale). Linear trend of TCs' annual accumulated power input is shown by contours. (C) Time series of normalized volume-integrated energy of cyclonic eddies (upper, blue dots) and anticyclonic eddies (lower, red dots) in the TC-active area. Linear trends are shown by solid lines. A 3-year running mean smoothing was applied to the time series. Each time series was normalized by dividing by its own 20-year mean.

as one of the most essential environmental factors shaping eddy characteristics, further modulates their energy and the associated evolution process. Near the tropics, both solar heating and ocean stratification change less across different seasons than they do at higher latitudes (dashed contours in Fig. 2A), whereas TC activity is much stronger, leaving TCs' seasonal forcing largely responsible for the seasonality of eddies' decay.

Our eddy energy analysis is performed in a Lagrangian framework (see supplementary materials): For each eddy identified by altimetry, the sum of kinetic and available potential energy is calculated on a daily basis along its track, and the 15-day low-pass-filtered changing rate is subsequently computed. More important, the volume integration instead of the surface component of energy is evaluated so as to include the effect of ocean stratification in driving the seasonality of the energy decay.

The TC-active region east of Taiwan ( $20^\circ$  to  $30^\circ\text{N}$ ,  $120^\circ$  to  $130^\circ\text{E}$ ) not only has the strongest storms on average but also has displayed an obvious trend in TC intensity over the past decades, primarily due to intensified very strong storms (winds with speed above  $40 \text{ m s}^{-1}$ ; Fig. 3A). Because intense TCs are inclined to induce greater dissipation of anticyclonic eddies but to cause moderate to weak dissipation, or even discernible strengthening, of cyclonic

eddies, we anticipate relatively more energetic cyclonic eddies than anticyclonic eddies under intensifying TC activity. This expectation is confirmed by a trend analysis of energy difference between cyclonic and anticyclonic eddies in the entire basin. The result yields two regions of peak signals (Fig. 3B); the southern one located around  $25^\circ\text{N}$  displays a strong positive trend resulting from the strengthening of cyclonic eddies and the concurrent weakening of anticyclonic eddies (Fig. 3C). The region is nearly contiguous with the TC-active area (solid contours in Fig. 3B). Furthermore, its remarkable amplitude makes it distinct and isolated from both the neighboring areas and the latitudinal band farther to the east, from where eddies seen in this region are propagating. Therefore, the difference between the two types of eddies in this region is unlikely to be the result of any remote forcing. Instead, the strengthening of local TC activity introduces this new feature of the eddy field.

The Kuroshio Extension shows distinctly different trends between cyclonic eddies and anticyclonic eddies but with signs alternating zonally along the flow axis (Fig. 3B). Because eddies here are formed mostly by the pinch-off process of meanders, eddies generated from northward meanders are anticyclonic eddies with anomalous warm water at the core, and

those generated from southward meanders are cyclonic eddies with cold cores. In other words, north of the flow axis, anticyclonic eddies tend to dominate, whereas to the south cyclonic eddies prevail; however, with the meridional migration of the flow axis, the relative strength of the two types of eddies will be changed. For example, a region previously dominated by anticyclonic eddies will be filled with more cyclonic eddies as the axis moves to the north. Presumably the strong signals with alternating signs are related to spatial migration of the current axis, which is inhomogeneous in the zonal direction (34); these signals result from the redistribution of eddies but do not reflect net changes of the eddy field as a whole. Therefore, the only robust strengthening trend of cyclonic eddies relative to anticyclonic eddies in the North Pacific Ocean is the TC-driven trend east of Taiwan.

#### Strengthening of the Kuroshio current by eddies

The Kuroshio is primarily wind-driven. As the western boundary current of the North Pacific subtropical gyre, it acts as the return limb for the southward interior Sverdrup flow that is controlled by the basin-scale wind stress curl (32). Nonetheless, many other factors besides the basin-scale wind, such as the El Niño–Southern Oscillation (ENSO), the Pacific Decadal Oscillation (PDO), and the local

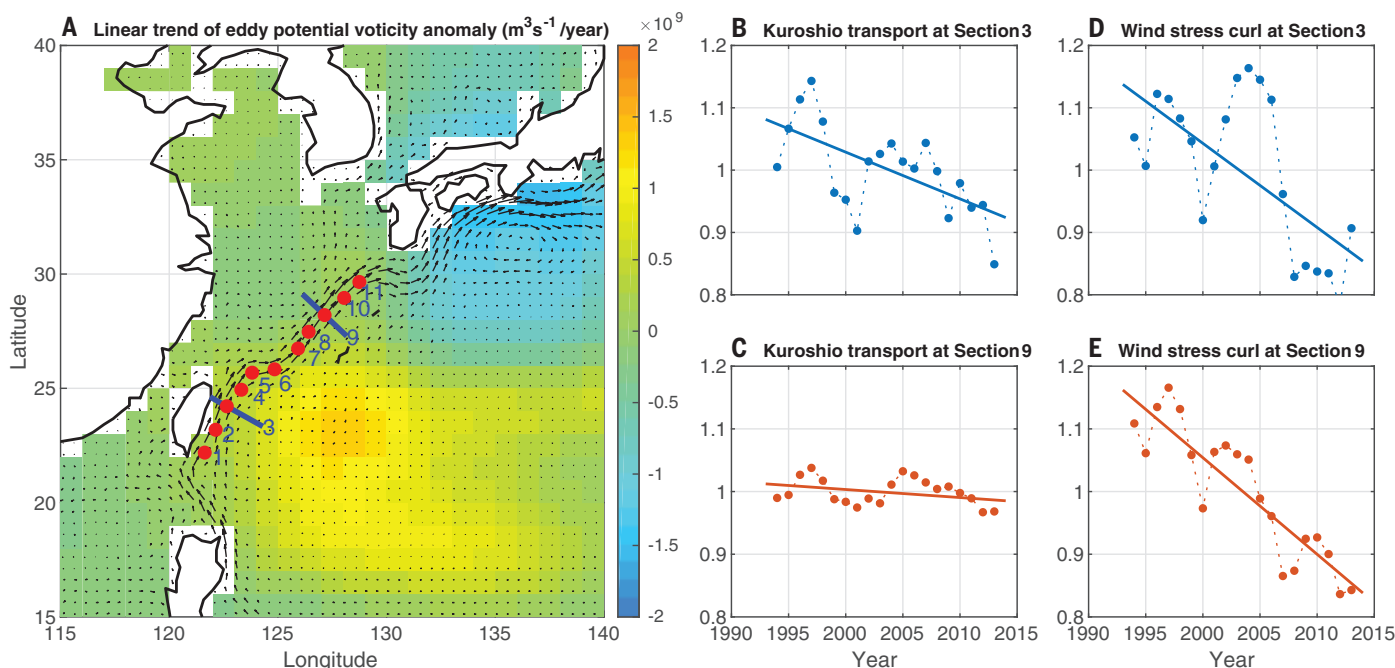


**Fig. 4. Variation of Kuroshio transport along its path.** (A) Linear trend of eddy potential vorticity (PV) anomaly in the western North Pacific Ocean (color scale). Mean velocity (arrow directions and lengths indicate direction and magnitude of velocity), coastlines (contour), and locations of cross sections (red dots) are shown. Sections 3 and 9 are denoted by solid blue lines. (B) Time series of normalized Kuroshio transport across section 3 (blue). (C) Same as (B) but for section 9 (red). (D) Time series of normalized strength of the wind

stress curl (blue) zonally averaged across the basin and meridionally within the latitudinal range of section 3 (20° to 25°N). (E) Same as (D) but for section 9 (25° to 30°N). Dots denote annual mean values with a 3-year running mean smoothing applied; solid lines denote linear trends. The Kuroshio transport across each section was calculated as the along-section integration of perpendicular surface geostrophic velocity. In (B) to (E), each time series was normalized by dividing by its own 20-year mean.

wind stress and topography, influence it as well (35–37). In particular, eddy activity has been suggested as a main modulator of the Kuroshio east of Taiwan (37, 38). Because this segment of the Kuroshio is also on the western edge of the TC-active region, a question naturally arises as to how the current is affected by the strengthening trend of cyclonic eddies relative to anticyclonic eddies discussed above.

The eddy flux of potential vorticity (PV) is the key to answering this question, because it comprehensively reflects the dynamical and thermodynamical links between the mean and eddy components of the flow field (39). A crucial difference between a cyclonic and an anticyclonic eddy is that the former has a positive PV anomaly while the latter has a negative one, both of which are carried westward like passive tracers by these fairly non-linear and isolated eddies. Because cyclonic eddies are relatively stronger than anticyclonic eddies, the associated positive PV anomaly prevails (Fig. 4A), leading to a westward flux of net positive PV anomaly toward the mean current. According to the turbulent Sverdrup balance theorized by Rhines and Holland in 1979 (40), the westward positive eddy PV flux works to increase the PV of the mean com-

ponent by accelerating the current northward (see supplementary materials). As shown below, this is the underlying mechanism for the downstream acceleration of the Kuroshio in recent decades.

In the past two decades (1994–2013), Kuroshio transport east and downstream of Taiwan has undergone an obvious decreasing trend. The trend has been ascribed to the weakening of the subtropical wind stress curl (41), which, according to the classical Sverdrup balance, sets the transport of the western boundary current (42), but apparently this is not the whole story. For example, across both section 3 and section 9, the Kuroshio transport was noticeably weakened, but the upstream transport was reduced more remarkably: a 13% decrease at section 3 (Fig. 4B) versus a 3% decline at section 9 (Fig. 4C). Meanwhile, the strength of the basin-scale wind stress curl within this latitudinal band experienced a much greater decline than that of the Kuroshio transport, and the reduction amplitude slightly strengthened northward: a 27% decrease around the latitudes of section 3 (Fig. 4D) versus a more vigorous one, 31%, at section 9 (Fig. 4E). Therefore, some other factors must be accelerating the Kuroshio and counteracting the decelerating effects of the basin-scale wind.

To get a clearer picture, we take the difference between the two sections. The difference of Kuroshio transport reveals a large positive trend suggesting that the flow has increased downstream in the past 20 years (Fig. 5A). The difference of the strength of the basin-scale wind stress curl, however, demonstrates a slight downward trend, corresponding to a tendency for downstream deceleration of the current (Fig. 5B). Hence, the classical Sverdrup balance depicting the dominant role of the basin-scale wind field cannot explain the observed acceleration of the current, and therefore, consistent with the turbulent Sverdrup balance theory, eddy PV flux is implicated.

Calculation of the eddy PV flux (see supplementary materials) between the two sections yields a curve (Fig. 5C) that is in good agreement with the downstream transport change (correlation coefficient of 0.69) in terms of both the interannual variability and the long-term upward trend. Moreover, at other locations along the current axis from south of Taiwan toward south of Japan (red dots in Fig. 4A), trends of the downstream change of Kuroshio transport and trends of the corresponding eddy PV flux (Fig. 5D) show a linear relation between the two that is consistent with our theoretical prediction.

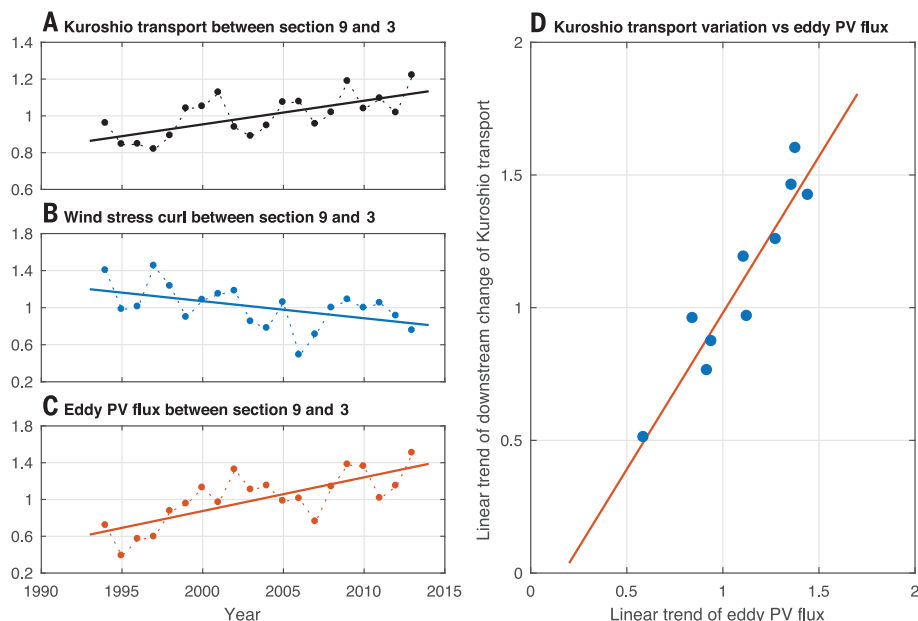


**Fig. 5. Modulation of Kuroshio transport by eddy potential vorticity (PV) flux.** (A) Time series of normalized Kuroshio transport difference between section 9 and section 3 (black). (B) Same as (A) but for the normalized strength of the wind stress curl zonally averaged across the basin (blue). (C) Same as (A) but for the normalized eddy PV flux (see supplementary materials) in the area bounded by the two sections (red). Dots denote annual

mean with a 3-year running mean smoothing applied; solid lines denote linear trends. (D) Scatterplot of linear trends of the normalized Kuroshio transport difference between section 2, 3, 4, 5, 6, 7, ..., 11 and section 1, and linear trends of the normalized eddy PV flux in corresponding areas. Linear fitting result is shown as a solid line. In (A) to (C), each time series was normalized by dividing by its own 20-year mean.

All the above pieces of evidence point to the eddy effect as the reason for the increasing strength of Kuroshio transport despite the weakening basin-scale wind stress curl, indicating a linkage between TC activity and the Kuroshio transport change. Relative to TCs, oceanic eddies usually have much longer life spans and much slower translation speeds. Thus, eddies facilitate slow oceanic responses to TCs' more rapid forcing, which would further feed back onto the longer-term variations of the large-scale ocean circulation and climate change through eddy-mean flow interactions.

## Conclusions

The kinetic energy of the ocean circulation is dominated by mesoscale eddies, which have been receiving much attention since they were first discovered in the early 1960s. Here, we have demonstrated a linkage between TC forcing and the substantial decay of the underlying eddy field, from which energy is transferred progressively downscale to smaller scales that are vulnerable to dissipation and mixing processes. Moreover, this decay process has pronounced seasonality due to the seasonal variation of TC occurrence, which paces the downscale energy cascade as well as the enhancement of the related mixing in the deep ocean. Finally, we have shown that the modifi-

cation of the eddy field by TCs results in a positive feedback between TCs and climate change by modifying Kuroshio transport.

As the western boundary current of the North Pacific Ocean, the Kuroshio serves as a conduit for transporting warm water northward from its equatorial source region, thus playing a crucial role in modulating the ocean and climate in mid- to high latitudes (43, 44). As a result of global warming in recent decades, the western Pacific Warm Pool has warmed notably, which may cause more heat to be carried northward by the Kuroshio, although to some extent this could be moderated by the weakening of Kuroshio transport. Global warming also may cause more intense TCs to occur at a higher frequency, which should increase the ratio of cyclonic eddies to anticyclonic eddies and thereby increase the trend of positive eddy-PV flux impinging onto the Kuroshio. That should accelerate downstream transport and contribute to further warming at higher latitudes. Notwithstanding the lack of a quantitative determination of the warming effect of TCs, it seems quite likely that overlooking this positive feedback mechanism could induce measurable bias in climate predictions. For a proper representation of eddies in climate models, more theoretical and modeling studies are needed to improve our understanding of the physical processes involved in

the interactions among eddies, TCs, and large-scale ocean circulation.

## REFERENCES AND NOTES

1. K. A. Emanuel, *Nature* **326**, 483–485 (1987).
2. G. J. Holland, *J. Atmos. Sci.* **54**, 2519–2541 (1997).
3. K. Oouchi et al., *J. Meteorol. Soc. Jpn.* **84**, 259–276 (2006).
4. K. A. Emanuel, *Proc. Natl. Acad. Sci. U.S.A.* **110**, 12219–12224 (2013).
5. K. Emanuel, *Proc. Natl. Acad. Sci. U.S.A.* **114**, 12681–12684 (2017).
6. Y. K. Lim, S. D. Schubert, R. Kovach, A. M. Molod, S. Pawson, *Sci. Rep.* **8**, 16172 (2018).
7. K. Emanuel, *J. Geophys. Res.* **106**, 14771–14781 (2001).
8. M. F. Jansen, R. Ferrari, *Geophys. Res. Lett.* **36**, L06604 (2009).
9. R. Ferrari, C. Wunsch, *Tellus A* **62**, 92–108 (2010).
10. R. Ferrari, C. Wunsch, *Annu. Rev. Fluid Mech.* **41**, 253–282 (2009).
11. Z. Zhang, W. Wang, B. Qiu, *Science* **345**, 322–324 (2014).
12. B. Jaimes, L. K. Shay, *Mon. Weather Rev.* **136**, 4188–4207 (2009).
13. L. K. Shay, G. J. Goni, P. G. Black, *Mon. Weather Rev.* **128**, 1366–1383 (2000).
14. N. D. Walker et al., *Geophys. Res. Lett.* **41**, 7595–7601 (2014).
15. C.-C. Wu, C.-Y. Lee, I.-I. Lin, *J. Atmos. Sci.* **64**, 3562–3578 (2007).
16. L. Sun et al., *J. Geophys. Res. Oceans* **119**, 5585–5598 (2014).
17. X. Shang, H. Zhu, G. Gen, C. Xu, Q. Yang, *Adv. Meteorol.* **340432** (2015).
18. Z. Lu, G. Wang, X. Shang, *J. Phys. Oceanogr.* **46**, 2403–2410 (2016).
19. C.-G. Rossby, *J. Mar. Res.* **1**, 239–263 (1938).
20. A. E. Gill, *J. Fluid Mech.* **77**, 603–621 (1976).
21. H. W. Ou, *J. Phys. Oceanogr.* **14**, 994–1000 (1984).

22. A. C. Kuo, L. M. Polvani, *J. Fluid Mech.* **394**, 1–27 (1999).
23. A. Coutino, M. Stastna, *Nonlin. Processes Geophys.* **24**, 61–75 (2017).
24. A. Cahn Jr., *J. Meteorol.* **2**, 113–119 (1945).
25. B. Jaimes, L. K. Shay, *J. Phys. Oceanogr.* **40**, 1320–1337 (2010).
26. L.-L. Fu, *J. Geophys. Res.* **88**, 4331–4341 (1983).
27. N. Ducet, P. Y. Le Traon, G. Reverdin, *J. Geophys. Res.* **105**, 19477–19498 (2000).
28. D. B. Chelton, M. G. Schlax, R. M. Samelson, *Prog. Oceanogr.* **91**, 167–216 (2011).
29. J. Gould et al., *Eos* **85**, 179–184 (2004).
30. Z. Zhang, Y. Zhang, W. Wang, R. X. Huang, *Geophys. Res. Lett.* **40**, 3677–3681 (2013).
31. K. Emanuel, *Annu. Rev. Earth Planet. Sci.* **31**, 75–104 (2003).
32. B. Qiu, in *Encyclopedia of Ocean Sciences* (Academic Press, 2001), pp. 1413–1426.
33. B. Qiu, *J. Phys. Oceanogr.* **29**, 2471–2486 (1999).
34. B. Qiu, S. Chen, N. Schneider, *J. Clim.* **30**, 9591–9605 (2017).
35. C. Hwang, R. Kao, *Geophys. J. Int.* **151**, 835–847 (2002).
36. C.-R. Wu, *Prog. Oceanogr.* **110**, 49–58 (2013).
37. D. Zhang, T. N. Lee, W. E. Johns, C.-T. Liu, R. Zantopp, *J. Phys. Oceanogr.* **31**, 1054–1074 (2001).
38. Y.-C. Hsin, *J. Geophys. Res. Oceans* **120**, 1792–1808 (2015).
39. G. K. Vallis, *Atmospheric and Oceanic Fluid Dynamics* (Cambridge Univ. Press, 2006).
40. P. B. Rhines, W. R. Holland, *Dyn. Atmos. Oceans* **3**, 289–325 (1979).
41. Y.-L. Wang, C.-R. Wu, *Sci. Rep.* **8**, 14633 (2018).
42. J. Pedlosky, *Geophysical Fluid Dynamics* (Springer, ed. 2, 1987).
43. H. Bryden, S. Imawaki, in *Ocean Circulation and Climate*, G. Siedler, J. Church, J. Gould, Eds. (Academic Press, 2001), pp. 455–474.
44. Y.-O. Kwon et al., *J. Clim.* **23**, 3249–3281 (2010).

#### ACKNOWLEDGMENTS

We acknowledge discussions with J. Pedlosky. **Funding:** Supported by National Natural Science Foundation grants 4172602,

41730535, and 41876007; National Basic Research Priorities Program of China grant 2015CB954300; and National Program on Global Change and Air-Sea Interaction grant GASI-IPOVAI-04. **Author contributions:** Y.Z. and W.W. conceived the project and developed data analysis methodology; Y.Z., Z.Z., and W.W. carried out data analyses; Y.Z. wrote the manuscript; and B.Q. and D.C. reviewed and edited the manuscript. **Competing interests:** The authors declare that they have no competing interests. **Data and materials availability:** The sources of the data used in this paper are listed in the supplementary materials.

#### SUPPLEMENTARY MATERIALS

science.sciencemag.org/content/368/6494/988/suppl/DC1  
Materials and Methods  
Figs. S1 and S2  
References (45–47)

7 April 2019; accepted 30 March 2020  
10.1126/science.aax5758

## SYNTHETIC BIOLOGY

# Electrogenetic cellular insulin release for real-time glycemic control in type 1 diabetic mice

Krzysztof Krawczyk<sup>1\*</sup>, Shuai Xue<sup>1,2</sup>, Peter Buchmann<sup>1</sup>, Ghislaine Charpin-El-Hamri<sup>3</sup>, Pratik Saxena<sup>1</sup>, Marie-Didiée Hussherr<sup>1</sup>, Jiawei Shao<sup>2,4</sup>, Haifeng Ye<sup>2</sup>, Mingqi Xie<sup>1,4</sup>, Martin Fussenegger<sup>1,5†</sup>

Sophisticated devices for remote-controlled medical interventions require an electrogenetic interface that uses digital electronic input to directly program cellular behavior. We present a cofactor-free bioelectronic interface that directly links wireless-powered electrical stimulation of human cells to either synthetic promoter-driven transgene expression or rapid secretion of constitutively expressed protein therapeutics from vesicular stores. Electrogenetic control was achieved by coupling ectopic expression of the L-type voltage-gated channel Cav1.2 and the inwardly rectifying potassium channel Kir2.1 to the desired output through endogenous calcium signaling. Focusing on type 1 diabetes, we engineered electrosensitive human  $\beta$  cells (Electro $\beta$  cells). Wireless electrical stimulation of Electro $\beta$  cells inside a custom-built bioelectronic device provided real-time control of vesicular insulin release; insulin levels peaked within 10 minutes. When subcutaneously implanted, this electrotriggered vesicular release system restored normoglycemia in type 1 diabetic mice.

**P**recise control of dosage is essential for the success of any drug-based therapy (1–4). However, taking pills or administering biopharmaceuticals at regular intervals based on body weight, as is standard medical practice, is far from being precise and does not reflect the dynamics required for sophisticated metabolic interventions (1–4). Cell-based therapies capitalizing on implanted encapsulated designer cells engineered to fine-tune in situ production and systemic delivery of protein therapeutics

in response to chemical and physical cues have shown promising results in proof-of-concept studies (5, 6). Because chemical control input is often limited, traceless physical cues such as light (optogenetics) (7–10) or heat [transmitted by magnetic fields (magnetogenetics) or radio waves (radiogenetics) (11–14)] are attractive for achieving rapid remote control of therapeutic transgene expression because they avoid the side effects of chemical trigger compounds (15, 16) as well as the challenges they may present with respect to bioavailability or pharmacodynamics (17–20). However, available physically triggered gene switches may require a high energy input (6, 7, 9), often involve complex chemical or inorganic cofactors (12, 21), and may require fine-tuning of the transcription of the therapeutic transgenes, which slows down the overall response dynamics (5, 6, 9, 12, 22). Thus, direct cofactor-free wireless electrical stimulation of engineered cells to control vesicular secretion of protein therapeutics in a

robust, adjustable, and repeatable manner would offer substantial advantages for medical applications by enabling direct communication between electronic devices and designer cells.

Although cellular metabolism and human-made electronics share similar operating principles in terms of input sensing, information processing, and output production, the core information transfer and processing functions of living and electronic systems are different, which limits their interoperability. Humans use ion gradients across insulated membranes to simultaneously process slow analog chemical reactions and communicate information in multicellular systems through soluble or gaseous molecular signals. In contrast, electronic systems use multicore central processing units to control the flow of electrons through insulated metal wires with gigahertz frequency and communicate information across networks via wired or wireless connections. Thus, direct electrical stimulation of gene expression or vesicular secretion requires a bioelectronic interface that manages electrical conduction between electrodes and electrosensitive designer cells, as well as conversion of electronic information via depolarization to protein production and release.

The first attempts to create an electrogenetic interface were reported more than a decade ago (23, 24), but that interface was neither direct nor usable under physiological conditions. More recently, a SoxR-based redox system that can control gene expression in *Escherichia coli* was reported (25), but this was also indirect and was too toxic for in vivo application. Thus, despite decades of expertise in converting trigger-inducible bacterial and fungal repressor-operator interactions into synthetic mammalian gene switches, simple translation of bacterial electrogenetics into a mammalian cellular context has been unsuccessful because of the cytotoxicity, limited bioavailability, and poor clinical compatibility of electrosensitive redox compounds (23).

<sup>1</sup>Department of Biosystems Science and Engineering, ETH Zurich, CH-4058 Basel, Switzerland. <sup>2</sup>Shanghai Key Laboratory of Regulatory Biology, Institute of Biomedical Sciences and School of Life Sciences, East China Normal University, Shanghai 200241, People's Republic of China. <sup>3</sup>Département Génie Biologique, Institut Universitaire de Technologie Lyon 1, F-69622 Villeurbanne Cedex, France. <sup>4</sup>Key Laboratory of Growth Regulation and Transformation Research of Zhejiang Province, School of Life Sciences, Westlake University, Hangzhou, People's Republic of China. <sup>5</sup>Faculty of Science, University of Basel, CH-4058 Basel, Switzerland.

\*Present address: Novartis Pharma AG, CH-4002 Basel, Switzerland. **†Corresponding author.** Email: fussenegger@bsse.ethz.ch

With the advent of optogenetics, it became possible to use illumination to control target gene expression remotely, and thus to indirectly link electrical stimulation via a light source with cellular transcription control (6, 10). This enabled glycemic control of experimental type 2 diabetes by controlling an optogenetic biomedical implant with a smartphone to upload instructions for designer cells to produce and systemically deliver a therapeutic dose of an insulinogenic peptide (6). However, the optogenetic device requires a considerable amount of energy to operate the light source (6, 10). The power efficiency associated with direct electrical stimulation is a major reason why clinically licensed pacemakers can be battery-powered for a lifespan of at least 15 years (26). Other major challenges to the clinical application of optogenetic technology include illumination-based cytotoxicity (27), the use of bacterial components (6, 10, 18–20), and the need for sophisticated chemical or inorganic cofactors that have side effects (28–30), poor bioavailability, or short half-lives in vivo (31). Other traceless physical control technologies based on electro-induced heat transmission, such as magneto- and radiogenetics, share the same challenges (12, 21, 32, 33).

Diabetes is a common, chronic condition, and so is an attractive target for individualized precision treatment. Regulation of blood glucose levels is a closed-loop homeostatic process. Glucose-stimulated insulin release by pancreatic  $\beta$  cells involves uptake and metabolism of glucose, adenosine triphosphate-mediated closure of potassium channels, depolarization of the plasma membrane, and opening of the voltage-gated calcium channels, which results in an intracellular  $\text{Ca}^{2+}$  surge and concurrent rapid release of insulin from intracellular storage vesicles (34). For intervention in this process, we aimed to design a bioelectronic interface consisting of an implantable platform that combines electronics and electrosensitive designer cells that can release insulin on demand. The implant would incorporate a cell chamber containing semi-permeable membranes that permit nutrient supply and product delivery via fibrous connective tissue, while protecting the designer cells from cellular host responses (35, 36) and securely containing them for safety reasons (37). To address this need, we describe here a direct cofactor-free electrogenetic interface to trigger vesicular secretion of insulin by using electrical stimulation to modulate the membrane polarization of human  $\beta$  cells engineered for ectopic expression of calcium and potassium channels ( $\text{Electro}\beta$  cells). Furthermore, to validate our approach, we incorporated these electrosensitive designer cells into a bioelectronics implant and evaluated its performance in a mouse model of type 1 diabetes.

### Membrane depolarization-based transcriptional control in mammalian cells

L-type voltage-gated calcium channels consist of  $\alpha_1$ ,  $\alpha_2$ ,  $\delta$ , and  $\beta$  subunits and are essential for the functioning of cardiomyocytes, neurons, and endocrine cells (38). These channels open upon membrane depolarization, and the resulting calcium influx regulates muscle contraction, vesicular secretion of hormones, and

NFAT (nuclear factor of activated T cells)-driven induction of target genes (39).

To design a mammalian transcription-control circuit responsive to membrane depolarization, we cotransfected human embryonic kidney (HEK) 293T cells with one of the three L-type voltage-gated calcium channels— $\text{Ca}_v1.2$ ,  $\text{Ca}_v1.3_{\Delta 42\Delta}$ , or  $\text{Ca}_v1.3_{\Delta 42}$ —encoded by the common  $\alpha_2/\delta_1$  ( $\text{pCa}_v\alpha_2\delta_1$ ,  $\text{P}_{\text{HCMV}}\alpha_2/\delta_1$ -pA) and  $\beta_3$  ( $\text{pCa}_v\beta_3$ ,

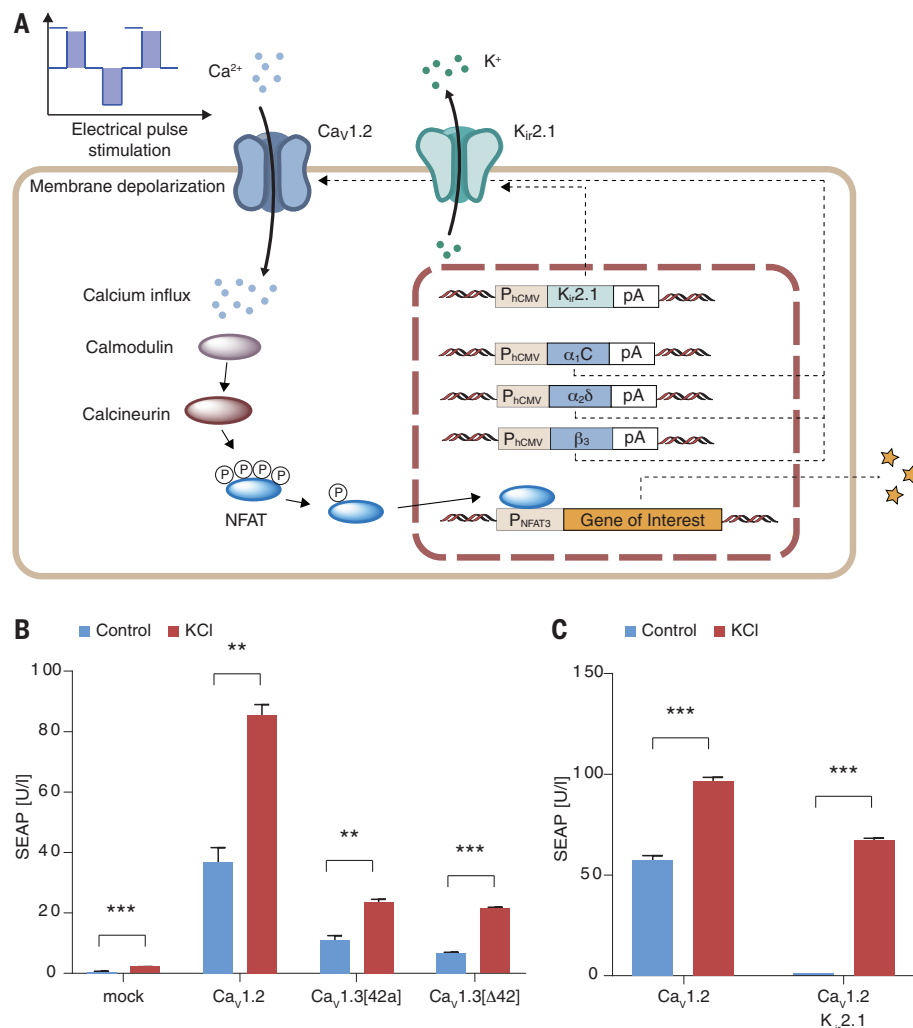


**Fig. 1. Design of the electrogenetic circuit in mammalian cells.** (A) Schematic representation of the electrogenetic circuit. The inwardly rectifying potassium channel lowers the resting membrane potential of HEK-293T cells, and electrical pulses depolarize the plasma membrane and open the L-type voltage-gated calcium channel. Calcium influx activates the calmodulin/calcineurin pathway, which leads to dephosphorylation of NFAT and its translocation to the nucleus, where it activates the NFAT-sensitive promoter and triggers transgene expression. (B) Comparative performance of three L-type voltage-gated calcium channels. Cells were cotransfected with  $\text{P}_{\text{NFAT3}}$ -driven SEAP reporter plasmid (pMX57), plasmids encoding  $\alpha_2/\delta_1$  ( $\text{pCa}_v\alpha_2\delta_1$ ,  $\text{P}_{\text{HCMV}}\alpha_2/\delta_1$ -pA) and  $\beta_3$  ( $\text{pCa}_v\beta_3$ ,  $\text{P}_{\text{HCMV}}\beta_3$ -pA), and one of the pore-forming subunits:  $\alpha_1\text{C}$  ( $\text{pCa}_v1.2$ ,  $\text{P}_{\text{HCMV}}\alpha_1\text{C}$ -pA),  $\alpha_1\text{D}_{42\Delta}$  ( $\text{pCa}_v1.3_{\Delta 42\Delta}$ ,  $\text{P}_{\text{HCMV}}\alpha_1\text{D}_{42\Delta}$ -pA), and  $\alpha_1\text{D}_{\Delta 42}$  ( $\text{pCa}_v1.3_{\Delta 42}$ ,  $\text{P}_{\text{HCMV}}\alpha_1\text{D}_{\Delta 42}$ -pA), to form  $\text{Ca}_v1.2$ ,  $\text{Ca}_v1.3_{\Delta 42\Delta}$ , and  $\text{Ca}_v1.3_{\Delta 42}$ , respectively. pcDNA3.1(+) was used as a mock plasmid. The cell membrane was depolarized with 40 mM potassium chloride (red bars); after 24 hours, SEAP was quantified in the supernatant. Blue bars show negative controls. (C) Coexpression of L-type voltage-gated calcium channel  $\text{Ca}_v1.2$  and inwardly rectifying potassium channel  $\text{K}_{ir2.1}$ . Cells were cotransfected with  $\text{pCa}_v1.2$  ( $\text{P}_{\text{HCMV}}\alpha_1\text{C}$ -pA),  $\text{pCa}_v\alpha_2\delta_1$  ( $\text{P}_{\text{HCMV}}\alpha_2/\delta_1$ -pA),  $\text{pCa}_v\beta_3$  ( $\text{P}_{\text{HCMV}}\beta_3$ -pA),  $\text{pK}_{ir2.1}$  ( $\text{P}_{\text{HCMV}}\text{K}_{ir2.1}$ -pA), and pMX57 ( $\text{P}_{\text{NFAT3}}$ -SEAP-pA) in the molar proportions 1:1:1:1:3. Cells were depolarized with 40 mM KCl for 24 hours (red bars) and SEAP was quantified in supernatant samples. Data are means  $\pm$  SEM;  $n = 3$ . \*\* $P < 0.01$ , \*\*\* $P < 0.001$  (versus control).

$P_{hCMV}\beta_3$ -pA) subunits and the respective channel-forming subunits  $\alpha_1C$  ( $pCa_{v1.2}$ ,  $P_{hCMV}\alpha_1C$ -pA),  $\alpha_1D_{42A}$  ( $pCa_{v1.3_{42A}}$ ,  $P_{hCMV}\alpha_1D_{42A}$ -pA), or  $\alpha_1D_{442}$  ( $pCa_{v1.3_{442}}$ ,  $P_{hCMV}\alpha_1D_{442}$ -pA), as well as the reporter plasmid pMX57 encoding the human placental secreted alkaline phosphatase (SEAP) driven by the  $P_{NFAT3}$  promoter (pMX57,  $P_{NFAT3}$ -SEAP-pA) (Fig. 1A). Depolarization of channel-transgenic HEK-293T cells with 40 mM KCl revealed that ectopic expression of  $Ca_{v1.2}$  showed the highest depolarization-triggered SEAP induction (Fig. 1B).

Coexpression of the inwardly rectifying potassium channel  $K_{ir2.1}$  ( $pK_{ir2.1}$ ,  $P_{hCMV}K_{ir2.1}$ -pA), which has been reported to decrease the resting membrane potential of mammalian cells (40), substantially decreased basal SEAP expression and improved the overall induction profile of the depolarization-triggered  $Ca_{v1.2}$ -mediated transcription control device (Fig. 1C). Combinatorial analysis of the importance of  $Ca_{v1.2}$ 's individual components for overall depolarization-triggered transcription control revealed that the channel-forming  $\alpha_1C$  subunit was essential, whereas  $\alpha_2/\delta_1$  and  $\beta_3$  were not, although their absence reduced the maximum SEAP expression (fig. S1). Therefore, we used cells expressing the full  $Ca_{v1.2}$  with the  $\alpha_1C$ ,

$\alpha_2/\delta_1$ , and  $\beta_3$  components as well as Kir2.1, referred to as  $ElectroHEK$ , in all follow-up experiments. Note that  $ElectroHEK$  cells are not activated by physiological ion concentrations, not even at life-threatening levels of KCl [6.5 mM (27)] or at  $CaCl_2$  levels representing a medical emergency [3.5 mM (28)] (fig. S2).

### Design and characterization of a synthetic electrogenetic mammalian transcription-control device

To test whether transgene expression could be directly triggered by electrically stimulated membrane depolarization, we used voltage-controlled square unipolar pulses with alternate polarization to electrostimulate the  $ElectroHEK$  cells transfected with the  $P_{NFAT3}$ -driven SEAP expression vector (pMX57,  $P_{NFAT3}$ -SEAP-pA) (41–43) (Fig. 2A). Indeed, electric pulse stimulation triggered pMX57-transgenic  $ElectroHEK$  cells to produce high levels of SEAP (Fig. 2, B to D). The electrostimulated transgene expression could be fine-tuned by voltage (maximum SEAP induction at 50 V) (Fig. 2B) and could also be adjusted by altering the pulse length (maximum SEAP induction at 2 ms) (Fig. 2C). Full activation of the system was reached after 4 hours of stimulation (Fig. 2D). Electrostim-

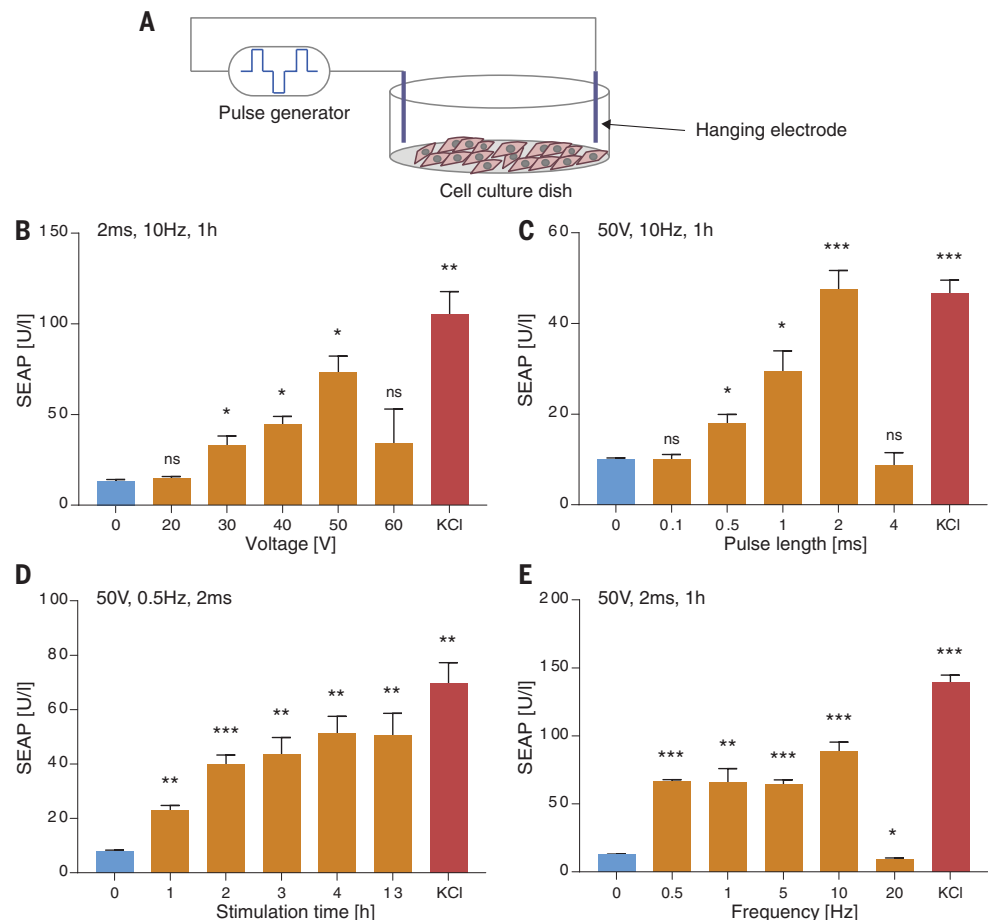
ulation efficiency did not depend on the pulsing frequency within the range of 0.5 to 10 Hz (Fig. 2E). The parameter set used for effective electrostimulation did not decrease cell viability (fig. S3, A to D). Additionally,  $Ca_{v1.2}$ -deficient HEK-293T cells were insensitive to electrostimulation (fig. S3E). Kinetic experiments revealed maximum SEAP expression 7 hours after the beginning of stimulation (fig. S4A) and confirmed the reversibility of the system (fig. S4B).

### Design of the bioelectronic implant

Translation of electrostimulated gene expression into a clinical proof-of-concept bioelectronic implant required a more compact design for electrodes and electrostimulation. Simple miniaturization of the free-hanging electrodes used in the device described above did not provide efficient electrostimulation. Thus, we designed a custom-engineered cell culture insert containing electrodes on either side of a semipermeable membrane harboring a monolayer of electrosensitive  $ElectroHEK$  cells (Fig. 3A). Electrostimulation of pMX57 ( $P_{NFAT3}$ -SEAP-pA)-transfected  $ElectroHEK$  cells resulted in peak SEAP levels at 7.5 V (Fig. 3, B and C), which is one order of magnitude lower than that of the

### Fig. 2. Characterization of the electrogenetic circuit in vitro. (A) Schematic representation of electrical stimulation setup.

Cells were stimulated with carbon hanging electrodes producing monopolar pulses with alternate polarization. (B to E) Cells were cotransfected with p $Ca_{v1.2}$  ( $P_{hCMV}\alpha_1C$ -pA), p $Ca_{v1.2}\delta_1$  ( $P_{hCMV}\alpha_2/\delta_1$ -pA), p $Ca_{v1.2}\beta_3$  ( $P_{hCMV}\beta_3$ -pA), pKKO5 ( $P_{hCMV}K_{ir2.1}$ -pA), and pMX57 ( $P_{NFAT3}$ -SEAP-pA) in the molar proportions 1:1:1:1:3. SEAP assay was performed 24 hours after the beginning of the electrical stimulation procedure. Blue, orange, and red bars respectively denote unstimulated controls, electrically stimulated samples, and cells depolarized with 40 mM KCl. (B) Voltage dependence. Electrical stimulation was performed for 1 hour with 2-ms pulses at 10 Hz and the indicated voltage. (C) Pulse length effect. Electrical stimulation was performed for 1 hour at 10 Hz, 50 V, and the indicated pulse length. (D) Time course. Electrical stimulation was performed for the indicated period of time with 2-ms pulses at 0.5 Hz and 50 V. (E) Frequency effect. Electrical stimulation was performed for 1 hour with 2-ms pulses at 50 V and at the indicated frequency. Data are means  $\pm$  SEM;  $n = 3$ . \* $P < 0.05$ , \*\* $P < 0.01$ , \*\*\* $P < 0.001$  (versus control); ns, not significant.



previous free-hanging electrode arrangement, and at shorter pulse length (Fig. 3, D and E); both factors are important for high power efficiency of any electrostimulation device.

To enable electrostimulated transgene expression by electrosensitive cells in vivo, we designed a wireless-powered bioelectronic implant. The custom-engineered cell culture insert equipped with the electrodes was clicked into a 3D-printed FDA-licensed polyamide casing (Fig. 4, A and B) containing a sealed electronic switchboard (figs. S5 and S6) that generated the square unipolar pulses for electrostimulation of the encapsulated *Electro*HEK cells. The implant's electronic circuitry was inductively powered and controlled by an extracorporeal field generator that wirelessly communicated with the bioelectronic implant at the ISM (industrial, scientific, and medical) frequency of 13.56 MHz (Fig. 4B and figs. S7 and S8). The voltage of the square pulses generated by the implant was dependent on the distance to the center of the field generator (fig. S9). The electronic circuit was insensitive to temperatures between 25° and 50°C (table S1). A control run of the bioelectronic implant validated wireless-controlled electrostimulated SEAP expression of pMX57-transfected *Electro*HEK cells (Fig. 4C). We confirmed that the bioelectronic implants are rated IPX7 waterproof (International Protection Marking, IEC standard 60529) and show no cell leakage in a 5-day in vitro experiment (table S2).

#### *Electro*β cells provide electrostimulated vesicular secretion

Because *Electro*HEK-based insulin production is transcription-based, it lacks the rapid release dynamics of vesicular secretion characteristic of native pancreatic β cells (5). To engineer mammalian cells for electrostimulated vesicular release of insulin (Fig. 5A), we derived a monoclonal population, *INS<sub>Vesc</sub>*, from the pancreatic β cell line 1.1E7 (44) by selection for deficiency in glucose sensitivity (Fig. 6, E and F), but with retention of the vesicular insulin secretion machinery. Indeed, electron micrographs of *Electro*β cells, an *INS<sub>Vesc</sub>* variant stably transgenic for constitutive expression of *Ca<sub>v</sub>1.2* and *K<sub>ir</sub>2.1* channels (pKK66, *P<sub>hEF1α</sub>-α<sub>1</sub>C-P2A-K<sub>ir</sub>2.1-pA*; pMX251, *P<sub>hEF1α</sub>-α<sub>2</sub>/δ<sub>1</sub>-P2A-β<sub>3</sub>-pA*) as well as Proinsulin-NanoLuc, a designer construct engineered to co-secrete insulin and the *Oplophorus gracilirostris* luciferase (NanoLuc) at an equimolar ratio in endocrine cell types (45) (Fig. 5A), revealed storage vesicles reminiscent of insulin-containing granules of human islet-derived β cells (Fig. 5, D and E). Additionally, *Electro*β cells showed well-correlated vesicular insulin and NanoLuc secretion in response to KCl-mediated (Fig. 5, B and C) or electrostimulated (Fig. 6, A and B) membrane depolarization. The stability and functionality of the *Electro*β cell line were

confirmed over at least 30 passages during 3 months in continuous culture (fig. S10).

We profiled the depolarization-based insulin release dynamics by electrostimulating *Electro*β cells and recording the corresponding NanoLuc-mediated luminescence in the

culture supernatant (Fig. 6C). Peak NanoLuc levels were reached within 10 min after electrostimulation (Fig. 6C), whereas transcription-based insulin production and secretion by *Electro*HEK, HEK-β (5), and *Opto*HEK cells (9) required 8 hours (fig. S11). When repeatedly

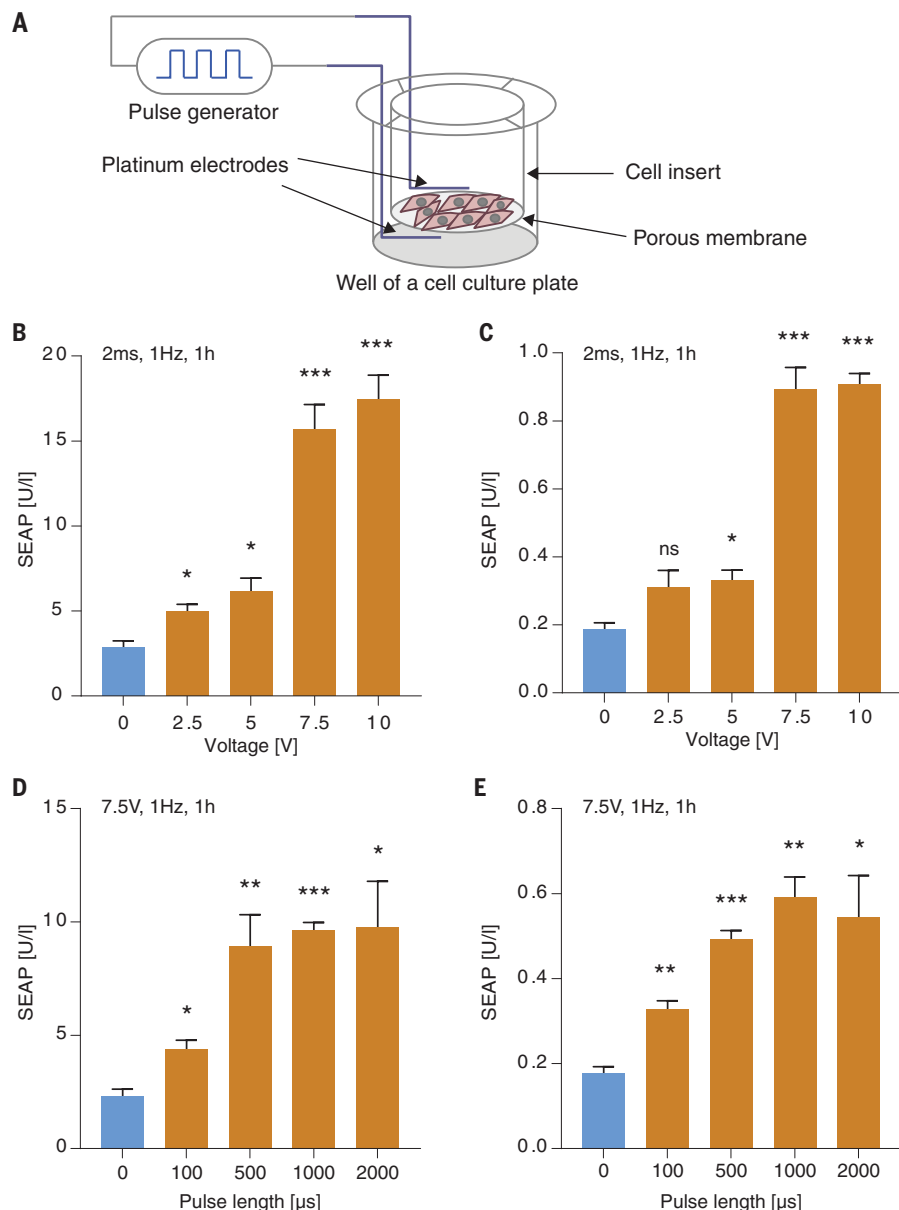


**Fig. 3. Design and functionality of the bioelectronic implant in vitro.** (A) Schematic representation of the stimulation setup in a cell culture insert. Two platinum electrodes (blue) were placed on opposite sides of the porous membrane covered with cells, and electrical pulse stimulation was applied. SEAP was quantified 24 hours after stimulation in the supernatants of the cell culture insert (above the membrane) and the well of the cell culture plate (below the membrane) to confirm that the secreted protein diffused across the membrane of the cell culture insert. (B and C) Voltage-dependent response of electrically stimulated pMX57-transfected *Electro*HEK cells grown in a cell culture insert. Cells were stimulated with 2-ms pulses at 1 Hz for 1 hour (orange bars). SEAP was measured in supernatant samples from the cell culture insert (above the membrane) (B) and from the cell culture well (below the membrane) (C). Blue bars denote negative controls. (D and E) Pulse length dependence. Cells were stimulated with 7.5 V pulses at 1 Hz for 1 hour (orange bars). SEAP was measured from supernatant samples from above (D) and below the cell layer (E). Blue bars denote negative controls. Data are means ± SEM; n = 3. \*P < 0.05, \*\*P < 0.01, \*\*\*P < 0.001 (versus unstimulated control).

electrostimulated,  $\text{Electro}\beta$  cells recovered full secretory capacity after 4 hours (Fig. 6D). Most important,  $\text{Electro}\beta$  cells did not show any glucose-sensitive insulin production, which ensures exclusive electrostimulation control of vesicular insulin secretion without interference from blood glucose levels (Fig. 6, E and F). Overall,  $\text{Electro}\beta$  cells showed electrostimulation parameters similar to those of  $\text{ElectroHEK}$  cells (fig. S12, A to D). To illustrate the broad applicability of our approach, we also demonstrated electrostimulated vesicular

secretion of glucagon by pancreatic alpha cells, which secrete the insulin counterregulatory hormone glucagon by calcium-triggered vesicular release (46) (fig. S13); this is akin to  $\beta$  cell-mediated insulin secretion.

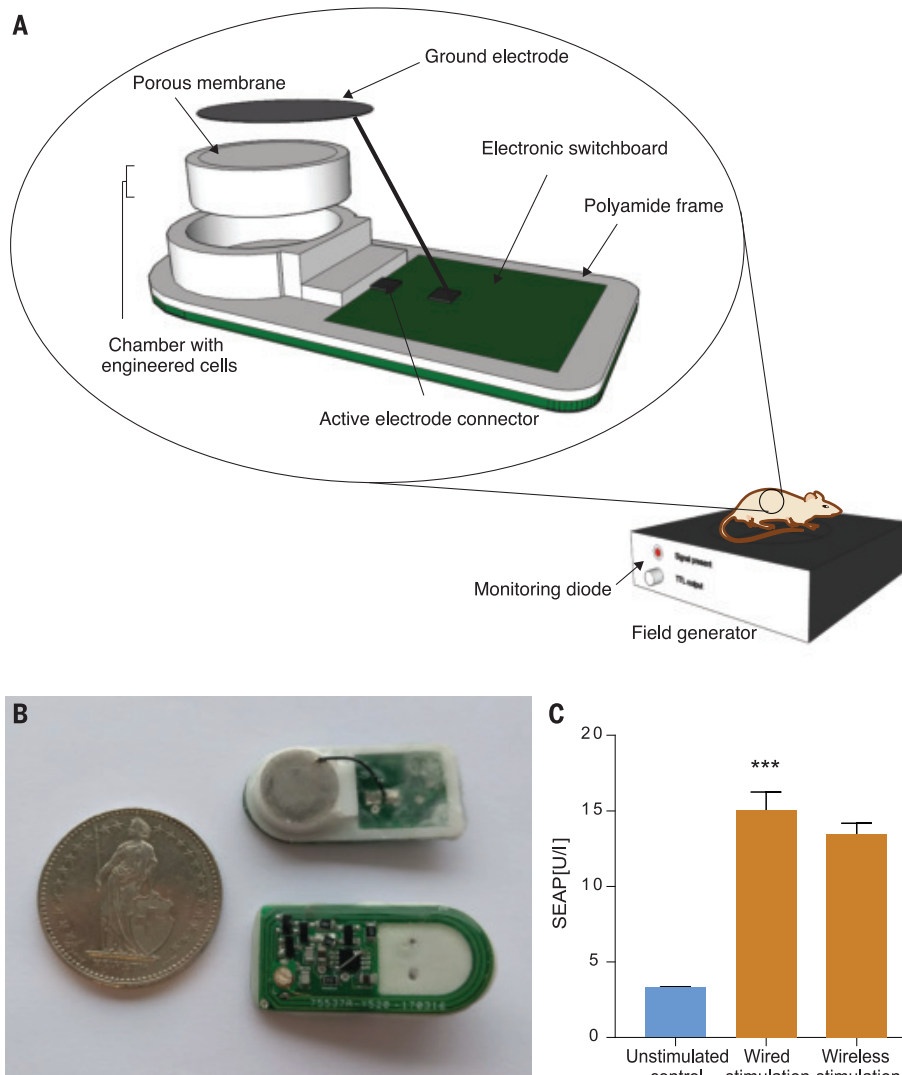
#### Wireless electrostimulated vesicular secretion of insulin provides rapid glycemic control in type 1 diabetic mice

Native pancreatic  $\beta$  cells release the insulin stored in granules via a process known as vesicular secretion (34). The immediate release of

stored insulin improves the response dynamics and rapidly restores blood glucose homeostasis in response to postprandial excursions. So far, designer cell-based proof-of-concept strategies to treat experimental diabetes have focused on transcriptional control, which is considered too slow to cope with postprandial blood glucose surges (5, 6, 12, 14, 21). For example, previously reported HEK- $\beta$  cells (5), which rely on transcriptional control and the classical secretory pathway for insulin release, require up to 24 hours to reach physiological blood insulin levels (fig. S14). Similar performance was observed for  $\text{OptoHEK}$  cells (9). In contrast, when placed into the wireless-powered bioelectronic implant (Fig. 4),  $\text{Electro}\beta$  cells could reestablish postprandial glucose metabolism in insulin-deficient type 1 diabetic mice after a brief electrostimulation without causing hypoglycemic excursions (Fig. 7A) and could rapidly decrease blood glucose levels to restore normoglycemia after electrostimulation (Fig. 7B). Notably, the results of glucose tolerance tests revealed comparable performance between  $\text{Electro}\beta$  cells and human pancreatic islets, which are known to release insulin by vesicular secretion upon glucose sensing (fig. S7A). Fast vesicular secretion was also confirmed by blood luminescence quantification (47), which showed a peak signal just 1 hour after electrostimulation, returning to baseline after 2 hours (Fig. 7C). Glycemia could also be controlled over longer periods of time without any sign of hypoglycemia (Fig. 7D).

#### Biocompatibility and functional longevity of the bioelectronic implant

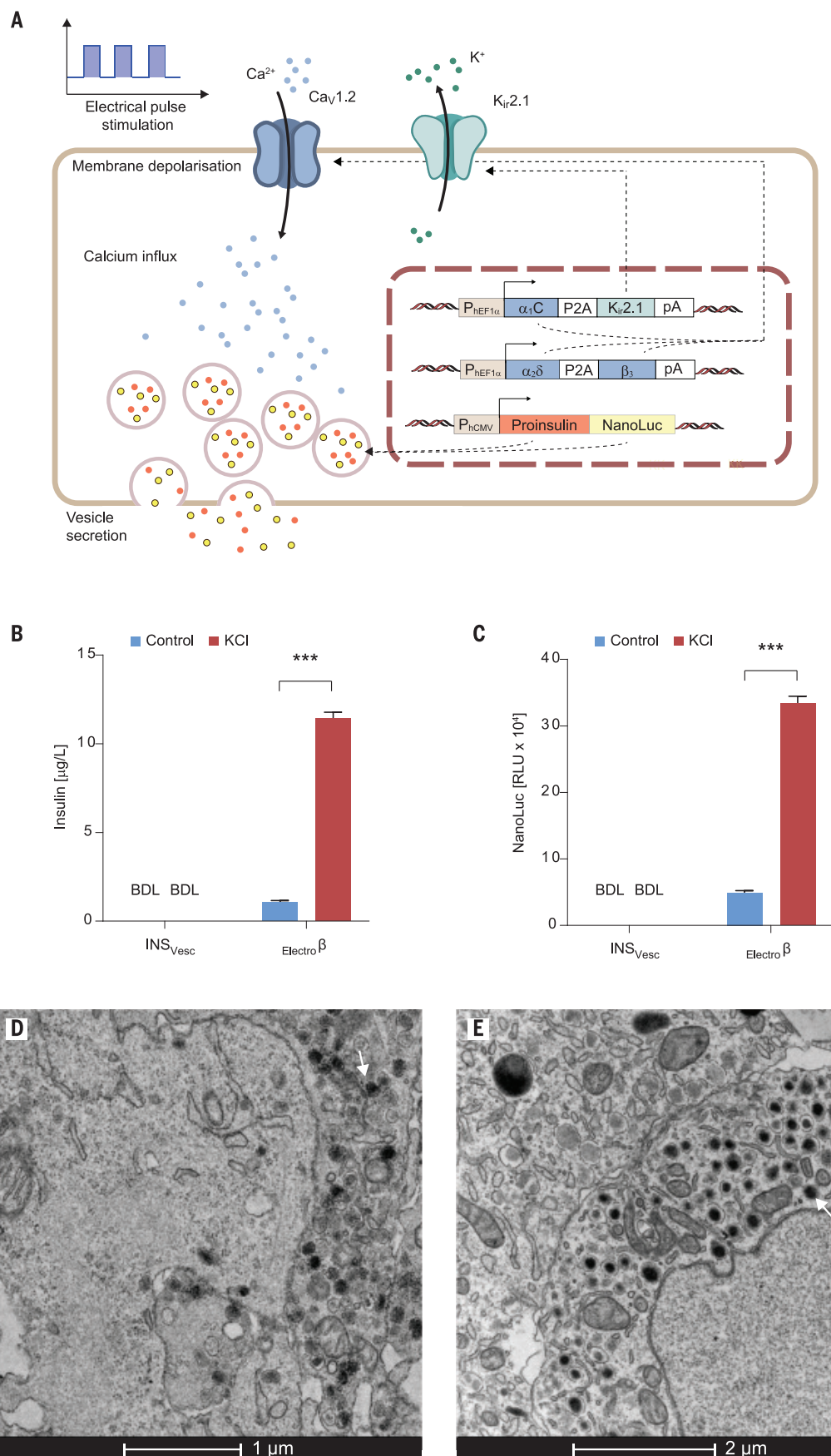
To validate the biocompatibility of the bioelectronic implants, we analyzed treated animals as well as explanted devices at 3 weeks after implantation, according to ISO 10993 (48), and we observed no material cytotoxicity, systemic kidney or liver toxicity, or alteration of hematologic profile or systemic immune responses; in addition, we saw no local immune-cell infiltration or substantial fibrotic tissue formation at the implant-tissue interface. There was no apparent indication of implant-related cytotoxicity (fig. S15) or systemic toxicity (table S3), and no apparent difference in hematologic profiles among cell-containing and cell-free bioelectronic implants and biocompatible control implants (table S4). Likewise, we found no marked difference in the well-vascularized fibrous capsule surrounding the implants (fig. S16) or in immune-cell infiltration (fig. S17 and table S5) among cell-containing, cell-free, and biocompatible control implants. Mice implanted with  $\text{Electro}\beta$  cell-containing bioelectronic devices showed no change of body weight relative to untreated animals; also, signs of irritation or inflammation, as well as serum levels of inflammatory cytokines, were



**Fig. 4. Bioelectronic implant in vitro.** (A) Three-dimensional model of a disassembled bioelectronic implant. A ring containing a porous membrane on one side can be assembled with a 3D-printed polyamide frame to form a cell chamber. The electronic switchboard is placed on the other side of the frame. The active platinum electrode (placed in the cell chamber; invisible in the model) is soldered to a connector on a switchboard. The ground electrode, made out of thin stainless steel mesh, is connected to the second connector on a switchboard. The bioelectronic implant can be placed subcutaneously on the dorsal side of the mouse, with the cell chamber facing down. The field generator provides wireless energy transmission. A red diode enables implant function monitoring. (B) Photograph of two bioelectronic implants with a coin (diameter 27.4 mm) for comparison. (C) Comparison of external generator-powered and implant-powered electrostimulation of pMX57-transfected  $\text{ElectroHEK}$  cells. SEAP was measured in supernatant samples from above the cell layer. Data are means  $\pm$  SEM;  $n = 3$ . \*\*\* $P < 0.001$  (versus control).

### Fig. 5. Electrogenetic engineering of $\beta$ cells.

**(A)** Schematic representation of the electrically inducible insulin secretion pathway. The inwardly rectifying potassium channel  $K_{ir}2.1$  lowers the resting membrane potential, which keeps the voltage-gated calcium channel  $Ca_v1.2$  closed. Electrical pulse stimulation causes membrane depolarization, opening of  $Ca_v1.2$ , and calcium influx, which stimulates vesicle secretion. Vesicles are loaded with pre-produced insulin (red dots) and NanoLuc (yellow dots). **(B and C)** Comparison of insulin secretion by  $INS_{Vesc}$  and  $Electro\beta$  cells. Vesicle secretion was quantified by insulin-specific enzyme-linked immunosorbent assay (ELISA) (B) and luminescence (C) before (blue bars) and after depolarization with 40 mM KCl (red bars). BDL, below detection limit. Data are means  $\pm$  SEM;  $n = 3$ . \*\*\* $P < 0.001$  (versus control). **(D)** Transmission electron microscopy (TEM) image of  $Electro\beta$  cells. White arrow indicates an insulin-containing vesicle. **(E)** TEM image of primary  $\beta$  cells from human pancreatic islets. White arrow indicates an insulin-containing vesicle.



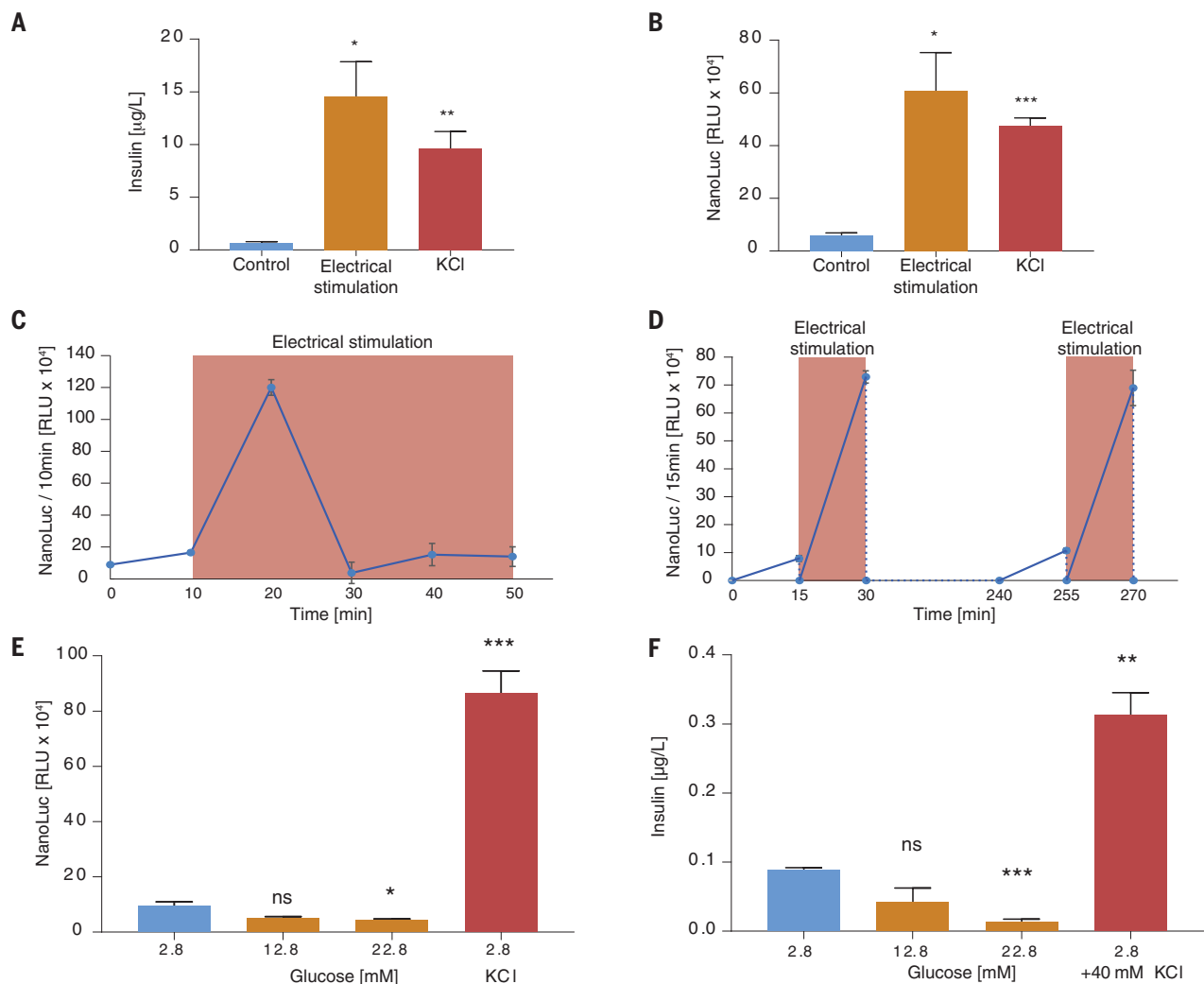


**Fig. 6. Functionality of  $\text{Electro}\beta$  cells in vitro.** (A and B) Electrostimulation of  $\text{Electro}\beta$  cells. Cells were seeded into cell culture inserts, and 24 hours later they were stimulated with electrical pulses (orange bars) or with 40 mM KCl (red bars). Blue bars denote negative controls. (A) Insulin content in the supernatant from inside the insert (above the cell layer) was measured by ELISA;  $n = 3$ . (B) Luminescence was measured in supernatant samples taken from inside the insert (above the cell layer);  $n = 3$ . (C) Secretion kinetics.  $\text{Electro}\beta$  cells were seeded into cell culture inserts and stimulated with electrical pulses (red frame). Luminescence was measured in supernatant samples every 10 min;  $n = 4$ . (D) Reversibility assay.  $\text{Electro}\beta$  cells were electrostimulated for 15 min twice, with

4-hour time intervals between the first and second electrostimulation;  $n = 4$ . (E) Glucose-induced insulin release.  $\text{Electro}\beta$  cells were incubated with various concentrations of glucose for 15 min (blue bar, 2.8 mM glucose; orange bars, elevated glucose; red bar, 2.8 mM glucose with 40 mM KCl). Luminescence was measured in supernatant samples;  $n = 3$ . (F) Glucose-induced insulin release.  $\text{INS}_{\text{vesc}}$  cells were incubated with various concentrations of glucose for 60 min (blue bar, 2.8 mM glucose; orange bars, elevated glucose; red bar, 2.8 mM glucose with 40 mM KCl). Insulin content was quantified in supernatant samples;  $n = 3$ . Data are means  $\pm$  SEM. \* $P < 0.05$ , \*\* $P < 0.01$ , \*\*\* $P < 0.001$  (versus control).

similar to or lower than those of animals treated with cell-free or biocompatible reference implants (figs. S18 and S19). Visual inspection of explanted bioelectronic devices showed no decomposition and no apparent erosion (fig. S20).

In view of the need for clinical translation toward a lifestyle-compatible therapeutic product, we adapted the bioelectronic implant architecture to allow repetitive exchange of individual cell batches over time (fig. S20A). Sequential in situ “refilling” of the implanted bioelectronic device with fresh batches of  $\text{Electro}\beta$  cells without the need for surgical

removal or replacement of the implant will reduce cost as well as implant-associated infections, while increasing patients’ convenience and treatment longevity. Insulin levels of type 1 diabetic mice, which had the  $\text{Electro}\beta$  cells of their bioelectronic implants replaced once a week for a period of 3 weeks, were restored after remote-controlled electrostimulated insulin release by  $\text{Electro}\beta$  cells (fig. S20, B and C). Together, these results suggest that the bioelectronic implant successfully integrates the advantages of electronics-based (49) and cell-based counterparts (5) and represents a promising approach to diabetes treatment.

## Discussion

In this work, we have eliminated the need to use light as a converter between electronics and genetics, advancing optogenetics into electrogenetics by engineering a direct, cofactor-free electrogenetic interface that enables electronics to directly program gene expression as well as vesicular secretion in human cells. Furthermore, by incorporating electrogenetic designer cells ( $\text{Electro}\beta$ ) containing this interface into a bioelectronic implant, we have successfully implemented a proof-of-concept device providing rapid electrostimulated insulin release for the treatment of experimental

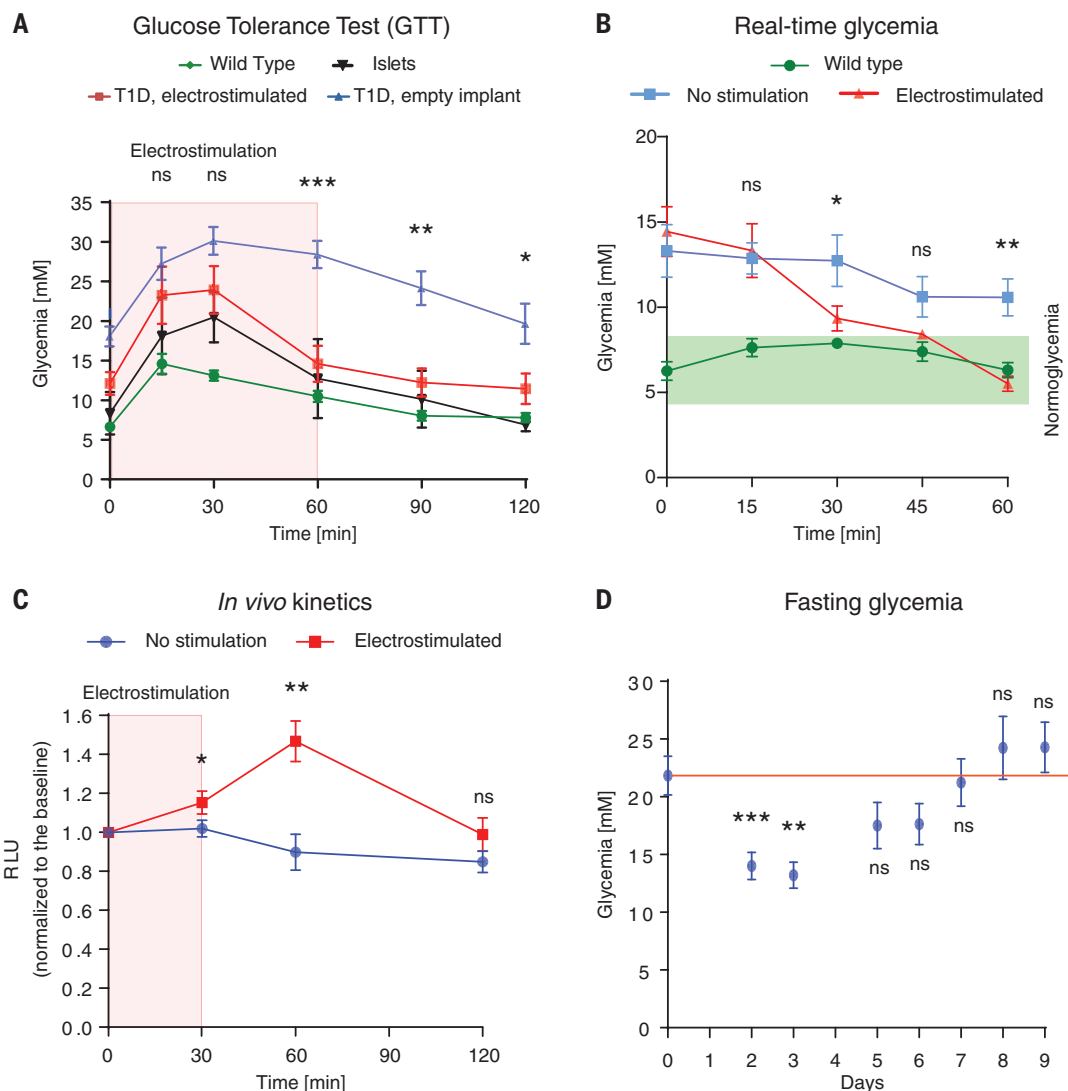


**Fig. 7. Comparative analyses of  $\text{Electro}\beta$ -containing bioelectronic implants in type 1 diabetic mice.** Type 1 diabetic mice implanted on the back with  $\text{Electro}\beta$ -containing bioelectronic devices were profiled for blood glucose dynamics. **(A)** Glucose tolerance test. At 48 hours after implantation, the  $\text{Electro}\beta$  cells inside the bioelectronic implant were electrostimulated for 60 min (red line), then the animals were given intraperitoneal glucose injections and their blood glucose levels were monitored. All groups received intraperitoneal glucose injection (2 g per kg body weight). Wild type,  $n = 8$ ; T1D, implant electrostimulated (type 1 diabetes, activated implant),  $n = 6$ ; T1D, empty implant (type 1 diabetes, implant without cells),  $n = 10$ ; islets (human pancreatic beta islets),  $n = 3$ . Statistical significance of differences between the electrostimulated and mock groups was calculated. **(B)** Real-time glycemia measurement. Fasted type 1 diabetic mice implanted with  $\text{Electro}\beta$ -containing bioelectronic implants were electrostimulated for 30 min and their glycemic profile was recorded.

Nonstimulated control (T1D, implanted mice),  $n = 6$ ; stimulated group (T1D, implanted mice),  $n = 7$ ; wild-type controls,  $n = 6$ . The green frame indicates the normoglycemic range (4.4 to 7.2 mM). Statistical significance was calculated between electrostimulated mice and nonstimulated controls. **(C)** Blood luciferase kinetics of animals implanted with  $\text{Electro}\beta$  cell-containing implants electrostimulated for 30 min (red line;  $n = 6$ ). NanoLuc was quantified from microliter-scale blood samples every 30 min. The blue line indicates the nonelectrostimulated negative control ( $n = 5$ ); red frame indicates electrostimulation time. Statistical significance of differences versus time point 0 was calculated with a paired  $t$  test. **(D)** Fasting glycemia. Type 1 diabetic mice were implanted with  $\text{Electro}\beta$ -containing bioelectronic implants and fasting glycemia was recorded for more than 1 week. Orange line indicates the initial level of average glycemia. Statistical significance of differences versus time point 0 was calculated with a paired  $t$  test. Data are means  $\pm$  SEM. \* $P < 0.05$ , \*\* $P < 0.01$ , \*\*\* $P < 0.001$ .

type 1 diabetes. The overall slow response dynamics associated with transcription-based control systems (5, 6, 9, 10, 12, 15, 16, 18–21) highlights the importance of vesicular secretion for the treatment of diabetes, which requires quick vesicular release of insulin to respond rapidly to postprandial blood glucose surges (50, 51). Indeed, we found that wireless

electrical stimulation of vesicular insulin release from our engineered  $\text{Electro}\beta$  cells encapsulated in a bioelectronic implant could attenuate postprandial hyperglycemia in type 1 diabetic mice with performance comparable to that of transplanted human pancreatic islets.

Taking account of the importance of economical manufacturing, we integrated all

components of the bioelectronic implant into a 3D-printed polyamide casing. Although the bioelectronic implant could in principle be powered by batteries (52) (table S4), for practical reasons, including the limited space for implantation and the intrusiveness of animal experimentation, we chose to power the device inductively at 13.56 MHz, an FCC-licensed

radio frequency that is reserved internationally for industrial, scientific, and medical devices and does not interfere with telecommunications. Because of the power efficiency of the implant, we speculate that wireless-powered control by wearable devices such as smartphones and smartwatches might be feasible in the near future.

However, reaching the full therapeutic potential of electrogenetics will require closed-loop control. Whereas classical medical interventions are open-loop, because the dose is largely determined by the physician on the basis of body weight, closed-loop systems enable feedback control that coordinates biomarker input to therapeutic output and provides an autonomous and self-sufficient interface with patients' metabolism. For electrogenetic type 1 diabetes control, this would mean using electronic blood glucose sensors to directly control electrostimulated insulin release in real time, much like the concepts currently being explored for prototypes of the bionic pancreas (53). However, electronic closed-loop systems operating in the bionic pancreas require frequent calibration and have a short lifespan of only a few days (49). On the other hand, incorporation of a microcontroller and/or a glucometer into our bioelectronic implant to achieve closed-loop insulin control should be a straightforward electrical engineering implementation. Most important, the delayed resorption of insulin from subcutaneous tissues to which insulin is delivered by the bionic pancreas requires dual-hormone control using glucagon to counteract or prevent insulin-mediated hypoglycemia (54, 55). We show here that glucagon can be released from pancreatic  $\alpha$  cells by vesicular secretion, just as insulin is from  $\beta$  cells; this suggests that a dual-hormone electrogenetic system using two types of engineered cells would be feasible. Nonetheless, dual-hormone control is not expected to be necessary with our electrogenetic system because, as noted above, the dynamics of electrostimulated vesicular insulin secretion from  $\text{Electro}\beta$  cells appear to be comparable with those of human pancreatic islets. Furthermore, the demonstration that our system works in two different types of cells suggests broad potential applicability of electrogenetics for electrostimulated hormone release in future cell-based therapies.

As in the case of the bionic pancreas (53), long-term functionality of cellular implants remains a major challenge in designing next-generation encapsulated cell-based therapeutic devices (56). A recent clinical trial using encapsulated pancreatic progenitor cells, the precursor phenotype of insulin-secreting  $\beta$  cells (ViaCyte's VC-01), confirmed the need for further technological development to promote engraftment (57). Long-term functionality of cells inside implants remains among

the challenges facing translation of academic proof-of-concept studies into clinical reality. In this context, the first initiatives to improve viability (Beta-O2 Technologies Ltd.;  $\beta$ Air) as well as vascularization of encapsulated cells (58) (e.g., ViaCyte's PEC Direct or Sernova's Cell Pouch System) have already begun in industry.

We have shown that wireless electrical stimulation of insulin release by electrosensitive designer cells inside a bioelectronic implant was able to rapidly restore normoglycemia in type 1 diabetic mice. The adoption of wireless electronic devices that can program the release of biopharmaceuticals, either via the secretory pathway or vesicular secretion, by means of direct communication between the device and implanted cells is expected to open up many new opportunities for advanced precision healthcare optimized for individuals.

## REFERENCES AND NOTES

- M. M. Aye, S. L. Atkin, *Drug Healthc. Patient Saf.* **6**, 55–67 (2014).
- A. Goto, O. A. Arah, M. Goto, Y. Terauchi, M. Noda, *BMJ* **347**, f4533 (2013).
- G. P. Leese et al., *Diabetes Care* **26**, 1176–1180 (2003).
- C. Uduku, N. Oliver, *Curr. Opin. Pharmacol.* **36**, 29–33 (2017).
- M. Xie et al., *Science* **354**, 1296–1301 (2016).
- J. Shao et al., *Sci. Transl. Med.* **9**, eaal2298 (2017).
- T. Kushibiki, S. Okawa, T. Hirasawa, M. Ishihara, *Gene Ther.* **22**, 553–559 (2015).
- T. Kim, M. Folcher, M. Daoud-El Baba, M. Fussenegger, *Angew. Chem. Int. Ed.* **54**, 5933–5938 (2015).
- H. Ye, M. Daoud-El Baba, R. W. Peng, M. Fussenegger, *Science* **332**, 1565–1568 (2011).
- M. Folcher et al., *Nat. Commun.* **5**, 5392 (2014).
- H. A. Andersson, Y. S. Kim, B. E. O'Neill, Z. Z. Shi, R. E. Serda, *Vaccines* **2**, 216–227 (2014).
- V. Ortner et al., *J. Control. Release* **158**, 424–432 (2012).
- H. Huang, S. Delikanli, H. Zeng, D. M. Ferkey, A. Pralle, *Nat. Nanotechnol.* **5**, 602–606 (2010).
- S. A. Stanley, J. Sauer, R. S. Kane, J. S. Dordick, J. M. Friedman, *Nat. Med.* **21**, 92–98 (2015).
- M. Fussenegger et al., *Nat. Biotechnol.* **18**, 1203–1208 (2000).
- W. Weber et al., *Nat. Biotechnol.* **20**, 901–907 (2002).
- B. G. Auner, C. Valenta, J. Hadgraft, *J. Control. Release* **89**, 321–328 (2003).
- M. Gitzinger, C. Kemmer, M. D. El-Baba, W. Weber, M. Fussenegger, *Proc. Natl. Acad. Sci. U.S.A.* **106**, 10638–10643 (2009).
- M. Gitzinger et al., *Nucleic Acids Res.* **40**, e37 (2012).
- H. Wang, H. Ye, M. Xie, M. Daoud El-Baba, M. Fussenegger, *Nucleic Acids Res.* **43**, e91 (2015).
- S. A. Stanley et al., *Science* **336**, 604–608 (2012).
- A. Prindle et al., *Nature* **508**, 387–391 (2014).
- W. Weber et al., *Nucleic Acids Res.* **37**, e33 (2009).
- W. Weber et al., *Nat. Biotechnol.* **22**, 1440–1444 (2004).
- T. Tschirhart et al., *Nat. Commun.* **8**, 14030 (2017).
- D. Katz, T. Akiyama, *Ann. Noninvasive Electrocardiol.* **12**, 223–226 (2007).
- J. H. Stockley et al., *Sci. Rep.* **7**, 849 (2017).
- T. D. Hinds Jr. et al., *J. Biol. Chem.* **291**, 25179–25191 (2016).
- Y. Uda et al., *Proc. Natl. Acad. Sci. U.S.A.* **114**, 11962–11967 (2017).
- Z. Hu et al., *Int. J. Mol. Sci.* **16**, 22621–22635 (2015).
- H. M. Beyer et al., *ACS Synth. Biol.* **4**, 951–958 (2015).
- G. Jarockyte et al., *Int. J. Mol. Sci.* **17**, 1193 (2016).
- B. A. Maher et al., *Proc. Natl. Acad. Sci. U.S.A.* **113**, 10797–10801 (2016).
- F. M. Ashcroft, P. Rorsman, *Nat. Rev. Endocrinol.* **9**, 660–669 (2013).
- R. Buzzetti, S. Zampetti, E. Maddaloni, *Nat. Rev. Endocrinol.* **13**, 674–686 (2017).
- D. Jacobs-Tulleneers-Thevissen et al., *Diabetologia* **56**, 1605–1614 (2013).
- T. Desai, L. D. Shea, *Nat. Rev. Drug Discov.* **16**, 338–350 (2017).
- G. W. Zamponi, J. Striessnig, A. Koschak, A. C. Dolphin, *Pharmacol. Rev.* **67**, 821–870 (2015).
- M. D'Arco, A. C. Dolphin, *Sci. Signal.* **5**, pe34 (2012).
- T. Kim et al., *Biochem. Biophys. Res. Commun.* **324**, 401–408 (2004).
- A. Luicà-Valledeperas et al., *J. Tissue Eng. Regen. Med.* **9**, E76–E83 (2015).
- M. H. Thelen, W. S. Simonides, C. van Hardeveld, *Biochem. J.* **321**, 845–848 (1997).
- Y. Manabe et al., *PLOS ONE* **7**, e52592 (2012).
- J. T. McCluskey et al., *J. Biol. Chem.* **286**, 21982–21992 (2011).
- S. M. Burns et al., *Cell Metab.* **21**, 126–137 (2015).
- J. Gromada, P. Chabosseau, G. A. Rutter, *Nat. Rev. Endocrinol.* **14**, 694–704 (2018).
- H. Yamashita, D. T. Nguyen, E. Chung, *Methods Mol. Biol.* **1098**, 145–151 (2014).
- B. Rattner, in *Host Response to Biomaterials*, S. Badyal, Ed. (Academic Press, 2015), pp. 37–51.
- S. J. Russell et al., *Lancet Diabetes Endocrinol.* **4**, 233–243 (2016).
- P. A. Hollander et al., *Diabetes Care* **24**, 983–988 (2001).
- S. E. Kahn et al., *J. Clin. Endocrinol. Metab.* **86**, 5824–5829 (2001).
- H. G. Mond, G. Freitag, *Pacing Clin. Electrophysiol.* **37**, 1728–1745 (2014).
- S. J. Russell et al., *N. Engl. J. Med.* **371**, 313–325 (2014).
- G. Schmelzeisen-Redeker et al., *J. Diabetes Sci. Technol.* **9**, 1006–1015 (2015).
- D. B. Keenan, J. J. Mastrototaro, G. Voskanyan, G. M. Steil, *J. Diabetes Sci. Technol.* **3**, 1207–1214 (2009).
- M. Qi, *Adv. Med.* **2014**, 429710 (2014).
- R. R. Henry et al., *Diabetes* **67** (suppl. 1), 138-OR (2018).
- Y. Evron et al., *Sci. Rep.* **8**, 6508 (2018).

## ACKNOWLEDGMENTS

We thank the Geneva Islet Transplantation Center and H. Zulewski for human pancreatic islets, which were obtained through the basic research program of the European Consortium for Islet Transplantation (ECIT). We thank S. Bürgel for help in the initial stage of the project, A. Hierlemann for providing pulse generators, M. Folcher for constructive discussions, E. Siringil for support with 3D printing, B. Lang for advice on statistical analysis, A. M. Palma Teixeira and G. Camenisch for preparation of the animal experimentation applications, A. Graff-Meyer and C. Genoud for taking electron microscopy images, and H. Zhao and N. Franko for their help in assembling implants. **Funding:** Supported by a European Research Council (ERC) advanced grant (ElectroGene; grant no. 785800) and in part by the Swiss National Science Foundation (SNF) National Centre of Competence in Research (NCCR) for Molecular Systems Engineering. ECIT was supported by the Juvenile Diabetes Research Foundation (JDRF; grant 31-2008-416). **Author contributions:** K.K. and M.F. designed the project; K.K. and P.S. performed the cell culture experiments and K.K. designed the implants; K.K., S.X., G.C., M.D.H., J.S., and H.Y. performed the animal experiments; P.B. designed the electronic switchboard; K.K., P.S., M.X., and M.F. designed the experiments and analyzed the results; K.K., P.S., M.X., and M.F. wrote the manuscript; and S.X., M.D.H., M.X., and M.F. designed the modified implants and the in vivo “refill” as well as the insulin kinetics experiments. **Competing interests:** The authors declare no competing financial interests. **Data and materials availability:** The authors declare that all the data supporting the findings of this study are available within the paper and its supplementary materials. Original plasmids are available upon request. All vector information is provided in table S7.

## SUPPLEMENTARY MATERIALS

science.sciencemag.org/content/368/6494/993/suppl/DC1  
Materials and Methods  
Figs. S1 to S20  
Tables S1 to S8  
References (59–69)

9 July 2018; resubmitted 11 February 2020  
Accepted 3 April 2020  
10.1126/science.aau7187

## REPORTS

## SEPARATIONS

## Control of zeolite pore interior for chemoselective alkyne/olefin separations

Yuchao Chai<sup>1\*</sup>, Xue Han<sup>2\*</sup>, Weiyao Li<sup>2</sup>, Shanshan Liu<sup>1</sup>, Sikai Yao<sup>1</sup>, Chong Wang<sup>3</sup>, Wei Shi<sup>4</sup>, Ivan da-Silva<sup>5</sup>, Pascal Manuel<sup>5</sup>, Yongqiang Cheng<sup>6</sup>, Luke D. Daemen<sup>6</sup>, Anibal J. Ramirez-Cuesta<sup>6</sup>, Chiu C. Tang<sup>7</sup>, Ling Jiang<sup>3</sup>, Sihai Yang<sup>2†</sup>, Naijia Guan<sup>1,4</sup>, Landong Li<sup>1,4†</sup>

The efficient removal of alkyne impurities for the production of polymer-grade lower olefins remains an important and challenging goal for many industries. We report a strategy to control the pore interior of faujasite (FAU) zeolites by the confinement of isolated open nickel(II) sites in their six-membered rings. Under ambient conditions, Ni@FAU showed remarkable adsorption of alkynes and efficient separations of acetylene/ethylene, propyne/propylene, and butyne/1,3-butadiene mixtures, with unprecedented dynamic separation selectivities of 100, 92, and 83, respectively. In situ neutron diffraction and inelastic neutron scattering revealed that confined nickel(II) sites enabled chemoselective and reversible binding to acetylene through the formation of metastable  $[\text{Ni}(\text{II})(\text{C}_2\text{H}_2)_3]$  complexes. Control of the chemistry of pore interiors of easily scalable zeolites has unlocked their potential in challenging industrial separations.

**M**ore than 350 million metric tons of lower olefins (ethylene, propylene, and 1,3-butadiene) are produced each year through the steam cracking of hydrocarbons. Separating large quantities of chemical mixtures into purer forms accounts for an enormous amount of global energy consumption (1). To obtain polymer-grade olefins, the by-products of alkynes (acetylene, propyne, and butyne) in the stream must be reduced to <5 parts per million (ppm), because these alkynes irreversibly poison the catalysts for polymerization (2). State-of-the-art techniques to purify olefins are based on the partial hydrogenation of alkynes over supported Pd-catalysts; however, such methods suffer from poor selectivity and high costs (3). Emerging porous sorbents, notably metal-organic frameworks (MOFs), show preferential adsorption of alkynes over olefins, suggesting alternative adsorption-based purification processes for ethylene (4–8) and propylene (9–11).

However, such processes have yet to be commercialized because of the inherently limited

stability and high production costs of MOFs. Additionally, the primary physisorption mechanism in MOFs that drives separations results in a trade-off between adsorption selectivity and capacity.

Zeolites have structural robustness and low-cost production, and they are widely used for industrial separations on the basis of their molecular sieving property (12), but they are not effective for alkyne/olefin separations because these molecules have similar molecular sizes and volatilities (13). Zeolites can act as useful scaffolds to stabilize active metal sites to uncover previously unidentified functions and properties. In this work, we confine isolated Ni(II) sites into faujasite (FAU) zeolite to achieve remarkable adsorption of alkynes from a range of alkyne/olefin mixtures. The strong yet fully reversible binding between alkyne and the open Ni(II) sites results in the formation of metastable  $[\text{Ni}(\text{alkyne})_3]$  complexes under dynamic conditions and enables the complete removal of alkynes from olefins (alkynes <1 ppm). The facile production and high stability of Ni@FAU reinforce its potential in the industrial purification of lower olefins.

M@FAU zeolites  $[\text{M} = \text{Ni}(\text{II}), \text{Cu}(\text{II}), \text{and Zn}(\text{II})]$  were synthesized from hydrothermal reactions of mixed gels {molar ratio of  $\text{SiO}_2:\text{Al}_2\text{O}_3:\text{Na}_2\text{O}:\text{M-TAPTS}:\text{H}_2\text{O} = 7.8:1.0:2.2:0.6:174$ ; TAPTS = 3-[2-(2-aminoethylamino)ethylamino]propyltrimethoxysilane} and subsequent processing (yield, 77 to 85%). The TAPTS ligand was used to coordinate Ni(II) ions for their inclusion in the zeolite pore structure at locations that can be difficult to access during conventional post-synthesis ion-exchange. Similar approaches based on (3-mercaptopropyl)trimethoxysilane ligand have been reported to introduce metal

sites or clusters into desirable sites of various zeolites, showing excellent catalytic activities (14, 15). Synchrotron x-ray powder diffraction data confirmed that M@FAU zeolites crystallize in the cubic space group,  $Fd\bar{3}m$ , adopting the FAU-topology, and there is an absence of bulk phase of metal oxides (fig. S1 and table S1).

The homogeneous distribution of transition-metal cations throughout the M@FAU crystals (3 to 5  $\mu\text{m}$ ) were confirmed by electron microscopy (figs. S2 and S3). Under ambient conditions, the pores of M@FAU samples were filled with water molecules that could be removed completely by heating to 623 K (fig. S4). The divalent oxidation state of the confined metal ions was confirmed by x-ray photoelectron spectroscopy (fig. S5), and the primary location of confined Ni(II) sites in FAU zeolite was studied using density functional theory (DFT) calculations (fig. S6) and in situ neutron powder diffraction (NPD) studies.

The adsorption capacities of desolvated M@FAU and the parent Na-FAU were first evaluated by measuring the adsorption isotherms of  $\text{C}_2\text{H}_2$  and  $\text{C}_2\text{H}_4$  (Fig. 1A and figs. S7 and S8). At 1 bar and 298 K, Ni@FAU,  $[\text{Ni}_{12}\text{Na}_{20}(\text{Al}_{44}\text{Si}_{148}\text{O}_{384})]$ , showed lower overall uptakes of  $\text{C}_2\text{H}_2$  [3.48 mmol/g; equivalent to  $\sim 3.7 \text{ C}_2\text{H}_2$  per Ni(II) site] and  $\text{C}_2\text{H}_4$  (2.36 mmol/g) compared with that of Na-FAU (5.15 and 4.06 mmol/g, respectively), because of the moderate decrease of Brunauer-Emmett-Teller surface areas on incorporation of Ni(II) sites (from 710 to 531  $\text{m}^2/\text{g}$ ; fig. S9). Notably, 2.0 mmol/g of  $\text{C}_2\text{H}_2$  uptake was recorded in Ni@FAU at 0.02 bar, a pressure that is relevant to the partial pressure of  $\text{C}_2\text{H}_2$  impurity in industrial  $\text{C}_2\text{H}_4$  streams. The steep  $\text{C}_2\text{H}_2$  uptake of Ni@FAU at low pressure was consistent with its higher heat of adsorption (48.6 kJ/mol) than that of Na-FAU (21.7 kJ/mol) and of  $\text{C}_2\text{H}_4$  uptake in Ni@FAU (25.8 kJ/mol), which were determined by differential scanning calorimetry (figs. S10 to S21, table S2, and supplementary text).

Temperature-programmed desorption (TPD) profiles of  $\text{C}_2\text{H}_2$ - and  $\text{C}_2\text{H}_4$ -loaded Ni@FAU revealed higher adsorption uptake of  $\text{C}_2\text{H}_2$  (1.75 mmol/g) than of  $\text{C}_2\text{H}_4$  (0.51 mmol/g) and showed desorption peaks centered at 363 and 329 K, respectively. When coadsorbed with an equimolar mixture of  $\text{C}_2\text{H}_2/\text{C}_2\text{H}_4$ , the TPD profile resembled that of  $\text{C}_2\text{H}_2$ -loaded Ni@FAU, and little desorption of  $\text{C}_2\text{H}_4$  was observed. Moreover, the pre-adsorbed  $\text{C}_2\text{H}_4$  molecules in Ni@FAU could be readily displaced by  $\text{C}_2\text{H}_2$  under dynamic conditions (Fig. 1B). The presence of strongly bound  $\text{C}_2\text{H}_2$  molecules in Ni@FAU is also confirmed by in situ Fourier transform infrared (FTIR) studies at 298 K (Fig. 1C). On adsorption in Ni@FAU,  $\nu_{\text{as}}(\text{CH})$  and  $\nu_{\text{s}}(\text{CH})$  bands of  $\text{C}_2\text{H}_2$  red-shifted to 2925 and 3010  $\text{cm}^{-1}$ , respectively, compared with gaseous or physisorbed  $\text{C}_2\text{H}_2$  (3100 to 3400  $\text{cm}^{-1}$ ) (16, 17), whereas no shift was observed for adsorbed  $\text{C}_2\text{H}_4$  molecules.

<sup>1</sup>School of Materials Science and Engineering and National Institute for Advanced Materials, Nankai University, Tianjin 300350, China. <sup>2</sup>Department of Chemistry, The University of Manchester, Manchester, M13 9PL, UK. <sup>3</sup>State Key Laboratory of Molecular Reaction Dynamics, Dalian Institute of Chemical Physics, Chinese Academy of Sciences, Dalian 116023, China. <sup>4</sup>Key Laboratory of Advanced Energy Materials Chemistry of Ministry of Education, Nankai University, Tianjin 300071, China. <sup>5</sup>ISIS Facility, Science and Technology Facilities Council (STFC), Rutherford Appleton Laboratory, Chilton, Oxfordshire, OX11 0QX, UK. <sup>6</sup>Neutron Scattering Division, Neutron Sciences Directorate, Oak Ridge National Laboratory (ORNL), Oak Ridge, TN 37831, USA. <sup>7</sup>Diamond Light Source, Harwell Science and Innovation Campus, Didcot, Oxfordshire, OX11 0DE, UK.

\*These authors contributed equally to this work.

†Corresponding author. Email: sihai.yang@manchester.ac.uk (S.Y.); lild@nankai.edu.cn (L.L.)

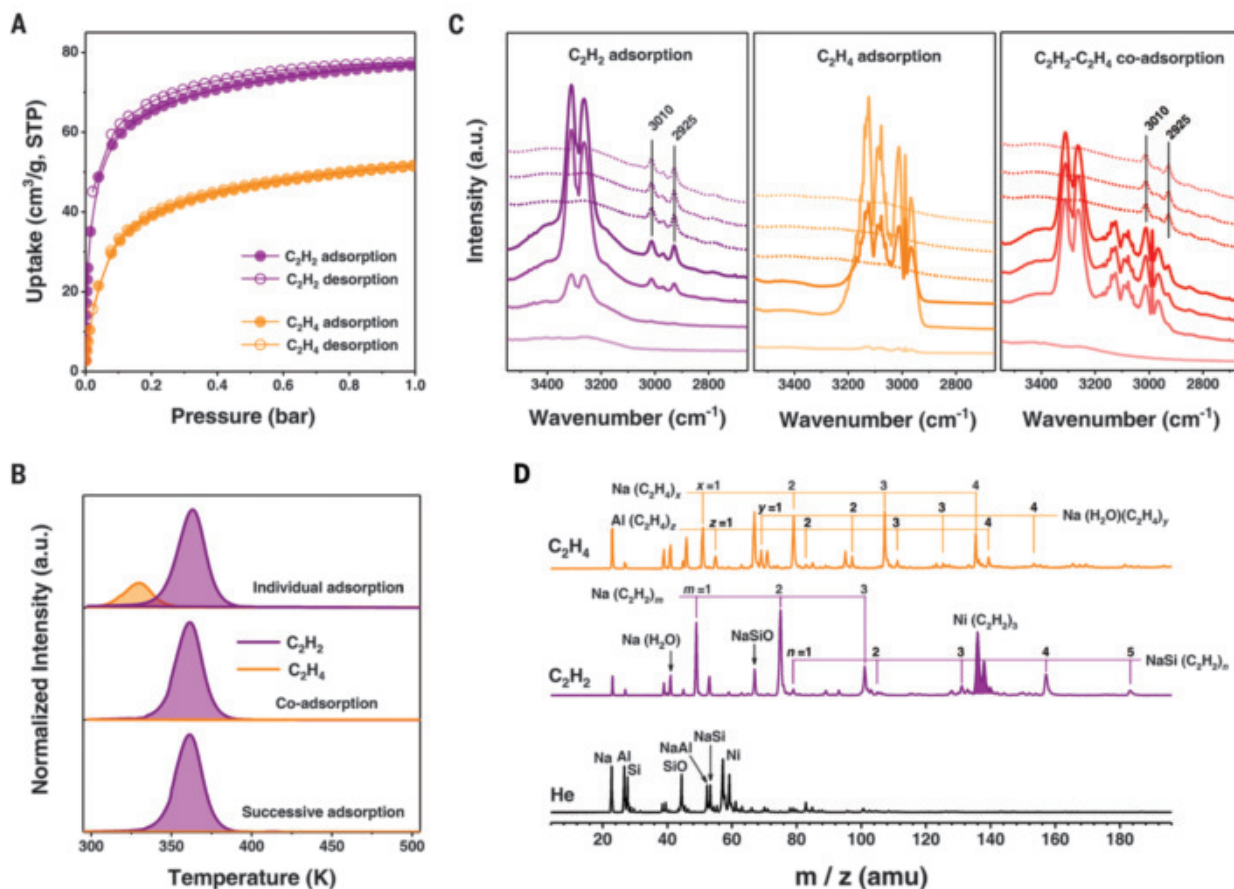


**Fig. 1. Adsorption data of  $\text{C}_2\text{H}_2$  and  $\text{C}_2\text{H}_4$  for  $\text{Ni@FAU}$ .** (A) Adsorption isotherms of  $\text{C}_2\text{H}_2$  and  $\text{C}_2\text{H}_4$  for  $\text{Ni@FAU}$  at 298 K. STP, standard temperature and pressure. (B) TPD profiles of  $\text{C}_2\text{H}_2$ - and  $\text{C}_2\text{H}_4$ -adsorbed  $\text{Ni@FAU}$  after their individual adsorption, coadsorption, and successive adsorption (first  $\text{C}_2\text{H}_4$  and then switched to  $\text{C}_2\text{H}_2$ ) at 298 K. a.u., arbitrary units.

(C) In situ FTIR spectra of  $\text{Ni@FAU}$  on adsorption of  $\text{C}_2\text{H}_2$  and  $\text{C}_2\text{H}_4$  followed by He purging (dotted lines) at 298 K. (D) Mass spectra of species produced by pulsed laser vaporization of the  $\text{Ni@FAU}$  target in the presence of carrier gas He,  $\text{C}_2\text{H}_2$  (2%)/He, and  $\text{C}_2\text{H}_4$  (2%)/He.  $m/z$ , mass/charge ratio; amu, atomic mass unit.

Infrared bands of bound  $\text{C}_2\text{H}_2$  molecules were observed in the equimolar  $\text{C}_2\text{H}_2/\text{C}_2\text{H}_4$  co-adsorbed  $\text{Ni@FAU}$ , demonstrating the selective uptake of  $\text{C}_2\text{H}_2$  under competitive adsorption.

The adsorption species in  $\text{C}_2\text{H}_2$ - and  $\text{C}_2\text{H}_4$ -loaded  $\text{Ni@FAU}$  were identified by mass spectrometry (18). The pulsed laser vaporization of  $\text{Ni@FAU}$  target in He produced a series of fragments, and Ni-containing fragments can be distinguished by the characteristic isotope ratio of nickel ( $^{58}\text{Ni}/^{60}\text{Ni} = 68\%/26\%$ ). On the basis of the control experiment of metallic Ni and Na-FAU (figs. S22 and S23), fragments corresponding to  $\text{Ni}(\text{C}_2\text{H}_2)_3$  species were identified as a key species in  $\text{C}_2\text{H}_2$ -adsorbed  $\text{Ni@FAU}$  (Fig. 1D), whereas no  $\text{Ni}(\text{C}_2\text{H}_4)_n$  ( $n = 1$  to 4) species were observed for  $\text{C}_2\text{H}_4$ -adsorbed  $\text{Ni@FAU}$ . These results demonstrated the highly selective adsorption of  $\text{C}_2\text{H}_2$  in  $\text{Ni@FAU}$  and its high capability to remove trace  $\text{C}_2\text{H}_2$  from the  $\text{C}_2\text{H}_4$  stream.

The ability of  $\text{M@FAU}$  ( $\text{M} = \text{Ni}, \text{Cu}$ , and  $\text{Zn}$ ) to separate  $\text{C}_2\text{H}_2/\text{C}_2\text{H}_4$  mixtures under dynamic conditions was evaluated by breakthrough experiments. All of the samples showed sufficient dynamic adsorption of  $\text{C}_2\text{H}_2$  and could

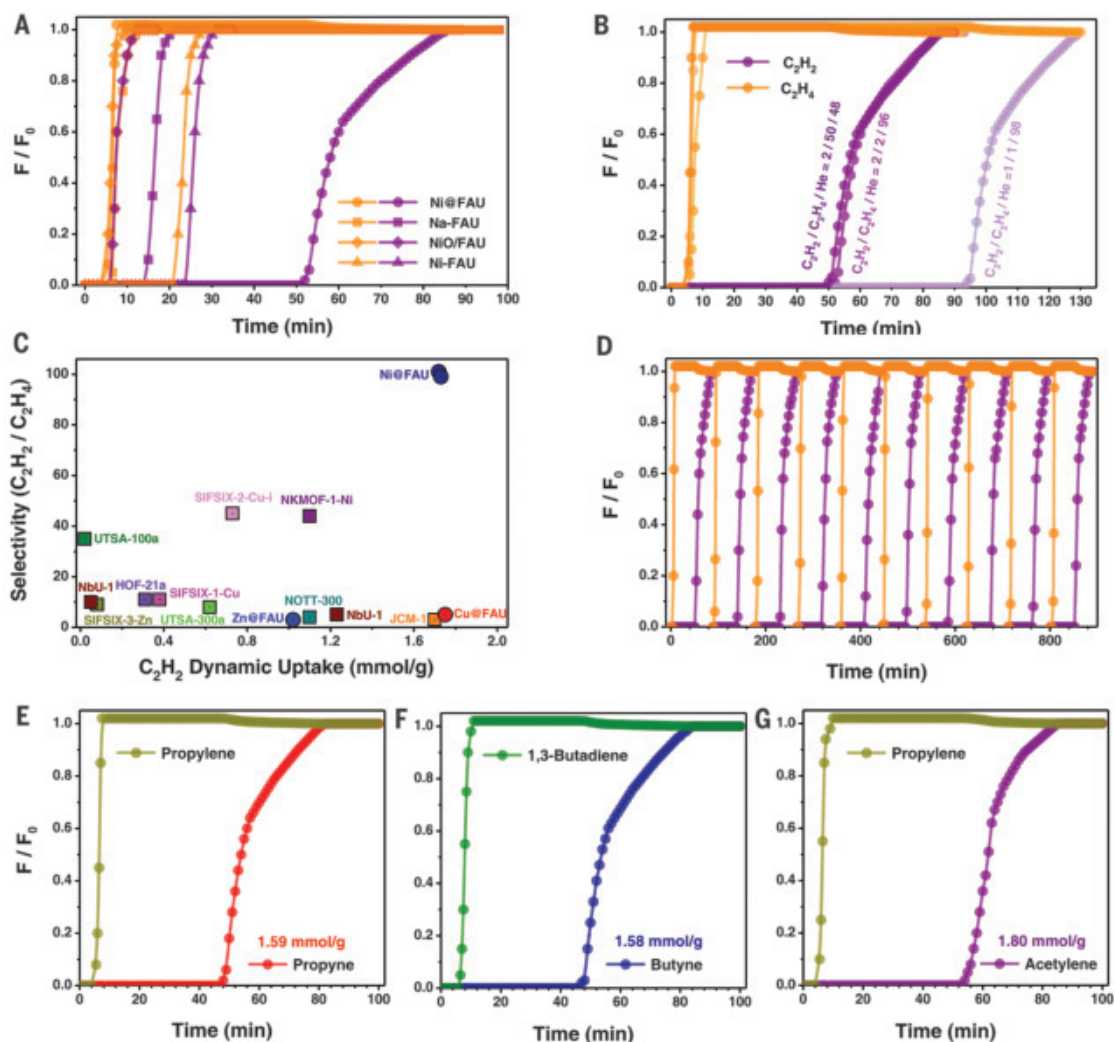
produce ultrapure  $\text{C}_2\text{H}_4$  ( $\text{C}_2\text{H}_2 < 1$  ppm) streams at the outlet of the fixed beds at 298 K (Fig. 2A and figs. S24 and S25). The dynamic  $\text{C}_2\text{H}_2$  uptakes calculated from column breakthrough curves (2%  $\text{C}_2\text{H}_2$ :2%  $\text{C}_2\text{H}_4$ ) were 0.91, 1.26, and 1.72 mmol/g for  $\text{Zn@FAU}$ ,  $\text{Cu@FAU}$ , and  $\text{Ni@FAU}$ , respectively. The dynamic  $\text{C}_2\text{H}_2$  uptake of  $\text{Ni@FAU}$  remained the same when the  $\text{C}_2\text{H}_4$  concentration was increased to 50% or the  $\text{C}_2\text{H}_2$  concentration decreased to 1% (Fig. 2B). This capability is distinct to the porous sorbents functioning solely through physisorption (6), which show rapid reductions of dynamic uptakes with decreasing gas concentrations.

Furthermore, this dynamic uptake compared favorably to the leading MOFs—for example, 1.70 mmol/g of JCM-1 (19), 1.18 mmol/g of UTSA-200a (20), 1.23 mmol/g of NbU (21), and 0.73 mmol/g of SIFSIX-2-Cu-i (4). Additionally,  $\text{Ni@FAU}$  showed a higher overall acetylene productivity (116.8 mmol/g) compared with that of leading MOFs, such as NKMOF-1-Ni (96.0 mmol/g) (8), UTSA-200a (85.7 mmol/g) (20), and SIFSIX-2-Cu-i (53.3 mmol/g) (4). Also,  $\text{Ni@FAU}$  exhibited a very low dynamic uptake

of  $\text{C}_2\text{H}_4$  (0.02 mmol/g) under the same conditions, and a remarkable  $\text{C}_2\text{H}_2/\text{C}_2\text{H}_4$  dynamic selectivity of  $\sim 100$  was achieved, compared with reported state-of-the-art sorbents (table S3). A comparison of experimentally determined  $\text{C}_2\text{H}_2/\text{C}_2\text{H}_4$  dynamic selectivity against the dynamic uptake of  $\text{C}_2\text{H}_2$  demonstrated the remarkable performance of  $\text{Ni@FAU}$  for  $\text{C}_2\text{H}_2/\text{C}_2\text{H}_4$  separation (Fig. 2C).

We observed similar separation capability with  $\text{Ni@FAU}$  after increasing the column temperature from 298 to 308 K (fig. S26) or adding  $\text{CO}_2$  or  $\text{H}_2\text{O}$  into the gas stream (fig. S27), whereas an  $\sim 25\%$  decrease in the adsorption capability of  $\text{C}_2\text{H}_2$  was observed for a  $\text{Ni@FAU}$  sample that has been preadsorbed with  $\text{H}_2\text{O}$  (fig. S28). The performance of  $\text{Ni@FAU}$  was further evaluated at 5 bar, where excellent  $\text{C}_2\text{H}_2/\text{C}_2\text{H}_4$  separations were observed and the dynamic uptakes of  $\text{C}_2\text{H}_2$  and  $\text{C}_2\text{H}_4$  increased to 2.25 and 0.39 mmol/g, respectively (fig. S29). Moreover,  $\text{Ni@FAU}$  could be used to separate mixtures of propyne/propylene, butyne/1,3-butadiene, and acetylene/propylene with high dynamic alkyne uptakes of 1.58 to 1.80 mmol/g

**Fig. 2. Column breakthrough studies for alkyne/olefin separations.** (A) Column breakthrough curves for a  $C_2H_2/C_2H_4$  (2%/2%) mixture using various zeolite samples at 298 K.  $C_2H_2$  and  $C_2H_4$  are shown in purple and orange, respectively. F, flow rate;  $F_0$ , initial flow rate. (B) Effects of feed gas composition on  $C_2H_2/C_2H_4$  separation over Ni@FAU at 298 K. (C) Plot of  $C_2H_2/C_2H_4$  dynamic selectivity against  $C_2H_2$  dynamic uptake under ambient conditions with state-of-the-art sorbent materials. (D) View of recyclability of Ni@FAU for the separation of  $C_2H_2/C_2H_4$  (2%/2%) at 298 K. Sample regeneration was achieved by treatment in He at 423 K for 30 min. (E to G) Column breakthrough curves for propyne/propylene (2%/2%) (E), butyne/1,3-butadiene (2%/2%) (F), and acetylene/propylene (2%/2%) (G) over fixed beds packed with Ni@FAU at 298 K. Total gas flow, 6.0 mL/min; sample weight, 0.2 g.



and notable breakthrough selectivities of 92, 83, and 109, respectively, under ambient conditions (Fig. 2, E to G).

These results signal the potential of Ni@FAU for the adsorptive removal of alkynes from industrial olefin streams. Practical sorbents must be recyclable. After 10 cycles of  $C_2H_2/C_2H_4$  separations with Ni@FAU, we observed no decline in the retention time and full sorbent regeneration at 373 K between each cycle (Fig. 2D). In contrast, Cu@FAU exhibited poor reversibility for  $C_2H_2/C_2H_4$  separations because of the formation of oligomers on Cu(II) sites blocking the pores (fig. S30). To understand the role of Ni(II) in Ni@FAU, we introduced the metal ions into the FAU zeolites using different methods, such as ion-exchange (denoted as Ni-FAU) or wet impregnation (denoted as NiO/FAU) (figs. S31 and S32). These two samples exhibited very poor separation of  $C_2H_2/C_2H_4$  (Fig. 2A), which suggests that the excellent performance of Ni@FAU originates from its binding environment of the confined Ni(II) sites within the pores.

In situ NPD studies enabled identification of the locations of the confined Ni(II) sites and the adsorbed gas ( $C_2D_2$ ,  $C_2D_4$ ,  $C_3D_4$ , and  $C_3D_6$ ) molecules within Ni@FAU (figs. S33 to S38 and table S4). Fourier difference map analysis of the desolvated Ni@FAU [ $Ni_{12}Na_{20}(Al_{44}Si_{148}O_{384})$ ] confirmed the structural integrity and the absence of residual nuclear density in the supercage. In-depth analysis revealed apparent residual nuclear density near the six-membered ring of the sodalite cage, which we assigned as Ni(II) ions stabilized by framework oxygen centers (fig. S39). This assignment is consistent with DFT calculations (fig. S6). By contrast, Ni(II) sites within Ni-FAU were primarily hexagonal prism sites, which were sterically hindered by the highly confined void (diameter of  $\sim 2.5$  Å) for gas binding. This finding was consistent with its poor separation performance (fig. S40 and supplementary text).

Upon gas loading, variations in Bragg peak intensities were observed, and the binding domains of gases were successfully interpreted by Fourier difference map analysis (Fig. 3, A to E)

and Rietveld refinements. At low loading in [ $Ni_{12}Na_{20}(Al_{44}Si_{148}O_{384})$ ] $\cdot(C_2D_2)_{12}$  (equivalent to  $\sim 1$  mmol/g  $C_2D_2$  uptake), all adsorbed  $C_2D_2$  molecules were located at a single site, which is distributed over six equivalent positions in the supercage and exhibited a side-on interaction to the Ni(II) sites [ $C \cdots Ni = 3.87$  to  $4.08$  Å,  $\angle C \equiv C \cdots Ni = 91.1^\circ$ ], which suggests the binding interaction between the  $C \equiv C$  bond and Ni(II) centers (fig. S41). Additionally, supplementary hydrogen bonds between  $D_{C_2D_2}$  and framework oxygen were observed [ $D \cdots O = 2.99$  Å,  $\angle C-D \cdots O = 161^\circ$ ] (Fig. 3B). A similar host-guest binding mechanism [ $C \cdots Ni = 3.83$  to  $4.05$  Å,  $\angle C \equiv C \cdots Ni = 91.9^\circ$ ] was observed in [ $Ni_{12}Na_{20}(Al_{44}Si_{148}O_{384})$ ] $\cdot(C_2D_2)_{26}$  (equivalent to  $\sim 2.3$  mmol/g  $C_2D_2$  uptake) with weaker hydrogen bonds to the framework oxygen [ $D \cdots O = 3.27$  Å,  $\angle C-D \cdots O = 151^\circ$ ]. The overall binding geometry is in marked agreement with cation-acetylene  $\pi$  complexation (13, 22). X-ray absorption near-edge structure (XANES) analysis confirmed the retention of a divalent oxidation state of Ni(II) sites on

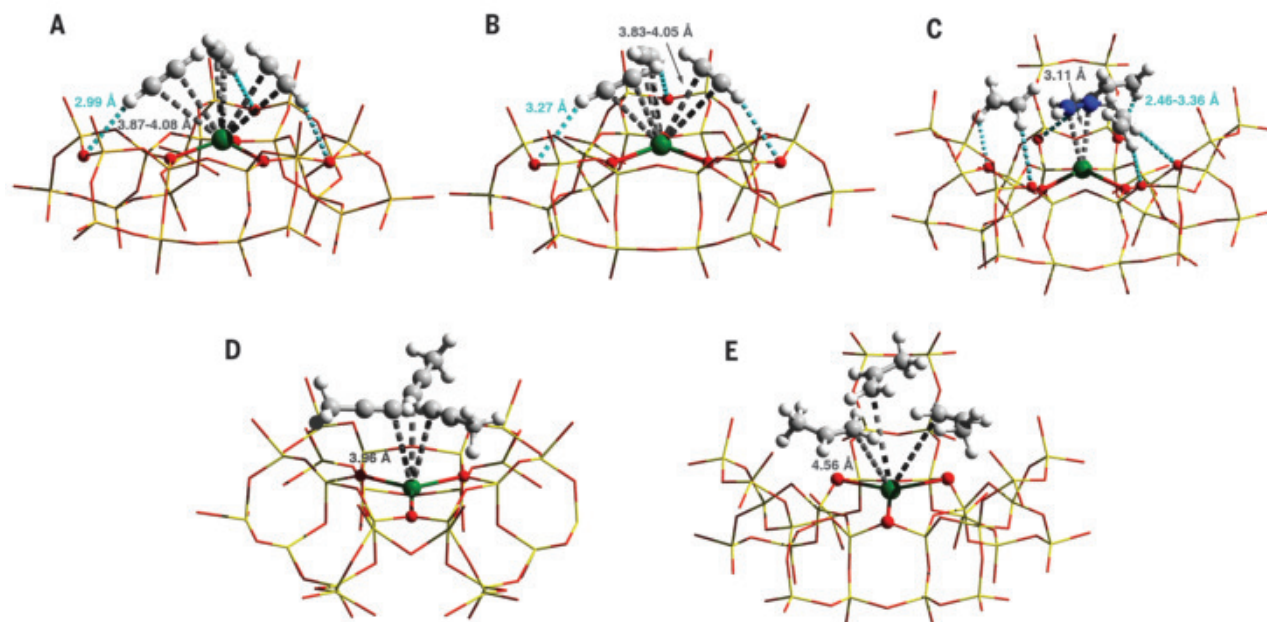


**Fig. 3. Views of crystal structures for the Ni@FAU zeolite as a function of gas loading.** All structures were derived from Rietveld refinements of NPD data at 7 K [Si and Al: yellow; O: red; Ni: green; C: gray; D: white;  $C_2D_4$  (**1**) is highlighted in blue for clarity]. The host-guest interactions are highlighted by dashed lines, and the estimated

standard deviation values for binding distances are typically within 0.02 to 0.08 Å. Views are of binding sites for adsorbed gas molecules in  $[Ni_{12}Na_{20}(Al_{44}Si_{148}O_{384})] \cdot (C_2D_2)_{12}$  (**A**),  $[Ni_{12}Na_{20}(Al_{44}Si_{148}O_{384})] \cdot (C_2D_2)_{26}$  (**B**),  $[Ni_{12}Na_{20}(Al_{44}Si_{148}O_{384})] \cdot (C_2D_4)_{17}$  (**C**),  $[Ni_{12}Na_{20}(Al_{44}Si_{148}O_{384})] \cdot (C_3D_4)_{26}$  (**D**), and  $[Ni_{12}Na_{20}(Al_{44}Si_{148}O_{384})] \cdot (C_3D_6)_{26}$  (**E**).

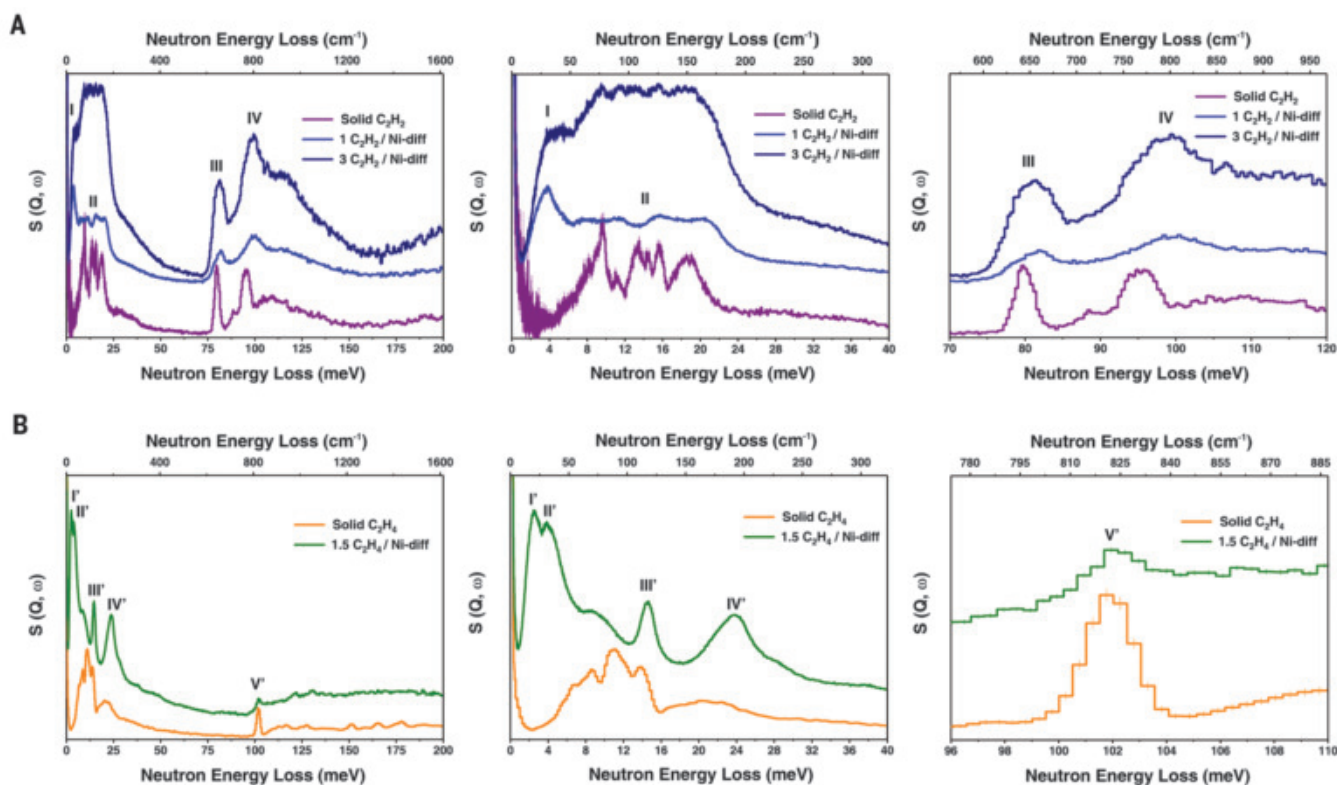


**Fig. 4. INS spectra for Ni@FAU as a function of gas loading.** (**A**) Comparison of INS spectra of  $C_2H_2$ -loaded Ni@FAU and that of solid  $C_2H_2$ . (**B**) Comparison of INS spectra of  $C_2H_4$ -loaded Ni@FAU and that of solid  $C_2H_4$ . Enlarged details show the translational or librational and the internal vibrational modes of

adsorbed  $C_2H_2$  and  $C_2H_4$  molecules. Difference spectra were produced by removing signals of the bare zeolite and sample holder. Raw spectra are provided in the supplementary materials. Peaks are labeled with Roman numerals. S, dynamic structure factor; Q, momentum transfer;  $\omega$ , frequency change.

acetylene binding (fig. S42), and no elongation of C–C distance in bound  $C_2D_2$  was found in the NPD analysis. These results were consistent with the selective yet reversible sorption.

However,  $[Ni_{12}Na_{20}(Al_{44}Si_{148}O_{384})] \cdot (C_2D_4)_{17}$  (equivalent to  $\sim 1.5$  mmol/g  $C_2D_4$  uptake) exhibited a different binding geometry with two distinct sites (**1** and **2**) in the supercage (fig. S41).  $C_2D_4$  (**1**) molecules (accounting for  $\sim 40\%$  of adsorbed  $C_2D_4$ ) interact with Ni(II) [ $C \cdots Ni = 3.11 \text{ \AA}$ ,  $\angle C = C \cdots Ni = 77.8^\circ$ ] in a similar side-on manner to that of  $C_2D_2$ , whereas  $C_2D_4$  (**2**) (accounting for  $\sim 60\%$  of adsorbed  $C_2D_4$ ) showed no interaction with Ni(II) but did show multiple hydrogen bonds to the framework oxygen [ $D \cdots O = 2.46$  to  $3.36 \text{ \AA}$ ,  $\angle C-D \cdots O = 124$  to  $178^\circ$ ]. These NPD studies revealed the explicit difference between  $C_2D_2$  and  $C_2D_4$  upon adsorption in Ni@FAU. Additional  $\pi$  electrons in  $C_2D_2$  and its linear geometry (and thus low spatial hindrance) enabled the formation of metastable  $[Ni(II)(C_2D_2)_3]$  complexes in the supercage of FAU, which is fully consistent with the mass spectrometry results. In contrast, the Ni(II) sites were heavily blocked by the bulky  $C_2D_4$  by the formation of a dynamic 1:1 adduct, which led to most of the adsorbed  $C_2D_4$  molecules being stabilized through weak hydrogen bonding and intermolecular guest-guest interactions. Similar host-guest binding interactions were observed in the structure models of  $[Ni_{12}Na_{20}(Al_{44}Si_{148}O_{384})] \cdot (C_3D_4)_{20}$  and  $[Ni_{12}Na_{20}(Al_{44}Si_{148}O_{384})] \cdot (C_3D_6)_{26}$  with  $C \cdots Ni$  distances of 3.96 and 4.56  $\text{\AA}$ , respectively (only one binding site observed in each model; Fig. 3, D and E). Thus, the distinct nature of sorbent-gas interaction construed the high selectivity of Ni@FAU toward alkyne adsorption.

To visualize the binding dynamics of adsorbed  $C_2H_2$  and  $C_2H_4$  molecules, inelastic neutron scattering (INS) studies were conducted with Ni@FAU as a function of gas loading at 5 K (figs. S43 to S48). Compared with the INS spectra of solid  $C_2H_2$  and  $C_2H_4$ , the difference INS spectra (i.e., signals of adsorbed gas molecules) had differences in the low-energy region ( $<30$  meV) that were correlated to the translation and libration modes of molecular vibration. In the solid state, molecules interact with adjacent ones in all three dimensions (figs. S49 to S54 and table S5), which results in coupling and dispersion of the modes (23). When adsorbed onto Ni(II) sites, gas molecules become isolated and restricted in an anisotropic environment, which results in distinct INS features. The peak frequencies and (anisotropic) amplitude were directly dictated by the Ni(II)-gas interactions and the local environment.

We assigned the sharp and intense INS peaks at 3.8 meV for bound  $C_2H_2$  (peak I) and 2.5 to 3.8 meV for adsorbed  $C_2H_4$  (peaks I' and II') to the motion of gas molecules within the

plane perpendicular to the Ni(II)-gas axis, because these vibrational modes are the least hindered and had the lowest frequencies and largest displacement. These INS spectra were in marked agreement with the binding sites elucidated by NPD, in terms of peak I correlating to the sole binding site of  $C_2H_2$ , whereas peaks I' and II' resulting from the two  $C_2H_4$  sites with the former being the major adsorption site. Peak I for bound  $C_2H_2$  occurred at a higher average energy, which confirmed that the interaction between Ni@FAU and  $C_2H_2$  was stronger than that of  $C_2H_4$ .

Additionally, adsorbed gas molecules may rotate or twist around the axis perpendicular to the Ni(II)-gas axis and move toward or away from the Ni(II) sites, contributing to the peaks at 10 to 15 meV and at 15 to 30 meV, respectively. Moreover, the trans- and cis-C–H bending modes for bound  $C_2H_2$  at 81.5 and 99 meV, respectively, were blue-shifted compared with those of solid  $C_2H_2$  (80 and 95 meV, respectively; Fig. 4A), which indicates that these internal modes were strongly hindered upon binding on the Ni(II) sites. In contrast, no apparent shift was observed for the in-plane C–H rocking mode of  $C_2H_4$  at 102 meV upon adsorption (Fig. 4B). Overall, the INS study showed marked agreement with NPD, adsorption, and breakthrough results, and it identified the crucial role of confined Ni(II) sites on the chemoselective binding of  $C_2H_2$  in Ni@FAU.

Solid-sorbent-based techniques hold increasing promise to improve the operational efficiency of existing separation processes in petrochemical industries, and the separation of alkyne impurities from olefins can only be realized by exploiting the differences in their properties, such as dimensions (24, 25), shapes (26), conformation (27), polarisabilities (4), coordination abilities (28), binding affinity (29), and the geometry-matching with the sorbent pores (30). Zeolites with well-defined channels have been considered to be viable candidates for gas separation for decades, primarily on the basis of their molecular sieving property (12). By confining atomically dispersed Ni(II) sites in the FAU zeolite channels, the discrimination between alkyne and olefin binding was amplified in Ni@FAU, which enabled the production of polymer-grade olefins under conditions relevant to practical processes. Combining its facile synthesis at large scale and its notable stability, the Ni@FAU sorbent offers a potential practical solution to the challenging alkyne/olefin separations.

## REFERENCES AND NOTES

- D. S. Sholl, R. P. Lively, *Nature* **532**, 435–437 (2016).
- H. Zimmermann, R. Walz, in *Ullmann's Encyclopedia of Industrial Chemistry* (Wiley, 2000).
- A. Borodziński, G. C. Bond, *Catal. Rev., Sci. Eng.* **48**, 91–144 (2006).
- X. Cui et al., *Science* **353**, 141–144 (2016).
- S.-C. Xiang et al., *Nat. Commun.* **2**, 204 (2011).

- S. Yang et al., *Nat. Chem.* **7**, 121–129 (2015).
- T. L. Hu et al., *Nat. Commun.* **6**, 7328–7335 (2015).
- Y.-L. Peng et al., *Angew. Chem. Int. Ed.* **57**, 10971–10975 (2018).
- L. Li et al., *J. Am. Chem. Soc.* **139**, 7733–7736 (2017).
- L. Li et al., *Angew. Chem. Int. Ed.* **57**, 15183–15188 (2018).
- L. Yang et al., *Adv. Mater.* **30**, 1705374 (2018).
- R. T. Yang, *Gas Separation by Adsorption Processes* (Imperial College Press, 1997).
- S. Patai, *The Chemistry of the Carbon-Carbon Triple Bond* (Wiley, 1978).
- M. Choi, Z. Wu, E. Iglesia, *J. Am. Chem. Soc.* **132**, 9129–9137 (2010).
- S.-W. Choi et al., *J. Catal.* **345**, 113–123 (2017).
- J. Erkelens, W. J. Wösten, *J. Catal.* **54**, 143–154 (1978).
- M. P. Lapinski, J. G. Ekerdt, *J. Phys. Chem.* **94**, 4599–4610 (1990).
- P. Wang et al., *Angew. Chem. Int. Ed.* **56**, 8716–8720 (2017).
- J. Lee et al., *Angew. Chem. Int. Ed.* **57**, 7869–7873 (2018).
- B. Li et al., *Adv. Mater.* **29**, 1704210 (2017).
- J. Li et al., *J. Am. Chem. Soc.* **141**, 3807–3811 (2019).
- J. H. Nelsen, H. B. Jonassen, *Coord. Chem. Rev.* **6**, 27–63 (1971).
- P. C. H. Mitchell, S. F. Parker, A. J. Ramirez-Cuesta, J. Tomkinson, *Vibrational Spectroscopy with Neutrons with Applications in Chemistry, Biology, Material Science and Catalysis* (World Scientific Publishing, 2005).
- A. Cadiou, K. Adil, P. M. Bhatt, Y. Belmabkhout, M. Eddaoudi, *Science* **353**, 137–140 (2016).
- P. J. Bereciartua et al., *Science* **358**, 1068–1071 (2017).
- Z. R. Herm et al., *Science* **340**, 960–964 (2013).
- P.-Q. Liao, N.-Y. Huang, W.-X. Zhang, J.-P. Zhang, X.-M. Chen, *Science* **356**, 1193–1196 (2017).
- E. D. Bloch et al., *Science* **335**, 1606–1610 (2012).
- K. Lee, J. D. Howe, L.-C. Lin, B. Smit, J. B. Neaton, *Chem. Mater.* **27**, 668–678 (2015).
- S. M. Kuznicki et al., *Nature* **412**, 720–724 (2001).

## ACKNOWLEDGMENTS

We thank C. Wang from China Petrochemical Corporation (SINOPEC) for helpful discussions. **Funding:** Supported by the National Natural Science Fund of China (21722303, 21421001, and 21688102), the Municipal Natural Science Fund of Tianjin (18JCJC47400 and 18JCZDJC37400), the 111 Project (B12015 and B18030), the U.K. Engineering and Physical Sciences Research Council (EP/P011632/1), and the University of Manchester and Newton Advanced Fellowship by the Royal Society (to W.S. and S.Yan.). Beamlines WISH and I11 were accessed through the STFC ISIS Facility and Diamond Light Source, respectively. INS experiments were conducted at the VISION beamline at ORNL's Spallation Neutron Source, which is supported by the Scientific User Facilities Division, Office of Basic Energy Sciences (BES), U.S. Department of Energy (DOE), under contract no. DE-AC0500OR22725 with UT Battelle, LLC. The computing resources were made available through the VirtuES and the ICEMAN projects, funded by the Laboratory Directed Research and Development program at ORNL. **Author contributions:** Y.Cha. conducted zeolite syntheses and performance tests. S.L. and S.Yao participated in sample characterization. C.W. and L.J. performed mass spectrometry analyses. W.S. and N.G. analyzed the data and provided helpful discussions. X.H., W.L., I.-d.-S., P.M., Y.Che., L.D.-d., A.J.R.-C., and C.C.T. collected and analyzed synchrotron x-ray diffraction, neutron diffraction, and INS data. S.Yan. and L.L. directed and supervised the project. Y.Cha., X.H., S.Yan., and L.L. prepared the manuscript. **Competing interests:** The authors from Nankai University are inventors of a patent (CN202010177858.0) on materials reported in this work. **Data and materials availability:** Crystallographic data for the structures reported in this article have been deposited at the Cambridge Crystallographic Data Centre under deposition numbers CCDC 1939577 to 1939585. Copies of the data can be obtained free of charge from [www.ccdc.cam.ac.uk/structures/](http://www.ccdc.cam.ac.uk/structures/). Other data needed to evaluate the conclusions in the Report are present in the paper or the supplementary materials.

## SUPPLEMENTARY MATERIALS

[science.sciencemag.org/content/368/6494/1002/suppl/DC1](https://science.sciencemag.org/content/368/6494/1002/suppl/DC1)  
Materials and Methods  
Supplementary Text  
Figs. S1 to S55  
Tables S1 to S5  
References (31–55)

23 July 2019; resubmitted 16 January 2020  
Accepted 10 April 2020  
10.1126/science.ayy8447

## ORGANIC CHEMISTRY

## Total synthesis of bryostatin 3

Barry M. Trost\*, Youliang Wang, Andreas K. Buckl, Zhongxing Huang,  
Minh H. Nguyen, Olesya Kuzmina

Bryostatins are a family of 21 complex marine natural products with a wide range of potent biological activities. Among all the 21 bryostatins, bryostatin 3 is structurally the most complex. Whereas nine total syntheses of bryostatins have been achieved to date, bryostatin 3 has only been targeted once and required the highest number of steps to synthesize (43 steps in the longest linear sequence and 88 total steps). Here, we report a concise total synthesis of bryostatin 3 using 22 steps in the longest linear sequence and 31 total steps through a highly convergent synthetic plan by the use of highly atom-economical and chemoselective transformations in which alkynes played a major role in reducing step count.

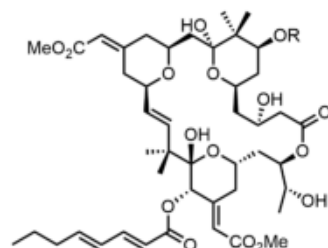
The bryostatins, first isolated by Pettit *et al.* (1, 2) from the marine bryozoan *Bugula neritina*, are a family of 21 macrolides (3–6) with potent antineoplastic (7, 8), immunopotentiating (9), synaptogenesis-inducing (10), and latent HIV-modulating (11) activity. Beneficial effects as a post-stroke treatment (12) and for restoring the blood-brain barrier after traumatic blast injuries (13) have also been demonstrated. Although the exact mechanism of action remains an ongoing area of research (14), it has become clear that bryostatins act as agonists of protein kinase C (PKC), with low nanomolar affinities for their target. Their pharmacological potential together with their intriguingly complex structures have attracted the attention of numerous synthetic organic chemists over the past 30 years. To date, nine completed total syntheses have been reported (Fig. 1): bryostatin 1 (Keck, 2011; Wender, 2017) (15, 16), bryostatin 2 (Evans, 1999) (17), bryostatin 3 (Yamamura, 2000) (18), bryostatin 7 (Masamune, 1990; Krische, 2011) (19, 20), bryostatin 8 (Song, 2018) (21), bryostatin 9 (Wender, 2011) (22), and bryostatin 16 (Trost, 2008) (23). In addition, Hale has developed a formal synthesis of bryostatin 7 (24–27), and other groups also have made important contributions to this area (28–32). All of these synthetic studies serve as guidelines toward the ultimate goal of a concise route to bryostatins that is practical and flexible, addressing the supply problem and allowing for ready access to analogs for structure-activity-relationship (SAR) studies.

Topologically, all bryostatins share a 26-membered lactone and three highly functionalized tetrahydropyrans integrated in the macrocycle. Bryostatin 3, 19, and 20 are rather exceptional because of an additional butenolide unit directly fused to the macrocycle (Fig. 1, bryostatin 3, for example). This distinguishing butenolide unit is found in

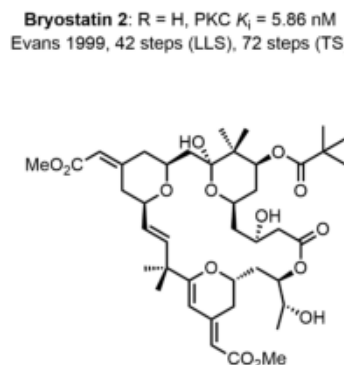
the region of the molecule crucial for binding to its biological target, PKC (33). Although changes in this recognition domain substantially attenuated binding affinities in SAR studies, bryostatin 3 retained low nanomolar affinity for PKC [inhibition constant ( $K_i$ ) = 2.75 nM] (33), comparable with that of bryostatin 1 ( $K_i$  = 1.35 nM). From a synthetic perspective, the butenolide unit renders such bryostatins, especially bryostatin 3, structurally more complex and thus more challenging to synthesize. Among all the completed syntheses (15–23), only one

targeted the butenolide-containing bryostatin: the Yamamura group's synthesis of bryostatin 3 (18). Not surprisingly, both the longest linear step count (43) and the total step count (88) are highest of all the bryostatin syntheses. With the goal of developing practical and flexible approaches to the bryostatin family by using atom-economical and selective reactions, we report a concise total synthesis of bryostatin 3 by using only 22 steps in the longest linear sequence and 31 total steps.

Retrosynthetically, we proposed that bryostatin 3 could be synthesized from the macrocyclic intermediate **1** through a late-stage oxidative functionalization of the dihydropyran ring C and a palladium-catalyzed carbonylative esterification of the stereodefined vinyl bromide (Fig. 2). Intermediate **1** could then be disassembled into intermediate **2** and fragment **3** on the basis of three key transformations: the palladium-catalyzed alkyne-alkyne coupling reaction to construct the C20–C21 bond, the gold-catalyzed 6-*endo-dig* cyclization to generate the dihydropyran ring C, and the Yamaguchi macrolactonization to form the macrocycle from the C1 carboxylic acid and the C25 alcohol. Furthermore, intermediate **2** could be disconnected into fragments **4** and **5** based on another two key

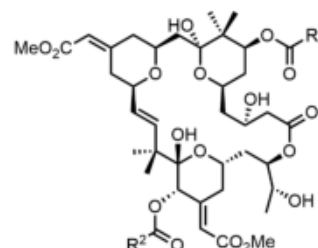


**Bryostatin 1:** R = Ac, PKC  $K_i$  = 1.35 nM  
Keck 2011, 31 steps (LLS), 58 steps (TS)  
Wender 2017, 19 steps (LLS), 29 steps (TS)



**Bryostatin 2:** R = H, PKC  $K_i$  = 5.86 nM  
Evans 1999, 42 steps (LLS), 72 steps (TS)

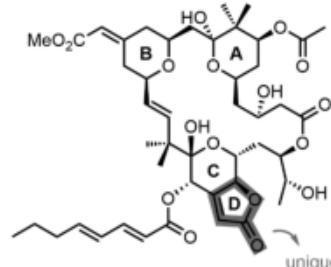
**Bryostatin 16:** PKC  $K_i$  = 118 nM  
Trost 2008, 28 steps (LLS), 42 steps (TS)



**Bryostatin 7:** R<sup>1</sup> = Me, R<sup>2</sup> = Me, PKC  $K_i$  = 0.84 nM  
Masamune 1990, 41 steps (LLS), 79 steps (TS)  
Krische 2011, 20 steps (LLS), 36 steps (TS)

**Bryostatin 8:** R<sup>1</sup> = *n*Pr, R<sup>2</sup> = *n*Pr, PKC  $K_i$  = 1.72 nM  
Song 2018, 29 steps (LLS), 51 steps (TS)

**Bryostatin 9:** R<sup>1</sup> = Me, R<sup>2</sup> = *n*Pr, PKC  $K_i$  = 1.31 nM  
Wender 2011, 25 steps (LLS), 43 steps (TS)



**Bryostatin 3:** PKC  $K_i$  = 2.75 nM  
Yamamura 2000, 43 steps (LLS), 88 steps (TS)  
This work, 22 steps (LLS), 31 steps (TS)

Fig. 1. Prior total syntheses of bryostatins.

Department of Chemistry, Stanford University, Stanford, CA 94305-5080, USA.

\*Corresponding author. Email: bmtrost@stanford.edu

reactions: the ruthenium-catalyzed alkene-alkyne coupling reaction to construct the C12–C13 bond and the intramolecular Michael addition reaction between the pendant C15 hydroxy group and the in situ generated enone to furnish the tetrahydropyran ring B. With this synthetic plan, bryostatin 3 was envisioned to be accessed from three basic fragments (**3**, **4**, and **5**) with comparable complexity in a highly convergent fashion.

The synthesis of fragment **3** commenced with the Sharpless asymmetric dihydroxylation of 3-pentenitrile to furnish diol **7** (Fig. 3A) (20). Subsequent protection of the diol as cyclopentylidene acetal **9** and partial reduction of the nitrile by diisobutylaluminum hydride (DIBAL-H) afforded aldehyde **10**. Use of the Stork-modified Wittig reaction (34) produced (*Z*)-vinyl iodide **11** in good yield as a single geometric isomer, which was then cross-coupled with methyl propiolate to generate alkynoate **12** with no loss of the *Z*-olefin stereochemistry (35). Another asymmetric dihydroxylation of enyne **12** furnished fragment **3** in excellent yield and moderate diastereoselectivity. Turning our attention toward diyne fragment **4**, we developed a three-step synthesis from 3-methyl butyne **13**. Double lithiation of **13** and successive quench with *N,N'*-dimethylformamide (DMF) and triethylchlorosilane (TESCl) delivered the alkynyl aldehyde **14** in exquisite chemo- and regioselectivity (Fig. 3B). This intermediate was exposed to a vinyl zinc reagent derived from (*Z*)-1-bromo-2-ethoxyethene **15**, followed by elimination under acidic conditions with aqueous sodium bisulfate to give enal **17**. A catalytic enantioselective propar-

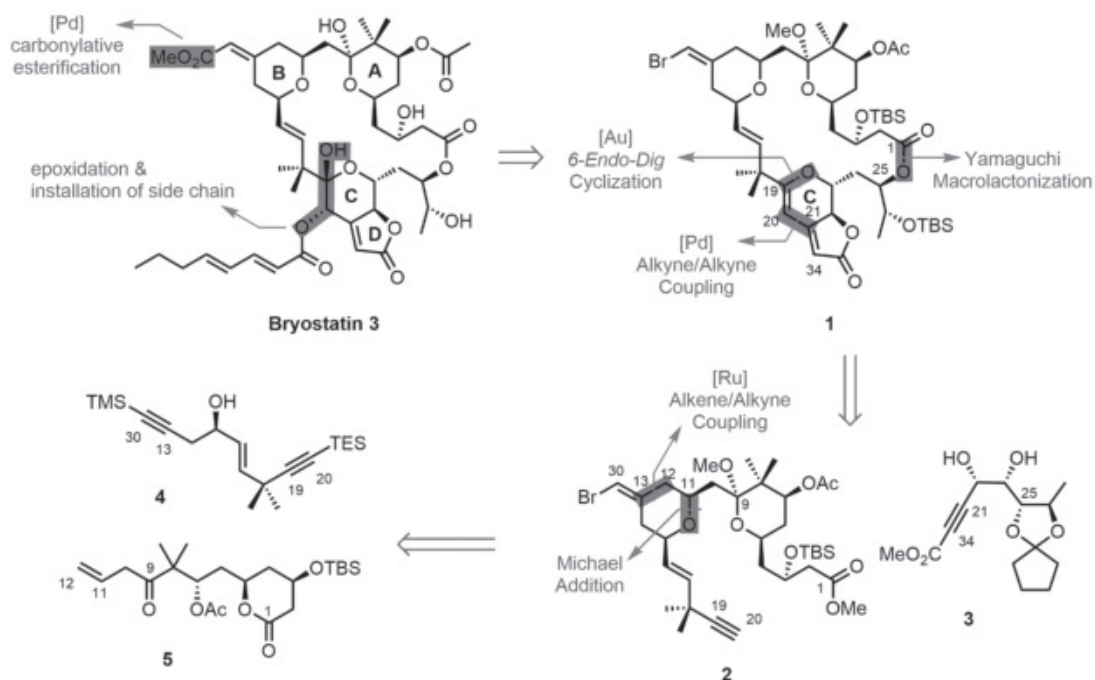
gylation of **17** afforded the diyne fragment **4** in 86% yield and 98% enantiomeric excess (36). The last key fragment **5** was prepared in eight steps according to Krische's procedure in their synthesis of Bryostatin 7 (20).

With fragments **3**, **4**, and **5** in hand, we proceeded with the fragment couplings and downstream elaborations. In the first key coupling, fragments **4** and **5** were assembled into tetrahydropyran **21** through a ruthenium-catalyzed alkene-alkyne coupling–Michael addition cascade (Fig. 3C) (37). The diyne fragment **4** underwent the desired coupling reaction with perfect chemoselectivity for the sterically more accessible alkyne. The cascade Michael addition reaction to construct the tetrahydropyran ring **B** was highly diastereoselective, with a >20/1 syn/anti ratio. The coupling product **21** was isolated in 48% yield (87% yield based on recovered starting material). Attempts to optimize the coupling reaction—including changing solvents [such as ethyl acetate, 3-pentanone, cyclopentanone, DMF, tetrahydrofuran (THF), and CH<sub>2</sub>Cl<sub>2</sub>], using additives [such as acetic acid, camphorsulfonic acid (CSA), acetonitrile, trimethylacetone, DMF, and 2,6-di-*tert*-butyl-4-methylpyridine], and varying reaction temperature and time—all led to detrimental effects. Fortunately, although the catalyst turnover was not ideal, the reaction was highly reproducible and easily performed at room temperature in air without precautions, and both unreacted coupling partners could be recovered in good yield and reused for multiple runs. The resulting vinyl silane **21** was *ipso*-brominated with complete retention of olefin geometry to furnish the vinyl bromide

**22**. Treatment of the latter with pyridinium *p*-toluenesulfonate (PPTS) in methanol afforded the bis-tetrahydropyran **23** through an acid-promoted ring-opening transesterification and ring-closing ketalization sequence. Such a cascade reaction was notably clean and chemoselective, with no transesterification of the C7 acetate. Intermediate **23** was then treated with silver(I) nitrate in aqueous THF to achieve a selective desilylation of the triethylsilyl (TES)-protected alkyne in the presence of the *tert*-butyldimethylsilyl (TBS)-protected C3 alcohol. The advanced intermediate **2** was isolated in 87% yield.

Intermediate **2** was then merged with fragment **3** by using a palladium-catalyzed alkyne-alkyne coupling reaction to give the transient intermediate **24** (Fig. 4) (38). The stereoselective nature of the coupling reaction accounted for the geometrically defined enoate of **24** which, in combination with the pendant-free diol, facilitated a spontaneous ring-closing transesterification to generate the requisite butenolide ring D of bryostatin 3 (39). The process was exclusively chemoselective, with no six-membered lactone formation, presumably owing to kinetic control of cyclization. The juxtaposition of the remaining free hydroxyl group and the alkyne deriving from the alkyne-alkyne coupling process in intermediate **25** set the stage for a 6-*endo-dig* cyclization to form the dihydropyran ring C in intermediate **26**. Thanks to the relatively acidic and mild conditions of the previous alkyne-alkyne coupling reaction, a stock solution of cationic gold catalyst could be directly injected to the reaction flask, without solvent exchange, to implement

Fig. 2. Retrosynthetic analysis of bryostatin 3.



the desired cyclization. After full conversion was indicated by means of thin-layer chromatography (TLC), a stock solution of  $\text{ZrCl}_4$  in methanol was added to the above crude reaction mixture, again with no need of sol-

vent removal or exchange, to hydrolyze the C25-C26 cyclopentylidene acetal in situ. After the above three orthogonal operations in one pot, the triol **27** could be isolated in 48% overall yield. Although the C3-OTBS group was de-

silylated during the acetonide deprotection process, it was reinstalled by subjecting the triol to silylation conditions that resulted in bis-silylated product **28** in 60% yield. Moving forward with intermediate **28**, trimethyltin

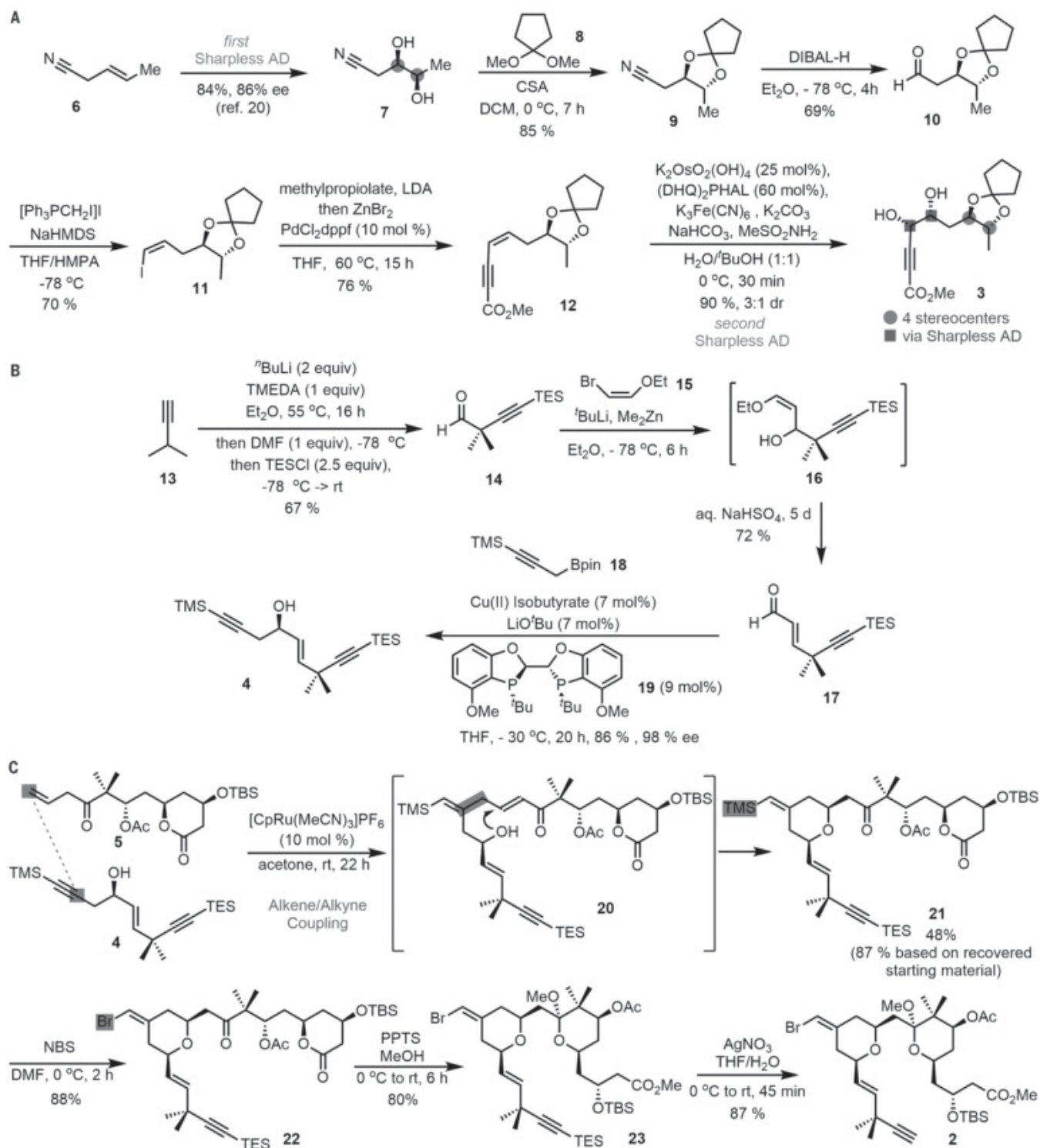


**Fig. 3. Synthesis of **2**, **3**, and **4**.** (A) Synthesis of fragment **3**. (B) Synthesis of fragment **4**. (C) Synthesis of intermediate **2**. CSA, camphorsulfonic acid; DIBAL-H, diisobutylaluminum hydride; NaHMS, sodium hexamethyldisilazide; dppf, 1,1'-bis(diphenylphosphino)ferrocene; TMEDA, *N,N,N',N'*-tetramethylethylenediamine; DMF, *N,N*-dimethylformamide; TES, triethylsilyl; NBS, *N*-bromosuccinimide; PPTS, pyridinium *p*-toluenesulfonate; THF, tetrahydrofuran.

hydroxide selectively hydrolyzed the methyl ester to give *seco*-acid **29** in 80% yield (**40**), which was then cyclized under the modified Yamaguchi conditions to afford the macrocyclic intermediate **1** in near quantitative yield (**41**).

With an established route to the macrocyclic intermediate **1**, we proceeded to complete the total synthesis by means of an oxidative functionalization of the dihydropyran ring C, an esterification of the B-ring vinyl-bromide, and a global deprotection (Fig. 5). The dihydropyran ring C of intermediate **1** was chemoselectively epoxidized with methylrhenium trioxide/urea hydroperoxide (MTO/UHP) and 1-methylimidazole under the Yamazaki conditions (**42**). 1-Methylimidazole proved to be the superior additive for this process, presumably by buffering the Lewis acidity of MTO, accelerating the reaction and increasing the metal complex's lifetime. Although the reaction was relatively clean with high conversion according to nuclear magnetic resonance (NMR) monitoring of the crude product, the epoxide **30** was rather acid sensitive, and attempts to purify it only led to low and variable yields. Thus, after workup, the crude epoxide was directly subjected to the following acid-promoted ring-opening methanolysis step to furnish the  $\alpha$ -hydroxyl ketal intermediate **31**, which was again unstable for purification and storage. Consequently, the crude  $\alpha$ -hydroxyl ketal **31** was esterified immediately through acylation by using 2,4-octadienoic anhydride to give a stable intermediate **33**, which could be purified and stored regularly. The three-step, one-purification process with purification only at the end was highly reproducible and scalable. With the C-ring fully functionalized, we then turned to the carbonylation of the B-ring vinyl-bromide to install the requisite exocyclic vinyl ester. Treatment of the vinyl-bromide **33** with  $\text{Pd}_2(\text{dba})_3 \cdot \text{CHCl}_3$  (20 mol %) and Xantphos (60 mol %) under one atmosphere of CO and with MeOH as a cosolvent furnished the desired vinyl ester **34** in 50% yield. At this stage, a protected form of bryostatin 3, **34**, was obtained. All that remained was deprotection by means of hydrolysis of the two methyl ketals and removal of the two silyl groups. Previously, Song's synthesis of bryostatin 8 (**21**) required the same type of final global deprotection. However, distinct from their synthesis in which aqueous HF in acetonitrile enabled the global deprotection in one pot, the treatment of our intermediate **34** under similar conditions only led to disappointingly complicated mixtures, as indicated by the messy NMR spectra and streaky TLC plates. Inspired by Yamamura's synthesis of bryostatin 3 (**18**), we performed the final global deprotection in two separate steps: The protected bryostatin **34** was first treated with aqueous hydrofluoride (HF) in acetonitrile to re-

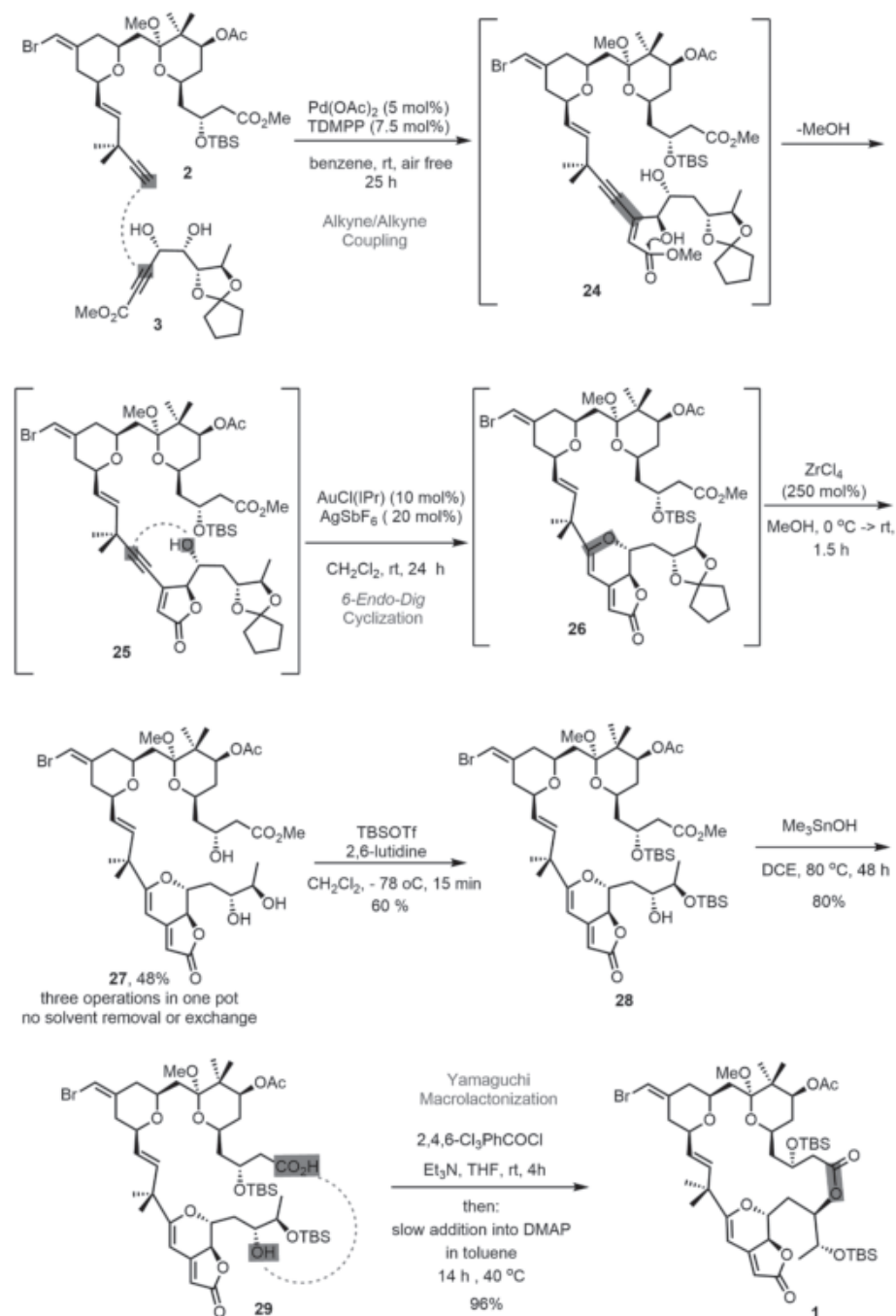


**Fig. 4. Coupling of fragment 3 and intermediate 2 and further elaborations.** TDMPP, tris(2,6-dimethoxyphenyl)phosphine; IPr, 1,3-bis(2,6-diisopropylphenyl)imidazol-2-ylidene; TBS, *tert*-butyldimethylsilyl; DCE, 1,2-dichloroethane; DMAP, 4-dimethylaminopyridine; THF, tetrahydrofuran.

move the two silyl groups and one methyl ketal. After workup, the crude residue was stirred in trifluoroacetic acid (TFA)- $\text{H}_2\text{O}$ - $\text{CH}_2\text{Cl}_2$  for 1 hour to hydrolyze the remaining methyl ketal. Through the two-step deprotection procedure, 0.9 mg of bryostatin 3 was obtained in 60% overall yield from **34**.

The identification of our synthetic bryostatin 3 was initially problematic because

its  $^1\text{H}$ -NMR was observed to be concentration dependent. Such a property has also been documented for other bryostatins (**15**, **16**, **43**). We were able to closely compare our synthetic bryostatin 3 with 1 mg of bryostatin 3 from K. Ohmori and found that the data of TLC,  $^1\text{H}$ -NMR,  $^{13}\text{C}$ -NMR, optical rotation, and high-performance liquid chromatography matched excellently (supplementary materials).

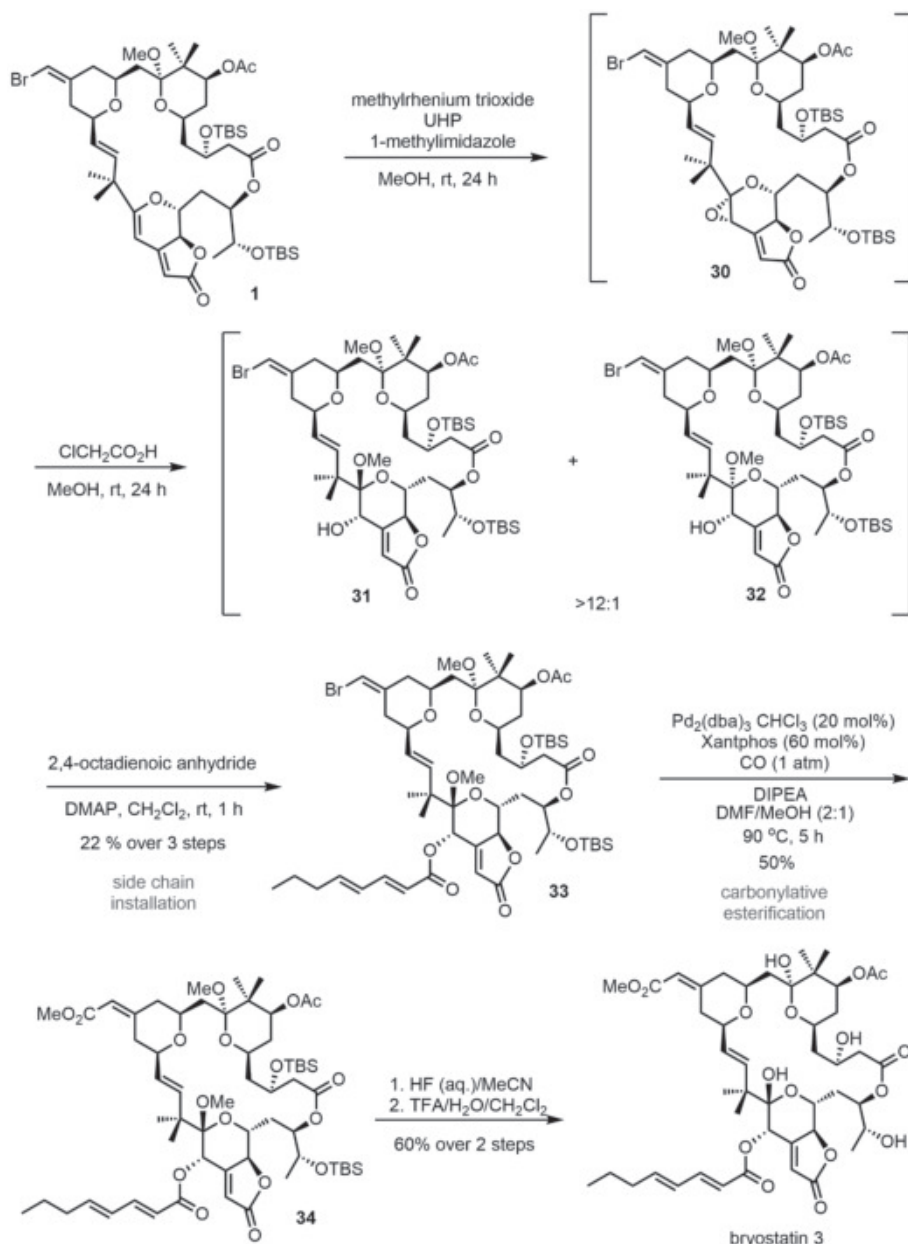


**Fig. 5. Completion of bryostatin 3 synthesis.** UHP, urea hydroperoxide; DMAP, 4-dimethylaminopyridine; DIPEA, *N,N*-diisopropylethylamine; Xantphos, 9,9-dimethyl-4,5-bis(diphenylphosphino)xanthene; DMF, *N,N*-dimethylformamide; TFA, trifluoroacetic acid.

This concise total synthesis showcases the value of the alkyne functionality that emanates from its chemoselectivity and its flexibility in elaborating the required structural details. The synthetic strategy and synthetic technologies in this work are expected to have implications toward the ultimate goal of practical, flexible, and concise synthesis of bryostatins and their bioactive analogs.

## REFERENCES AND NOTES

- G. R. Pettit, J. F. Day, J. L. Hartwell, H. B. Wood, *Nature* **227**, 962–963 (1970).
- G. R. Pettit et al., *J. Am. Chem. Soc.* **104**, 6846–6848 (1982).
- K. J. Hale, S. Manaviazar, *Chem. Asian J.* **5**, 704–754 (2010).
- K. J. Hale, M. G. Hummerson, S. Manaviazar, M. Frigerio, *Nat. Prod. Rep.* **19**, 413–453 (2002).
- R. Wu et al., *Chem. Eur. J.* **26**, 1166–1195 (2020).
- H.-B. Yu et al., *J. Nat. Prod.* **78**, 1169–1173 (2015).
- G. K. Schwartz, M. A. Shah, *J. Clin. Oncol.* **23**, 9408–9421 (2005).
- S. Wang, Z. Wang, P. Dent, S. Grant, *Blood* **101**, 3648–3657 (2003).
- S. P. Shaha et al., *Clin. Exp. Immunol.* **158**, 186–198 (2009).
- D. L. Alkon, M.-K. Sun, T. J. Nelson, *Trends Pharmacol. Sci.* **28**, 51–60 (2007).
- R. Mehla et al., *PLOS ONE* **5**, e11160 (2010).
- M.-K. Sun, J. Hongpaisan, D. L. Alkon, *Proc. Natl. Acad. Sci. U.S.A.* **106**, 14676–14680 (2009).
- B. P. Lucke-Wold et al., *Mol. Neurobiol.* **52**, 1119–1134 (2015).
- B. A. Loy et al., *J. Am. Chem. Soc.* **137**, 3678–3685 (2015).
- G. E. Keck, Y. B. Poudel, T. J. Cummins, A. Rudra, J. A. Covell, *J. Am. Chem. Soc.* **133**, 744–747 (2011).
- P. A. Wender et al., *Science* **358**, 218–223 (2017).
- D. A. Evans et al., *J. Am. Chem. Soc.* **121**, 7540–7552 (1999).
- K. Ohmori et al., *Angew. Chem. Int. Ed.* **39**, 2290–2294 (2000).
- M. Kageyama et al., *J. Am. Chem. Soc.* **112**, 7407–7408 (1990).
- Y. Lu, S. K. Woo, M. J. Krische, *J. Am. Chem. Soc.* **133**, 13876–13879 (2011).
- Y. Zhang et al., *Angew. Chem. Int. Ed.* **57**, 942–946 (2018).
- P. A. Wender, A. J. Schrier, *J. Am. Chem. Soc.* **133**, 9228–9231 (2011).
- B. M. Trost, G. Dong, *Nature* **456**, 485–488 (2008).
- K. J. Hale, J. A. Lennon, S. Manaviazar, M. H. Javadi, C. J. Hobbs, *Tetrahedron Lett.* **36**, 1359–1362 (1995).
- K. J. Hale, M. Frigerio, S. Manaviazar, *Org. Lett.* **5**, 503–505 (2003).
- K. J. Hale, M. Frigerio, S. Manaviazar, *Org. Lett.* **3**, 3791–3794 (2001).
- S. Manaviazar et al., *Org. Lett.* **8**, 4477–4480 (2006).
- J. V. Allen et al., *Tetrahedron Lett.* **49**, 6352–6355 (2008).
- B. J. De, M. Vandewalle, *Pure Appl. Chem.* **68**, 715–718 (2009).
- R. Roy, A. W. Rey, M. Charron, R. Molino, *J. Chem. Soc. Chem. Commun.* **18**, 1308–1310 (1989).
- E. A. Voight, H. Seradj, P. A. Roethle, S. D. Burke, *Org. Lett.* **6**, 4045–4048 (2004).
- J. S. Yadav, A. Bandyopadhyay, A. C. Kunwar, *Tetrahedron Lett.* **42**, 4907–4911 (2001).
- P. A. Wender et al., *Proc. Natl. Acad. Sci. U.S.A.* **85**, 7197–7201 (1988).
- G. Stork, K. Zhao, *Tetrahedron Lett.* **30**, 2173–2174 (1989).
- E. Negishi, M. Qian, F. Zeng, L. Anastasia, D. Babinski, *Org. Lett.* **5**, 1597–1600 (2003).
- D. R. Fandrick et al., *J. Am. Chem. Soc.* **132**, 7600–7601 (2010).
- B. M. Trost, H. Yang, G. Wuitschik, *Org. Lett.* **7**, 4761–4764 (2005).
- B. M. Trost, M. T. Sorum, C. Chan, G. Rüther, *J. Am. Chem. Soc.* **119**, 698–708 (1997).
- B. M. Trost, M. C. McIntosh, *J. Am. Chem. Soc.* **117**, 7255–7256 (1995).
- K. C. Nicolaou, A. A. Estrada, M. Zak, S. H. Lee, B. S. Safina, *Angew. Chem. Int. Ed.* **44**, 1378–1382 (2005).
- J. Inanaga, K. Hirata, H. Saeki, T. Katsuki, M. Yamaguchi, *Bull. Chem. Soc. Jpn.* **52**, 1989–1993 (1979).
- S. Yamazaki, *Org. Biomol. Chem.* **8**, 2377–2385 (2010).
- D. E. Schaufelberger, G. N. Chmurny, M. P. Koclek, *Magn. Reson. Chem.* **29**, 366–374 (1991).

## ACKNOWLEDGMENTS

S. Lynch is acknowledged for conducting two-dimensional NMR experiments. We thank K. Ohmori from the Tokyo Institute of Technology for the generous sharing of 1 mg of bryostatin 3.

**Funding:** We are grateful to the Tamaki Foundation for financial support. O.K. thanks Deutsche Forschungsgemeinschaft (DFG) for sponsoring the postdoctoral research. **Author**

**contributions:** B.M.T. conceived and designed the project. Y.W., A.K.B., Z.H., M.H.N., and O.K. carried out the experiments. Y.W. and A.K.B. wrote the manuscript. B.M.T., Z.H., and J. S. Tracy proofread the manuscript. All authors analyzed the data and discussed the results. **Competing interests:** The authors declare no competing interests. **Data and materials availability:** All data are available in the main text or the supplementary materials.

## SUPPLEMENTARY MATERIALS

science.sciencemag.org/content/368/6494/1007/suppl/DC1  
Materials and Methods  
Supplementary Text  
Tables S1 and S2  
NMR Spectra

13 March 2020; accepted 22 April 2020  
10.1126/science.abb7271

## CORONAVIRUS

## Comparative pathogenesis of COVID-19, MERS, and SARS in a nonhuman primate model

Barry Rockx<sup>1\*</sup>, Thijs Kuiken<sup>1</sup>, Sander Herfst<sup>1</sup>, Theo Bestebroer<sup>1</sup>, Mart M. Lamers<sup>1</sup>, Bas B. Oude Munnink<sup>1</sup>, Dennis de Meulder<sup>1</sup>, Geert van Amerongen<sup>2</sup>, Judith van den Brand<sup>1†</sup>, Nisreen M. A. Okba<sup>1</sup>, Debby Schipper<sup>1</sup>, Peter van Run<sup>1</sup>, Lonneke Leijten<sup>1</sup>, Reina Sikkema<sup>1</sup>, Ernst Verschoor<sup>3</sup>, Babs Verstrepen<sup>3</sup>, Willy Bogers<sup>3</sup>, Jan Langermans<sup>4,5</sup>, Christian Drosten<sup>6</sup>, Martje Fentener van Vlissingen<sup>7</sup>, Ron Fouchier<sup>1</sup>, Rik de Swart<sup>1</sup>, Marion Koopmans<sup>1</sup>, Bart L. Haagmans<sup>1\*</sup>

The current pandemic coronavirus, severe acute respiratory syndrome–coronavirus 2 (SARS-CoV-2), was recently identified in patients with an acute respiratory syndrome, coronavirus disease 2019 (COVID-19). To compare its pathogenesis with that of previously emerging coronaviruses, we inoculated cynomolgus macaques with SARS-CoV-2 or Middle East respiratory syndrome (MERS)–CoV and compared the pathology and virology with historical reports of SARS-CoV infections. In SARS-CoV-2–infected macaques, virus was excreted from nose and throat in the absence of clinical signs and detected in type I and II pneumocytes in foci of diffuse alveolar damage and in ciliated epithelial cells of nasal, bronchial, and bronchiolar mucosae. In SARS-CoV infection, lung lesions were typically more severe, whereas they were milder in MERS-CoV infection, where virus was detected mainly in type II pneumocytes. These data show that SARS-CoV-2 causes COVID-19–like disease in macaques and provides a new model to test preventive and therapeutic strategies.

**A**fter the first reports of an outbreak of an acute respiratory syndrome in China in December 2019, a novel coronavirus, severe acute respiratory syndrome–coronavirus 2 (SARS-CoV-2), was identified (1, 2). As of 14 March 2020, over 140,000 cases were reported worldwide with more than 5400 deaths, surpassing the combined number of cases and deaths of two previously emerging coronaviruses, SARS-CoV and Middle East respiratory syndrome (MERS)–CoV (3). The disease caused by this virus, coronavirus disease 2019 (COVID-19), is characterized by a range of symptoms, including fever, cough, dyspnoea, and myalgia in most cases (2). In severe cases, bilateral lung involvement with ground-glass opacity is the most common chest computed tomography (CT) finding (4). Similarly to the 2002–2003 outbreak of SARS, the severity of COVID-19 disease is associated with increased age and/or a comorbidity, although severe disease is not limited to these risk groups (5). However, despite the large number of cases and deaths, limited information is available on the pathogenesis of this virus infection.

Two reports on the histological examination of the lungs of three patients showed bilateral diffuse alveolar damage (DAD), pulmonary edema, and hyaline membrane formation, indicative of acute respiratory distress syndrome (ARDS), as well as characteristic syncytial cells in the alveolar lumen (6, 7), similar to findings during the 2002–2003 outbreak of SARS-CoV (8). The pathogenesis of SARS-CoV infection was previously studied in a nonhuman primate model (cynomolgus macaques) where aged animals were more likely to develop disease (9–13). In the current study, SARS-CoV-2 infection was characterized in the same animal model and compared with infection with MERS-CoV and historical data on SARS-CoV (9, 10, 12).

First, two groups of four cynomolgus macaques [both young adult (young), 4 to 5 years of age; and old adult (aged), 15 to 20 years of age] were inoculated by a combined intratracheal (IT) and intranasal (IN) route with a SARS-CoV-2 strain from a German traveler returning from China. No overt clinical signs were observed in any of the infected animals, except for a serous nasal discharge in one aged animal on day 14 post inoculation (p.i.). No significant weight loss was observed in any of the animals during the study. By day 14 p.i., all remaining animals seroconverted as revealed by the presence of SARS-CoV-2–specific antibodies against the virus S1 domain and nucleocapsid proteins in their sera (fig. S1).

As a measure of virus shedding, nasal, throat, and rectal swabs were assayed for virus by reverse transcription–quantitative polymerase chain reaction (RT–qPCR) and virus culture. In nasal swabs, SARS-CoV-2 RNA peaked by day 2 p.i. in young animals and by day 4 p.i. in

aged animals and was detected up to at least day 8 p.i. in two out of four animals and up to day 21 p.i. in one out of four animals (Fig. 1A). Overall, higher levels of SARS-CoV-2 RNA were detected in nasal swabs of aged animals compared with young animals. SARS-CoV-2 RNA in throat swabs peaked at day 1 p.i. in young and day 4 p.i. in aged animals and decreased more rapidly over time by comparison with the nasal swabs but could still be detected intermittently up to day 10 p.i. (Fig. 1B). Low levels of infectious virus were cultured from throat and nasal swabs up to day 2 and 4, respectively (table S1). In support of virus shedding by these animals, environmental sampling was performed to determine potential contamination of surfaces. Environmental sampling indicated the presence of low levels of SARS-CoV-2 RNA on surfaces through both direct contact (hands) and indirect contamination within the isolator (table S2). SARS-CoV-2 RNA was only detected in a rectal swab from one animal on day 14 p.i., and no viral RNA was detected in whole blood at any time point throughout the study.

On autopsy of four macaques on day 4 p.i., two had foci of pulmonary consolidation in the lungs (Fig. 2A). One animal (aged: 17 years) showed consolidation in the right middle lobe, representing less than 5% of the lung tissue. A second animal (young: 5 years) had two foci in the left lower lobe, representing about 10% of the lung tissue (Fig. 2A). The consolidated lung tissue was well circumscribed, red-purple, level, and less buoyant than normal. The other organs in these two macaques, as well as the respiratory tract and other organs of the other two animals, were normal.

Virus replication was assessed by RT–qPCR on day 4 p.i. in tissues from the respiratory, digestive, urinary, and cardiovascular tracts and from endocrine and central nervous systems, as well as from various lymphoid tissues. Virus replication was primarily restricted to the respiratory tract (nasal cavity, trachea, bronchi, and lung lobes) with highest levels of SARS-CoV-2 RNA in lungs (Fig. 1C). In three out of four animals, SARS-CoV-2 RNA was also detected in ileum and tracheo-bronchial lymph nodes (Fig. 1C).

The main histological lesion in the consolidated pulmonary tissues of both the young and aged animals involved the alveoli and bronchioles and consisted of areas with acute or more advanced DAD (Fig. 2B). In these areas, the lumina of alveoli and bronchioles were variably filled with protein-rich edema fluid, fibrin, and cellular debris; alveolar macrophages; and fewer neutrophils and lymphocytes (Fig. 2, C to E). There was epithelial necrosis with extensive loss of epithelium from alveolar and bronchiolar walls. Hyaline membranes were present in a few damaged alveoli. In areas with more advanced lesions, the alveolar walls

<sup>1</sup>Department of Viroscience, Erasmus University Medical Center, Rotterdam, Netherlands. <sup>2</sup>Viroclinics Xplore, Schaijk, Netherlands. <sup>3</sup>Department of Virology, Biomedical Primate Research Centre, Rijswijk, Netherlands. <sup>4</sup>Animal Science Department, Biomedical Primate Research Centre, Rijswijk, Netherlands. <sup>5</sup>Population Health Sciences, Unit Animals in Science and Society, Faculty of Veterinary Medicine, Utrecht University, Netherlands. <sup>6</sup>Institute of Virology, Charité–Universitätsmedizin, Berlin, Germany. <sup>7</sup>Erasmus Laboratory Animal Science Center, Erasmus University Medical Center, Rotterdam, Netherlands.

\*Corresponding author. Email: b.rockx@erasmusmc.nl (B.R.); b.haagmans@erasmusmc.nl (B.L.H.) †Present address: Division of Pathology, Faculty of Veterinary Medicine, Utrecht University, Utrecht, Netherlands

were moderately thickened and lined by cuboidal epithelial cells (type II pneumocyte hyperplasia), and the alveolar lumina were empty. Alveolar and bronchiolar walls were thickened by edema fluid, mononuclear cells, and neu-

trophils. There were aggregates of lymphocytes around small pulmonary vessels. Moderate numbers of lymphocytes and macrophages were present in the lamina propria and submucosa of the bronchial walls, and a few neutrophils

were detected in the bronchial epithelium. Regeneration of epithelium was seen in some bronchioles, visible as an irregular layer of squamous to high cuboidal epithelial cells with hyperchromatic nuclei. There were occasional

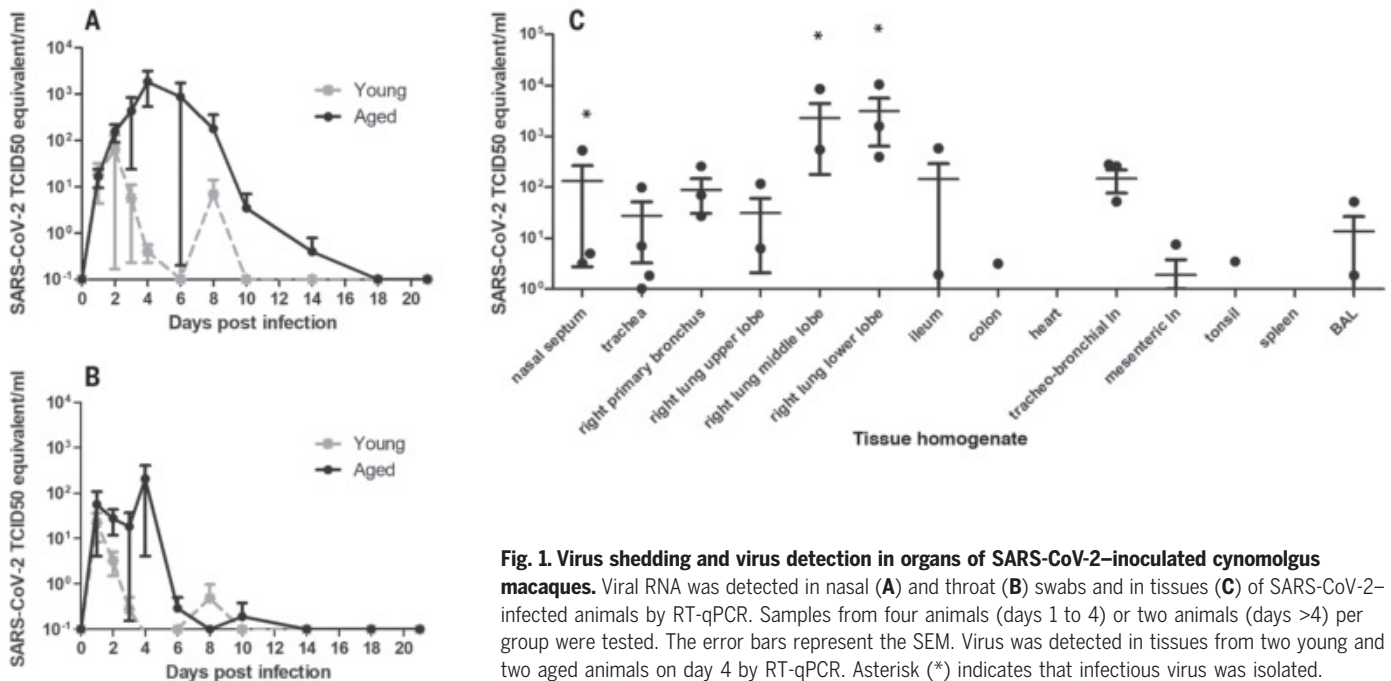


**Fig. 1. Virus shedding and virus detection in organs of SARS-CoV-2-inoculated cynomolgus macaques.** Viral RNA was detected in nasal (A) and throat (B) swabs and in tissues (C) of SARS-CoV-2-infected animals by RT-qPCR. Samples from four animals (days 1 to 4) or two animals (days >4) per group were tested. The error bars represent the SEM. Virus was detected in tissues from two young and two aged animals on day 4 by RT-qPCR. Asterisk (\*) indicates that infectious virus was isolated.

**Table 1. Comparative pathogenesis of SARS-CoV-2, MERS-CoV, and SARS-CoV infections in cynomolgus macaques.** Max, maximum; Ref., reference.

| Virus      | Age category | No. | Clinical signs | Max. excretion from throat* | Max. excretion from nose* | Viral titer in lung† | Virus in extra-respiratory tissues | Pulmonary lesions at 4 days post inoculation |                   |                    |                        |                         | Ref.       |
|------------|--------------|-----|----------------|-----------------------------|---------------------------|----------------------|------------------------------------|--|-------------------|--------------------|------------------------|-------------------------|------------|
|            |              |     |                |                             |                           |                      |                                    | % affected lung                              | Hyaline membranes | Alveolar edema     | Leukocyte infiltration | Cell type tropism       |            |
| SARS-CoV   | Young        | 4   | No             | 10e3.5                      | 10e4.2                    | 10e6.5               | No                                 | 0–5  | No                | No                 | Yes                    | Type I & II pneumocytes | (10–12)    |
| SARS-CoV   | Aged         | 4   | Yes            | 10e3.0                      | 10e3.0                    | 10e6.2               | Kidney                             | 0–60   | Yes               | Yes                | Yes                    | Type I & II pneumocytes | (10–12)    |
| MERS-CoV   | Young        | 4   | No             | 10e5.3                      | 10e4.3                    | 10e4.4               | Spleen                             | 0–5  | No                | Yes (small amount) | Yes                    | Type II pneumocytes     | This study |
| SARS-CoV-2 | Young        | 2   | No             | 10e1.8                      | 10e2.4                    | 10e4.0               | Ileum, colon, tonsil               | 0–10   | Yes               | Yes                | Yes                    | Type I & II pneumocytes | This study |
| SARS-CoV-2 | Aged         | 2   | No             | 10e2.9                      | 10e3.7                    | 10e3.1               | Ileum, colon, tonsil               | 0–5  | No                | No                 | Yes                    | Type I & II pneumocytes | This study |

\*TCID50eq per ml.

†TCID50eq per gram of tissue.

multinucleated giant cells (syncytia) free in the lumina of bronchioles and alveoli (Fig. 2F) and, based on positive pan-keratin staining and negative CD68 staining, these appeared to originate from epithelial cells (Fig. 2F, inset).

SARS-CoV-2 antigen expression was detected in moderate numbers of type I pneumocytes and a few type II pneumocytes within foci of DAD (Fig. 2, G and H, and fig. S2). The pattern of staining was similar to that in lung tissue from SARS-CoV-infected macaques (positive control). SARS-CoV-2 antigen expression was not observed in any of the syncytia. In addition, SARS-CoV-2 antigen expression

was detected in nonlesional tissues of all lung lobes in three out of four macaques (both young and one aged) in a few type I and II pneumocytes, bronchial ciliated epithelial cells, and bronchiolar ciliated epithelial cells. The other aged macaque, without virological or pathological evidence of SARS-CoV-2 infection in the lungs, did have SARS-CoV-2 antigen expression in ciliated epithelial cells of nasal septum (Fig. 2I), nasal concha, and palatum molle, in the absence of associated histopathological changes. No SARS-CoV antigen expression was detected in other sampled tissues, including brain and intestine.

To assess the severity of infection with SARS-CoV-2 compared with MERS-CoV, we inoculated young cynomolgus macaques (3 to 5 years of age) with MERS-CoV via the IN and IT route. All animals remained free of clinical signs. At day 21 p.i., all remaining animals ( $n = 2$ ) seroconverted as revealed by the presence of MERS-CoV-specific antibodies in their sera by ELISA (fig. S3).

MERS-CoV RNA was detected in nasal (Fig. 3A) and throat swabs (Fig. 3B) on days 1 to 11 p.i., with peaks on days 1 and 2 p.i., respectively. Low levels [between 1 and 85 median tissue culture infectious dose (TCID<sub>50</sub>) equivalent/

**Fig. 2. Characteristic pathological changes and virus antigen expression in the lungs of SARS-CoV-2-inoculated cynomolgus macaques.**

(A) Two foci of pulmonary consolidation in the left lower lung lobe (arrowheads). (B) Area of pneumonia [staining with hematoxylin and eosin (H&E); bar, 0.5 cm]. (C) Edema fluid in alveolar lumina (H&E; bar, 25  $\mu$ m). (D) Neutrophils, as well as erythrocytes, fibrin, and cell debris, in an alveolar lumen flooded by edema fluid (H&E; bar, 10  $\mu$ m). (E) Mononuclear cells, either type II pneumocytes or alveolar macrophages, in an alveolar lumen flooded by edema fluid (H&E; bar, 10  $\mu$ m). (F) Syncytium in an alveolar lumen (H&E; 100 $\times$  objective). Inset: Syncytium expresses keratin, indicating epithelial cell origin [immunohistochemistry (IHC) for pan-keratin AE1/AE3; bar, 10  $\mu$ m]. (G) SARS-CoV-2 antigen expression is colocalized with areas of diffuse alveolar damage (IHC for SARS-CoV-nucleocapsid; bar, 50  $\mu$ m). (H) Type I (flat) and type II (cuboidal) pneumocytes in affected lung tissue express SARS-CoV-2 antigen (IHC for SARS-CoV-nucleocapsid; bar, 25  $\mu$ m). (I) Ciliated columnar epithelial cells of respiratory mucosa in nasal cavity express SARS-CoV-2 antigen (IHC for SARS-CoV-nucleocapsid; bar, 25  $\mu$ m).

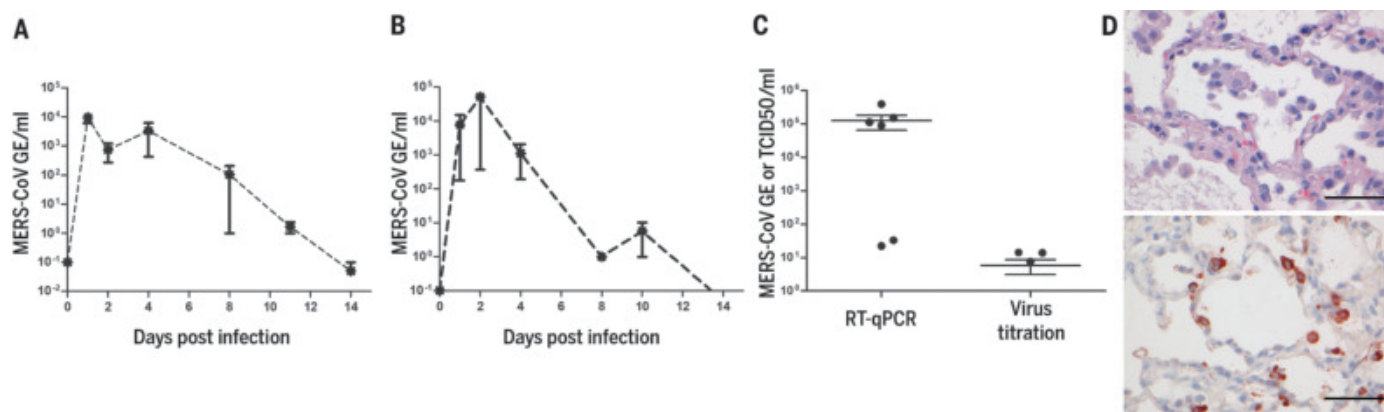
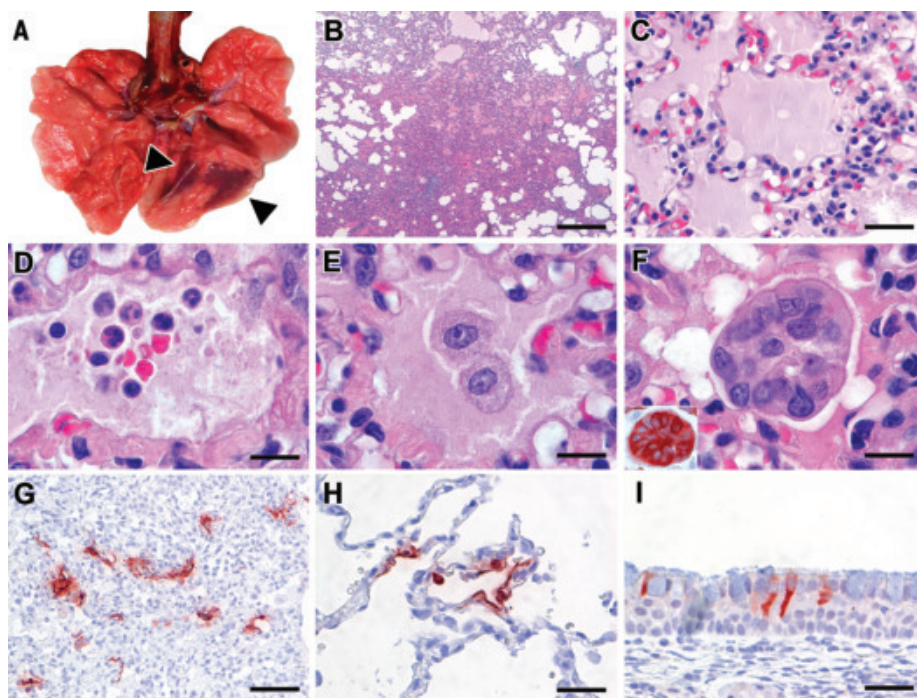


**Fig. 3. Virus shedding and virus detection in organs of MERS-CoV-inoculated cynomolgus macaques.** Viral RNA was detected in nasal (A) and throat (B) swabs and tissues (C) of MERS-CoV-infected animals by RT-qPCR. Samples from four animals per group were tested. The error bars represent the SEM. Virus was detected in tissues on day 4 by RT-qPCR. Histopathological changes (D) (left) with hypertrophic and hyperplastic type II pneumocytes in the alveolar septa and increased numbers of alveolar macrophages in the alveolar lumina and virus antigen expression (right) in type II pneumocytes. Bar, 50  $\mu$ m.

ml] of MERS-CoV RNA were detected in rectal swabs on days 2 and 3 p.i.

At autopsy of four macaques at day 4 p.i., three animals had foci of pulmonary consolidation, characterized by slightly depressed areas in the lungs, representing less than 5% of the lung tissue (Table 1). Similar to SARS-CoV-2 infection in both young and aged animals, on day 4 p.i., MERS-CoV RNA was primarily detected in the respiratory tract of inoculated animals (Fig. 3C). Infectious virus titers were comparable to those of SARS-CoV-2 infection, but lower compared to SARS-CoV infection, of young macaques (Table 1). In addition, MERS-CoV RNA was detected in the spleen (Table 1).

Consistent with the presence of virus in the lower respiratory tract at day 4 p.i., histopathological changes characteristic for DAD were observed in the lungs of inoculated animals (Fig. 3D). The alveolar septa were thickened owing to infiltration of neutrophils and macrophages, and to moderate type II pneumocyte hyperplasia and hypertrophy. In the alveolar lumina, there were increased numbers of alveolar macrophages and some edema fluid containing fibrin and some neutrophils (Fig. 3D). Few syncytial cells were seen in the alveolar lumina. MERS-CoV antigen was not detected in tissues on day 4 p.i. in any part of the respiratory tract. We therefore sampled four young macaques at day 1 p.i. At this time, we observed multifocal expression of viral antigen, predominantly in type II pneumocytes and occasionally in type I pneumocytes, bronchiolar and bronchial epithelial cells, and some macrophages (Fig. 3D).

In summary, we inoculated young and aged cynomolgus macaques with a low-passage clinical isolate of SARS-CoV-2, which resulted in productive infection in the absence of overt clinical signs. Recent studies in human cases have shown that presymptomatic and asymptomatic cases can also shed virus (14, 15). Increased age did not affect disease outcome, but there was prolonged viral shedding in the upper respiratory tract of aged animals. Prolonged shedding has been observed in both SARS-CoV-2 and SARS-CoV patients (16, 17). SARS-CoV-2 shedding in our asymptomatic model peaked early in the course of infection, similar to what is seen in symptomatic patients (16). Also, SARS-CoV-2 antigen was detected in ciliated epithelial cells of nasal mucosae at day 4 p.i., which was not seen for SARS-CoV (10) or MERS-CoV infections (this study) in this animal model. Viral tropism for the nasal mucosa fits with efficient respiratory transmission, as has been seen for influenza A virus (18). This early peak in virus shedding for SARS-CoV-2 is similar to that of influenza virus shedding (19) and may explain why case detection and isolation may not be as effective for SARS-CoV-2 as it was for the control of SARS-CoV (20). SARS-CoV-2 was

primarily detected in tissues of the respiratory tract; however, SARS-CoV-2 RNA was also detectable in other tissues such as intestines, in line with a recent report (21). Similar results regarding viral shedding and tissue and cell tropism were recently also reported after SARS-CoV-2 inoculation in rhesus macaques. However, unlike in our model, SARS-CoV-2 infection in rhesus macaques does result in transient respiratory disease and weight loss (22, 23).

Two out of four animals had foci of DAD on day 4 p.i. The colocalization of SARS-CoV-2 antigen expression and DAD provides strong evidence that SARS-CoV-2 infection caused this lesion. The histological character of the DAD, including alveolar and bronchiolar epithelial necrosis, alveolar edema, hyaline membrane formation, and accumulation of neutrophils, macrophages, and lymphocytes, corresponds with the limited pathological analyses of human COVID-19 cases (6, 7). In particular, the presence of syncytia in the lung lesions is characteristic of respiratory coronavirus infections. Whereas MERS-CoV primarily infects type II pneumocytes in cynomolgus macaques, both SARS-CoV and SARS-CoV-2 also infect type I pneumocytes. Injury to type I pneumocytes can result in pulmonary edema, and formation of hyaline membranes (24), which may explain why hyaline membrane formation is a hallmark of SARS and COVID-19 (7, 10) but not frequently reported for MERS (25, 26).

These data show that cynomolgus macaques are permissive to SARS-CoV-2 infection, shed virus for a prolonged period of time, and display COVID-19-like disease. In this non-human primate model, SARS-CoV-2 replicates efficiently in respiratory epithelial cells throughout the respiratory tract, including nasal cavity, bronchi, bronchioles, and alveoli. Replication in the upper respiratory tract fits with efficient transmission between hosts, whereas replication in the lower respiratory tract fits with the development of lung disease. An in-depth comparison of infection with SARS-CoV, MERS-CoV, and SARS-CoV-2 in this model may identify key pathways in the pathogenesis of these emerging viruses. This study provides a new infection model that will be critical in the evaluation and licensure of preventive and therapeutic strategies against SARS-CoV-2 infection for use in humans, as well as for evaluating the efficacy of repurposing species-specific existing treatments, such as pegylated interferon (12).

## REFERENCES AND NOTES

1. J. F. Chan et al., *Lancet* **395**, 514–523 (2020).
2. C. Huang et al., *Lancet* **395**, 497–506 (2020).
3. E. Mahase, *BMJ* **368**, m641 (2020).
4. H. Shi et al., *Lancet Infect. Dis.* **20**, 425–434 (2020).
5. N. Chen et al., *Lancet* **395**, 507–513 (2020).
6. Z. Xu et al., *Lancet Respir. Med.* **8**, 420–422 (2020).

7. S. Tian et al., *J. Thorac. Oncol.* **S1556-0864(20)**30132-5 (2020).
8. J. M. Nicholls et al., *Lancet* **361**, 1773–1778 (2003).
9. R. A. Fouchier et al., *Nature* **423**, 240 (2003).
10. T. Kuiken et al., *Lancet* **362**, 263–270 (2003).
11. S. L. Smits et al., *PLOS Pathog.* **6**, e1000756 (2010).
12. B. L. Haagmans et al., *Nat. Med.* **10**, 290–293 (2004).
13. B. Rockx et al., *PLOS ONE* **6**, e18558 (2011).
14. C. Li et al., *Emerg. Infect. Dis.* **26** (2020).
15. A. Kimball et al., *MMWR Morb. Mortal. Wkly. Rep.* **69**, 377–381 (2020).
16. L. Zou et al., *N. Engl. J. Med.* **382**, 1177–1179 (2020).
17. J. S. Peiris et al., *Lancet* **361**, 1767–1772 (2003).
18. M. Richard et al., *Nat. Commun.* **11**, 766 (2020).
19. C. C. Li et al., *Emerg. Infect. Dis.* **16**, 1265–1272 (2010).
20. X. Pang et al., *JAMA* **290**, 3215–3221 (2003).
21. F. Xiao et al., *Gastroenterology* **S0016-5085(20)**30282-1 (2020).
22. W. D. Linlin Bao et al., Reinfection could not occur in SARS-CoV-2 infected rhesus macaques. *bioRxiv* 2020.03.13.990226 (2020). <https://doi.org/10.1101/2020.03.13.990226>.
23. V. J. Munster et al., Respiratory disease and virus shedding in rhesus macaques inoculated with SARS-CoV-2. *bioRxiv* 2020.03.21.001628 (2020). <https://doi.org/10.1101/2020.03.21.001628>.
24. L. B. Ware, M. A. Matthay, *N. Engl. J. Med.* **342**, 1334–1349 (2000).
25. W. J. Shieh et al., *Hum. Pathol.* **36**, 303–309 (2005).
26. D. L. Ng et al., *Am. J. Pathol.* **186**, 652–658 (2016).

## ACKNOWLEDGMENTS

We thank L. de Meulder, A. van der Linden, I. Chestakova, and F. van der Panne for technical assistance. We also thank Y. Kap, D. Akkermans, V. Vaes, M. Sommers, and F. Meijers for assistance with the animal studies. **Funding:** This research is (partly) financed by the NWO Stevin Prize awarded to M.K. by the Netherlands Organisation for Scientific Research (NWO), H2020 grant agreement 874735-VEO to M.K., NIH/NIAD contract HHSN272201400008C to R.F., and H2020 grant agreement 101003651-MANCO to B.H. **Author contributions:** Conceptualization, B.R., T.K., R.F., M.K., R.d.S., M.F. B.H.; investigation, B.R., T.K., S.H., T.B., M.L., D.d.M., G.v.A., J.v.d.B., N.O., D.S., P.v.R., L.L.; resources, B.H., C.D., E.V., B.V., J.L.; supervision, B.R. and B.H.; writing, original draft, B.R., T.K., and B.H.; writing—review and editing, all authors; funding acquisition: S.H., B.H., R.F., and M.K. **Animal welfare:** Research was conducted in compliance with the Dutch legislation for the protection of animals used for scientific purposes (2014, implementing EU Directive 2010/63) and other relevant regulations. The licensed establishment where this research was conducted (Erasmus MC) has an approved OLAW Assurance no. A5051-01. Research was conducted under a project license from the Dutch competent authority and the study protocol (no. 17-4312) was approved by the institutional Animal Welfare Body. **Competing interests:** T.B., R.F., and B.H. are listed as inventors on a patent application related to MERS-coronavirus diagnostics, therapy and vaccines. Other authors declare no competing interests. **Data and materials availability:** All data are available in the main text or the supplementary materials. This work is licensed under a Creative Commons Attribution 4.0 International (CC BY 4.0) license, which permits unrestricted use, distribution, and reproduction in any medium, provided the original work is properly cited. To view a copy of this license, visit <https://creativecommons.org/licenses/by/4.0/>. This license does not apply to figures/photos/artwork or other content included in the article that is credited to a third party; obtain authorization from the rights holder before using such material.

## SUPPLEMENTARY MATERIALS

science.sciencemag.org/content/368/6494/1012/suppl/DC1  
Materials and Methods  
Figs. S1 to S3  
Tables S1 and S2  
References (27–30)  
MDAR Reproducibility Checklist

15 March 2020; accepted 15 April 2020  
Published online 17 April 2020  
10.1126/science.abb7314

## CORONAVIRUS

## Susceptibility of ferrets, cats, dogs, and other domesticated animals to SARS–coronavirus 2

Jianzhong Shi<sup>1\*</sup>, Zhiyuan Wen<sup>1\*</sup>, Gongxun Zhong<sup>1\*</sup>, Huanliang Yang<sup>1\*</sup>, Chong Wang<sup>1\*</sup>, Baoying Huang<sup>2\*</sup>, Renqiang Liu<sup>1</sup>, Xijun He<sup>3</sup>, Lei Shuai<sup>1</sup>, Ziruo Sun<sup>1</sup>, Yubo Zhao<sup>1</sup>, Peipei Liu<sup>2</sup>, Libin Liang<sup>1</sup>, Pengfei Cui<sup>1</sup>, Jinliang Wang<sup>1</sup>, Xianfeng Zhang<sup>3</sup>, Yuntao Guan<sup>3</sup>, Wenjie Tan<sup>2</sup>, Guizhen Wu<sup>2</sup>, Hualan Chen<sup>1†</sup>, Zhigao Bu<sup>1,3†</sup>

Severe acute respiratory syndrome–coronavirus 2 (SARS-CoV-2) causes the infectious disease COVID-19 (coronavirus disease 2019), which was first reported in Wuhan, China, in December 2019. Despite extensive efforts to control the disease, COVID-19 has now spread to more than 100 countries and caused a global pandemic. SARS-CoV-2 is thought to have originated in bats; however, the intermediate animal sources of the virus are unknown. In this study, we investigated the susceptibility of ferrets and animals in close contact with humans to SARS-CoV-2. We found that SARS-CoV-2 replicates poorly in dogs, pigs, chickens, and ducks, but ferrets and cats are permissive to infection. Additionally, cats are susceptible to airborne transmission. Our study provides insights into the animal models for SARS-CoV-2 and animal management for COVID-19 control.

In late December 2019, an unusual pneumonia emerged in humans in Wuhan, China, and rapidly spread internationally, raising global public health concerns. The causative pathogen was identified as a novel coronavirus (1–16) and named severe acute respiratory syndrome–coronavirus 2 (SARS-CoV-2) on the basis of a phylogenetic analysis of related

coronaviruses by the Coronaviridae Study Group of the International Committee on Taxonomy of Viruses (17). Subsequently, the disease caused by this virus was designated coronavirus disease 2019 (COVID-19) by the World Health Organization (WHO). Despite major efforts to control the COVID-19 outbreak, the disease is still spreading. As of 11 March

2020, SARS-CoV-2 infections have been reported in more than 100 countries, and 118,326 human cases have been confirmed, with 4292 fatalities (18). WHO has now officially declared COVID-19 a pandemic.

Although SARS-CoV-2 shares 96.2% of its identity at the nucleotide level with the coronavirus RaTG13—which was detected in horseshoe bats (*Rhinolophus* spp.) in Yunnan province, China, in 2013 (3)—it has not previously been detected in humans or other animals. The emerging public health crisis raises many urgent questions. Could the widely disseminated SARS-CoV-2 be transmitted to other animal species, which then become reservoirs of infection? The SARS-CoV-2 infection has a wide clinical spectrum in humans, ranging from mild infection to death, but how does

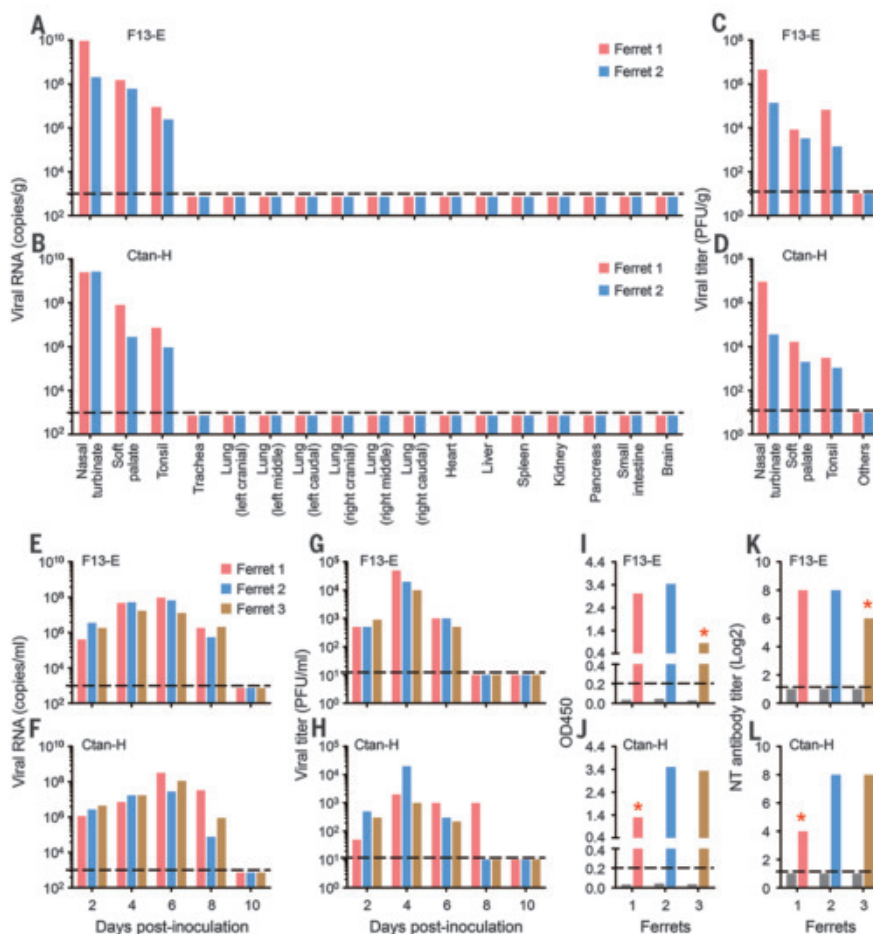
<sup>1</sup>State Key Laboratory of Veterinary Biotechnology, Harbin Veterinary Research Institute, Chinese Academy of Agricultural Sciences, Harbin 150069, People's Republic of China. <sup>2</sup>National Institute for Viral Disease Control and Prevention, China CDC, Beijing 102206, People's Republic of China. <sup>3</sup>National High Containment Laboratory for Animal Diseases Control and Prevention, Harbin 150069, People's Republic of China.

\*These authors contributed equally to this work.

†Corresponding author. Email: buzhihao@caas.cn (Z.B.); chenhuailan@caas.cn (H.C.); wugz@ivdc.chinacdc.cn (G.W.)

## Fig. 1. Replication of SARS-CoV-2 in ferrets.

Viral RNA in organs or tissues of ferrets inoculated with (A) F13-E virus strain or (B) CTan-H strain. Viral titers in organs or tissues of ferrets inoculated with F13-E (C) and CTan-H (D). The viral RNA–negative organs indicated in (A) and (B) were also negative for virus titration [indicated as “Others” in (C) and (D)]. Viral RNA (E and F) and viral titer (G and H) in nasal washes of ferrets inoculated with F13-E [(E) and (G)] and CTan-H [(F) and (H)]. Antibodies against SARS-CoV-2 tested by ELISA (I and J) and neutralization assay (K and L) with sera derived from ferrets inoculated with F13-E [(I) and (K)] and CTan-H [(J) and (L)]. Each color bar represents the value from an individual animal. The gray bars in (I) to (L) indicate the antibody values of sera collected from each animal before inoculation. Asterisks denote animals that were euthanized on day 13 p.i.; the other four animals were euthanized on day 20 p.i. The dashed lines in (I) and (L) show the cutoff value for seroconversion, and the dashed lines in the other panels indicate the lower limit of detection. OD450, optical density measured at 450 nm; NT antibody, neutralizing antibody.



the virus behave in other animals? As efforts progress toward vaccine and antiviral drug development, which animal(s) can be used to most accurately model the efficacy of such control measures in humans? To address these questions, we evaluated the susceptibility of different model laboratory animals, as well as companion and domestic animals, to SARS-CoV-2.

All experiments with infectious SARS-CoV-2 were performed in the biosafety level 4 and animal biosafety level 4 facilities in the Harbin Veterinary Research Institute (HVRI) of the Chinese Academy of Agricultural Sciences (CAAS), which was approved for such use by the Ministry of Agriculture and Rural Affairs of China. Details of the biosafety and biosecurity measures are provided in the supplementary materials (19). The protocols for animal study and animal welfare were reviewed and approved by the Committee on the Ethics of Animal Experiments of the HVRI of CAAS (approval number 2020-01-01JiPi).

Ferrets are commonly used as an animal model for viral respiratory infections in humans (20–26). We therefore tested the susceptibility of ferrets to SARS-CoV-2. Two virus strains were used in this study: (i) SARS-CoV-2/F13/environment/2020/Wuhan (F13-E), isolated from an environmental sample collected in the Huanan Seafood Market in Wuhan, and (ii) SARS-CoV-2/CTan/human/2020/Wuhan (CTan-H), isolated from a human patient. Pairs of ferrets were inoculated intranasally with  $10^5$  plaque-forming units (PFU) of F13-E or CTan-H and euthanized on day 4 post-inoculation (p.i.). The nasal turbinate, soft palate, tonsils, trachea, lung, heart, liver, spleen, kidneys, pancreas, small intestine, and brain from each ferret were collected for viral RNA quantification by quantitative polymerase chain reaction and virus titration in Vero E6 cells. Viral RNA (Fig. 1, A and B) and infectious virus (Fig. 1, C and D) were detected in the nasal turbinate, soft palate, and tonsils of all four ferrets inoculated with these two viruses but were not detected in any other organs tested. These results indicate that SARS-CoV-2 can replicate in the upper respiratory tract of ferrets, but its replication in other organs is undetectable.

To investigate the replication dynamics of these virus strains in ferrets, groups of three animals were inoculated intranasally with  $10^5$  PFU of F13-E or CTan-H, and each ferret was then placed in a separate cage within an isolator. Nasal washes and rectal swabs were collected on days 2, 4, 6, 8, and 10 p.i. from the ferrets for viral RNA detection and virus titration. Body temperatures and signs of disease were monitored for 2 weeks. Viral RNA was detected in the nasal washes on days 2, 4, 6, and 8 p.i. in all six ferrets inoculated with the two strains (Fig. 1, E and F). Viral RNA was also detected in some of the rectal swabs of

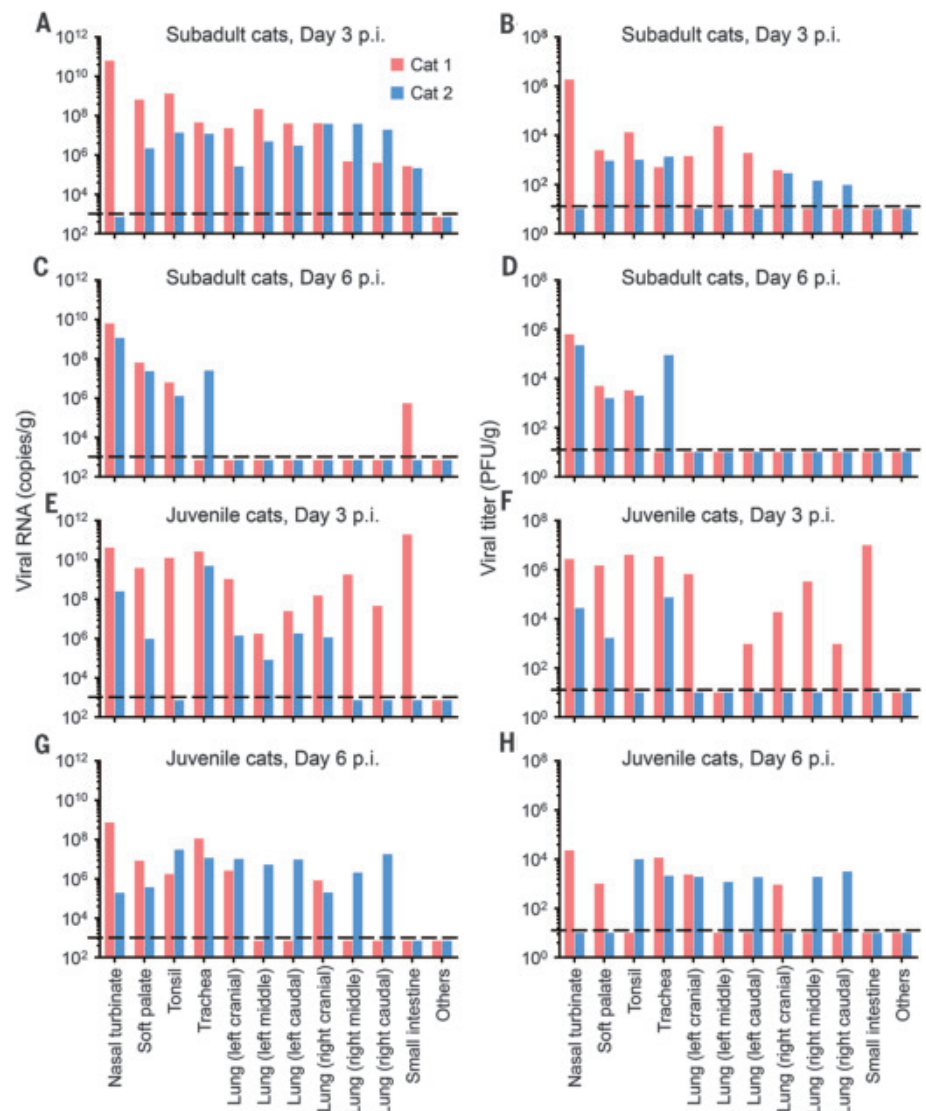


**Fig. 2. Replication of SARS-CoV-2 in cats.** Subadult cats and juvenile cats inoculated with CTan-H virus were euthanized on days 3 and 6 p.i., and their organs were collected for viral RNA detection and virus titration. (A) Viral RNA and (B) viral titers of subadult cats on day 3 p.i. (C) Viral RNA and (D) viral titers of subadult cats on day 6 p.i. (E) Viral RNA and (F) viral titers of juvenile cats on day 3 p.i. The values of red bars in (E) and (F) are from the cat that died on this day. (G) Viral RNA and (H) viral titers of juvenile cats on day 6 p.i. "Others" represents viral-negative organs, including the brain, heart, submaxillary lymph nodes, kidneys, spleen, liver, and pancreas. Each color bar represents the value from an individual animal. The dashed lines indicate the lower limit of detection.

the virus-inoculated ferrets, although the copy numbers were notably lower than those in the nasal washes of these ferrets (fig. S1, A and C). Infectious virus was detected from the nasal washes of all ferrets (Fig. 1, G and H) but not from the rectal swabs of any ferrets (fig. S1, B and D).

One ferret from each virus-inoculated group developed fever and loss of appetite on days 10 (CTan-H-inoculated) and 12 p.i. (F13-E-inoculated), respectively. To investigate whether these symptoms were caused by virus replication in the lower respiratory tract, we euthanized

the two ferrets on day 13 p.i. and collected their organs for viral RNA detection. However, viral RNA was not detected in any other tissues or organs of either ferret, except for a low copy number ( $10^{5.4}$  copies/g) in the turbinate of the ferret inoculated with CTan-H (fig. S2). Pathological studies revealed severe lymphoplasmacytic perivascularitis and vasculitis; increased numbers of type II pneumocytes, macrophages, and neutrophils in the alveolar septa and alveolar lumen; and mild peribronchitis in the lungs of the two ferrets euthanized on day 13 p.i. (fig. S3). Antibodies

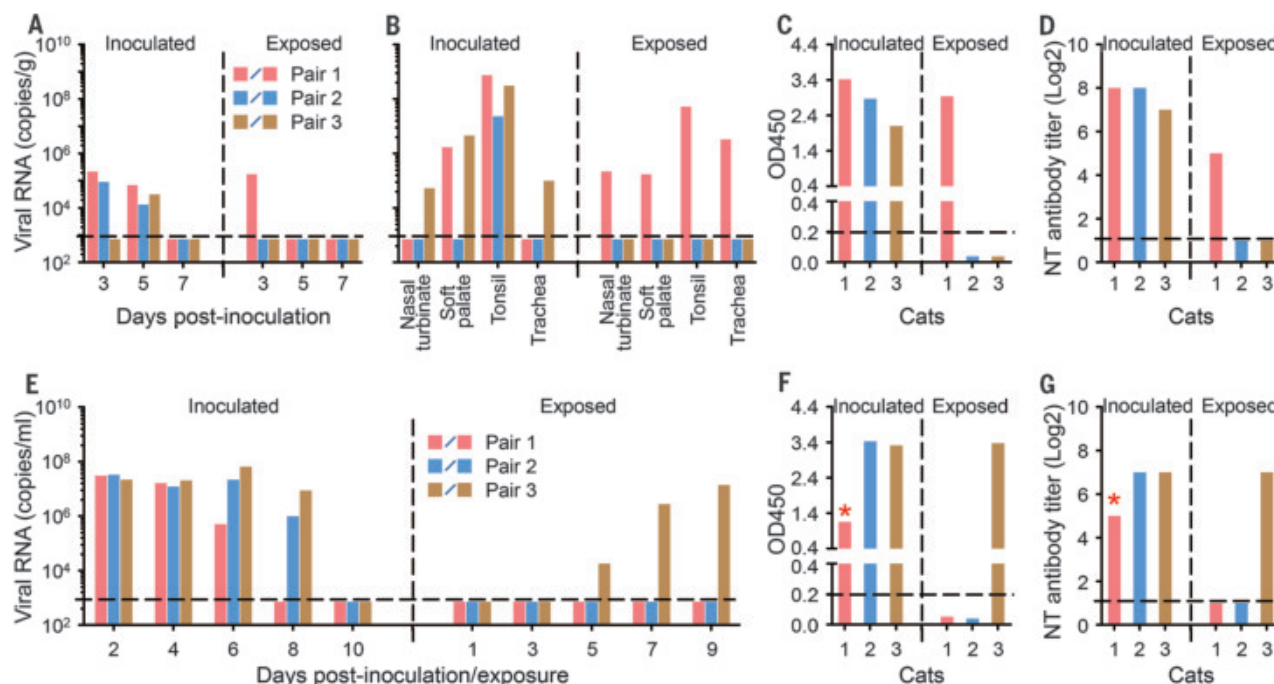


**Fig. 3. Transmission of SARS-CoV-2 in cats.** Transmission of the CTan-H virus strain was evaluated in subadult cats (A to D) and juvenile cats (E to G). (A) Viral RNA in the feces of virus-inoculated or virus-exposed subadult cats. (B) Viral RNA in tissues or organs of inoculated or exposed subadult cats euthanized on day 11 p.i. (pair 1, red bars) or day 12 p.i. (pairs 2 and 3). Antibodies against SARS-CoV-2 in these euthanized subadult cats were detected by ELISA (C) and neutralization assay (D). (E) Viral RNA in nasal washes of juvenile cats. Sera

from juvenile cats were collected on day 20 p.i., except for sera from one virus-inoculated animal that died on day 13 p.i. Antibody values for this cat (indicated by asterisks) were detected from sera collected on day 10 p.i.; antibodies against SARS-CoV-2 were detected by ELISA (F) and neutralization assay (G). Each color bar represents the value from an individual animal. The horizontal dashed lines in (C) and (F) show the cutoff value for seroconversion, and the horizontal dashed lines in the other panels indicate the lower limit of detection.

against SARS-CoV-2 were detected in all ferrets by an enzyme-linked immunosorbent assay (ELISA) and a neutralization assay, although the antibody titers of the two ferrets that were euthanized on day 13 p.i. were notably lower than those of the ferrets euthanized on day 20 p.i. (Fig. 1, I to L).

A virus attachment assay indicated that SARS-CoV-2 could attach to bronchiolar epithelial cells (fig. S4A) and some type II pneumocytes (fig. S4B) in ferret lungs. To further investigate whether SARS-CoV-2 replicates in the lungs of ferrets, we intratracheally inoculated eight ferrets with  $10^5$  PFU of CTan-H and euthanized two animals each on days 2, 4, 8, and 14 p.i. to look for viral RNA in the tissues and organs. Viral RNA was detected only in the nasal turbinate and soft palate of one ferret in each pair euthanized on days 2 and 4 p.i.; was detected in the soft palate of one ferret and in the nasal turbinate, soft palate, tonsils, and trachea of the other ferret euthanized on day 8 p.i.; and was not detected in either of the two ferrets euthanized on day 14 p.i. (fig. S5). These results indicate that SARS-CoV-2 can replicate in the upper respiratory tract of ferrets for up to 8 days without causing severe disease or death.

Cats and dogs are in close contact with humans; therefore, it is important to understand

their susceptibility to SARS-CoV-2. We first investigated the replication of SARS-CoV-2 in cats. Seven subadult cats (aged 6 to 9 months, outbred domestic cats) were intranasally inoculated with  $10^5$  PFU of CTan-H. Two animals were scheduled to be euthanized on days 3 and 6 p.i., respectively, to evaluate viral replication in their organs. Three subadult cats were placed in separate cages within an isolator. To monitor respiratory droplet transmission, an uninfected cat was placed in a cage adjacent to each of the infected cats. The aggressive behavior of the subadult cats made it difficult to perform regular nasal wash collection. To avoid possible injury, we only collected feces from these cats and checked for viral RNA in their organs after euthanasia.

Viral RNA was detected in the nasal turbinate of one animal, as well as in the soft palates, tonsils, tracheas, lungs, and small intestines of both animals euthanized on day 3 p.i. (Fig. 2A). In the animals euthanized on day 6 p.i., viral RNA was detected in the nasal turbinates, soft palates, and tonsils of both animals; in the trachea of one animal; and in the small intestine of the other. However, viral RNA was not detected in any lung samples from either of these animals (Fig. 2C). Infectious virus was detected in the viral RNA-positive nasal turbinates, soft palates, tonsils, tracheas, and

lungs of these cats but was not recovered from the viral RNA-positive small intestines (Fig. 2, B and D).

In the transmission study, viral RNA was detected in the feces of two virus-inoculated subadult cats on day 3 p.i. and in all three virus-inoculated subadult cats on day 5 p.i. (Fig. 3A). Viral RNA was detected in the feces of one exposed cat on day 3 p.i. (Fig. 3A). The pair of subadult cats with viral RNA-positive feces was euthanized on day 11 p.i. Viral RNA was detected in the soft palate and tonsils of the virus-inoculated animal and in the nasal turbinate, soft palate, tonsils, and trachea of the exposed animal (Fig. 3B), indicating that respiratory droplet transmission had occurred. We euthanized the other pairs on day 12 p.i. Viral RNA was detected in the tonsils of one virus-inoculated subadult cat and in the nasal turbinate, soft palate, tonsils, and trachea of the other virus-inoculated subadult cat but was not detected in any organs or tissues of the two exposed subadult cats (Fig. 3B). Antibodies against SARS-CoV-2 were detected in all three virus-inoculated subadult cats and one exposed cat via an ELISA and neutralization assay (Fig. 3, C and D).

We repeated the replication and transmission studies in juvenile cats (aged 70 to 100 days) (Figs. 2, E to H, and 3, E to G, and fig. S6).

**Table 1. Susceptibility of dogs, pigs, chickens, and ducks to SARS-CoV-2.** Animals were intranasally inoculated with  $10^5$  PFU (dogs and pigs) or  $10^{4.5}$  PFU (chickens and ducks) of the CTan-H virus strain. Two (dogs) or three (pigs, chickens, and ducks) uninfected animals were housed in the same room with their infected counterparts to monitor transmission of the virus. Oropharyngeal and rectal swabs from all animals were collected on the indicated days postinoculation (p.i.) for viral RNA detection. The "Other time points" category includes days 8, 10, 12, and 14 p.i.

| Viral RNA detection in animals inoculated with SARS-CoV-2 isolate CTan-H;<br>positive cases/total (copies, log <sub>10</sub> ) |            |                    |            |            |                      |                |            |            |                      |   |
|--|------------|--------------------|------------|------------|----------------------|----------------|------------|------------|----------------------|---|
| Animal   | Treatment  | Oropharyngeal swab |            |            |                      | Rectal swab    |            |            |                      | Seroconversion:<br>positive<br>cases/total† |
|  |            | Day 2 p.i.         | Day 4 p.i. | Day 6 p.i. | Other time<br>points | Day 2 p.i.     | Day 4 p.i. | Day 6 p.i. | Other time<br>points |   |
| Dog*   | Inoculated | 0/5                | 0/5        | 0/4        | 0/4                  | 2/5 (6.5, 5.4) | 0/5        | 1/4 (4.2)  | 0/4                  | 2/4   |
|  | Contact    | 0/2                | 0/2        | 0/2        | 0/2                  | 0/2            | 0/2        | 0/2        | 0/2                  | 0/2   |
| Pig  | Inoculated | 0/5                | 0/5        | 0/5        | 0/5                  | 0/5            | 0/5        | 0/5        | 0/5                  | 0/5   |
|  | Contact    | 0/3                | 0/3        | 0/3        | 0/3                  | 0/3            | 0/3        | 0/3        | 0/3                  | 0/3   |
| Chicken  | Inoculated | 0/5                | 0/5        | 0/5        | 0/5                  | 0/5            | 0/5        | 0/5        | 0/5                  | 0/5   |
|  | Contact    | 0/3                | 0/3        | 0/3        | 0/3                  | 0/3            | 0/3        | 0/3        | 0/3                  | 0/3   |
| Duck   | Inoculated | 0/5                | 0/5        | 0/5        | 0/5                  | 0/5            | 0/5        | 0/5        | 0/5                  | 0/5   |
|  | Contact    | 0/3                | 0/3        | 0/3        | 0/3                  | 0/3            | 0/3        | 0/3        | 0/3                  | 0/3   |

\*One virus-inoculated beagle was euthanized on day 4 p.i., but viral RNA was not detected in any of its collected organs, which included lung, trachea, nasal turbinate, soft palate, brain, heart, tonsils, kidneys, spleen, liver, pancreas, and small intestine (fig. S6). †Sera were collected from all animals on day 14 p.i., and antibodies against SARS-CoV-2 were detected by using a double-antigen sandwich ELISA kit (ProtTech, Luoyang, China).

Histopathologic studies performed on samples from the virus-inoculated juvenile cats that died or were euthanized on day 3 p.i. revealed massive lesions in the nasal and tracheal mucosa epitheliums and lungs (fig. S7). These results indicate that SARS-CoV-2 can replicate efficiently in cats and that younger cats are more vulnerable than older ones. Notably, our findings also reveal that the virus is transmissible between cats via the airborne route.

We next investigated the replication and transmission of SARS-CoV-2 in dogs. Five 3-month-old beagles were intranasally inoculated with  $10^5$  PFU of CTan-H and housed with two uninoculated beagles in a room. Oropharyngeal and rectal swabs from each beagle were collected on days 2, 4, 6, 8, 10, 12, and 14 p.i. for viral RNA detection and virus titration in Vero E6 cells. Viral RNA was detected in the rectal swabs of two virus-inoculated dogs on day 2 p.i. and in the rectal swab of one such dog on day 6 p.i. (Table 1). One dog that was positive for viral RNA by rectal swab on day 2 p.i. was euthanized on day 4 p.i., but viral RNA was not detected in any organs or tissues collected from this animal (fig. S8). Additionally, infectious virus was not detected in any swabs collected from any of these dogs. Sera were collected from all dogs on day 14 p.i. for antibody detection by an ELISA. Two virus-inoculated dogs seroconverted; the other two virus-inoculated dogs and the two contact-exposed dogs were all seronegative for SARS-CoV-2 (Table 1 and fig. S9). These results indicate that dogs have low susceptibility to SARS-CoV-2.

We also investigated the susceptibility of pigs, chickens, and ducks to SARS-CoV-2 by

using the same strategy as that used to assess dogs. However, viral RNA was not detected in any swabs collected from these virus-inoculated animals or from naïve contact animals (Table 1). In addition, all of these animals were seronegative for SARS-CoV-2 when tested by ELISA with sera collected on day 14 p.i. (Table 1). These results indicate that pigs, chickens, and ducks are not susceptible to SARS-CoV-2.

In summary, we found that ferrets and cats are highly susceptible to SARS-CoV-2; dogs have low susceptibility; and pigs, chickens, and ducks are not susceptible to the virus. Unlike influenza viruses and the other SARS-coronavirus known to infect humans (SARS-CoV-1), which replicate in both the upper and lower respiratory tract of ferrets (20, 22–24, 26, 27), SARS-CoV-2 replicates only in the nasal turbinate, soft palate, and tonsils of ferrets. SARS-CoV-2 may also replicate in the digestive tract, as viral RNA was detected in the rectal swabs of the virus-infected ferrets, but virus was not detected in lung lobes, even after the ferrets were intratracheally inoculated with the virus. It remains unclear whether the virus causes more severe disease in male ferrets than in female ferrets, as has been observed among humans (13, 28).

Several studies have reported that SARS-CoV-2 uses angiotensin-converting enzyme 2 (ACE2) as its receptor to enter cells (3, 29–37). ACE2 is mainly expressed in type II pneumocytes and serous epithelial cells of tracheo-bronchial submucosal glands in ferrets (25). Ferrets and cats differ by only two amino acids in the SARS-CoV-2 spike-contacting regions of ACE2 (table S1); therefore, the underlying mechanism that prevents the replication of

SARS-CoV-2 in the lower respiratory tract of ferrets remains to be investigated. The fact that SARS-CoV-2 replicates efficiently in the upper respiratory tract of ferrets makes them a candidate animal model for evaluating the efficacy of antiviral drugs or vaccines against COVID-19.

The cats we used in this study were outbreak and were susceptible to SARS-CoV-2, which replicated efficiently and was transmissible to naïve cats. Cats in Wuhan have been reported to be seropositive for SARS-CoV-2 (32). Surveillance for SARS-CoV-2 in cats should be considered as an adjunct to elimination of COVID-19 in humans.

## REFERENCES AND NOTES

1. L. Zou et al., *N. Engl. J. Med.* **382**, 1177–1179 (2020).
2. N. Zhu et al., *N. Engl. J. Med.* **382**, 727–733 (2020).
3. P. Zhou et al., *Nature* **579**, 270–273 (2020).
4. F. Wu et al., *Nature* **579**, 265–269 (2020).
5. A. Wu et al., *Cell Host Microbe* **27**, 325–328 (2020).
6. C. Wang, P. W. Horby, F. G. Hayden, G. F. Gao, *Lancet* **395**, 470–473 (2020).
7. Y. Pan, D. Zhang, P. Yang, L. L. M. Poon, Q. Wang, *Lancet Infect. Dis.* **20**, 411–412 (2020).
8. X. Pan et al., *Lancet Infect. Dis.* **20**, 410–411 (2020).
9. R. Lu et al., *Lancet* **395**, 565–574 (2020).
10. P. Liu, X. Z. Tan, *Radiology* **295**, 19 (2020).
11. Q. Li et al., *N. Engl. J. Med.* **382**, 1199–1207 (2020).
12. C. Huang et al., *Lancet* **395**, 497–506 (2020).
13. W. J. Guan et al., *N. Engl. J. Med.* **10.1056/NEJMoa2002032** (2020).
14. N. Chen et al., *Lancet* **395**, 507–513 (2020).
15. J. F. Chan et al., *Lancet* **395**, 514–523 (2020).
16. J. F. Chan et al., *Emerg. Microbes Infect.* **9**, 221–236 (2020).
17. Coronaviridae Study Group of the International Committee on Taxonomy of Viruses, *Nat. Microbiol.* **5**, 536–544 (2020).
18. World Health Organization (WHO), "Coronavirus disease 2019 (COVID-19): Situation Report – 51" (WHO, 2020); [www.who.int/docs/default-source/coronaviruse/situation-reports/20200311-sitrep-51-covid-19.pdf?sfvrsn=1ba62e57\\_4](http://www.who.int/docs/default-source/coronaviruse/situation-reports/20200311-sitrep-51-covid-19.pdf?sfvrsn=1ba62e57_4).
19. See supplementary materials.
20. J. Shi et al., *Cell Res.* **27**, 1409–1421 (2017).
21. K. J. Stittelaar et al., *Viruses* **8**, 168 (2016).

22. Q. Zhang *et al.*, *Science* **341**, 410–414 (2013).
23. M. Imai *et al.*, *Nature* **486**, 420–428 (2012).
24. S. Herfst *et al.*, *Science* **336**, 1534–1541 (2012).
25. J. M. van den Brand *et al.*, *Vet. Pathol.* **45**, 551–562 (2008).
26. B. E. Martina *et al.*, *Nature* **425**, 915 (2003).
27. Y. K. Chu *et al.*, *Virology* **374**, 151–163 (2008).
28. Novel Coronavirus Pneumonia Emergency Response Epidemiology Team, *Zhonghua Liu Xing Bing Xue Za Zhi* **41**, 145–151 (2020) [in Chinese].
29. R. Yan *et al.*, *Science* **367**, 1444–1448 (2020).
30. M. Letko, A. Marzi, V. Munster, *Nat. Microbiol.* **5**, 562–569 (2020).
31. The *Cell* Editorial Team, *Cell* **181**, 1–3 (2020).
32. Q. Zhang *et al.*, SARS-CoV-2 neutralizing serum antibodies in cats: A serological investigation. *bioRxiv* (2020). <https://doi.org/10.1101/2020.04.01.021196>.

## ACKNOWLEDGMENTS

We thank S. Watson for editing the manuscript. **Funding:** This work was supported by the National Key R&D Program of China

(2020YFC0846500, 2018YFC1200601, and 2016YFD0500301). **Author contributions:** J.S., Z.W., G.Z., H.Y., C.W., B.H., R.L., X.H., L.S., Z.S., Y.Z., P.L., L.L., P.C., J.W., X.Z., and Y.G. performed experiments; J.S., Z.W., G.Z., H.Y., C.W., W.T., G.W., H.C., and Z.B. analyzed data; and Z.B. and H.C. designed the study and wrote the manuscript. **Competing interests:** None of the authors have any competing interests. **Data and materials availability:** All data are available in the manuscript or the supplementary materials. Sequences of the viruses used in this study have been deposited in GISAID previously with the accession numbers EPI\_ISL\_402119 and EPI\_ISL\_408514. Two strains of 2019 novel coronavirus (CTan-H and F13-E) were obtained from the China CDC under a material transfer agreement that allows use only in P3+ or P4 facilities, prevents live virus sharing, and prevents commercial use. This work is licensed under a Creative Commons Attribution 4.0 International (CC BY 4.0) license, which permits unrestricted use, distribution, and reproduction in any medium, provided the original work is properly cited. To view a copy of this license, visit <https://creativecommons.org/licenses/by/4.0/>.

This license does not apply to figures/photos/artwork or other content included in the article that is credited to a third party; obtain authorization from the rights holder before using such material.

## SUPPLEMENTARY MATERIALS

[science.sciencemag.org/content/368/6494/1016/suppl/DC1](https://science.sciencemag.org/content/368/6494/1016/suppl/DC1)  
Materials and Methods  
Supplementary Text  
Figs. S1 to S10  
Table S1  
References and Notes (33–35)  
MDAR Reproducibility Checklist

12 March 2020; accepted 7 April 2020  
Published online 8 April 2020  
10.1126/science.abb7015

## ICE SHEETS

# Delicate seafloor landforms reveal past Antarctic grounding-line retreat of kilometers per year

J. A. Dowdeswell<sup>1\*</sup>, C. L. Batchelor<sup>1,2</sup>, A. Montelli<sup>1</sup>, D. Ottesen<sup>3</sup>, F. D. W. Christie<sup>1</sup>, E. K. Dowdeswell<sup>1</sup>, J. Evans<sup>4</sup>

A suite of grounding-line landforms on the Antarctic seafloor, imaged at submeter horizontal resolution from an autonomous underwater vehicle, enables calculation of ice sheet retreat rates from a complex of grounding-zone wedges on the Larsen continental shelf, western Weddell Sea. The landforms are delicate sets of up to 90 ridges, <1.5 meters high and spaced 20 to 25 meters apart. We interpret these ridges as the product of squeezing up of soft sediment during the rise and fall of the retreating ice sheet grounding line during successive tidal cycles. Grounding-line retreat rates of 40 to 50 meters per day (>10 kilometers per year) are inferred during regional deglaciation of the Larsen shelf. If repeated today, such rapid mass loss to the ocean would have clear implications for increasing the rate of global sea level rise.

The ice shelves fringing about 75% of the Antarctic Ice Sheet represent a highly sensitive interface between ice and ocean, with potential for rapid grounding-line retreat and associated mass loss from the parent ice sheet (1, 2). It is not known, however, whether modern satellite-derived grounding-line retreat rates of tens to hundreds of meters per year, acquired over a time window of about 30 years at most (3, 4), are representative of the maximum possible magnitude of retreat in, for example, West Antarctica's Pine Island Bay.

An ice sheet grounding zone is the region over which seaward-flowing ice decouples from its underlying bed and becomes a freely floating ice shelf; the instantaneous, tidally modulated junction between grounded ice, the seafloor, and the resulting sub-ice shelf ocean-water cavity beyond is known as the ground-

ing line (5). The former grounding zone is often identified on high-latitude continental shelves by the presence of sedimentary depositional centers, or grounding-zone wedges (GZWs), which provide a well-preserved geological archive of the transition zone between grounded ice sheets and floating ice shelves (5–7). GZWs build up predominantly through delivery of soft deforming sediments from the ice sheet interior to the grounding zone along a line source. There is little space for vertical accretion in the restricted cavities immediately beyond the grounding zone (8), and GZWs are therefore typically subdued, asymmetrical features on the seafloor; they generally have a steeper ice-distal face of a few degrees in slope angle and a more extensive ice-proximal portion often less than 1° (5, 7). GZW volumes can be up to several cubic kilometers, with the rate of formation depending on sediment supply and the duration of any still-stand during regional grounding-line retreat (5, 9).

We investigated, using an autonomous underwater vehicle (AUV) (10), the morphology and shallow stratigraphy of an ~9-km<sup>2</sup> area of five GZWs within a 40-km-by-10-km

grounding-zone complex preserved after ice retreat beneath about 500 m of water on the continental shelf offshore of Larsen Inlet, eastern Antarctic Peninsula (Figs. 1 and 2 and fig. S1) (11). Multibeam echo-sounder data from the AUV have a horizontal resolution of a few tens of centimeters (materials and methods), representing a step-change in our ability to observe fine-scale landforms preserved on the seafloor and to understand the highly sensitive setting of a former ice sheet grounding zone and the processes operating there. The GZWs were deposited during deglaciation of the northeastern Antarctic Peninsula continental shelf following the Last Glacial Maximum (LGM), probably before the minimum age for the transition from grounded ice to ice shelf in the inner Larsen A embayment at 10,700 calibrated years before the present [derived by relative paleomagnetic intensity dating of core KC023, Fig. 1A (11–13)]. They have remained almost undisturbed since ice retreat, except for a thin drape of hemipelagic sediment (Fig. 2).

Surface-morphological evidence (Fig. 2A) and shallow acoustic stratigraphy (Fig. 2, C and D) demonstrate that the GZWs cross-cut one another, providing a relative chronology for formation (inset of Fig. 2B). Heights varying between about 10 and 20 m mark the outer edges of GZWs 3 to 5 and, together with limited acoustic-stratigraphic evidence (Fig. 2, C and D), imply that the depocenters are about 10 to 20 m thick. Their asymmetry (Fig. 2, A and D) is typical of more than 100 GZWs identified elsewhere in the polar continental-shelf record (5, 7). GZWs “a” and 2 to 5 rest on an older surface (labeled 1 in Fig. 2B) that includes streamlined landforms (Fig. 2A), and nearby cores VC318 and VC247 (Fig. 1A) contain soft (<8 kPa) diamictic subglacial traction till that has undergone deformation (11, 14). These elongate sedimentary features, which are interpreted as mega-scale glacial lineations (MSGs) (Fig. 2, A, E, and F), are orientated in the direction of regional ice flow (Fig. 1A). The presence of MSGs implies

<sup>1</sup>Scott Polar Research Institute, University of Cambridge, Cambridge, UK. <sup>2</sup>Norwegian University of Science and Technology, Trondheim, Norway. <sup>3</sup>Geological Survey of Norway, Trondheim, Norway. <sup>4</sup>Department of Geography, Loughborough University, Loughborough, UK.  
\*Corresponding author. Email: [jd16@cam.ac.uk](mailto:jd16@cam.ac.uk)

formation subglacially in soft sediments beneath actively flowing and probably fast-flowing ice before and during GZW deposition (15, 16). In addition, the ice-distal margin of the GZWs, marking former ice sheet grounding zones, contains a number of lobate forms 50 to 100 m long (Fig. 2, E and F) that are interpreted as debris flows, demonstrating wedge progradation as deformation till was delivered to the grounding line by active ice.

On the low-gradient GZW surfaces, a complex assemblage of fine-scale landforms is present, imaged at submeter resolution (Fig. 2A). The features are of two types, forming the appearance of “ladders” with numerous “rungs.” The sides of each ladder are linear features typically 2 to 4 m high, hundreds of meters long, spaced 50 to 200 m apart, and orientated subparallel to the past ice flow direction; they are interpreted as MSGLs. The MSGLs are formed within an acoustically semitransparent unit that is overlain by a thin (about 1 m) drape of sediment (Fig. 2, C and D). Overprinting the MSGLs are sets of delicate transverse-to-flow ridges or rungs that are typically <0.5 m high and spaced about 20 to 25 m apart (Table 1). These rungs are of relatively uniform morphology, with many having a steeper ice-distal side (Fig. 3, B to E).

This delicate submarine glacial landform assemblage, which we term “ladder and rung topography,” covers almost the whole imaged area of each GZW (Figs. 2A and 3). A maximum of 90 rungs have been identified on GZW 4 (Fig. 3 and Table 1). Although the rungs have greater seafloor expression in the depressions between MSGL crests, they can often be traced across the intervening and larger MSGLs, and series of up to 50 are continuous right across several of the GZWs (Fig. 3A). This implies that the rungs are younger than the larger flow-parallel MSGLs and the GZWs. The rungs are interpreted to have formed during retreat of the ice sheet grounding line across the GZW surface. Their regular spacing implies a cyclical formation mechanism.

Regularly spaced small transverse ridges have been observed occasionally at coarser resolution on high-latitude continental shelves and in fjords (17, 18). Graham *et al.* (18), for example, used an AUV to image distinctive sets of ridges along several individual transects beneath the floating tongue of Pine Island Glacier, West Antarctica, at 2-m grid-cell size. The dimensions, spacing, and plan-view and cross-sectional geometry of similar ridges observed on several Antarctic shelves are compared in table S1. Many of the sets of small ridges, which have been referred to previously as corrugation ridges, have been interpreted as the product of tidal action that moves ice regularly up and down on a sedimentary seafloor (19). The ice can be in the form of iceberg keels, sub-ice shelf keels, or a wider grounding line (supple-

mentary text and table S1). Where corrugation ridges are located within iceberg ploughmarks, they are likely to have been produced by the tidal motion of iceberg keels impinging on the seafloor (17). Corrugation ridges are also present within scours that are interpreted to have been produced by the forward ploughing of ice keels close to the grounding line (18). Where these ridges, or rungs, are more laterally extensive, as we observe over several kilometers on the Larsen shelf, and where they overprint MSGLs on the surface of GZWs (Fig. 2A), they likely form through regular vertical motion of an ice sheet grounding line that leads to the squeezing up of deforming soft sediment as small ridges on each falling tide (18). Indeed, it has been observed that short-lived perturbations in upstream longitudinal stress and ice flow, associated with tidal-induced flexure at the grounding zone, can cause small changes in the surface of the Antarctic Ice Sheet even tens of kilometers inland of the grounding line (20, 21). By contrast, recessional moraine ridges, which are typically larger and less regularly spaced than the rungs reported here (supplementary text and table S1), have been described from the Ross and Amundsen seas and are thought to form by short-lived readvances of the grounding line during overall retreat (22–24). In Svalbard fjords, such ridges form

during small winter readvances of tidewater glacier termini during regional glacier recession (25, 26).

Given their presence overprinting MSGLs on GZW surfaces, and continuity over at least 5 km, the rungs of our ladder and rung topography are interpreted to form by grounding-line sediment squeezing in successive tidal cycles (Figs. 2 and 3). Grounding-line retreat is necessary to preserve individual rungs produced as the ice presses into the underlying soft sediment on each falling tide; otherwise, the delicate rung would be deformed or partially eroded during the next tidal cycle. The individual rungs are generally well developed and simple in morphology, with little evidence of subsequent disturbance (Figs. 2 and 3). We provide a schematic model of the formation and preservation of ladder and rung topography at the retreating grounding line of an ice shelf (Fig. 4). Although we favor an interpretation in which rung formation occurs at the grounding line, it is possible that these features were produced subglacially, contemporaneous with the MSGLs. Subglacial processes for the formation of subdued transverse ridges could include sediment squeezing into basal crevasses as the ice moves forward and/or water flow over sediment in the depressions between the MSGLs (18).

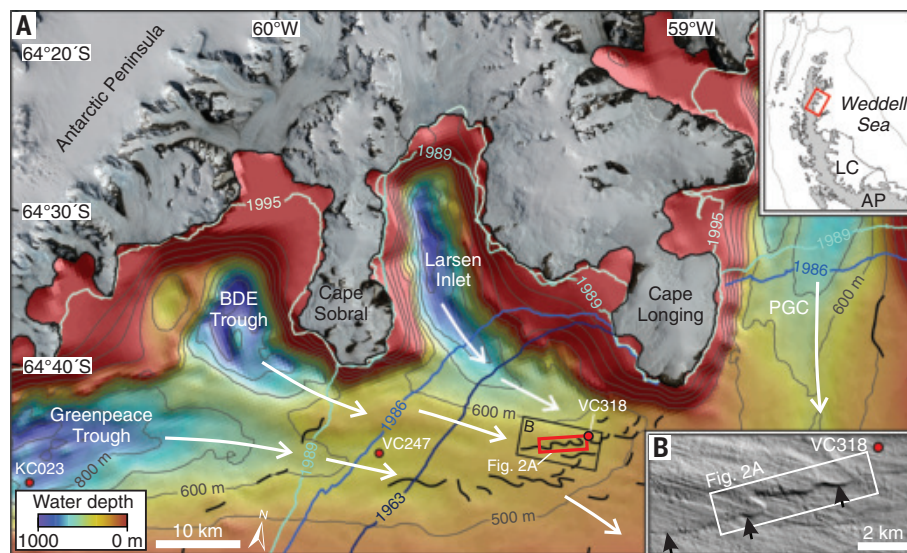


**Fig. 1. Map of the study area. (A)** Map showing the location of the surveyed GZW complex in Larsen Inlet (red box). Black lines are GZW crests (11). White arrows show the former ice flow direction. Red circles are locations of sediment cores KC023, VC247, and VC318. Background land area is from a Sentinel-2b Level-1C Top of Atmosphere reflectance image acquired on 5 December 2018. Background bathymetry is from the International Bathymetric Chart of the Southern Ocean (IBCSO) (38). BDE Trough is Bombardier, Dinsmoor and Edgemoor Trough. The 1986, 1989, and 1995 ice shelf frontal positions are from Cook *et al.* (39), and the 1963 ice shelf front position was ascertained from declassified Argon satellite imagery (40). The inset shows the location of the study area (red box) on the Antarctic Peninsula (AP). The dashed gray line is the present-day continental shelf break. LC, Larsen C Ice Shelf. **(B)** Bathymetric image of the GZW complex beyond Larsen Inlet, acquired from the RRS *James Clark Ross* in 2002 using a Kongsberg EM120 multibeam echo sounder with a frequency of 12 kHz. Grid-cell size is 50 m. The image is modified from Evans *et al.* (11). Black arrows show GZW crests.

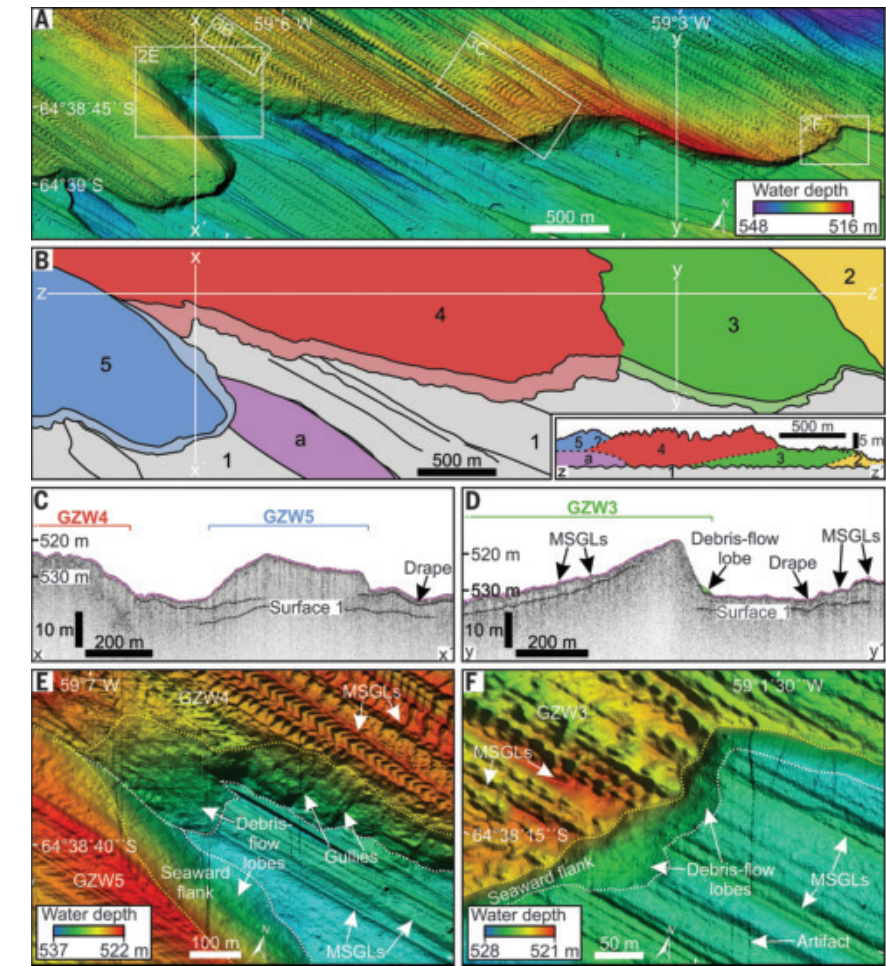


**Fig. 2. Geophysical data showing a GZW complex in Larsen Inlet, acquired from an AUV. (A)** Bathymetric data of the GZW complex, derived from an AUV-deployed multibeam echo sounder. Grid-cell size is 1 m. The location is shown in Fig. 1A. The boxes labeled 2E, 3B, 3C, and 2F show the locations of areas detailed in the corresponding figure panels. **(B)** Interpretation of individual GZWs within the grounding-zone complex. The inset is a schematic diagram showing GZW stratigraphy as derived from multibeam echo-sounder data and sub-bottom profiles. GZWs “a” and 2 to 5 rest on an older surface (labeled 1). GZW “a” overlies surface 1 and is beneath GZW 5, but its stratigraphic position relative to GZWs 2 to 4 is unknown. **(C and D)** Sub-bottom profiles along the GZWs, showing the GZW stratigraphy and a thin (~0.7 m) uppermost draping unit (pink fill). **(E and F)** Detail of debris-flow lobes on the seaward flank of the GZWs.

**Table 1. Morphological characteristics of rungs or transverse-to-flow ridges on GZW surfaces in the study area.** GZW thickness is maximum thickness derived from sub-bottom profiles. Dashed lines indicate where GZW thickness was not able to be ascertained. GZW area is only given for those parts of the GZWs that were surveyed from the AUV (Fig. 2A); the GZWs most likely extend beyond the study area. Average daily retreat and retreat duration values are calculated assuming that the ridges were produced by tidally influenced sit-downs of the grounding line (i.e., two rungs or ridges produced per day).

| GZW surface | GZW maximum thickness (m) | GZW planar area (km <sup>2</sup> ) | Number of ridges | Ridge height (m) | Average ridge spacing (m) | Average daily retreat (m) | Retreat duration (days) |
|-------------|---------------------------|------------------------------------|------------------|------------------|---------------------------|---------------------------|-------------------------|
| 1 (several) | —                         | 3.1                                | 71               | 0.1–0.4          | 20                        | 40                        | 35                      |
| a           | 3                         | 0.4                                | 33               | 0.2–0.3          | 24                        | 48                        | 16                      |
| 2           | —                         | 0.3                                | 28               | 0.2–0.6          | 25                        | 50                        | 14                      |
| 3           | 16                        | 1.4                                | 44               | 0.3–1.0          | 20                        | 40                        | 22                      |
| 4           | 15                        | 2.3                                | 90               | 0.5–1.5          | 21                        | 42                        | 45                      |
| 5           | 9                         | 1.0                                | 40               | 0.2–0.4          | 20                        | 40                        | 20                      |

Our interpretation of ladder and rung topography as a product of rapid, tidally modulated grounding-line migration allows the past rate of deglacial retreat to be calculated over days to weeks. This is only possible due to the sub-meter resolution of our AUV-derived multi-beam imagery (Figs. 2 and 3). In the absence of systematic tidal-gauge observations, an inverse model of Weddell Sea tides by Padman *et al.* (27) predicts semidiurnal tidal heights generally <1.5 m for Larsen area today; maximum tidal ranges can exceed 3 m in some places. During ship operations adjacent to Larsen C Ice Shelf in January 2019, we confirmed a strong coherency between the predictions of Padman *et al.*'s tidal model and our onboard observations. Although the configuration of the Weddell Sea during deglaciation will differ in detail from today owing to isostatic rebound and the presence of residual inner-shelf ice, gross basin form will be largely similar.

The rate of deglacial grounding-line retreat is derived from the spacing between each rung. Such an implication would be valid whether the rungs were produced along a whole section of the grounding line or by discrete ice-shelf keels impinging on the seafloor (18), although we favor the former mechanism for the Larsen shelf features given their considerable lateral continuity. Average rung spacing is between 20 and 25 m, and the number of observed rungs in the imaged area of each GZW is between 28 and 90 (Table 1); there are likely to be many more rungs on the unimaged distal surfaces of the GZWs. Assuming formation during each semidiurnal tidal cycle, this yields an average grounding-line retreat between 40 and 50 m/day over periods between 14 and 45 days. If extrapolated over the GZW surfaces landward of our imaged area, this gives a grounding-line retreat of about 18 km/year, which might conservatively be halved to about 10 km if we assume that winter sea ice cover might curtail ice shelf flexure associated with long-period swell waves for about half the year (28). This retreat rate of many kilometers per year is at least an order of magnitude higher than that observed between 1992 and 2011 at Pine Island Glacier (1.6 km/year) (29), which was itself two orders of magnitude greater than the average retreat rate for the past 10,000 years (30). Short-lived phases of very rapid post-LGM retreat, of up to 100 km/year, have also been simulated in numerical experiments by Jamieson *et al.* (31). The alternative model of rung formation, in which the rungs are produced subglacially (18), implies even higher rates of grounding-line retreat, because the ice would have to lift off from its bed near-instantaneously to preserve the delicate rungs.

The implication is that retreat across the imaged area of the GZW complex on the Larsen continental shelf could have taken place in

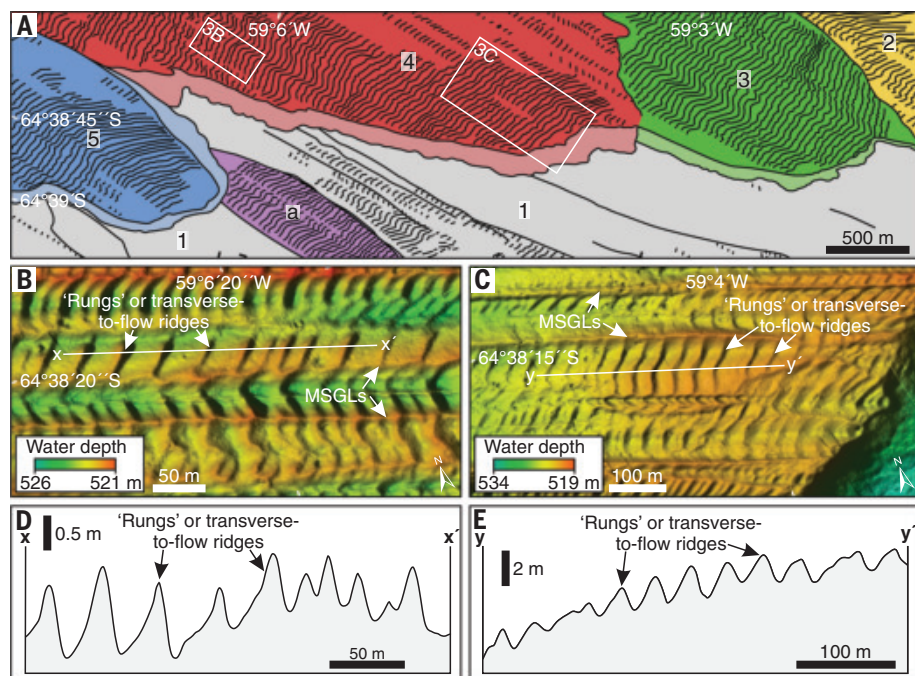


**Fig. 3. Detail of ladder and rung topography.** (A) The mapped distribution of rungs or transverse-to-flow ridges on GZW surfaces. The boxes labeled 3B and 3C show the locations of areas detailed in (B) and (C). (B and C) Details of transverse-to-flow ridges on GZW surfaces. (D and E) Profiles across the rungs shown in (B) and (C).

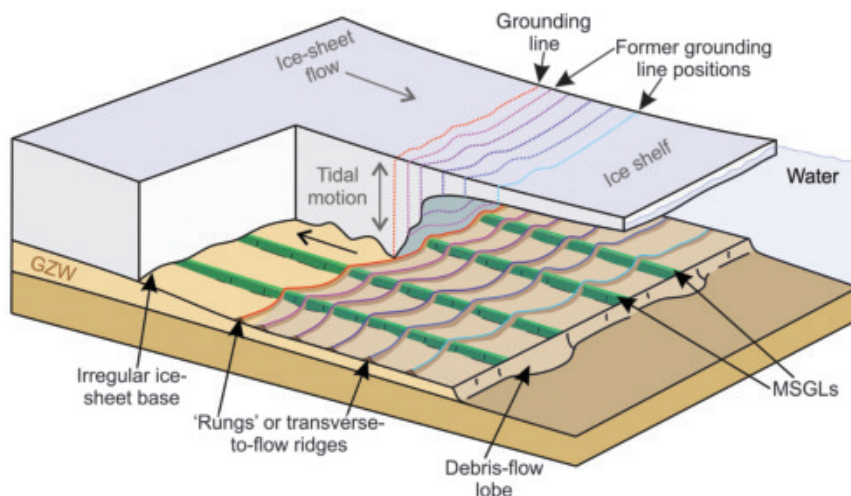


**Fig. 4. Schematic model (not to scale) of the hypothesized formation of rungs or transverse-to-flow ridges on the surface of a GZW.** When a glacier transitions into a floating ice shelf, delicate transverse-to-flow ridges can form by tidally influenced “sit-downs” of the grounding line. The ridges are formed at low tide by ice squeezing and pushing of sediments at the grounding line. The plan-view shape of the ridges reflects lateral variations in the shape of the grounding line. Series of parallel to subparallel ridges are formed when there is continuous grounding-line retreat. Because the ice is actively flowing during grounding-line retreat, as indicated by the presence of MSGLs, the parallel to subparallel nature of the rungs or ridges suggests that the shape of the ice sheet base remained relatively constant in the ice flow direction.

about 1 year. The multiple sets of GZWs suggest that periods of readvance and still-stand punctuated overall retreat, demonstrating the highly dynamic behavior of the grounding line. Presumably, final rapid retreat would

have exposed the distal sections of the GZW complex and continued through the remaining 30 km or so of Larsen Inlet, given the deepening water landward of our study area (Fig. 1A) and the increasing buoyancy of the

grounding zone that would result. Thus, it appears that final deglacial retreat from the still-stand represented by the last of the 10- to 20-m-thick GZWs was very rapid. This explains, too, why many streamlined glacial landforms, produced subglacially before deglaciation, are typically well preserved and not overprinted by other landforms—retreat is sufficiently rapid that there is little deposition. Grounding-line retreat, as inferred here over each tidal cycle, is not necessarily accompanied by retreat of the ice shelf frontal margin. For example, Pine Island Glacier underwent a sustained grounding-line retreat of ~30 km between 1992 and 2011 (3, 4) but did not experience any substantial change in its ice-shelf frontal position during that time (32).

The wider importance of our high-resolution observations of a past ice shelf GZW complex is to show, using the geological record, that very high rates of grounding-line retreat are possible, greater by an order of magnitude than those reported for ice shelves since satellite observations began. Thus, a grounding-line retreat of, for example, 10 km/year along a 5 km length of a 500-m-thick ice stream would yield a total ice mass loss of 25 km<sup>3</sup>/year [23 billion tonnes (Gt)/year using an assumed ice density of 916.7 kg/m<sup>3</sup>]. A similar calculation extrapolated across a 30-km-wide and 1-km-thick grounding line, the typical width and thickness of most ice stream centers in modern Pine Island Bay in West Antarctica, yields a total mass loss of 150 km<sup>3</sup>/year (138 Gt/year). This value is three to five times greater than mean contemporary (1992–2017) rates of mass loss integrated over Pine Island Glacier’s entire drainage basin (31 km<sup>3</sup>/year; 28.4 Gt/year) and the combined Thwaites–Pope–Smith–Kohler glacier drainage system (50.3 km<sup>3</sup>/year; 46.1 Gt/year), respectively (33). This implies that the rapid retreat of even a single Antarctic outlet glacier could, therefore, substantially increase the short-term mass loss from the ice sheet. This is without taking account of residual ice-dynamic effects associated with ice shelf loss (34); the removal of this buttressing effect provides an additional mechanism for substantial increases in ice discharge to the ocean from interior drainage basins (1, 2, 35). In addition, once retreat at this pace has begun, the self-stabilizing process of continuing subglacial sediment delivery to the grounding line to offset deglacial ice shelf thinning and/or sea level rise (36, 37) ceases to be important given the very short time, perhaps only a year or two, for sediment buildup.

#### REFERENCES AND NOTES

1. T. K. Dupont, R. B. Alley, *Geophys. Res. Lett.* **32**, L04503 (2005).
2. D. Goldberg, D. M. Holland, C. Schoof, *J. Geophys. Res. Earth Surf.* **114**, F04026 (2009).
3. J. W. Park et al., *Geophys. Res. Lett.* **40**, 2137–2142 (2013).

4. E. Rignot, J. Mouginot, B. Scheuchl, MEaSUREs Antarctic grounding line from differential satellite radar interferometry, version 2. NASA National Snow and Ice Data Center Distributed Active Archive Center (2016); doi: 10.5067/IKBWW4RYHF1Q.
5. C. L. Batchelor, J. A. Dowdeswell, *Mar. Geol.* **363**, 65–92 (2015).
6. R. B. Alley, D. D. Blankenship, S. T. Rooney, C. R. Bentley, *Mar. Geol.* **85**, 101–120 (1989).
7. J. A. Dowdeswell, E. M. G. Fugelli, *Bull. Geol. Soc. Am.* **124**, 1750–1761 (2012).
8. K. Christianson *et al.*, *J. Geophys. Res.* **121**, 1954–1983 (2016).
9. J. A. Dowdeswell *et al.*, in *Atlas of Submarine Glacial Landforms: Modern, Quaternary and Ancient*, J. A. Dowdeswell *et al.*, Eds. (Geological Society, London, Memoirs Series, 2016), vol. 46, pp. 519–552.
10. J. A. Dowdeswell *et al.*, *J. Glaciol.* **54**, 661–672 (2008).
11. J. Evans, C. J. Pudsey, C. Ó Cofaigh, P. W. Morris, E. W. Domack, *Quat. Sci. Rev.* **24**, 741–774 (2005).
12. S. Brachfeld *et al.*, *Geology* **31**, 749–752 (2003).
13. C. Ó Cofaigh *et al.*, *Quat. Sci. Rev.* **100**, 87–110 (2014).
14. C. J. Pudsey, J. W. Murray, P. Appleby, J. Evans, *Quat. Sci. Rev.* **25**, 2357–2379 (2006).
15. C. D. Clark, *Earth Surf. Process. Landf.* **18**, 1–29 (1993).
16. E. C. King, R. C. A. Hindmarsh, C. R. Stokes, *Nat. Geosci.* **2**, 585–588 (2009).
17. M. Jakobsson *et al.*, *Geology* **39**, 691–694 (2011).
18. A. G. C. Graham *et al.*, *J. Geophys. Res.* **118**, 1356–1366 (2013).
19. J. A. Smith *et al.*, *Nat. Commun.* **10**, 5635 (2019).
20. R. A. Bindshadler, M. A. King, R. B. Alley, S. Anandakrishnan, L. Padman, *Science* **301**, 1087–1089 (2003).
21. B. M. Minchew, M. Simons, B. Riel, P. Milillo, *J. Geophys. Res.* **122**, 167–190 (2017).
22. A. R. W. Halberstadt, L. M. Simkins, S. L. Greenwood, J. B. Anderson, *Cryosphere* **10**, 1003–1020 (2016).
23. J. P. Klages *et al.*, in *Atlas of Submarine Glacial Landforms: Modern, Quaternary and Ancient*, J. A. Dowdeswell *et al.*, Eds. (Geological Society, London, Memoirs Series, 2016), vol. 46, pp. 349–352.
24. L. M. Simkins *et al.*, *Nat. Geosci.* **10**, 691–697 (2017).
25. G. S. Boulton, *Sedimentology* **33**, 677–698 (1986).
26. D. Ottesen, J. A. Dowdeswell, *J. Geophys. Res.* **111**, F01016 (2006).
27. L. Padman, H. A. Fricker, R. Coleman, S. Howard, L. Erofeeva, *Ann. Glaciol.* **34**, 247–254 (2002).
28. R. A. Massom *et al.*, *Nature* **558**, 383–389 (2018).
29. E. Rignot, J. Mouginot, M. Morlighem, H. Seroussi, B. Scheuchl, *Geophys. Res. Lett.* **41**, 3502–3509 (2014).
30. C.-D. Hillenbrand *et al.*, *Geology* **41**, 35–38 (2013).
31. S. S. R. Jamieson *et al.*, *Nat. Geosci.* **5**, 799–802 (2012).
32. H. D. Pritchard *et al.*, *Nature* **484**, 502–505 (2012).
33. A. Shepherd *et al.*, *Geophys. Res. Lett.* **46**, 8174–8183 (2019).
34. J. Mouginot, E. Rignot, B. Scheuchl, *Geophys. Res. Lett.* **41**, 1576–1584 (2014).
35. T. A. Scambos, J. A. Bohlander, C. A. Shuman, P. Skvarca, *Geophys. Res. Lett.* **31**, L18402 (2004).
36. R. B. Alley, S. Anandakrishnan, T. K. Dupont, B. R. Parizek, D. Pollard, *Science* **315**, 1838–1841 (2007).
37. S. Anandakrishnan, G. A. Catania, R. B. Alley, H. J. Horgan, *Science* **315**, 1835–1838 (2007).
38. J. E. Arndt *et al.*, *Geophys. Res. Lett.* **40**, 3111–3117 (2013).
39. A. J. Cook, D. G. Vaughan, A. J. Luckman, T. Murray, *Antarct. Sci.* **26**, 614–624 (2014).
40. K. Kim, K. C. Jezek, H. Liu, *Int. J. Remote Sens.* **28**, 5357–5373 (2007).

## ACKNOWLEDGMENTS

AUV deployments were from the South African icebreaking research vessel *S.A. Agulhas II*, and we thank the captain, ice pilot, officers, and crew for their support of our work. The Copernicus/ESA Sentinel-2b image shown in Fig. 1A was acquired free-of-charge from the Copernicus Open Access Hub (<https://scihub.copernicus.eu/>). **Funding:** This research was funded by the Flotilla Foundation and Marine Archaeology Consultants Switzerland. The AUV and associated technical support were provided by Ocean Infinity and Deep Ocean Search. During this work, C.L.B. was in receipt of a grant from the Norwegian VISTA program. **Author contributions:** All authors took part in the acquisition and interpretation of the marine-geophysical data included in this paper. J.A.D. wrote the paper, and each co-author contributed comments and suggestions during a number of iterations of the text and figures. **Competing interests:** The authors declare no competing interests. **Data and materials availability:** All data are shown in the main text or the supplementary materials.

## SUPPLEMENTARY MATERIALS

[science.sciencemag.org/content/368/6494/1020/suppl/DC1](https://science.sciencemag.org/content/368/6494/1020/suppl/DC1)  
Materials and Methods  
Supplementary Text  
Fig. S1  
Table S1  
References (41–57)

28 August 2019; accepted 16 April 2020  
10.1126/science.aaz3059

By Tess Torregrosa

# You never know until you try

**O**ne hot July morning, I put on a business casual dress and headed to a biotech company for the first day of my internship. It felt daunting. Academia was my safe space; I had never worked anywhere else. When I arrived at the office, I was ushered into an orientation room, where people in formal business attire told me about the company's mission, products, and research areas. As the morning wore on, my unease about working for a for-profit company grew. I left the orientation wondering whether pausing my Ph.D. research to take on the internship had been a mistake.

When I started my Ph.D. program, I was open with my advisers about my career intentions, telling them that I wanted to work outside academia. I enjoyed doing research, but I wasn't interested in sitting at a desk writing grants for the rest of my career—something I knew I'd have to do a lot of if I became a professor.

My university had a program that enabled students to take a break from their research to do an internship at a company or government agency. My advisers told me about the program early on, and they encouraged me to plan on doing an internship during my final year. They thought that the experience would help me build connections and figure out what to do after graduation.

So I started to search for internships during my fourth year, at first focusing my search on science policy because I'd grown increasingly interested in that career path. I was disheartened to find that paid internships in science policy in my city were few and far between. I needed a solid paycheck and couldn't afford to relocate to another city temporarily, so I widened my search and started to look at positions in the biotech industry. My university had connections with local companies, so it was easier to find industry positions.

After the orientation session on my first day at the company, my manager sat me down to chat. I noticed her sneakers, colorful T-shirt, and cool haircut, and I remember thinking that she didn't look anything like the corporate representatives I'd listened to that morning. She asked me what I wanted to do after I graduated. After hearing of my interest in science policy, she asked, "Are you sure that the day-to-day experience of science policy professionals appeals to you?" I couldn't come up with an answer that felt satisfying; all I could say was that I



**"I'd spent years  
dreaming up potential jobs  
based on my interests."**

thought the work would be important. "You should take on a short-term position to find out if you'll like it," she advised. Suddenly, it hit me that I'd spent years dreaming up potential jobs based on my interests, but I didn't have any experience to know whether I'd like any of them.

Over the past 11 months, I've learned that her advice to give a new career path a try was spot on. I'd gone into my company internship expecting to do standard experiments devoid of creative thought. I was prepared to get bored quickly. But there's more creativity in industry than I imagined. Few products actually make it to market, and my company is willing to try different ideas and experimentation methods, even if

they ultimately lead to a dead-end. I have been surprised by how much I've enjoyed my work.

My experience at the company has been so positive that my manager and I agreed to extend my internship to a full year. My Ph.D. advisers even allowed me to include some of the experiments I performed at the company in my dissertation.

I successfully defended my Ph.D. this month, and I am on the hunt for my first post-Ph.D. job. I've been applying for scientist positions in industry—now convinced that industry is where I would like to work after all. On the side, I hope to volunteer for groups that are working in the realm of science policy. I haven't given up on that dream, but I understand that you never know whether you'll like something until you try it out. ■

Tess Torregrosa recently completed her Ph.D. at Northeastern University in Boston, and she is in the final month of her internship at Biogen. Do you have an interesting career story to share? Send it to [SciCareerEditor@aaas.org](mailto:SciCareerEditor@aaas.org).

## Pushing the Boundaries of Knowledge

As AAAS's first multidisciplinary, open access journal, *Science Advances* publishes research that reflects the selectivity of high impact, innovative research you expect from the *Science* family of journals, published in an open access format to serve a vast and growing global audience. Check out the latest findings or learn how to submit your research: **[ScienceAdvances.org](https://www.scienceadvances.org)**

Science  
Advances  
 AAAS

---

**GOLD OPEN ACCESS, DIGITAL, AND FREE TO ALL READERS**

---

# Custom Antibodies for Research & Immunotherapy

Antibody Development and Production Services



*ProMab Biotechnologies has two decades of experience generating highly specific and potent monoclonal antibodies*



- Mouse / Rat Monoclonal Antibody
- Rabbit Monoclonal Antibody
- Human Monoclonal Antibody



- Recombinant Antibody
- Bispecific Antibody
- Antibody Humanization



- Antibody Sequencing
- Stable Cell Line Generation
- Antibody Production

**All products are for research only**

Discover more | [www.ProMab.com](http://www.ProMab.com)



2600 Hilltop Dr, Building B, Suite C320, Richmond, CA 94806  
1.866.339.0871 | [info@promab.com](mailto:info@promab.com)